A Multi-messenger View of the Transient Sky

DISSERTATION

zur Erlangung des akademischen Grades

doctor rerum naturalium

(Dr. rer. nat.)

im Fach Physik

Spezialisierung: Experimentalphysik

eingereicht an der
Mathematisch-Naturwissenschaftlichen Fakultät
der Humboldt-Universität zu Berlin

von
M.Sc. Mbarubucyeye Jean Damascène

Präsidentin der Humboldt-Universität zu Berlin:
Prof. Dr. Julia von Blumenthal

Dekan der Mathematisch-Naturwissenschaftlichen Fakultät :
Prof. Dr. Emil List-Kratochvil

Gutachter/innen:	1. Prof. Dr. David Berge
	2. Prof. Dr. Nial Tanvir
	3. PD. Dr. Winter Walter
Tag der mündlichen Prüfung:	01.12.2025

Selbständigkeitserklärung

Ich erkläre, dass ich die Dissertation selbständig und nur unter Verwendung der von mir gemäß§7 Abs. 3 der Promotionsordnung der Mathematisch-Naturwissenschaftlichen Fakultät, veröffentlicht im Amtlichen Mitteilungsblatt der Humboldt-Universität zu Berlin Nr. 42/2018 am 11.07.2018 angegebenen Hilfsmittel angefertigt habe.

Berlin, May 28, 2025

Jean Damascène Mbarubucyeye

To my father Munyandinda Jean

Abstract

In this thesis, I use the multiwavelength (MWL) data from radio to γ-rays to study the broadband non-thermal emission processes in gamma-ray bursts (GRBs). To explore the highest-energy emission, I used observations from the High Energy Stereoscopic System (H.E.S.S.). H.E.S.S. is an array of five ground-based Imaging Atmospheric Cherenkov Telescopes (IACTs), which measure Very High Energy (VHE) γ-rays between $\sim$30 TeV to 100 TeV. Two decades ago H.E.S.S. started following up GRBs reported by other telescopes. Since then, nearly 200 GRBs have been observed. However, the first GRB that was firmly detected in the VHE range only occurred in 2018 by H.E.S.S.. This was due to improvements in the observation strategy, which allowed the detection of a second GRB by H.E.S.S. the year after. Using this follow-up strategy, in 2022 H.E.S.S. observed the brightest GRB of all time (the BOAT) `GRB 221009A` $\sim$52 hours post-trigger, although no significant emission was detected in 6 nights of observation. Upper limits are obtained and placed in the context with the radio, optical, X-ray, and lower energy γ-ray properties of this event. The generated H.E.S.S. upper limits help constrain the steep VHE γ-ray decays observed by *LHAASO*. The afterglow emission is modeled by a numerical calculation of a 1-zone Synchrotron Self-Compton (SSC) model, and parameters that best describe the data are obtained and presented in this work. The radio-to-X-ray observations are well explained by the synchrotron emission where the peak of the Spectral Energy Distribution (SED) occurs in the X-ray band. H.E.S.S. upper limits obtained in this work contributed to the bigger picture of understanding the emission mechanism of the BOAT despite the lack of detection. One of the SSC model that could constrain H.E.S.S. the upper limits given the predicted flux is presented in this work. This same procedure is also used to study a sample of 6 GRBs observed by H.E.S.S. between 2019 and 2022. The sample is selected based on specific criteria such as: being well-localized, having a known and low redshift (z$\leq$2), and having optical to X-ray data. Since no detection is observed in any of the GRBs, upper limits are computed and placed in the context of lower energy observations. The afterglow emission from these GRBs is modeled with the same numerical SSC model used for the BOAT when possible. While the lower energy observations are well described by the synchrotron emission of the SED, the H.E.S.S. upper limits do not constrain the SSC model primarily due to the strong attenuation of the VHE γ-ray emission caused by the Extragalactic Background Light (EBL). This appeared to be correct for both the constant density medium or wind medium. I particularly investigated the effect of the EBL for different redshifts and I found that for the H.E.S.S. upper limits to constrain the SSC model, the observation should be conducted for GRBs reported below a redshift of 0.5. A discussion of the implications of the results is given. Finally, an analysis of a sample of real-time neutrino alert follow-ups by H.E.S.S. between 2021 and 2022 is presented. The sample includes both public IceCube alerts, and others exchanged as part of the H.E.S.S. and IceCube joint program. The interesting coincidence with γ-ray sources is discussed in detail especially the Active Galactic Nucleus (AGN) `PKS 0625-35`, detected by H.E.S.S. back in 2018. Since no detection is obtained, upper limits are estimated and placed in context with the available MWL and archive data for well-localized events. Otherwise, the integral upper limit maps of the H.E.S.S. observations at 95% confidence limit are presented. In conclusion, the model and upper limits presented in this thesis are placed within the framework of the current understanding of the emission mechanism in GRBs. In addition, the current follow-up strategy of the neutrino events with current and future prospects of the VHE γ-ray detectors are also discussed.

Kurzzusammenfassung

In dieser Arbeit nutze ich Multiwellenlängen-Daten (MWL) von Radio- bis hin zu γ-Strahlen, um die Emissionsprozesse in Gamma-Ray-Bursts (GRBs) zu untersuchen. GRBs zeigen eine breitbandige, helle, nicht-thermische Emission, die anhand von Beobachtungen mit dem High Energy Stereoscopic System (H.E.S.S.) analysiert wurde. H.E.S.S. ist ein Array von fünf bodengestützten Imaging Atmospheric Cherenkov Teleskopen (IACTs), das sehr hochenergetische (VHE) γ-Strahlen im Bereich von $\sim$ 30 GeV bis 100 TeV misst. Vor zwei Jahrzehnten begann H.E.S.S. mit Nachverfolgungsbeobachtungen von GRBs, die durch Multi-Messenger-Beobachtungen gemeldet wurden. Seitdem wurden fast 200 GRBs beobachtet. Es dauerte jedoch bis 2018, bis der erste GRB im VHE-Bereich durch H.E.S.S. eindeutig nachgewiesen werden konnte, nachdem signifikante Verbesserungen in der Beobachtungsstrategie vorgenommen worden waren. Diese ermöglichten bis heute den Nachweis von zwei GRBs im VHE-Bereich durch H.E.S.S..

Mithilfe dieser Nachverfolgungsstrategie verfolgte H.E.S.S. im Jahr 2022 den hellsten GRB aller Zeiten (den sogenannten BOAT), `GRB 221009A`, $\sim$52 Stunden nach dem Ausbruch. Es wurde jedoch in sechs Nächten mit Beobachtungsdaten keine signifikante Emission festgestellt. Obergrenzen wurden bestimmt und im Kontext der Radio-, optischen, Röntgen- und γ-Strahlungseigenschaften dieses Ereignisses eingeordnet. Die in dieser Arbeit erzeugten Obergrenzen begrenzen zusätzlich die Steigung der *LHAASO* beobachteten Lichtkurve. Die Nachleucht-Emission wurde durch eine numerische Berechnung eines 1-Zonen-Synchrotron-Self-Compton-(SSC)-Modells modelliert, und die Parameter, die die Daten am besten beschreiben, wurden ermittelt und in dieser Arbeit vorgestellt. Die Beobachtungen von Radio- bis hin zu Röntgenstrahlen werden gut durch Synchrotronemission erklärt, wobei das Maximum der spektralen Energiedichte (SED) im Röntgenbereich liegt. Ein vollständiges Bild des BOAT konnte dank der H.E.S.S.-Obergrenzen trotz des fehlenden Nachweises gewonnen werden, jedoch sind diese nicht mit der Inversen-Compton-Komponente (IC) konsistent.

Zusätzlich wurde eine Analyse einer Stichprobe von sechs GRBs durchgeführt, die zwischen 2019 und 2022 beobachtet wurden, um nach einer möglichen Detektion der Nachleucht-Emission zu suchen. Die Stichprobe wurde anhand spezifischer Kriterien ausgewählt, nämelich gute Lokalisierung, bekannte Rotverschiebung ($z \leq 2$) und Beobachtungen im optischen bis Röntgenbereich sowie durch H.E.S.S. Die MWL-Lichtkurven wurden analysiert, und da in keinem der GRBs eine Detektion festgestellt wurde, wurden Obergrenzen berechnet und im Kontext der optischen bis Fermi Large Area Telescope (*Fermi*-LAT)-Beobachtungen eingeordnet. Die Nachleucht-Emission dieser GRBs wurde mit demselben numerischen SSC-Modell wie für den BOAT modelliert, mit Ausnahme von `GRB 210731A`, der autonom von H.E.S.S. beobachtet wurde, was auf eine prompte Emission oder eine sehr frühe Nachleucht-Emission hinweist. Während die niederenergetischen Beobachtungen (optisch bis Röntgen) gut durch die Synchrotronemission der SED beschrieben werden, liegt die VHE-Emission inkonsistent weit über der IC-Komponente, was hauptsächlich durch die starke Abschwächung der Extragalaktischen Hintergrundstrahlung (EBL) verursacht wird. Dies gilt sowohl für Medien mit konstanter Dichte wie das interstellare Medium (ISM) als auch für windige Umgebungen. Eine Diskussion der Implikationen der Ergebnisse wird gegeben.

Schließlich wird eine Analyse einer Stichprobe von Echtzeit-Neutrino-Alerts, die zwischen 2021 und 2022 von H.E.S.S. verfolgt wurden, präsentiert. Die Stichprobe umfasst sowohl öffentliche IceCube-Alerts als auch solche, die im Rahmen des gemeinsamen Programms von H.E.S.S. und IceCube ausgetauscht wurden. Die interessante Koinzidenzen mit γ-Quellen werden detailliert diskutiert, insbesondere ein Aktiver galaktischer Kern (AGN) `PKS 0625−35`, der 2018 von H.E.S.S. detektiert wurde. Falls keine Detektionen vorliegen, werden Obergrenzen berechnet und in den Kontext der verfügbaren MWL- und Archivdaten für gut lokalisierte Ereignisse gesetzt. Andernfalls werden die integralen Obergrenzenkarten der H.E.S.S.-Beobachtungen mit einer 95%-Konfidenzgrenze präsentiert.

Zusammenfassend werden das Modell und die Obergrenzen, die in dieser Arbeit vorgestellt werden, im Rahmen des aktuellen Verständnisses der Emissionsmechanismen in GRBs sowie der aktuellen und zukünftigen Nachverfolgungsstrategien für Neutrino-Ereignisse mit VHE-γ-Detektoren eingeordnet.

Acknowledgments

First and foremost, I would like to express my gratitude to my official supervisors Prof. Dr. David Berge, Dr. Stefan Ohm who introduced me to the DESY-H.E.S.S. group and supervised me daily until he left the institute. I thank Dr. Ifatch Sadeh who introduced me to the Gamma-ray bursts world and the machine learning topics for the first time. I am thankful for their guidance, support, advice, and expertise. I am also thankful for the opportunity to attend national and international conferences, where I had the privilege to present part of my work.

I would also like to extend my heartfelt thanks to my advisor, Dr. Sylvia Zhu, whose guidance greatly deepened my understanding of Gamma-ray bursts. Her continual support, insightful discussions, and encouragement were very useful throughout this process. I feel incredibly lucky to have had the opportunity to write this thesis under her supervision.

To the H.E.S.S.-GRB team of the H.E.S.S. collaboration, I have so much gratitude for each one of you, and I cherish the time I've spent learning and working with you, especially those I spent as the burst advocate. I am thankful to the whole H.E.S.S. collaboration for quick comments and discussions when I needed them the most, to improve my publications and for their guidance during my time as a day shifter. I thank all the desyian PhD students for making life inside and outside DESY look very easy for me. A big thank you also goes to Marc Klinger who is also my friend for explaining me the basics theory behind the GRB afterglows and so many discussions and laughs we held together both inside and outside DESY. Though my time in DESY institute was challenged by the COVID pandemic, I felt very supported by the flexibility and guidance offered by DESY, so thank you! I thank Dr. Brian Reville and his group at MPIK for explaining me his SSC model for GRB afterglows, which I applied through out my thesis, during my stay at MPIK.

I thank everyone who helped me review my thesis. Victor, Tim, Zack, Sylvia, Dan, and David all took the time to read one chapter or many parts of the thesis and provided useful feedback that helped me to improve both the text and the clarity of my objectives.

A very special thank you to my officemates and friends: Ruslan, Jowita, Tim, Dima and Abhay. you guys made my PhD time so much more enjoyable and I can only pray that my future officemates are as supportive and hilarious.

Thank you Prof Felicia McBride and Prof Nkundabakura Pheneas for introducing me to the world of astronomy and astrophysics. Special thanks to McBride, for leading my graduate (masters) thesis and helped improve my first academic publication and so many discussions we had about life as a scientist and as a human being outside academia.

To my friends and family, you have made my life so much richer, and I am grateful for all that we have shared together. You have seen me through graduate school, a global pandemic and everything in between, so thank you. I could not have done any of this without your love and support.

Finally, I would like to thank my wife and kids for always standing by me, understanding, patience and supporting me through the difficulties of the long path of the PhD. Your love and support pushed me and kept me alive up to this point. Thank you!

List of Acronyms

AGN	active galactic nucleus
BAT	Burst Alert Telescope
BOAT	brightest of all time
CTAO	Cherenkov Telescope Array Observatory
CR	cosmic ray
DM	Dark Matter
EM	Electromagnetic
EGRET	Energetic Gamma-Ray Experiment Telescope
EBL	extragalactic background light
Integral	International Gamma-Ray Astrophysics Laboratory
ISM	Interstellar Medium
IC	Inverse Compton
IR	Infrared
IACT	Imaging Atmospheric Cherenkov Telescope
UV	Ultraviolet
H.E.S.S.	High Energy Stereoscopic System
GRB	Gamma-Ray Burst
HAWC	High Altitude Water Cherenkov Observatory
KN	Klein-Nishina
LAT	Large Area Telescope
LHAASO	Large High Altitude Air Shower Observatory
MAGIC	Major Atmospheric Gamma Imaging Cherenkov Telescope
SED	spectral energy distribution
FoV	Field of View
SAS-2	Small Astronomy Satellite (SAS-2)
SWGO	Southern Wide-field Gamma-ray Observatory
SN	Supernova
SSC	Synchrotron Self-Compton emission
SNR	Supernova remnant
TDE	Tidal Disruption Event
VERTAS	Very Energetic Radiation Imaging Telescope Array System
VHE	Very High Energy
UHECR	Ultra-High Energy Cosmic Ray

Contents

Abstract III

Kurzzusammenfassung V

Acknowledgments VII

List of Acronyms IX

List of Figures XV

List of Tables XIX

1. Introduction 1

2. Gamma-Ray Bursts 5

- 2.1. Introduction . . . 5
- 2.2. History of GRB observations . . . 6
- 2.3. Communication Networks . . . 11
- 2.4. The Fireball Model . . . 12
- 2.5. Prompt Emission . . . 14
  - 2.5.1. Spectral properties . . . 14
- 2.6. Afterglow emission . . . 17
- 2.7. Particle acceleration and radiation mechanism in GRBs . . . 19
  - 2.7.1. Introduction . . . 19
  - 2.7.2. Synchrotron Radiation . . . 20
  - 2.7.3. Inverse Compton scattering . . . 21
  - 2.7.4. Synchrotron-self-Compton emission . . . 22
- 2.8. HE and VHE Spectrum . . . 23
  - 2.8.1. EBL absorption of VHE γ-rays . . . 26
- 2.9. Multi-messenger Observations . . . 28
- 2.10. Conclusion . . . 29

3. The High energy stereoscopic system (H.E.S.S.) experiment 31

3.1. Cosmic rays and γ-ray production 31
3.2. γ-ray astronomy with IACTs 33
  3.2.1. Atmospheric Air Showers 33
  3.2.2. Cherenkov Radiation and its properties 36
3.3. The H.E.S.S. telescope Array 38
3.4. The H.E.S.S. data acquisition system 39
3.5. H.E.S.S. data analysis 40
  3.5.1. Data calibration 40
  3.5.2. Data quality check 43
  3.5.3. Shower reconstruction 45
  3.5.4. Gamma-hadron separation 47
  3.5.5. Acceptance effects and Effective area 49
  3.5.6. Sky Maps 51
  3.5.7. Background estimation 51
  3.5.8. Signal extraction and significance estimation 52
  3.5.9. Flux and Spectral information 54
  3.5.10. Tools and analysis configuration 55
3.6. Conclusive remarks and outlooks 56

4. GRB 221009A: The BOAT 57

4.1. GRB 221009A: Observations 60
  4.1.1. Initial Discovery 60
  4.1.2. H.E.S.S. Observations 61
4.2. H.E.S.S. analysis and results 62
4.3. Multi-wavelength context 68
  4.3.1. *Swift*-XRT analysis 68
  4.3.2. *Fermi*-LAT analysis 72
  4.3.3. *LHAASO* results in context 75
4.4. Modeling the afterglow emission 75
  4.4.1. Introduction 75
  4.4.2. A brief description of the 1-zone SSC model 78
  4.4.3. Model prediction and Discussion 78
4.5. Concluding remarks 79

5. A sample of long GRBs observed by H.E.S.S. 83
5.1. Introduction 83
5.2. Sample selection 83
5.3. Observations 86
    5.3.1. *GRB 190627A* 88
    5.3.2. *GRB 201024A* 88
    5.3.3. *GRB 210610B* 88
    5.3.4. *GRB 210619B* 89
    5.3.5. *GRB 210731A* 90
5.4. Data analysis and results 90
    5.4.1. *Swift*-XRT analysis 90
    5.4.2. HESS analysis 94
    5.4.3. *Fermi*-LAT analysis 97
    5.4.4. Optical data 97
5.5. Afterglow Modeling 101
5.6. Discussions of individual GRBs 101
5.7. Conclusions 108

6. H.E.S.S. follow-up observations on H.E IceCube neutrino events 111
6.1. Introduction 111
6.2. Origin and propagation processes of neutrinos 113
6.3. H.E.S.S. neutrino follow-up program 115
6.4. Sample characterization 115
6.5. H.E.S.S. data analysis 116
6.6. Multiwavelength observations 117
    6.6.1. *Fermi*-LAT analysis 117
    6.6.2. *Swift*-XRT analysis 118
    6.6.3. Optical data 118
    6.6.4. Other multiwavelength data 118
6.7. Results and discussion of individual events 120
    6.7.1. IC–211125A 120
    6.7.2. IC-211208A 120
    6.7.3. GFU PKS 0829+046 124
    6.7.4. GFU PKS 0625–35 125
    6.7.5. IC-220425A 126
    6.7.6. GFU 1ES0229+200 126

6.8. Conclusions 127

7. Conclusions and Outlook **129**

Bibliography **131**

Appendices **153**

A. Flux re-scaling with different redshift **153**

A.1. The Inverse Square Law and re-scaling the fluxes 153

B. Numerical calculation of 1-zone SSC afterglow model **155**

B.1. Shock parameters 155

B.2. SSC spectrum parameters 159

List of Figures

2.1. Angular distribution . . . 7
2.2. Bimodal distribution of GRBs . . . 7
2.3. Redshift distribution . . . 9
2.4. Swift . . . 10
2.5. Fermi Telescope . . . 10
2.6. General Coordinates Network (GCN) . . . 12
2.7. Fireball Model of GRBs . . . 13
2.8. GRB lightcurves . . . 15
2.9. GRB 990123 spectrum . . . 16
2.10. Canonical XRT LC . . . 18
2.11. SED . . . 25
2.12. EBL wavelength dependence . . . 27
2.13. EBL absorption coefficient. . . . 28

3.1. All particles cosmic-ray spectrum . . . 32
3.2. Extensive Air Shower: Heitler Model . . . 34
3.3. Development of atmospheric air showers . . . 35
3.4. Cherenkov Radiation . . . 36
3.5. H.E.S.S. Telescope . . . 39
3.6. Pedestal Distribution . . . 41
3.7. Flat-field distribution . . . 42
3.8. Geometrical representation of Hillas parameters . . . 46
3.9. Hillas Parameters and direction Reconstruction . . . 47
3.10. Comparison of Hillas and ImPACT analysis . . . 48
3.11. Gamma-Hadron separation with BDT . . . 50
3.12. Ring and Reflected background model . . . 53

4.1. Comparison of EBL absorption factor from known VHE GRBs . . . 58
4.2. GBM and XRT fluence distribution. . . . 59
4.3. Comparison of XRT emission from known VHE GRBs . . . 61

4.4. GRB visibility 62
4.5. Atmospheric coefficient 63
4.6. Atmospheric correction 65
4.7. Significance and excess maps 67
4.8. GRB 221009A Upperlimits 69
4.9. Extended *Swift*-XRT time slices against H.E.S.S. observations window where the gray windows enclose the XRT data used in the per-night analyses. 71
4.10. The differential energy flux spectrum E^2 dN/dE derived from fitting the XRT data. 73
4.11. The H.E.S.S. integral energy flux upper limits (red circles; 95% C.L.) are derived assuming an intrinsic E^{-2} spectrum. The automated XRT data (gray) are obtained from the Burst Analyser [226]; multiple XRT observations around the H.E.S.S. observations are then combined and refit (blue, 1σ uncertainty). Note that the Burst Analyser assumes a larger value of intrinsic absorption than we find in our analysis and therefore returns a larger unabsorbed energy flux. The extension of the H.E.S.S. error bars in the x direction, depicting the duration of the H.E.S.S. observations, is smaller than the size of the markers. 73
4.12. The H.E.S.S. integral energy flux upper limits (red circles; 95% C.L.) are derived assuming an intrinsic E^{-2} spectrum. The *LHAASO* energy fluxes integrated within the [1–5] TeV energy range (red points; shared in private communication by *LHAASO* personnel) are shown for comparison to *HAWC* (darkred) and H.E.S.S. in the same energy range (in red). The black point are the *LHAASO* energy fluxes integrated over 0.3 TeV to 5 TeV. The green and magenta curves indicate the slow and steep decay segments of the broken power law model fitting the *LHAASO* data in different energy ranges, respectively. 76
4.13. The H.E.S.S. 95% upper limits on Night 3 (red) are plotted along with the XRT (blue, 1σ) best-fit spectrum and LAT (purple, 95% C.L.) upper limit, as well as publicly available radio data from the Submillimeter Array (black open circle; [239]) and an optical flux (green square; extracted from Figure 2 of [240]) in a multiwavelength SED. An example set of synchrotron (blue) and SSC (red) emission components — arising from a single, partially cooled electron population described in Table 4.6 — are also shown to illustrate a possible explanation of the multiwavelength observations. 80

5.1. A sample of observed H.E.S.S. GRBs 85
5.2. GRB fluence distribution 87
5.3. MWL *Swift*-XRT and H.E.S.S. LCs 91

5.4. MWL *Swift*-XRT and H.E.S.S. LCs. Continued'... 92

5.5. MWL *Swift*-XRT and H.E.S.S. LCs. Continued'... 93

5.6. GRB 210610B Differential fluxes 96

5.7. GRB 210610B Differential fluxes 99

5.8. Application of modeling GRB 190829A using the method described above 102

5.9. *GRB 190627A* modelling 104

5.10. *GRB 201024A* modelling 104

5.11. *GRB 210610B* modelling 105

5.12. *GRB 210619B* modelling 106

5.13. GRB Amati-relation 107

5.14. MWL SED of GRB 210731A 108

5.15. MWL SED of GRB 190627A 110

6.1. Arrival direction 112

6.2. Neutrino propagation 114

6.3. The *Fermi*-LAT analysis results for the blazar *PKS 0735+178 (4FGL J0738.1+1742)*, which coincides with a neutrino event (*IC-211208A*), are presented. Various Skymaps illustrate the IceCube 90% containment region (yellow ellipse), with the blazar's position marked in red alongside the neutrino event's reported position (yellow cross). The maps display: (a) the counts of detected γ-ray-like events, (b) the predicted γ-ray event counts from the model, (c) the excess counts calculated as the difference between observed data and the model, and (d) the statistical significance of the excess counts. 119

6.4. `IC-211125A` integral upper limits map of H.E.S.S. observations at 95% C.L. The red point shows the *Fermi*-LAT position of the neutrino counterpart within the reported 90% of the positional uncertainty. In addition, the reported classical nova counterpart was found to be away of the revised and the initial 90% and 50% positional uncertainty but within the H.E.S.S. field of view. 121

6.5. The SED of the candidate source 4FGL J0258.1+2030 with *Fermi*-LAT upper limits (orange) and *Swift*-XRT data (red). The simultaneous H.E.S.S. follow-up of this neutrino event resulted in 95% C.L. upperlimits (magenta). 121

6.6. `IC-211208A` integral upper limits map of H.E.S.S. observations at 95% C.L. estimated within [0.433 - 10] TeV energy range. The map also shows 3 possible gamma-ray counterparts of the neutrino event. Potential interest by H.E.S.S. was directed towards the flaring (in that period) blazars (red) although it was located outside the error positions of 90% reported in GNC (yellow) and two other re-estimated error radius (dotted green contour 50% and solid green contour 90%) on the neutrino position. 122

6.7. The SED of PKS 0735+178 in December 2021 is shown with archival data spanning from radio to UV bands (gray filled circles). Spectra from *VERITAS* and H.E.S.S. were averaged over the ToO observation period. *Fermi*-LAT spectrum was averaged over four weeks. A magenta shaded region indicates the best-fit log-parabola model to the *Fermi*-LAT spectrum. Figure obtained from [190]. . . 123

6.8. The SED of the PKS 0829+046 (a potential counterpart of the neutrino event) using data from H.E.S.S., *Fermi*-LAT, *Swift*-XRT, and ATOM observed simultaneously. Archival data are displayed in gray. The multiwavelength observations are averaged over the two days of the H.E.S.S. ToO observation period. 124

6.9. The SED of the blazar PKS 0625−35 as observed by H.E.S.S. corrected for EBL effect (magenta) and simultaneous to *Fermi*-LAT (green), *Swift*-XRT − UVOT (in different filters), and ATOM (in different filters). Shown are also the H.E.S.S. observation of 2018 corrected for EBL (in orange) [298] and archival data (in gray).125

6.10. `IC-220425A` integral upper limits map of H.E.S.S. observations at 95% C.L. The H.E.S.S. observations are performed outside the re-estimated (90% and 50%) error radius of the neutrino position. The green star shows the updated neutrino position with its statistical error positions refined offline. 126

6.11. The SED of the HBL `GFU 1ES0229+200` showing simultaneous data from H.E.S.S., *Fermi*-LAT, *Swift*-XRT, and ATOM (in its 3 filters) all of which are averaged over 5 nights spanning the ToO observation period. Archival data are displayed in gray. 127

List of Tables

4.1. H.E.S.S. observations of GRB 221009A. Column 2 denotes the number of nights after T_0. Columns 3 and 4 represent the run start and end time since T_0, in seconds, respectively. Column 5 shows the average zenith angle under which the observations were conducted and column 6 shows the Atmospheric Transparency Coefficient (ATC). 64

4.2. Source statistics of GRB 221009A per each night after correcting for atmospheric effects. The results are derived using ***loose_ImPACT*** analysis configuration. . 66

4.3. Results of a 1D reflected background analysis. Column 1, 2 & 3 denote the reference energy, minimum and maximum energy in different bins, respectively. Column 4, shows the 95% C.L differential flux upperlimits. The last three columns represent the ON and OFF counts in different energy bins as well as the ratio between the on-source and off-source exposure in each bin, respectively. Note that all flux upperlimits are EBL corrected. 70

4.4. Enlarged *Swift*-XRT time slices. 71

4.5. Results of analyses of XRT and H.E.S.S. data. The entries in the first column correspond to the second column of Table 4.1. The second through fourth columns show the results of fitting XRT data in time intervals bracketing the nights during which H.E.S.S. observed the GRB, with 1σ uncertainties (statistical only). The last column lists the H.E.S.S. energy flux upper limits for the time interval defined by the third and fourth columns of Table 4.1. The XRT energy flux is calculated in the 0.3–10 keV range and the H.E.S.S. energy flux in the 0.65–10 TeV range. . 74

4.6. Parameters used for single zone model fit, adopting the constant external-density solution of Bland & McKee [92]. 79

5.1. Properties of the GRBs selected satisfying our selection criteria. The three first columns correspond to the name of the GRB in standard nomenclature, the name of the satellite that initially detected and reported the GRB, and trigger number for that satellite, respectively. The fourth column shows the T_{90} in seconds. The fifth through seventh column show the Right Ascension (R.A.), declination (Decl.), and the positional error in arc-seconds, reported by the detecting satellite, respectively. Reported also are the energy fluence in 15–150 keV energy range with statistical errors (90% confidence region) in the column 8 to 10, respectively . The two last column shows the redshift of the source and the average zenith angle at which HESS observed the source. 84

5.2. The *Swift*-XRT results of the spectral analysis for all GRBs from the sample. The first column corresponds to the GRB name in the standard nomenclature. The second column is the number of night that a GRB is observed with reference to HESS observations. The following three columns show the starting and ending time of observation after the trigger, and the exposure time in kilo-seconds. The fifth and sixth columns show the results of fitting *Swift*-XRT data in time intervals bracketing the nights during which H.E.S.S. observed the GRB, with 1σ uncertainties (statistical only) with the fitting statistics shown in the last column. The eighth column corresponds to the *Swift*-XRT integrated energy flux, calculated in the 0.3–10 keV energy range. The ninth and tenth columns show the Galactic columns density obtained with the automatic data analysis and the intrinsic column density obtained after re-fitting the data (with 1σ statistical uncertainty). 95

5.3. H.E.S.S. observations of the GRB sample. Column 2 denotes the number of nights after T_0. Columns 3 and 4 represent the run start and end time since T_0, in seconds, respectively. Column 5 shows the average zenith angle under which the observations were conducted. The last two columns indicate which telescopes participated in the observation and the atmospheric transparency coefficient during the observation respectively. For the runs without ATC values in the H.E.S.S. database due to technical issues, we assessed the good weather and good atmospheric condition, by looking visually whether the trigger rates are consistent with internal H.E.S.S. recommended values. 98

5.4. Results of the H.E.S.S. analysis for all GRBs from the sample. Column 1 corresponds to the name of the GRB in standard nomenclature, and the second column represents the the starting time of the HESS observation in UTC. The following columns represent the number of ON and OFF event counts, and α which the exposure ratio between the ON and OFF regions, and the excess counts and the significance. The last columns represent the energy thresholds, and the integral energy flux upper limits (EBL-corrected) above energy threshold, respectively. . 99
5.5. Results of the *Fermi*-LAT analysis for all GRBs from the sample. Column 1 represents the name of the GRB for which *Fermi*-LAT observations exists and in Column 2 we show the resulting differential energy upperlimit flux for each of the GRB from our sample. 100
5.6. Results of the optical flux calculation for all GRBs from the sample. Column 1 represents the name of the GRB for which optical observations simultaneous to H.E.S.S. observation times exist and in Column 2 we show the central wavelengths (in nanometers) for each GRB. In column 3 and 4, we present the energy (in eV) and the differential energy flux for each GRB from our sample. 100
5.7. Fitting parameters for all GRBs for uniform medium (constant density). 101
5.8. Fitting parameters for all GRBs for windy medium. 102

6.1. A sample of six neutrino ToOs observed between 2021–2022. The first and second columns represent the name of the ToO and associated sources, respectively. . . . 116
6.2. *Swift*-XRT data analysis parameters. The unabsorbed energy flux is obtained by integrating over the full energy range 0.3-10 keV, correcting for the Galactic column density value [292]. 118

1. Introduction

Since ancient times, humanity has gazed skyward, contemplating the mysterious phenomena they witnessed. With the introduction of optical telescopes, we acquired the capacity to closely examine celestial objects, revealing their origins and the fundamental physical processes at play. However, it is important to note that the human eye's sensitivity is restricted to a narrow segment of the Electromagnetic (EM) spectrum, rendering most of the radiation emitted by astrophysical objects imperceptible to us. In the realm of extremely high energies, surpassing the optical spectrum by more than a hundred thousand times in energy, reside the γ-rays. In addition, γ-rays are neutral charged, therefore, they could not be deflected by interstellar magnetic filed. With this property, the source of γ-rays remain traceable due to their straight line paths that point back to their source of origin called particle accelerators.

The γ-rays are produced through different mechanisms such as the decay of neutral pions (π^0), synchrotron radiation, and inverse Compton scattering. These production mechanisms can be tested and verified through various experimental setups in laboratory and astrophysical observations. Therefore, they offer a unique opportunity to explore particle physics phenomena in astrophysical objects and systems. The γ-ray energy window differs from the low-energy waveband due to their production mechanisms that involve non-thermal processes. Non-thermal radiation usually indicates that the production of photons with γ-ray energies cannot be produced through thermal processes. The absence of a heating mechanism to produce effectively γ-rays, implies the existence of an efficient particle acceleration mechanism.

In 1912, Victor Franz Hess discovered cosmic rays (CRs) [1]. CRs are charged particles produced in astronomical sources. The CRs detected at Earth span a very wide energy range ($\sim 10^{15}$ eV), and the Ultra High Energy CRs (UHECRs) with energy surpassing $\sim 10^{18}\,$eV are expected to come from extragalactic sources. However, the sources of UHECRs are still unclear. The interactions of CRs were predicted to produce high-energy photons in the γ-ray energy range ($>$ 100 keV) in the electromagnetic spectrum. Among the candidates of potential origin of γ-rays with energy above $10^{18}\,$eV there are Gamma-Ray Bursts (GRBs, which are the focus of this thesis).

GRBs are brief, extremely energetic explosions that occur and brighten the entire universe in just a few seconds. They emerge after the merger of two compact objects or the collapse of a supermassive star, where in either case, a highly collimated, narrow stream of particles moving at relativistic speeds (referred to as a Jet) is launched. In principle, GRBs offer a good opportunity to study particle acceleration and they could provide enough magnetic field to confine high-energy (HE; $100\,\mathrm{MeV} < \mathrm{E} < 100\,\mathrm{GeV}$) particles.

The first GRB was accidentally identified by the United States Vela satellites, which were launched in the early 1960s to monitor Russian activities regarding nuclear weapon tests in space. Though they did not uncover any nuclear weapon test, they unveiled a new astrophysical phenomena called the GRB. The Vela discovery was only made public after a few years of conducting the detection of dozens of GRBs confirming that they were indeed of astrophysical origin [2].

Given that the Earth's atmosphere acts as a formidable shield against γ-rays, their detection necessitates observation either from space or indirectly from the ground. Space-based detectors can only observe up to GeV energies. At these energies, γ-rays are not severely affected by the atmospheric absorption that affect high-energy γ-rays. In addition, their physical size and weight constraints limit the volume of detector material, which impact their ability to detect high-energy (TeV and above) γ-rays efficiently. TeV and higher-energy γ-rays are detected indirectly with ground-based detectors. Ground-based detectors are characterised by a large effective area, allowing them to detect even lower fluxes of higher-energies.

Some important GRB missions after their discovery by Vela include the (to name few): The Burst and Transient Source Experiment (BATSE) which was part of the Compton Gamma-Ray Observatory (CGRO) launched in 1991 and retired in 2000. *BATSE* played significant discovery such as GRB isotropic distribution across the sky and identification of two GRB classes (long and short durations bursts). Later in 1996 the *BeppoSAX*, Italian-Dutch X-ray satellite was launched and lasted until 2002. *BeppoSAX* provided precise localisation of GRBs and enabled detection of long-lived emission in X-ray, optical and radio wavelengths. It also confirmed the cosmological origin of GRBs by associating them with distant galaxies. The current important space-based GRB detectors, include *Swift* and *Fermi* observatories. *Swift* provides rapid localisation and follow-up, enhancing understanding of the short and long lived GRBs. On the other hand, *Fermi* extended observations into the GeV range capturing high-energy details of GRBs. In the contemporary landscape of γ-ray astronomy, the Large Area Telescope aboard the Fermi satellite (Fermi-LAT) holds a prominent position as one of the foremost γ-ray observatories [3], observing in $20\,\mathrm{MeV}$ up to $\geq 300\,\mathrm{GeV}$ energy ranges.

Observations of Very High Energy (VHE; $100\,\mathrm{GeV} < \mathrm{E} < 100\,\mathrm{TeV}$) γ-rays are conducted by ground-based facilities known as Imaging Atmospheric Cherenkov Telescopes (IACTs), designed to detect γ-ray-induced air showers. Air showers are produced when a primary γ-ray (photon) enters our atmosphere and interacts with particles resulting in a cascade of secondary particles which, since they are moving faster than the speed of light, emit the so-called Cherenkov radiation. This radiation can be seen from the ground based observatories as short-duration (usually few tens of nano-seconds) with a wavelength ranging from near ultraviolet (UV, 300 nm) to visible (optical, 700 nm) light covering large areas on the ground. Currently, there are several noteworthy facilities in operation including the High Energy Stereoscopic System (H.E.S.S.) [4], the Major Atmospheric Gamma Imaging Cherenkov Telescope (MAGIC) [5], the Very Energetic Radiation Imaging Telescope Array System (VERITAS) [6]. There exists an alternative technique to study Cherenkov radiation produced by air shower particles using the large water tanks. Among the current water Cherenkov radiation detector one can list are: the High Altitude Water Cherenkov Observatory (HAWC) [7], the Tibet ASγ experiment [8] and the Large High Altitude Air Shower Observatory (LHAASO) [9, 10]. In addition, the ongoing data collection by LHAASO, as well as the prospective Southern Wide-field Gamma-ray Observatory (SWGO) [11, 12], and the fourth-coming Cherenkov Telescope Array (CTA) [13] are poised to significantly enhance current measurements in this field.

Many sources of VHE γ-rays have already been identified. These include Galactic sources such as Pulsar Wind Nebulae (PWN), Supernova Remnants (SNRs), pulsars, binaries, and stellar clusters, as well as extragalactic sources like Active Galactic Nuclei (AGN), starburst galaxies. In addition, recent studies have shown that GRBs are also sources of VHE γ-ray [14–17], but identifying the mechanism behind the VHE emission component remains a challenge. Despite these progresses, there are still unanswered questions about the origins of VHE γ-rays from some sources. For example, are GRBs the sources of the cosmic ray spectrum? What is the origin of HE astrophysical neutrinos, and what astrophysical processes are responsible for their production?

The advancements in instrumentation over the last century have marked the beginning of the era of multi-messenger astronomy. Recently, the discovery of neutrino and gravitational wave messengers, and their connections to astrophysical sources, has been witnessed [18, 19], marking the discovery of new messengers beside γ-rays and CRs. Multi-messenger observations aim to address these unanswered questions through collaborations between different infrastructures and scientific communities. For instance, ongoing follow-up observations of AGN, discussed in this thesis, are being conducted to search for neutrinos. Additionally, GRBs, which are the focus of this thesis, are candidates for producing neutrinos and GWs.

This thesis is structured as follows: We begin with a general introduction to GRBs as VHE sources with a focus on prompt and afterglow properties in Chapter 2. Chapter 3 is dedicated to providing an overview of the technical setup and fundamental operational principles of the H.E.S.S. experiment. It also introduces the key physical principles underpinning ground-based γ-ray astronomy utilizing Imaging Atmospheric Cherenkov Telescopes (IACTs). In addition, it briefly covers the customary methods for analysis, reconstruction, and calibration within the framework of the H.E.S.S. experiment. Furthermore, this chapter outlines the tools and techniques employed in the analyses presented in this work and introduces briefly different satellite for which the data in this thesis were used. In chapter 4 we present and discuss the H.E.S.S follow-up observations of the brightest GRB of all time (BOAT). We discuss the SSC model and discuss the multi-wavelength modelling from different observations during the H.E.S.S. observation period. Chapter 5 is dedicated to the analysis of selected long-duration GRBs as observed by H.E.S.S. since the upgrade of its biggest camera. We will also apply an analytical SSC model to assess the VHE γ-ray emission from these GRBs. In chapter 6, we present the analysis of real-time follow-ups of IceCube alerts on high-energy neutrino events by H.E.S.S. Last but not least we close with our conclusions and outlook in Chapter 7.

2. Gamma-Ray Bursts

2.1. Introduction

Our understanding of the γ-ray energy regime above 100 GeV (the VHE γ-ray domain) has significantly improved with the discovery of transients such as GRBs. Energetic photons are produced by highly relativistic particles, indicating that GRBs are likely generated by highly relativistic matter. GRBs originate from the deaths of very massive stars and the mergers of compact objects such as neutron stars. GRBs are classified as multi-messenger events due to their expected neutrino emission and their association with the recent detection of gravitational waves (GW 170817). GRBs are some of the most violent explosions in the Universe. A typical GRB emits a huge amount of energy, ranging from $10^{48} - 10^{54}$ erg, within mere seconds to hundreds of seconds. In comparison, a Solar rest mass energy is about $10^{54}\, erg$. The initial GRB emission phase, during which bursts of γ-rays are emitted, is called *the prompt* emission (see Sect. 2.5). Due to Earth's protective atmosphere, we are shielded from γ-rays with energies that are produced in GRB prompt emission, making observation of these luminous events best suited for instruments beyond our planet's confines. Ever since the Vela satellites detected the initial GRB in 1967 [2], multiple generations of scientific instruments have been developed to illuminate this field of study (see section 2.2). With their energy releases and the relativistic effects they exhibit, GRBs are excellent laboratories for testing particle acceleration in relativistic conditions.

On average, GRBs are observed at a rate of about 1-3 events per day appearing randomly across the sky [20], and the estimated rate of GRBs in the entire Universe varies from 1 to 10 events per $\mathrm{Gpc}^3/\mathrm{yr}$ (see [21, 22] for detailed review). In this chapter, I begin by providing a historical background on GRBs and discussing the observed properties as obtained from various γ-ray observatories over the past few decades. I highlight the important discoveries and instruments that enabled them. I then continue to review the key characteristics of GRB prompt and afterglow emissions observed over the past few decades. I explore how GRBs and their afterglow significantly improve our understanding on the GRB research and highlighting significant events and models that have shaped our understanding of these phenomena.

2.2. History of GRB observations

GRBs were first discovered by the United States (US) spy satellites called "Vela" in the 1960s, but their discovery was not publicly disclosed until the 1970s [2, 23]. During the first few decades, the number of proposed GRB models exceeded the number of actual GRB detections. Before the 1960s there were a lack of γ-ray observatories capable of detecting high-energy γ-rays from space. Most of the early space missions focused mainly on low-energy wavebands, leaving γ-rays largely unexplored. Another challenge is that with their unpredictable nature, GRBs presented no regular pattern or known source. Their brief duration often lasting few seconds to minutes makes them difficult to detect without dedicated, wide-field γ-ray detectors. The early γ-ray detectors had limited technology, since they were not specifically designed to study GRBs, and therefore their equipment lacked the sensitivity needed for systematic observation of GRBs. Such detectors could only provide rough, imprecise (poor) localization of GRBs in the sky. In addition, GRBs initially were thought to be of terrestrial origin, which delays their recognition as a cosmic phenomenon, and therefore, for the first few decades no known theoretical framework existed predicting such energetic bursts from cosmic sources.

Significant discoveries started in the early 1990s with the launch of the Compton Gamma-ray Observatory (CGRO), equipped with the Burst and Transient Experiment (BATSE, with energy range [10 keV − 100 MeV]) and the Energetic Gamma Ray Experiment Telescope (EGRET, with energy range [20 MeV − 30 GeV]) as well as two other detectors. During its mission, EGRET was the first to detect high-energy GeV emission from GRBs showing the first hints of the high-energy spectra of GRBs [24]. Meanwhile, BATSE over its entire mission was able to detect a total of 2704 GRBs and substantial evidence for a non-thermal origin for the emission. BATSE confirmed that the angular distribution of the detected GRBs in the Universe is isotropic (see skymap[1] in Figure 2.1), indicating that they originate either in distant Galaxies or very locally [25]. BATSE also made a significant discovery regarding the prompt[2] duration of GRBs, revealing a notable bimodal distribution with a dip occurring at $\geq 2\,\mathrm{s}$ (see Figure 2.2). The duration of GRBs is commonly measured using T_{90}, denoting the time interval during which 5% to 95% of the counts are accumulated by the detector. This distribution highlights the existence of two distinct types of GRBs: short-duration GRBs (sGRB, $\mathrm{T}_{90} < 2\,s$) and long-duration GRBs (lGRB, $\mathrm{T}_{90} > 2\,s$). The 2-sec division is more of the useful guideline and not a hard boundary as there is a significant overlap between the two distribution. Within the BATSE energy band, the proportion of short to long GRBs stands at 1:3. It's important to note that this ratio is not consistent across all energy ranges and is influenced by factors such as instrument sensitivity [27].

---

[1] `https://gammaray.nsstc.nasa.gov/batse/grb/skymap/`

[2] refers to the initial, intense burst of γ-ray that is emitted during the early phase of the GRB event.

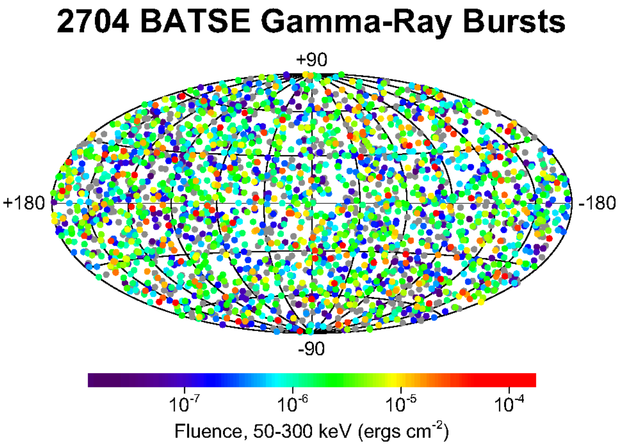

Figure 2.1.: Illustration of the spatial distribution of GRBs in the BATSE 4B catalogue [20]. The distribution is presented in the equatorial coordinate system using a Mollweide projection. Each point represents a GRB, and the color indicates the GRB fluence in the 50–300 keV band. The plot is modified from [26]

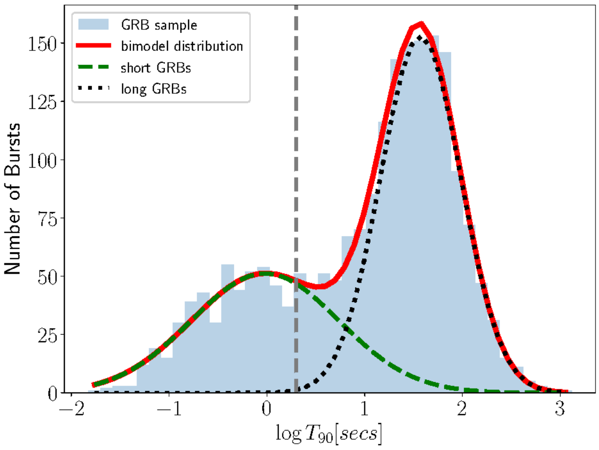

Figure 2.2.: Bimodal distribution of the GRBs. T_{90} distribution for GRBs reported in 4B BATSE catalogue. Short bursts have durations of less than 2 seconds, while long bursts last for longer periods. The dashed line indicate the classical duration separation between the long and the short GRBs. While the green and black dashed distribution indicate the 1-D Gaussian distribution indicating the distribution of the short and the long GRB distribution respectively. The red curve is the combination of the green and black curves.

In addition, it was found that most prompt emission spectra could be fit by an empirical function, called the Band function [28], a smoothly broken power law with a specific curvature (see also Eq. 2.1), and the properties of the Band function indicated a non-thermal origin of the γ-rays. However, while BATSE was able to detect hundreds of GRBs each year during the 1990s, the localization uncertainties it provided were too extensive for other telescopes to carry out follow-up observations.

The new era in GRB research was introduced following the launch of the Italian-Dutch satellite called Beppo-SAX in April 1996. BeppoSAX was equipped with three distinct instruments, each serving a specific purpose. These instruments included the Gamma-Ray Burst Monitor (GRBM), the Wide Field Camera (WFC) comprising two units, and four Narrow Field Instruments (NFI). They operated within different energy ranges, spanning from 60 to 700 keV, 2 to 30 keV, and 0.1 to 120 keV [29], and the two larger FoV instruments (GRBM and WFC) would detect prompt emission. The whole satellite could then re-point so that the NFI could detect late time, lower energy emission. This design made BeppoSAX exceptionally well-suited for detecting GRB X-ray long lasting emissions [30]. Due to the fact that it could provide localization with uncertainties of 3 arcminutes [31], the discovery of the first optical counterpart and the subsequent first ever redshift measurement for a GRB was achieved [32, 33], providing a compelling evidence that GRBs originate in far away galaxies, at cosmological distance. In fact, GRBs exhibit a wide range of redshifts with measured values extending from z = 0.008 [15] to 9.4 [34] as depicted in Figure 2.3. GRBs being at cosmological distance, suggests that, their total energy released must be extraordinary large. For example, if they were to emit isotropically, their energy would be up to $E_{iso} \sim 10^{55}$ erg, which is comparable to the Sun's mass energy. Such energetics are quite difficult to explain, however, it can imply that the GRB emission is collimated into jets[3] [21, 35]. The late time lower energy emission that occurs after the initial burst is called the *afterglow* (see Sect.2.6 for details). Further observations have demonstrated that afterglows can range from X-rays to radio waves, with the emission progressively transitioning from higher to lower energies over time. Later in the late 1990's, for the first time, Core-collapse Supernovae were discovered in late-time observations of long GRBs [37, 38], suggesting that long GRBs come from the collapse of massive stars[4]. Several observational discoveries followed including the detection of prompt optical flashes [39] and the identification of achromatic steepening in the afterglow lightcurves [35], which later supported the already proposed interpretation of the jetted GRB *fireball* models (see Sec. 2.4).

The experience gained from previous missions underscored the critical importance of rapid localization and the timely dissemination of this information for conducting high-quality follow-up

---

[3] refers to very narrow and highly collimated streams of relativistic particles.

[4] Short GRBs come from the mergers of compact objects.

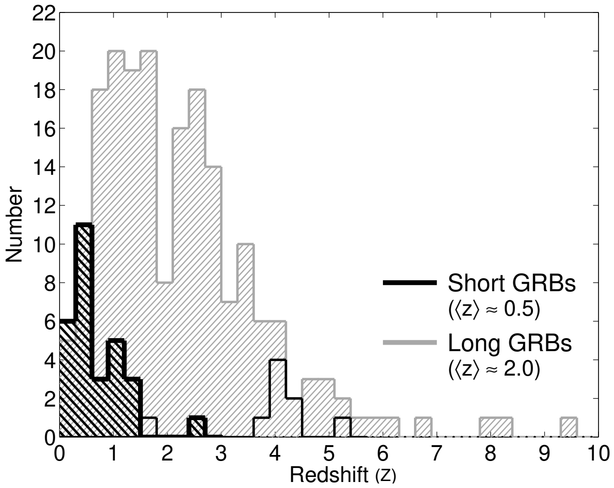

Figure 2.3.: The redshift distribution of short and long GRBs, each exhibiting a mean redshift of 0.5 and 2.0, respectively. The figure is modified from [36].

observations of GRBs in multiple wavelengths. The next significant advancement in the field of GRB research came with the Neil Gehrels *Swift* Observatory.

Launched in November 2004, the *Swift* satellite was purpose-built to focus on GRB science by collecting multi-wavelength observations, spanning from optical to γ-ray wavelengths, and to slew autonomously whenever a burst is detected, enabling it to provide good temporal coverage. This mission features three instruments: a wide Field of View Burst Alert Telescope (BAT; [40]), a narrow Field of View X-ray Telescope (XRT), optimized to detect soft X-ray photons in the 0.2-10 keV range [41], and the Ultraviolet Optical Telescope (UVOT), designed for tracking optical afterglows in seven different bands [42]. Figure 2.4 shows the *Swift* satellite with its different instruments.

The *Swift*-BAT, operating in the 15-350 keV range, features a 1.4 sr FoV and promptly localizes any new GRB it detects with a localization uncertainty of just a few arc-minutes. The whole satellite then repositions itself to these localizations so that the GRB falls within the *Swift*-XRT and *Swift*-UVOT's FoVs. Thanks to its capacity for source localization with an accuracy of arcseconds and quick data dissemination, *Swift* enables follow-up observations to be conducted quickly. In addition, thanks to its decent FoV and sensitivity, *Swift* has detected over 1800 GRBs[5]. *Swift*'s extensive collection of X-ray afterglow data, made possible by the XRT, has led to the discovery of a canonical X-ray afterglow lightcurve (see Figure 2.10).

To observe the high-energy Universe, the Fermi Gamma-ray Space Telescope, was launched on June 11, 2008 with GRBs one of the many science cases to study. Its payload includes

---

[5] `https://swift.gsfc.nasa.gov/archive/grb_table/fullview/`

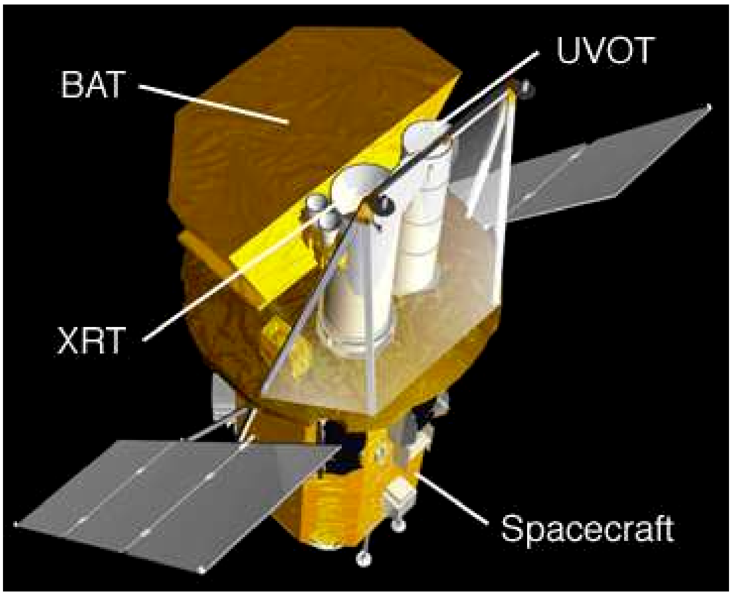

Figure 2.4.: The Swift satellite with its payloads [43].

two instruments (see Figure 2.5): the Large Area Telescope (LAT) and the Gamma-ray Burst Monitor (GBM)[44].

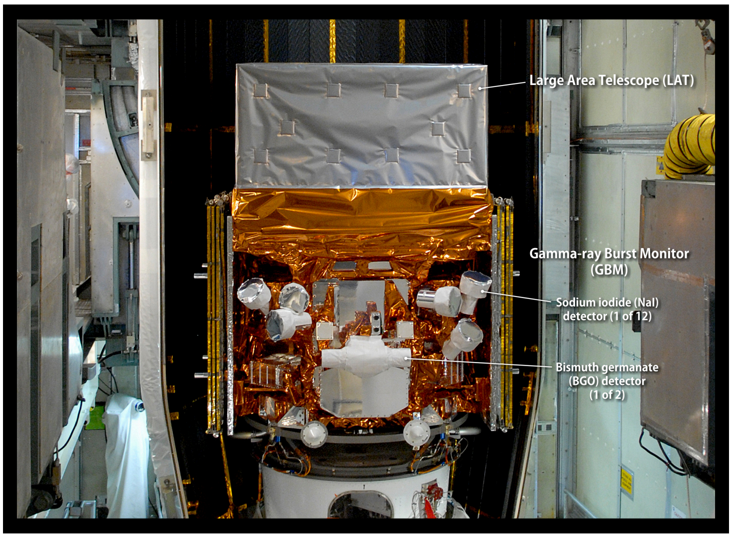

Figure 2.5.: The *Fermi* Gamma-ray Space Telescope before launch with the Large Area Telescope at the top, and the Gamma-ray Burst Monitor at the middle bottom side of the instrument. The solar panels are folded at the side. Photo credit (NASA/Kim Shiflett) after modification.

The *Fermi*-GBM covers an energy range from 8 keV to 40 MeV, and observes the entire sky with 12 sodium iodide detectors (NaI) and two bismuth germanate detectors (BGO). The NaI detectors are active in the 8 keV to 1 MeV energy band, while the BGO detectors function in the 0.2-40 MeV energy range [45]. The *Fermi*-LAT is an imaging γ-ray telescope designed to record photons in the range of 20 MeV to 300 GeV within its FoV, covering approximately 20% of the sky [3]. The *Fermi*-LAT can detect the corresponding high-energy gamma-ray emissions from GRBs. By combining observations from the *Fermi*-GBM and the *Fermi*-LAT, it becomes possible to span approximately 7 decades in energy.

Typically, only very bright GRBs detected by the *Fermi*-GBM are also detected by *Fermi*-LAT. The high-energy emission is consistently found to be delayed by up to few seconds compared to the emission in the keV to MeV range [46]. It also exhibits a longer duration, and at late times is characterized by a power-law decay in energy flux over time ($\mathrm{F} \propto$ to $\mathrm{t}^{-\alpha}$, with F representing the energy flux, and α a temporal decay index which is 2 on average from most of LAT detected GRBs). The highest energy photons detected by *Fermi*-LAT have rest frame energies above 100 GeV [47–50]. This discovery has imposed stringent constraints on the particle acceleration and radiation mechanisms of the relativistic shocks believed to be present in GRBs.

2.3. Communication Networks

In today's technological landscape, spaceborne GRB missions have the capability to calculate the GRB position close to real-time. To facilitate the swift dissemination of this positional information, the General Coordinates Network (GCN) was established. There are both automated GCN notices that are sent by instruments containing detection information and human-written GCN circulars with more information such as spectra, lightcurves as well as the updated localization. GCN is designed to automatically collect and distribute this data, ensuring that the astronomical community and researchers can utilize it in a timely manner. The practice of publicly sharing GRB coordinates began after the failed BATSE onboard tape recorders, leading to the development of the first version of the GCN known as the BATSE Coordinate Distribution Network (BACODINE). During this hardware failure, BACODINE enabled real-time data transmission to avoid losing critical information. This incident led to the establishment of protocols for rapidly distributing coordinates of transient events, such as GRBs, to a wider scientific community. GCN has become a highly influential tool for both receiving and disseminating crucial information. In addition, multi-messenger alerts such as GW alerts and neutrino alerts, are now included in GCN for distribution. This expanded network not only benefits the GRB community but also provides valuable information for a broader range of transient events.

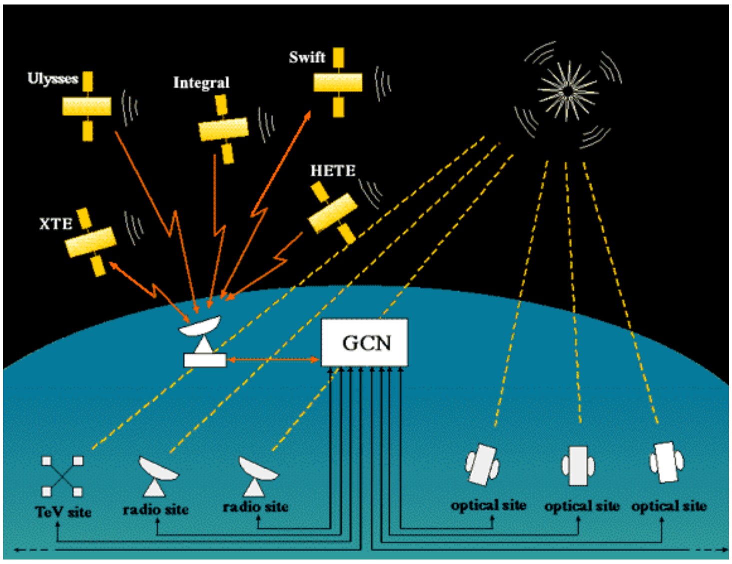

Figure 2.6.: Gamma-ray Coordinates Network. The Observatories detecting new transient events send alerts to the GCN. The GCN shares these alerts with a group of opt-in subscribers, typically astronomers and researchers. Subscribers conduct their independent observations and may report their findings. This system encourages collaboration in observing and studying transient phenomena. [Credit: NASA.]

2.4. The Fireball Model

The fireball model is the prevailing explanation for the production of GRB emission [51–54]. According to this model, the fireball represents an expanding, isotropic outflow of photon pairs with a small proportion of baryons and its initial energy far exceeds its rest mass. The jet is assumed to have negligible magnetization, and its dynamics are primarily governed by relativistic hydrodynamics.

The evolution of the fireball model involves three important phases: acceleration, coasting, and deceleration. As outlined in [56], the fireball originates as a hot outflow from the compact central engine, beginning at an initial radius of $\sim 10^7$ cm. During this phase, photons and pairs are in equilibrium, while baryons remain essentially at rest. The central engine continuously releases energy, leading to the adiabatic expansion of the fireball. In the early stages, when the fireball is lepton-dominated, it expands with the bulk Lorentz factor (Γ) proportionally to the radius (R) from the central engine. As the fireball transitions to being baryon-dominated and optically thin, Γ reaches its maximum, and the jet enters a coasting phase with a constant $\sim \Gamma_0$. The deceleration phase commences when the jet starts interacting significantly with the surrounding circumburst medium.

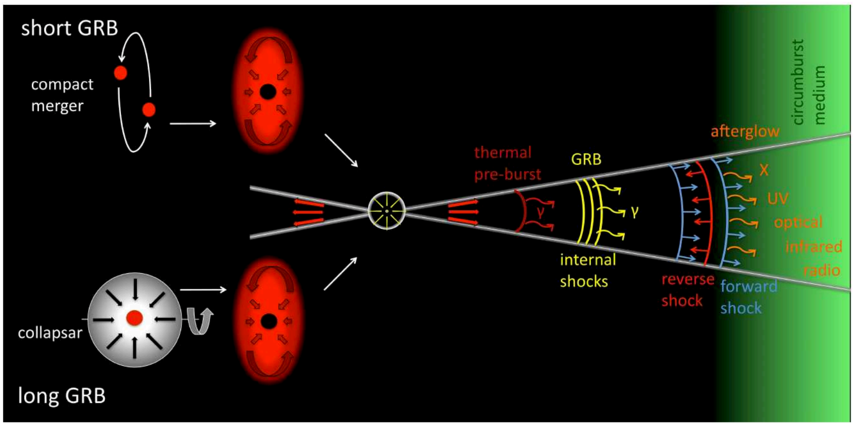

Figure 2.7.: Illustrative sketch showing the different phases of the GRB formation and evolution steps for short and long GRBs in the context of a fireball model, extending from the progenitor up to the production of gamma-rays and afterglow [55].

The physics of GRBs is thought to be consistent across different progenitors (see for detail, a representation in Figure 2.7). Whether the central engine forms after a core-collapse supernova, or the result of a neutron star merger or possibly a neutron star merging with a black hole, it ejects a significant amount of energy into a confined space. This energy powers a collimated relativistic outflow that is initially dense and optically thick, but as it expands, it becomes optically thin and releases thermal radiation at the photosphere. Additional energy is generated internally within the jet, through mechanisms like colliding shock fronts [57] and magnetic dissipation [58–60], which produce the non-thermal radiation seen as GRB prompt emission (see discussions in section 2.5). As the jet extends outward and interacts with the surrounding circumburst medium creating external shocks, it gives rise to the long lasting multi-wavelength afterglow (see section 2.6), well-described by synchrotron shock models [61] observed in X-ray, Optical and radio wavelengths.

Within the fireball model framework, the proposal of collisionless internal shocks as explained in [57] emerges as a significant mechanism for dissipating internal energy. In this scenario, the entire jet exhibits a large-scale bulk Lorentz factor and comprises multiple shells of material moving at different Lorentz factors, a variability that may stem from intermittent central engine activity or intrinsic inhomogeneity of the outflow. The collision between faster-trailing shells and slower forward shells gives rise to shock fronts, where accelerated particles emit radiation through processes such as synchrotron radiation, inverse Compton scattering, and other non-thermal processes. Internal shocks can convert kinetic energy back into radiation at collision sites, offering a natural explanation for the multiple pulses and rapid variability observed in GRB lightcurves. However, models of internal shocks predict efficiencies for gamma-ray production of only a few percent [62–65], while observations have suggested efficiencies as high as 90% [64–66]. Consequently, internal shocks can only explain low-efficiency GRBs (i.e. only a small fraction of the central engine's total energy contributes to the actual GRB).

Alternative models proposing the magnetic reconnection of the outflow, such as the work by [67], predict higher efficiencies and can also replicate fundamental aspects of GRB lightcurves and spectra [68]. Polarization measurements are therefore crucial in determining the degree of magnetization within the jet and understanding the radiation mechanisms involved [69]. Despite a few claims of linear polarization in GRBs (e.g., [70–73]), these detections are either of low significance or inconsistent with previous reports. A comprehensive explanation of GRB prompt emission likely entails a combination of matter-dominated and magnetically-dominated components [74]. The acceleration and interaction of matter in the jet and with the surroundings is governed by different radiation mechanisms that I summarize in Section 2.7.2. In the following, I introduce different properties of the prompt emission of the GRBs.

2.5. Prompt Emission

The prompt emission of GRBs refers to the hard X-ray and γ-ray radiation that is generally observed in bursts or flashes, which trigger space instruments that in turn initiate multi-wavelength follow-up observations. In general, GRBs exhibit a variety of overlapping emission episodes across a broad range of time scales during their prompt phase. The temporal and spectral diversity observed in GRBs (see for example Figure 2.8) suggests that a complex interplay of processes is likely at work. There are critical open questions remaining about the properties of GRB jets. Like for example, whether GRB jets are composed primarily of matter or Poynting flux, which impacts how the energy dissipated within these jets and how photons are emitted through them. However, at this time, no single theoretical model accounts for all observed characteristics.

2.5.1. Spectral properties

The majority of GRBs observed exhibit a non-thermal continuum radiation spectrum during their prompt phase, often modeled by a phenomenological model called the "Band function" [28]. The Band function (expressed as a function of photon energy in keV), is a smoothly broken power-law model:

$$N(E) = A \begin{cases} E^{\alpha} \exp -\frac{E}{E_0}, & E < (\alpha-\beta)E_0, \\ \Big[(\alpha-\beta)E_0\Big]^{(\alpha-\beta)} \exp{(\beta-\alpha)} E^{\beta}, & E \geq (\alpha-\beta)E_0, \end{cases} \tag{2.1}$$

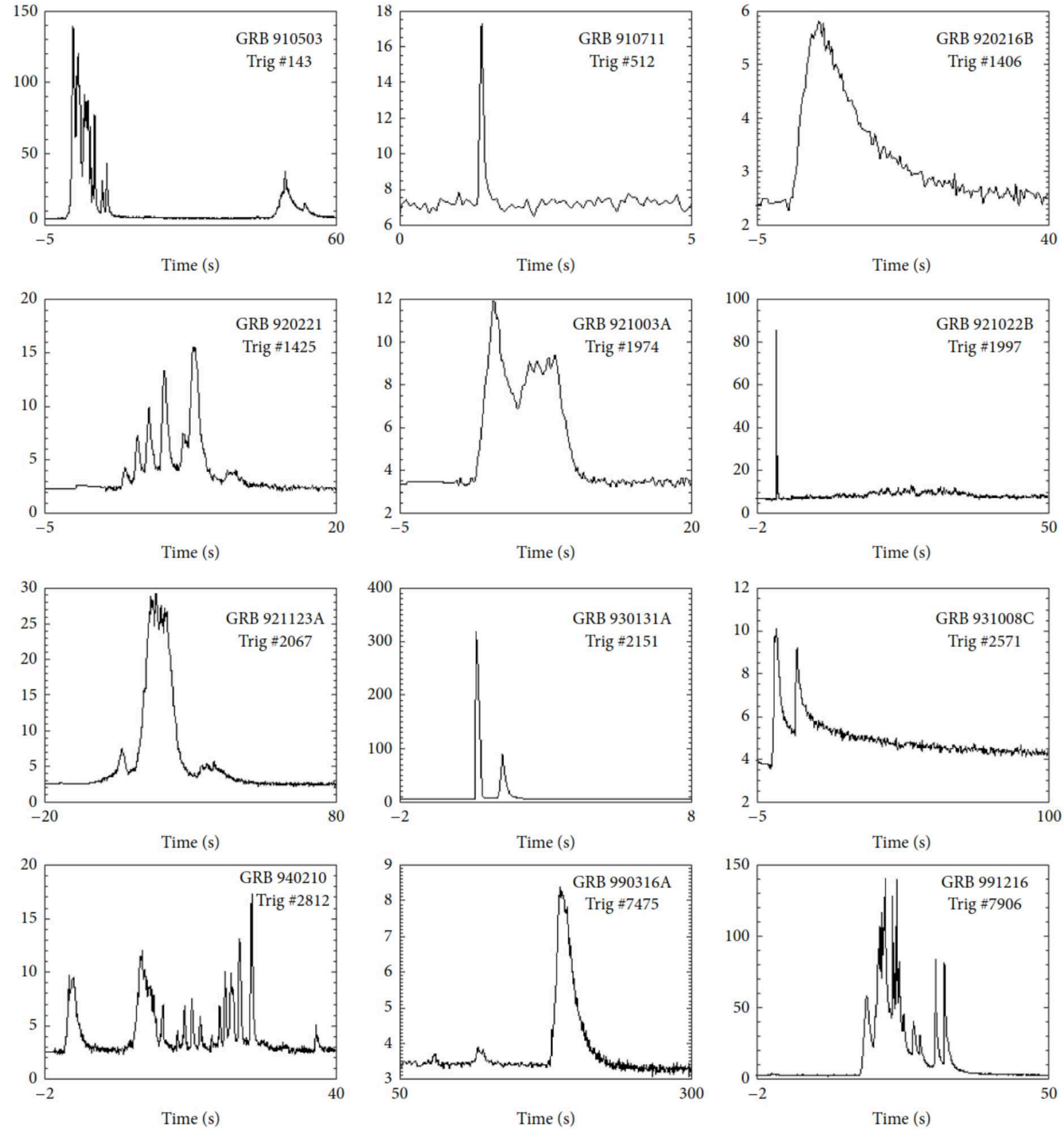

Figure 2.8.: These are examples of highly variable gamma-ray burst (GRB) lightcurves extracted from the GRB BATSE catalog [75].

where A is a constant parameter, α denotes the low-energy spectral index, β represents the high-energy spectral index, and E_0 stands for the break energy. When $\alpha = \beta$, the band function simplifies to a simple power-law. On the other hand, if β has a large value, the band function transforms into an exponential cutoff powerlaw model. The band function is shown for example fitting GRB 990123 data in Figure 2.9 [76]. The relation between the peak energy (E_p) in the spectral energy distribution (SED) in the form E^2dN/dE and E_0 is expressed as:

$$E_p = (2 + \alpha)E_0$$

Typical spectral indices observed in BATSE GRB data are reported to be $\alpha \approx 1 \pm 1$ and $\beta \approx -2^{+1}_{-2}$ for the GRBs observed within the 20–2000 keV band [77], a characterization later confirmed by *Fermi* observations [60, 78, 79]. The peak energy (E_p) typically falls around few hundred keV for GRBs. However, E_p can vary within a range spanning from a few keV for bright GRBs [80] to several MeV [81]. The Band function is widely interpreted as being associated with synchrotron radiation (see Sect. 2.7.2), which aligns with the general understanding of GRB emission mechanism. However, the Band function also has its limitations (see e.g. details in [77, 82–84]).

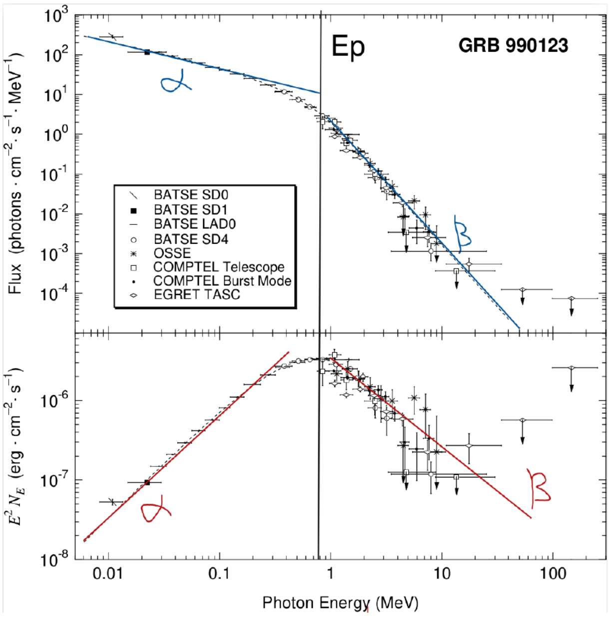

Figure 2.9.: The GRB high energy spectrum fitted with Band function. Figure was adapted from [76].

2.6. Afterglow emission

The existence of the afterglow was foreseen within the framework of the fireball model (see Sect. 2.4 for details) before it was observed. According to this model, relativistic flow generated by the central engine expands into the surrounding medium colliding with the circumburst medium (CBM) surrounding the central engine [85, 86]. The observed afterglow emission has been explained by synchrotron shock radiation from a powerlaw distribution of electrons (see section 2.7.2). However, the exact properties of the observed emission can differ depending on factors like the density of the surrounding environment, whether there is ongoing energy injection and structured jet [61, 87, 88].

Afterglow lightcurves are typically characterized using a set of powerlaw segments that express the relation between flux (F_ν), time and frequency as follows:

$$F_\nu \propto t^{-\alpha}\nu^{-\beta}, \tag{2.2}$$

with α and β representing the temporal and spectral indices, respectively. Under certain assumptions about the environment and external shock conditions, these indices display relationships between them in different scenarios in closure relations, which are used to compare afterglow models with observational data. While not discussed in detail in this thesis, the reader is refereed to research that discusses these closure relations such as: [61, 88–91]. The GRB afterglows theoretical framework was developed back in the 1970s by Blandford and McKee [92]. In this scenario an ultra-relativistic spherically symmetric shell with a width $\approx \frac{R}{\Gamma^2}$ moves through the external medium surrounding the progenitor [93]. When this outflow collides with the circumburst medium, it generates two shocks: a forward shock that moves outward and is primarily responsible for the main afterglow emission at X-rays and lower energies, and a reverse shock that travels back into the ejecta in the reference frame of the head of the jet, potentially producing a brief optical flash [94].

In the simplest case of the Blandford-McKee model, also considered in this thesis, the CBM is assumed to have a uniform density. An alternative option is to adopt a radial density profile that follows a powerlaw distribution of the form $\rho = Ar^{-k}$, where k=2 indicate a wind-like environment created with materials ejected by the progenitor star before the explosion of the GRB.

The afterglow of a GRB is most often detected in X-rays due to its brightness and the quick onset [95]. A typical X-ray lightcurve consists of five main stages (see Figure 2.10): (I) an initial steep decline, (II) a plateau, (III) a normal decay phase, (IV) a jet break, and (V) X-ray flares (see more details in [22]).

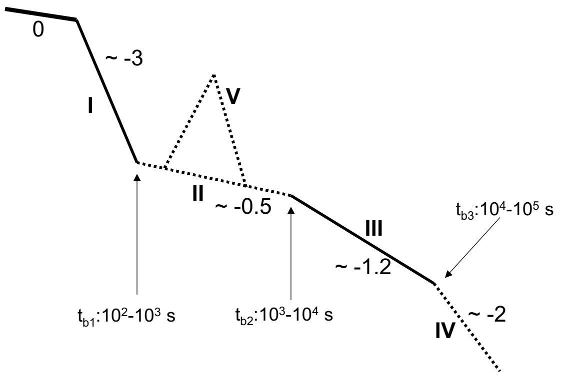

Figure 2.10.: The figure illustrates the various segments constituting the afterglow lightcurve of GRBs. Each segment, except for segment V representing X-ray flares, can be characterized by a power-law decay, with the mean measured decay index indicated in the figure. The figure is taken from [90].

- **I. Initial decay phase:** The initial decay phase of the afterglow shows a quick drop in brightness with a temporal slop of ~ 3. This likely implies the transition from prompt to the afterglow emission phase which happens as the central engine powers down and the forward shock builds up enough material to emit brightly.
- **II. Plateau phase:** Following the initial steep decay, we sometimes observe a plateau phase, during which the lightcurve can level out into a plateau with a slope is nearly equal to 0, or if it shows a slower decay with a slope >-1 [22]. This phase is believed to be caused by ongoing energy injection into the external shock, possibly due to prolonged central engine activity or irregularities within the jet [96].
- **III. Normal decay phase:** During this phase, the lightcurve follows a slope of ≈-1, which matches the expected behavior of the external forward shock [22, 61].
- **IV. Post-jet-break phase:** In the post-jet-break phase the lightcurve steepens significantly due to a geometric effect. During this phase, the expanding jet becomes wider than the beaming angle, which is caused by the relativistic bulk motion of the jet (i.e. $\theta \sim \Gamma^{-1}$), leading to a rapid decrease in flux across all wavelength [97, 98]. For a top-hat jet moving through a medium with a constant density, the jet opening angle θ_j can be determined from the jet break time, t_j (in days) as follows [99]:

$$\theta_j = 0.057\Big(t_j\Big)^{\frac{3}{8}}\left(\frac{1+z}{2}\right)^{\frac{-3}{8}}\left(\frac{E_{iso}}{10^{53}\,erg}\right)^{\frac{-1}{8}}\left(\frac{n}{0.1\,cm^{-3}}\right)^{\frac{1}{8}}, \tag{2.3}$$

where E_{iso} is the observed isotropic equivalent γ-ray energy calculated from the prompt emission, η_γ is the efficiency of converting kinetic energy into γ-rays, and n is the particle number density of the external medium.

- **V. X-ray flares:** They are sudden bursts of re-brightening that are observed in many X-ray afterglows (see also details in [100]). These flares usually exhibit a harder spectrum and are considered to have a different origin than the underlying emission, since the temporal slope of the underlying emission remains unaffected by the flare. It is believed that these flares are associated with brief periods of re-brightening of the central engine [100, 101].

Optical afterglows have also been observed in a fraction of GRBs. These late-time light curves generally showed a powerlaw decay, however, broken powerlaw curves were also observed, providing evidence of jet breaks in the optical band [102]. Note that these jet breaks should occur simultaneously across all wavelengths like optical and X-rays. Some early optical afterglows also exhibited a sharp decline that could be explained by reverse shock emission [103]. While most optical afterglows display similar behavior to their X-ray counterparts, some show different temporal slopes and decay patterns [104]. This discrepancy could be due to the evolution of the synchrotron spectrum, lateral expansion of only part of the jet, or multiple emission sites (e.g., [105]). Another important observation is that the detection rate of optical afterglows is lower than that of X-rays. It soon became clear that some GRBs lacked optical counterparts despite extensive searches [106–109], because they were intrinsically faint in the optical band.

The radio afterglow is the long-lasting phase of a GRB afterglow, and can be detectable for up to around 1000 days after the initial burst. Despite this, only few GRBs so far have had their radio afterglow detected. Radio afterglow lightcurves typically exhibit multiple power-law segments, showing a transition from relativistic to non-relativistic phases, according to the external shock model. This evolution displays similar temporal indices and jet break structures seen in other wavelengths but occurs more slowly and over an extended duration. In some bright GRBs, the early reverse shock can also be detected at radio wavelengths [110].

2.7. Particle acceleration and radiation mechanism in GRBs

2.7.1. Introduction

In GRB theory, the physical parameters, with the shock's internal energy partitioned into fractions for magnetic energy density (ϵ_β), protons/ions energy density (ϵ_p) and electron energy density (ϵ_e) can be used to describing the shock acceleration. In the circumburst region, in the direction of Forward shock (FS), the ejecta region is expected to have a low magnetic field, however, some GRBs afterglow observations suggest the presence of a high magnetic field [111]. It is, therefore, possible that relativistic shocks undergo magnetic field instabilities (see for e.g. [112–115]) allowing particles to accelerate.

GRB radiation can be explained mostly with three important mechanisms: Synchrotron and Inverse Compton (IC) radiations and the combination of the two mechanisms called the Synchrotron-Self-Compton (SSC) mechanism (See detail reviews and discussions in [116, 117]).

2.7.2. Synchrotron Radiation

Synchrotron radiation occurs when charged particles are subject to a magnetic field and are accelerated perpendicular to their velocity, causing them to emit radiation. In astrophysical environments, synchrotron emission is predominantly observed from electrons because the energy loss due to synchrotron radiation is proportional to m^{-4} (where m represents the mass of the particle). Electrons being much lighter than other charged particles (and also protons being harder to accelerate), experience more significant energy losses and are therefore the primary contributors to synchrotron radiation in this context.

For electrons with energies in the tera-electronvolt (TeV) range, the energy E_{syn} of photons generated through synchrotron emission is directly related to the square of each individual electron's initial energy (E_e) and the strength of the magnetic field (B) through which electrons are moving, and can be expressed as:

$$E_{syn} = 0.2 \frac{B}{10\,\mu\mathrm{G}} \left(\frac{E_e}{1\,\mathrm{TeV}} \right)^2 \mathrm{eV}. \tag{2.4}$$

The average radiated power for synchrotron radiation at a given electron Lorentz factor is given by:

$$P_{syn}(\gamma_e) = -\frac{dE_e}{dt} = \frac{2}{3\mu_0} \sigma_T c B^2 \beta^2 \gamma_e^2, \tag{2.5}$$

where β is the averaged electron velocity (v/c) over a pitch angle, and μ_0 represents the vacuum magnetic permeability, γ_e is the electron Lorentz factor, and $\sigma_T = \frac{8\pi}{3} r_e^2 \approx 6.7 \times 10^{25}\, cm^2$ represents the Thomson cross-section and $r_e = \frac{1}{4\pi\epsilon_0} \frac{e^2}{m_e c^2}$ is the electron radius. The energy spectrum of γ-rays produced by synchrotron emission is influenced by both the acceleration and cooling times of the electrons involved in the process. This interplay between acceleration and cooling times can lead to the emergence of complex and intricate spectral patterns [118]. For a relativistic electron with $\beta \approx 1$, the cooling time is given by:

$$t_{syn} = \frac{E_e}{-dE_e/dt} \propto B^{-2}E_e^{-1}.$$

The synchrotron radiation emission has a peak at a specific frequency given by:

$$\nu_{peak} = 1.5 \times 10^{-5}\, GeV \left(\frac{E_e}{1\, TeV}\right)^2 \left(\frac{B}{1\, G}\right). \tag{2.6}$$

The peak frequency of synchrotron radiation therefore provides valuable information about the energy distribution of electrons and the characteristics of the magnetic field in astrophysical sources. If one considers a powerlaw distribution of electron energies, denoted as $N(E_e)dE_e = \kappa E_e^{-p} dE_e$, then it can be assumed that the emitted radiation primarily, originates from electrons with energy E_e within a specific differential energy interval. Consequently, since from eq. (2.6) $\nu \propto E_e^2 B$ implying that $E_e \propto \nu^{1/2}B^{-1/2}$, therefore, $dE_e \propto \nu^{-1/2}B^{-1/2}d\nu$ and the energy flux per unit frequency can be expressed as [119]:

$$I(\nu) = -\int \frac{dE_e}{dt} N(E_e)dE_e \propto B^{(p+1)/2}\nu^{(1-p)/2},$$

where the exponent of ν is the spectral index ($\alpha = (1-p)/2$) is the slope of the electron spectrum.

2.7.3. Inverse Compton scattering

The Inverse Compton (IC) scattering occurs when a relativistic particle such as a high energy electron collides with a photon and scatters transferring part of its energy to the photon. This process is known to be the primary leptonic source of observed VHE γ-ray emission from astrophysical sources in general. In this process, low-energy photons are boosted to high energies through interactions with relativistic electrons. The cross-section of this radiation process is given by [22, 120]:

$$\sigma_{IC} = \frac{3\sigma_T}{8x}\left[\left(1 - \frac{2(x+1)}{x^2}\right)\ln(2x+1) + \frac{1}{2} + \frac{4}{x} - \frac{1}{2(2x+1)^2}\right],$$

where $x = E_\gamma/E_e$ and E_γ representing the initial energy of the photon in the co-moving frame of the electron and E_e being the rest frame energy of the electron ($E_e = m_e c^2$). In the case of non-relativistic electron energies (i.e. with $x \ll 1$), $\sigma_{IC} \approx \sigma_T(1-2x)$ which is known as the Thomson regime. However, for ultra-relativistic electron energies (i.e. with $x \gg 1$), each interaction causes electrons to loose a significant portion of their energy and relativistic effects come into play, causing the cross-section to decrease. This scenario is known as the Klein-Nishina

(KN) regime, and the cross-section becomes:

$$\sigma_{KN} \approx \frac{3}{8}\sigma_T \ln(4x)/x$$

In the Thomson regime, the energy loss rate of the IC scattering is given by [22]:

$$P_{IC} = -\frac{dE_e}{dt} = \frac{4}{3}\sigma_T c E_\gamma n_{ph} E_e^2, \tag{2.7}$$

where n_{ph} represents the photon-field number density while the cooling time is similar to the case of synchrotron radiation ($\tau_{IC} \propto 1/E_e$). The energy loss in the Thomson regime depends heavily on the electron energy (E_e^2) which implies the steepening of the spectrum with time, as higher electrons lose energy quickly. For the Klein-Nishina regime, the energy loss rate does weakly depend on the electron energy and hence the spectrum tends to be harder as time moves forward. The KN energy loss rate can written as [22, 117]:

$$P_{KN} = -\frac{dE_e}{dt} = \frac{3}{8}\frac{\sigma_T c n_{ph}}{E_\gamma}(ln(4x\gamma) - 11/6), \tag{2.8}$$

where $\gamma = E_e/mc^2$.

2.7.4. Synchrotron-self-Compton emission

When photons generated through Synchrotron radiation of electrons are further boosted in energy (performing IC scattering) by the very same population of electrons, the process is called Synchrotron Self-Compton emission (SSC) [121]. This process has the potential to occur iteratively, resulting in SSC of first, second, third, and so on, orders. However, it's worth noting that high-order SSC is not typically extensively studied, mainly because KN effects strongly inhibit this process [22].

As synchrotron radiation and inverse-Compton scattering are closely related processes, it can be inferred from Equation 2.5 and Equation 2.7 that the ratio of the radiated power is equivalent to the ratio of the radiation field due to synchrotron process (U_{syn}) to the magnetic field energy density (U_B):

$$\frac{P_{IC}}{P_{syn}} = \frac{U_{syn}}{U_B} \tag{2.9}$$

By defining $X = P_{IC}/P_{syn}$, we can express higher-order SSC processes as follows: $\mathrm{X}_1 = \mathrm{X}$, $\mathrm{X}_2 = \mathrm{P}_{\mathrm{SSC},2}/\mathrm{P}_{\mathrm{SSC},1}$, etc. In this context, X_1 denotes the initial ratio, while X_2 represents the ratio between the powers of successive SSC processes (e.g., second-order SSC to first-order SSC).

Hence, the total emission power of the electron is given by [22]:

$$P_{tot} = P_{syn}(1 + X_1 + X_1 X_2 + ...).$$

Therefore, the cooling that occurs in the SSC process is equivalent to synchrotron cooling, but with the inclusion of additional X-factors. In the straightforward and typical scenario, only the first SSC term holds significance, resulting in a total $P_{tot} = P_{syn}(1 + X)$. However, in cases where the KN effect becomes significant, a correction factor denoted as $X_{KN} \leq 1$ is introduced and is given by [22]:

$$X_{KN}(\gamma) \sim min\left[1, \left(\frac{\Gamma mc^2}{\gamma h\nu_{syn}}\right)^2\right],$$

where Γ and γ are the Lorentz factor of the outflow and the electron in a co-moving frame respectively, m denoting the electron mass and ν_{syn} representing the peak synchrotron frequency as observed in the observer's frame. The implication of these radiation mechanisms in the context of GRBs is briefly discussed in Section 2.8.

2.8. HE and VHE Spectrum

Observations of HE and VHE photons from GRBs help constrain the acceleration conditions and radiation mechanisms introduced in Section 2.7. In 2018, the first observation of VHE photons was reported with the detection of GRB 180720B by H.E.S.S. [17]. Subsequently, a handful of other GRBs have been detected in the TeV energy range, including GRB 190114C observed by MAGIC [16] and GRB 190829A detected by H.E.S.S. [15]. Notably, a remarkably intense and very bright GRB 221009A was recently detected in the TeV energy range by LHAASO [122]. This event was closely monitored by various satellites and ground-based instruments, including H.E.S.S. (as detailed in Chapter **??**). These findings collectively confirm the presence of VHE photons during the afterglow and late-prompt phase of the GRB. The HE emissions are observed during both the prompt and afterglow phases. A few instances of GRB emissions above 100 MeV were detected by CGRO/EGRET, such as an 18 GeV photon from `GRB 940217`, observed 1.5 hours after the burst [123].

Fermi-LAT detects approximately 10 GRBs annually, some with energies surpassing 1 GeV. It has been observed that the GeV emission tends to lag the sub-MeV emission in their detection [124] and often persists longer than MeV emission. Additionally, a hard spectral component in the *Fermi*-LAT energy range was identified in many GRBs during the prompt emission measured by *Fermi*-GBM [49], usually interpreted as the early onset of the afterglow. However, the mechanism responsible for accelerating photons to even higher energies remains a topic of ongoing debate [125].

Fermi-LAT observations have set constraints on the minimum bulk Lorentz factor (Γ)[6], necessary for producing the highest energy photons near the pair production threshold. Typically, the obtained values for Γ are in the order of hundreds.

A significant theoretical constraint for photons detected at VHE is the synchrotron burn-off limit. This limit is determined by balancing the time scale of electron acceleration and the energy loss caused by synchrotron radiation. This manifests as a cutoff in the synchrotron spectrum at approximately $\mathrm{E}^{\mathrm{syn}}_{\mathrm{cutoff}} = 50\,\mathrm{MeV}\,\Gamma/(1+\mathrm{z})$, where Γ is expected to be of the order of 10 in the afterglow phase but decreasing with time. This suggests that photons in the GeV range surpass the synchrotron burn-off limit, indicating the potential need for an additional emission process to produce these photons. Measuring the VHE photons would shed additional light on this additional process such as refining the understanding of particle acceleration and energy loss processes in GRBs. Additionally, simultaneous appearance of VHE and lower-energy photons might suggest that a single electron population is responsible both synchrotron and inverse Compton emissions.

In 2019, VHE γ-ray emission was detected by the MAGIC telescopes from *GRB 190114C* in the 0.2-1 TeV range starting 50 seconds after the initial burst, considered to be the early afterglow [126]. This came after the initial detection of 100-440 GeV emission from GRB 180720B detected by H.E.S.S. in 2018, in about 10 hours after the initial burst [17, 120]. The afterglow spectrum of `GRB 190114C` exhibited two peak structures, as depicted in Figure 2.11 (a). The first peak was attributed to synchrotron emission, while the second peak was interpreted as a result of the inverse Compton process [126]. In this scenario, electrons moving individually at relativistic speeds within a jet that has a bulk motion with a bulk Lorentz factor $\Gamma \geq 100$ generate Synchrotron radiation in the keV-MeV energy range. Subsequently, when these photons undergo inverse-Compton scattering by the same population of electrons, their energies can increase by a factor of Γ^2 ($\nu_{\mathrm{IC}} \approx \Gamma^2 \nu_{\mathrm{syn}}$) [127]. A few months after the *MAGIC*-detected GRB, H.E.S.S. detected the afterglow emission from GRB 190829A, in 2019, starting about four hours after the initial burst and extending up to 55.9 hours after the GRB began. However, the VHE photons were not well described by the Inverse Compton (or SSC) model (see Figure 2.11 (b)), because the spectral index at VHE energies was harder than what would be expected in the Klein-Nishina regime.

The VHE component is expected to be explained by the so-called SSC model. Therefore, the SSC mechanisms introduce a distinct spectral component at high energies, with the spectral shape depending on if the emission occurs in the Thomson or Klein-Nishina regime. The hadronic processes could also produce emission, with obvious one being proton synchrotron but which

---

[6] a measure of the bulk motion of the jet outflow produced by the GRB ejecta during the burst.

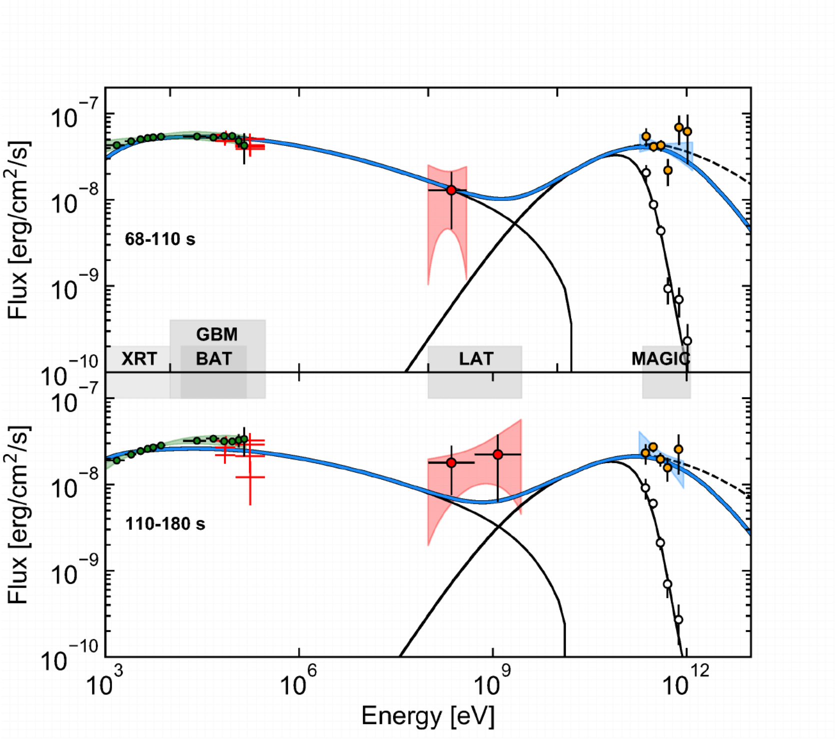

(a) GRB 190114C

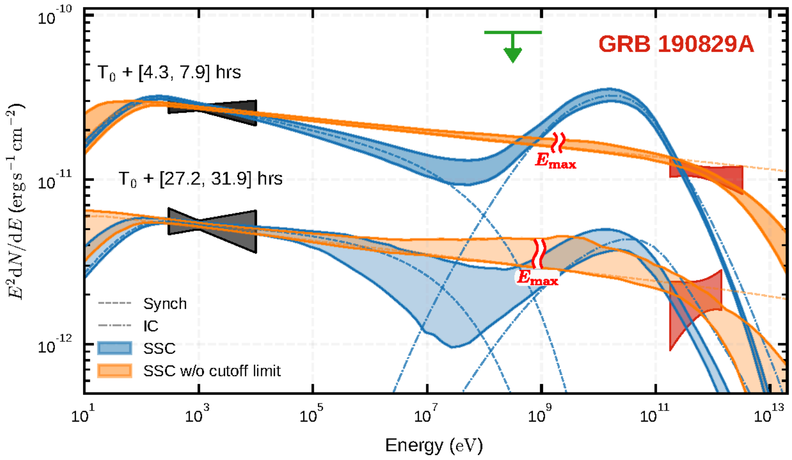

(b) GRB 190829A

Figure 2.11.: The spectral energy distribution of GRB 190114C (top panel) [128]. The SED of GRB 190829A (bottom panel) [15]

has a difficulty of a much heavier charged particle and that could meet the energetic requirements to accelerate emission to high energies [129]. In this scenario, a proton-synchrotron scenario faces a challenge due to the relatively long variability timescales, which are further increased in models considering the presence of photo-hadronic cascading to address the low radiation efficiency of proton synchrotron. In addition, hadronic processes would produce other messengers such as neutrinos and cosmic rays (see Section 2.9 for details). Consequently, this process is believed to contribute only minimally to high energy afterglows [130].

2.8.1. EBL absorption of VHE γ-rays

γ-rays are attenuated as they travel through the Universe. The extragalactic background light (EBL) encompasses the emission of low-energy photons by stars and various cosmological entities throughout different cosmic eras, which then undergo alterations through red-shifting and attenuation as a consequence of the Universe's expansion. γ-rays of TeV energy are mostly affected by infrared (IR) photons. Directly measuring the EBL is a challenging task due to the presence of strong foreground sources within our solar system and in our own Galaxy [131, 132]. Furthermore, any direct measurement would provide information only about the current integrated state of the EBL, making it difficult to understand its evolution over time. This affects how the interaction of the VHE γ-rays and the EBL are interpreted, as well as how the Universe and VHE is studied.

VHE γ-rays traveling through the cosmos are absorbed by the EBL via the process of positron and electron (e^+, e^-) pair creation [133, 134] and such process can be written as:

$$\gamma_{ebl} + \gamma_{\gamma-ray} \rightarrow e^- + e^+$$

The pair production cross-section can be given by (see also [132] for details):

$$\sigma_{\gamma\gamma} = \frac{1}{2}\pi r_0^2(1-\beta^2)\left[2\beta(\beta^2-2) + (3-\beta^4)\ln\left(\frac{1+\beta}{1-\beta}\right)\right], \tag{2.10}$$

where $\pi r_0^2 = \frac{3\sigma_T}{8}$, and σ is the Thomson cross-section. In this expression, β carries the dependence on the scattering angle θ and can be written as:

$$\beta = \sqrt{1 - \frac{2m_e^2c^4}{E\epsilon(1-\cos\theta)}} \tag{2.11}$$

With ϵ the energy of the background photon and E the energy of the source photon. For the case where, $\cos\theta \rightarrow 0$ (for isotropic background photons), $\sigma_{\gamma\gamma} \approx 0.25\sigma_T$ at $\epsilon E \simeq 4m_e^2c^4$. Therefore, the cross-section is maximized when the energy $\epsilon(\mathrm{E}) \approx \left(1\,\mathrm{TeV/E}\right)$ eV.

The energy E and ϵ are inversely proportional, which implies that the lower energy background photons preferentially interact with higher energy γ-rays. Depending on the redshift of the light in galaxies, there are different estimations of EBL derived from the semi-empirical model (see for e.g. [135–138]). Figure 2.12 displays the EBL spectrum as a function of the wavelength of background photons.

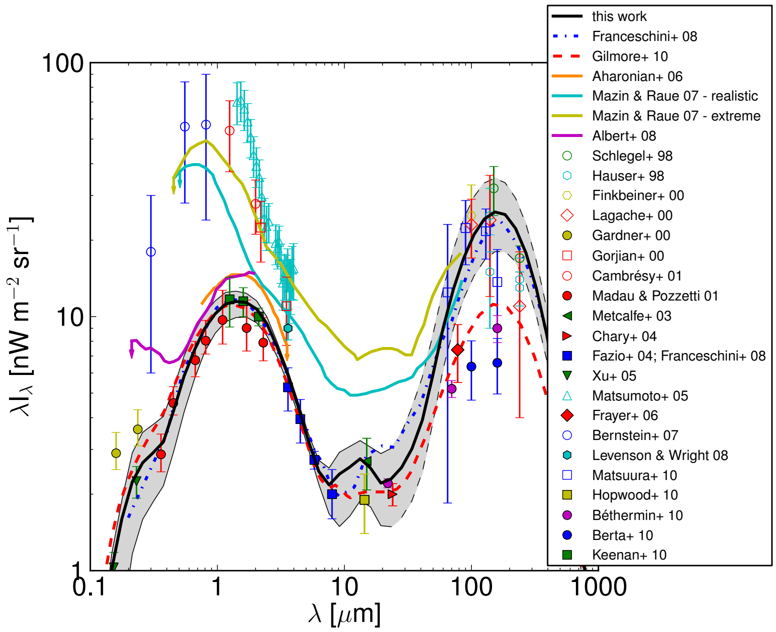

Figure 2.12.: The EBL spectrum represents a composite of measurements gathered from numerous experiments and deductions drawn from different models. A variability in λI_λ accross different models around $1\,\mu$m reflects observational uncertainties from foreground contamination and model discripancies impacting VHE attenuation particular in GRBs. The figure is taken from [137].

When VHE photons are emitted from a source, their interaction with the EBL leads to the presence of a spectral cutoff in the observed data expressed as:

$$F_{obs}(E) = F_{int} e^{-\tau_{\gamma\gamma}(E,z)}, \tag{2.12}$$

where F_{int} and F_{obs} represent the intrinsic and observed spectra, respectively, and the exponential term describes the EBL absorption. The term $\tau(E, z)$ represents the optical depth, which relies on the cross-section $\sigma_{\gamma\gamma}$ for a source photon with energy E, the EBL density, and the source's distance z. The absorption factor for several redshifts as a function of the energy of the source photon is shown in Figure 2.13.

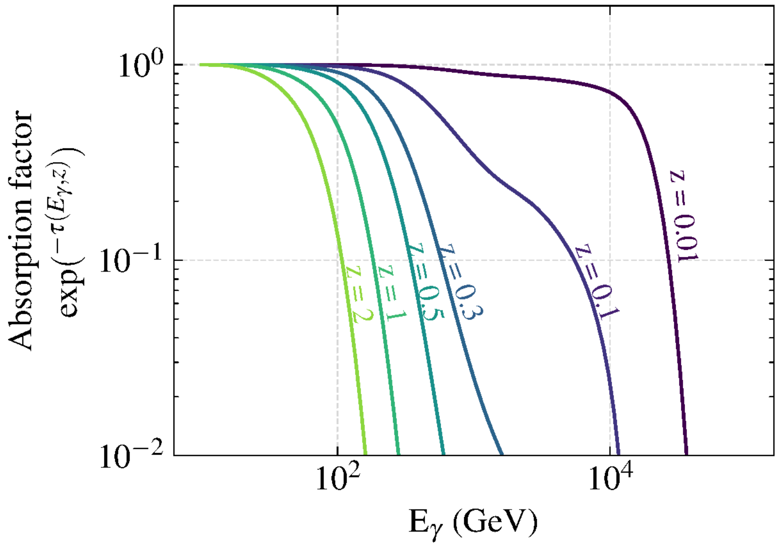

Figure 2.13.: The EBL absorption factor for gamma photons from the sources at different redshifts (z) as a function of the energy for a particular EBL model described in [137]. At these redshifts, a large fraction of emitted VHE photons will get absorbed before arriving on the Earth.

2.9. Multi-messenger Observations

Observing Multi-messenger (MM) emission from GRBs involves searching for signals from different astrophysical messengers: γ-rays, neutrinos, gravitational waves (GW) and CRs, all originating from the same GRB event, providing a more complete picture of the underlying picture of the astrophysical processes within the GRB. Astrophysical HE neutrinos are expected to be produced in GRBs through processes involving accelerated protons or heavy nuclei. In this scenario, protons interact with the surrounding photons leading to pion production, which decays into HE neutrinos and γ-rays [56, 139, 140]. Neutrino and GWs detectors have been searching for emission from GRBs for years. Currently, the IceCube neutrino observatory, located at the south pole, stands as the sole instrument actively searching for TeV – PeV neutrinos in all three flavours: electron, muon, and tau neutrinos. While IceCube has searched for neutrino associated with GRBs detected by other instrument, no statistically significant temporal or spatial correlations have been found and a definitive detection of neutrinos from GRBs has not yet achieved. However, these observations play a key role in constraining our understanding of neutrino and ultra-high-energy CR (UHECR) production from GRBs [141].

The era of multi-messenger astrophysics from GRBs was strengthened following the discovery of the NS-NS merger event *GW 170817* detected by the Advanced LIGO and Virgo gravitational-wave detectors. This remarkable event was linked to a low-luminosity short GRB identified as GRB 170817A [142–145], detected just 1.7 seconds after the GW signal. Following the prompt emission, an afterglow was detected in X-ray, optical, and radio wavelengths. The afterglow evolved over many months, providing crucial information about the jet's structure and environment about the GRB [144, 145]. It was localized to within the galaxy NGC 4993 at a distance of about 40 Mpc. The temporal and spatial coincidence of this GW event and the short GRB, along with the identification of a kilonova confirmed that some short GRBs are produced by the mergers of compact objects. Follow-up observations in the VHE γ-ray range were carried-out by H.E.S.S. on this event, in about 5.3 hours after the GW detection, and place upperlimits on the VHE γ-ray flux from the event [146]. While no VHE γ-rays were detected, these follow-ups observations provided useful constraints on the energy output and emission mechanisms of the events. The lack of the VHE detection is consistent with the fact that the relativistic jet was misaligned with our line of sight. Additionally, the energy dissipated in the processes generating VHE γ-rays could have been relatively low.

2.10. Conclusion

In the more than 50 years ago since GRBs were accidentally discovered, much has been learned about their nature. Multi-wavelength data contributed extensively to the understanding the afterglow phase of the GRBs, we know that GRBs are isotropically distributed and most their observational properties are well studied. Optical follow-ups of GRBs confirmed their different progenitors origin and their host galaxies. The afterglow emissions from GRBs could be detectable up to $z \sim 9$ thanks to these optical observations, making them a unique tool to study the early universe (see also [147] for a review). Short GRBs are now associated with binary neutron star mergers. The current VHE observatories have detected VHE γ-ray emission in GRBs. The radiation mechanism responsible for explaining the multi-wavelength emission from GRBs especially in the VHE regime is still an open question. In this thesis, I explore whether the SSC model can fully explain the VHE component in GRBs.

3. The High energy stereoscopic system (H.E.S.S.) experiment

Astrophysical phenomena emit a range of particle species, encompassing electromagnetic radiation across diverse frequencies as well as cosmic rays, neutrinos, and gravitational waves. Each of these messengers carries unique information, but the combination of observational techniques holds special interest as they help in understanding the nature of the sources that emit different messengers. In this chapter, I introduce the working principles of the H.E.S.S. experiment. The fundamental principles of ground-based gamma-ray astronomy using Imaging Atmospheric Cherenkov Telescopes (IACTs), along with typical analysis, reconstruction methods, and calibration procedures, are briefly outlined within the framework of the H.E.S.S. experiment. To better describe the H.E.S.S. experiments, I will briefly introduce cosmic rays and γ-rays.

3.1. Cosmic rays and γ-ray production

The discovery of CRs can be traced back to the late 19^{th} and early 20^{th} centuries when scientists were studying ionization in gases. In 1911 and 1912, Victor Hess [148] conducted a series of balloon flights to study ionization in the Earth's atmosphere. He found that the ionization rate increased with altitude; in his historic balloon flight to an altitude of over 5,000 meters, he measured an even higher level of ionization than he had previously observed. This led him to conclude that there must be a source of ionizing radiation outside the Earth's atmosphere, which he called "cosmic rays". For this work, he was awarded a Nobel Prize in 1936 (shared with Carl D Anderson for the discovery of positrons). In 1929, Walter Bothe and Werner Kohloerster identified CRs as composed of electrons, protons, and light-element nuclei [149]. The cosmic-ray spectrum, depicted in Figure 3.1 follows a power law represented by $dN/dE \propto E^{\alpha}$, where α is the spectral index (with $\alpha \sim$ -2.6 valid for protons and nuclei energies). These particles consist of protons or Nuclei (98%) and the remaining are electrons (2%). The main contribution comes from protons (90% of hadrons), alpha particles (9%) and heavier nuclei (1%) [116]. Particles with

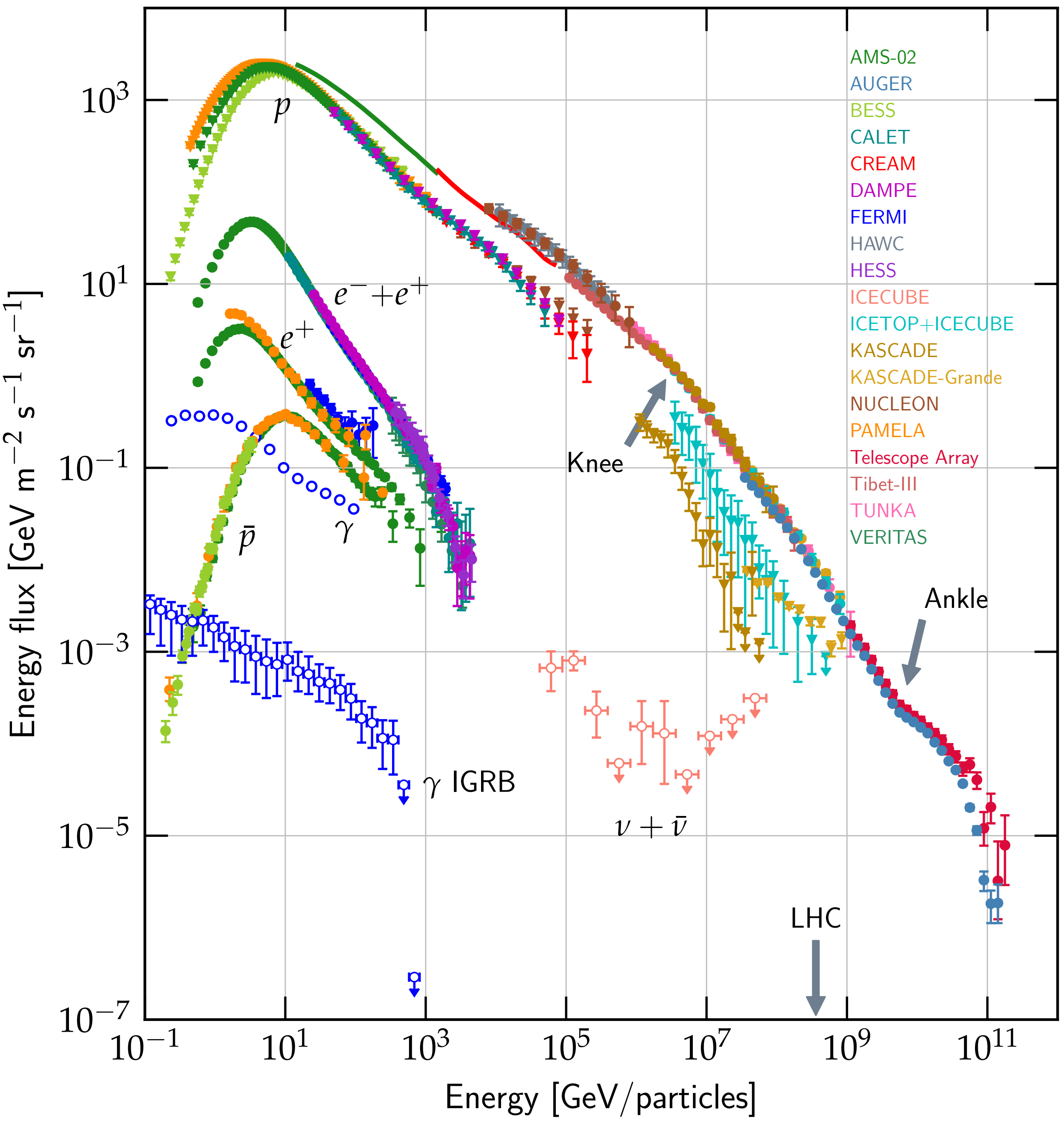

Figure 3.1.: The cosmic-ray spectral-energy distribution of all particles, observed through numerous experiments, as a function of particle energy E from air shower measurements. The spectrum can be likened to a leg with a knee and an ankle. The Figure is modified from [150] and data are referred to therein.

energies between the knee [1] to the ankle[2] indicate a transition from Galactic to extragalactic CRs. GRBs have been proposed as a source of extragalactic CRs [151]. The acceleration mechanism in such extreme extragalactic sources at very energetic energies above the knee is not fully understood and therefore requires a better description of how these CRs within energetic astrophysical environments such as GRBs are accelerated (see Chapter 2.7 for a brief discussion).

γ-rays are produced when CRs are accelerated and propagate within the Universe. In this way, CRs interact with particles within the environment, losing energy and producing photons, where the amount of energy that is lost depends on what type of CR is propagating. For instance, a TeV electron interacting with a photon in the presence of a magnetic field would lose energy and produce photons via synchrotron radiation, inverse compton scattering (as discussed in 2.7). VHE γ-rays can also be produced when an accelerated electron is cooled through multiple interactions during propagation through the Universe, particularly via IC scattering. However, detecting these γ-rays especially with ground-based instruments is not straightforward as it required a detailed understanding of their interaction with the Earth's atmosphere before reaching the detector, which I discuss in the next section 3.2.

3.2. γ-ray astronomy with IACTs

3.2.1. Atmospheric Air Showers

The detection techniques of γ-rays on the ground are not trivial because the Earth's atmosphere is not transparent to CRs and γ-rays in particular. When a primary CR or γ-ray hits the atmosphere and starts interacting with molecules contained in the atmosphere, it initiates a cascade of billions of secondary particles. These particles move at relativistic speed, collectively forming an extended, laterally spread-out shower-like structure called atmospheric "Extensive Air Shower" (EAS) (see Figure 3.2). γ-rays with energies above tens of GeV can be detected on Earth in this way.

Air showers initiated by γ-rays and electrons or positrons are called electromagnetic showers while the ones initiated by hadronic particles such as protons are called hadronic showers. In electromagnetic showers (see Fig. 3.2 (a)), a γ-ray starts by interacting with an air molecule nucleus via the Coulomb field which results in the production of an electron-positron pair. The pair then emit high-energy photons through Bremsstrahlung processes which repeatedly continue

---

[1] This is featured around $3\times10^{15}\,eV$, where the CR spectrum steepens with spectral index increasing from ≈ 2.7 to 3.0. It is believed that CRs in this energy regime have a Galactic origin.

[2] This is region around 5×10^{18} eV on CR spectrum and it's believed that the CRs in this energy regime have an extragalactic origin.

creating a cascade of particles and photons, until ionization losses dissipate the energy of the pair leading to the end of the cascade. A toy model (Heitler's model) describing the processes (EM and hadronic air showers) is shown in Figure 3.2 [152]. After undergoing this process involving n radiation lengths, the total number of particles in the shower becomes $N = 2^n$, with each particle having an energy $E = E_0/2^n$, where E_0 is the initial energy of the primary particle. At a specific point in the development of the shower, a critical energy level known as E_c is reached. At this energy, no more particles can be produced. For electrons in the atmosphere, the critical energy $E_{ce} \approx 84$ MeV. When the shower reaches this critical energy, it has achieved its maximum development and the shower dies out. On the other hand, hadronic air showers are initiated by CRs primarily protons, and interact with air nuclei in the atmosphere via the strong force. The hadronic interactions give rise to various secondaries including neutral pions (π^0) and charged pions ($\pi^{\pm}$). Neutral pions decay rapidly into gamma-rays, which subsequently contribute to sub-electromagnetic showers, and charged pions decay into muons ($\mu^{\pm}$) and neutrinos.

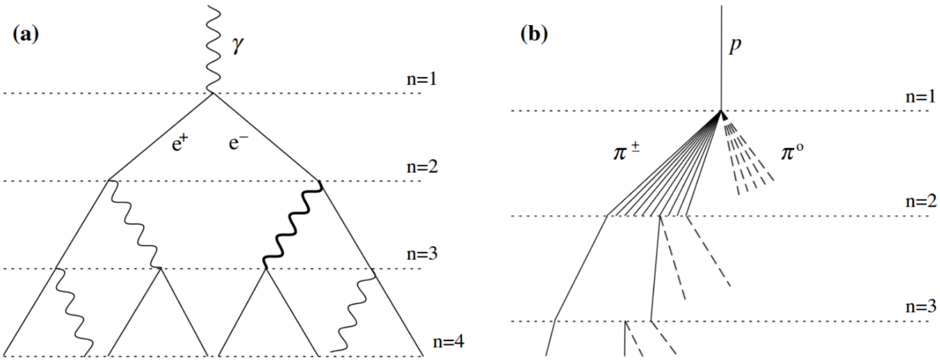

Figure 3.2.: The left panel (a) illustrates a scheme of an electromagnetic air shower. In this type of shower, photons produce electron-positron pairs, and electrons produce photons through Bremsstrahlung after traveling a certain distance (splitting length). The right panel (b) depicts a scheme of a hadronic air shower. In this scenario, a primary proton produces several charged pions, and these pions continue to interact and produce secondary particles at every splitting length. Additionally, the primary proton generates several neutral pions, which eventually decay into photons. However, these neutral pions are not shown in the illustration. Figure adapted from [152].

The theory of lateral and longitudinal distribution of particles in extensive air showers was developed and described independently by Greisen and Kamata and Nishimura [153, 154]. Figure 3.3 shows, a Monte Carlo simulation that illustrates the development of both electromagnetic (left) and hadronic (right) showers each initiated by a primary particle with an energy of 50 GeV (photon) and 100 GeV (proton). These show the differences between electromagnetic and hadronic showers, due to the presence of muons within hadronic showers. Muons have a tendency to disperse a substantial amount of the overall energy toward the outer regions of the shower. In contrast, electromagnetic showers display a more concentrated and compact spacial arrangement with a lower abundance of muons. The particles within these extensive atmospheric showers move at relativistic speeds and can be detected either at the Earth's surface or within the atmosphere itself. Detecting these particles involves the observation of Cherenkov light emitted by them.

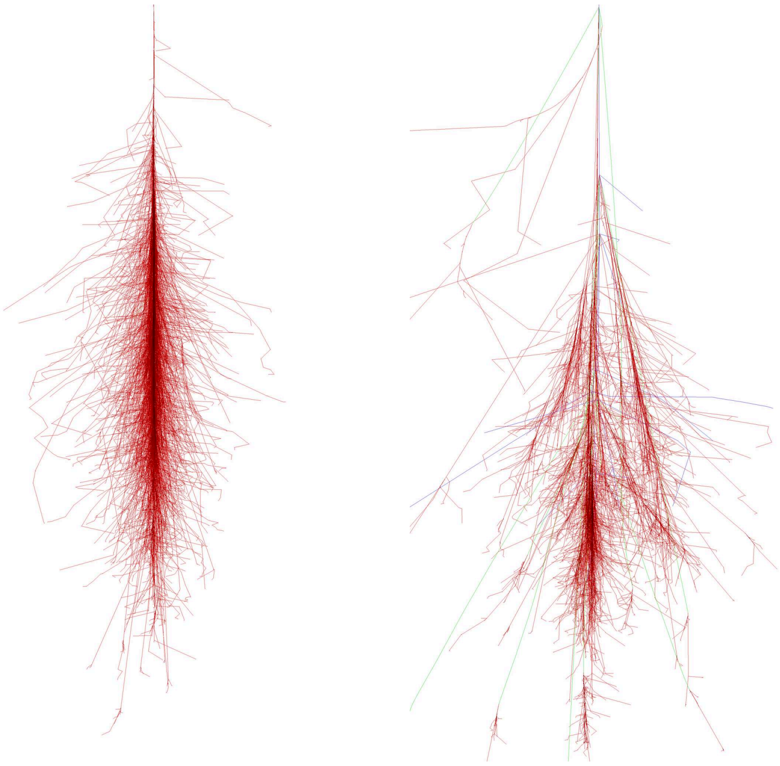

(a) Photon Showers development (b) Proton Showers development

Figure 3.3.: The evolution of atmospheric showers can be understood through simulations. In this context, simulations of atmospheric showers were performed using the Monte Carlo software package CORSIKA [a], focusing on primary particles with energy of 50 GeV for photon and 100 GeV for proton. Figure is taken from [155].

---

[a] CORSIKA (COsmic Ray SImulations for KAscade) is a software dedicated to the detailed simulation of extensive air showers initiated by high energy cosmic ray particles.

3.2.2. Cherenkov Radiation and its properties

Cherenkov radiation is emitted when charged particles move at a speed higher than the speed of light (c_n) in a given medium with a refractive index (n). Pavel A. Cherenkov first discovered the phenomenon in 1934 for which he was awarded the Nobel prize in 1958[3] and it has since been studied in detail [116, 156]. As shown in Figure 3.4, the emission of the Cherenkov radiation occurs as a shock wave forming a cone of an opening (θ_c) and it is given by:

$$\cos(\theta_c) = \frac{c}{vn} = \frac{1}{n\beta}, \tag{3.1}$$

where $\beta = \mathrm{v/c}$ is the ratio between the speed of light and the particle speed, and n is the refractive index in the air.

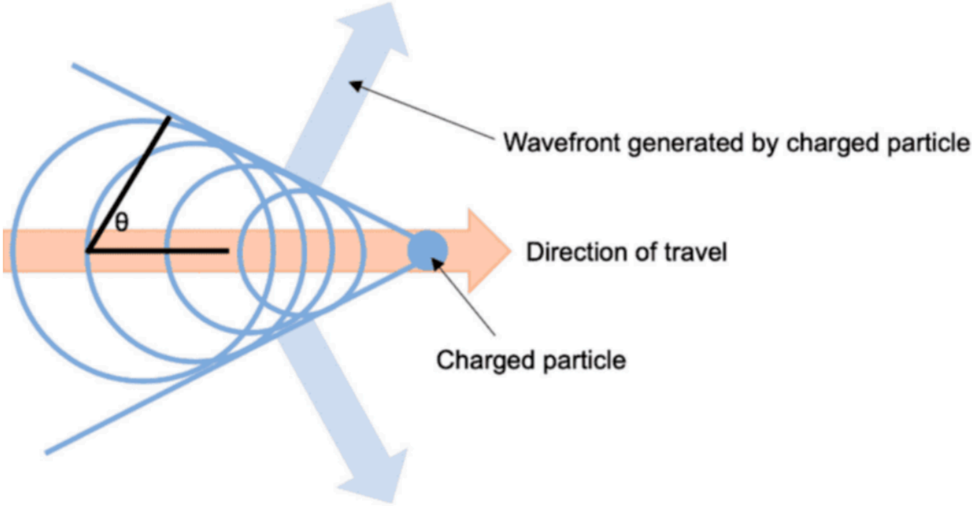

Figure 3.4.: Illustrative diagram of Cherenkov radiation. The radiation is produced when a charged particle traverses the material (red path) with a speed $\beta = v/c_n > 1$ and creates a coherent wavefront that takes on a conical shape (blue circles). Figure adapted from [157].

In the context of Cherenkov radiation in water, the refraction index is $\mathrm{n} = 1.33$ and the Cherenkov angle for $\mathrm{v} \geq \mathrm{c}$ is 41.2°. In the case of air, the Cherenkov angle at sea level around 1.4°, however, this value can vary depending on the atmospheric air density, which affects the refractive index. The air density varies with the altitude h and therefore, the refractive index n also changes through the barometric relationship as:

$$n(h) = 1 + n_0 e^{-h/h_0}, \tag{3.2}$$

---

[3] https://www.nobelprize.org/prizes/physics/1958/cerenkov/lecture/

where n_0 is the constant defined by: $\mathrm{n}_0 = \mathrm{n}(\mathrm{h}_0) = 2.9 \times 10^{-4}$ and $\mathrm{h}_0 = 7.1$ Km.

Typically the altitude at which the number of particles in the air shower is maximum occurs at around 10 Km above the sea level. This would result in a refractive index of about n = 1.0007 and hence, the Cherenkov aperture angle becomes $\theta_c = 0.7°$. Therefore, the Cherenkov cone would project onto the ground to form a circle with radius $\sim 122\,m$ for a typical vertical shower, and potentially much larger for inclined showers. The minimum energy required for a charged particle (e.g. an electron) to produce Cherenkov radiation, can be calculated with the following formula [158]:

$$E_{min} = \frac{m_0 c^2}{\sqrt{1 - n^{-2}}},$$

where m_0 is the rest mass of an electron, c is the speed of light in vacuum, and n is the refractive index in the air. Hence, particles with lower mass, like electrons, typically become the primary source of Cherenkov radiation. The number of photons (N) generated at a specific wavelength (λ) per unit length dx can be determined using the Frank-Tamm equation written as:

$$\frac{d^2N}{dx d\lambda} = 2\pi\alpha Z^2 \lambda^{-2}\left(1 - \frac{1}{\beta^2 n^2(\lambda)}\right), \tag{3.3}$$

where α represents the fine structure constant, $\beta = v/c$ and Z the charge of particle. Due to the spectrum's inverse square (λ^{-2}) dependence on the wavelength, Cherenkov light tends to reach its peak at shorter wavelengths, falling within the blue to near-ultraviolet (UV) range. However, when Cherenkov radiation is produced in the atmosphere, it interacts with air molecules and aerosols, and it is also absorbed by ozone. These interactions and absorption collectively lead to a shift in the peak of the Cherenkov light spectrum to longer wavelengths specifically at around 330 nm (i.e. due to the low energy photons that are largely absorbed in the atmosphere) and extends to the optical blue band.

The detection of Cherenkov radiation from γ-ray events by Imaging Atmospheric Cherenkov Telescope (IACTs) involves several key considerations due to the nature of the Cherenkov signal and the properties of air showers. For instance, a typical Cherenkov signal from a γ-ray event detected on the ground lasts on the order of ~ 10 nanoseconds (ns). A typical telescope mirror area of $\sim 100\,m^2$ can collect sufficient Cherenkov photons, which are faint and spread over a wide area and depending on the geometrical orientation of the Cherenkov cone relative to the pointing direction of the telescope. If the telescope is well aligned with the shower axis, it will detect a more concentrated signal, while the inclined shower axis will result in a more dispersed and weak signal. The IACTs detect γ-rays indirectly by capturing the Cherenkov radiation emitted by the secondary particles generated in the air showers when a high-energy γ-ray enters the atmosphere. To handle the detection of such short-duration Cherenkov pulses and the random (stochastic) nature of air showers require very sensitive photodetectors. As presented in the next section, these leads to technical challenges in the detection and the handling of the reconstruction of the initial γ-ray properties and distinguishing the real signal from the background noise.

3.3. The H.E.S.S. telescope Array

The High Energy Stereoscopic System (H.E.S.S.) comprises an array of IACTs situated in the Khomas Highland of Namibia at an elevation of 1835 meters above sea level (coordinates: 23°16'18.4"S, 16°30'0.8"E). Figure 3.5, shows the H.E.S.S. telescope array, where the control room building is clearly visible in the foreground. The array comprises five IACTs of different sizes of which the four smaller ones (CT1-4) were commissioned from 2004 and began to operate in 2004 (Phase I). They were placed in a square pattern with a side length of 120 meters, and with mirror areas of $107\,\mathrm{m}^2$ (12-meter diameter). In 2012, CT5 was integrated into the existing array (in the center) marking the beginning of the second phase of the H.E.S.S. experiment (phase II). With the addition of CT5, H.E.S.S. became the first experiment to utilize two different sizes of IACTs. The CT1-4 offer a large Field of View (FoV) of 5 degrees in diameter, and are well-suited for studying VHE phenomena with energies ranging from 30 GeV up to 100 TeV across larger regions of the Southern celestial sky, including the Galactic plane and its central region.

The inclusion of CT5 with a 3.2° FoV and covering energy range from $\approx$10 GeV to several tens of TeV, significantly reduced the energy threshold of the system, due to improved sensitivity and camera optimization. It also enhanced its capability for real-time response to transient phenomena, facilitated by the implementation of a fully automatic transients alert and real-time follow-up system [160]. CT5 has the capacity to re-point to any part of the sky within a few seconds [161] which makes it further an excellent telescope for fast follow-up of transient events such as GRBs, and GW alerts. In 2015 and 2016, the cameras of CT1-4 were upgraded featuring improved electronics, leading to a doubling of the data-taking rate compared to the initial cameras used in phase I. The observations conducted by the H.E.S.S. telescopes primarily occur during astronomical darkness, amounting to $\geq$ 1000 hours/year, ensuring that the photomultiplier tubes (PMTs) can operate without risk of damage. Currently, the H.E.S.S. system is able to conduct observations even during moderate moonlight[4] and twilight conditions which

---

[4] H.E.S.S. performs observation in two different standard runs: The ObservationRun mode used for regular astronomical observations during dark conditions, and the MoonlightObservationRun mode that employs an increased trigger threshold to accommodate observations under higher ambient light conditions caused by the moonlight. These moonlight conditions apply when the moon is above the horizon and the following criteria are met: moon phase is less than 40%, and the separation angle is between the target and the moon ranges from 45% to 145%. If the moon exceeds these criteria, no observations are conducted.

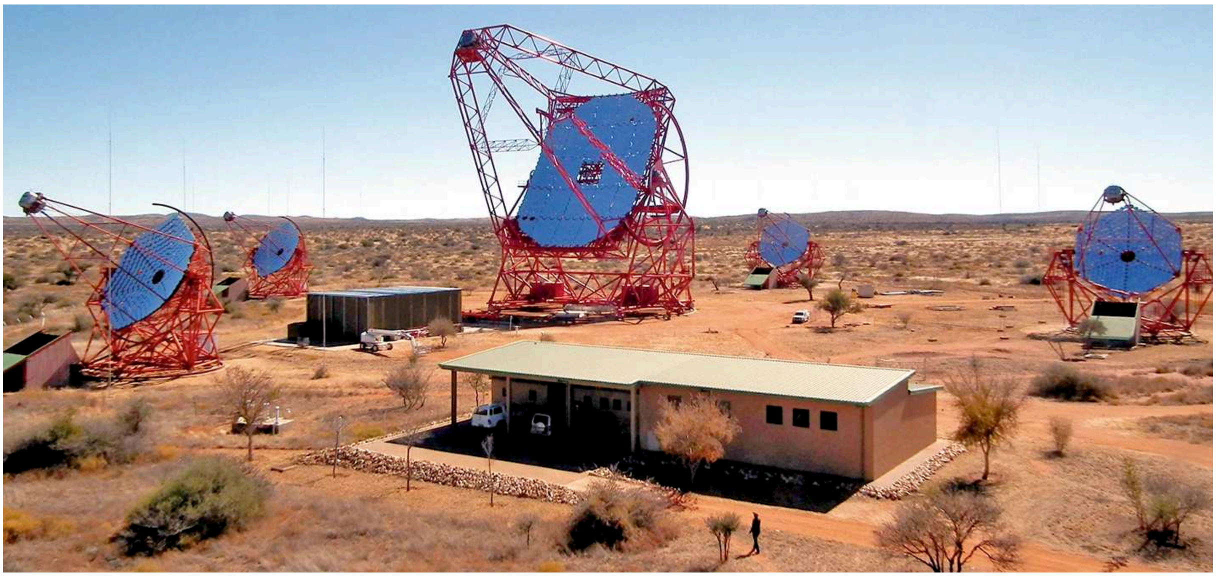

Figure 3.5.: The five telescopes of the H.E.S.S. array on the Khomas Highland of the Namibia desert. The first four small telescopes (CT1, CT2, CT3, and CT4) are placed forming a squared array of about 150 m in length, and the biggest telescope CT5 is placed at the center of the array. A figure adapted from [159].

increases the available time of observations. Alongside the scheduled observations, Target of Opportunity (ToO) observations, involving the pursuit of alerts from other instruments, have become a key component of the H.E.S.S. observation strategy. The identification of astrophysical targets for ToO observations is conducted via an internal proposal evaluation process.

3.4. The H.E.S.S. data acquisition system

The Data Acquisition (DAQ) system manages control of the five telescopes in the H.E.S.S. array and handles data management from each of the five cameras. It enables the array to operate in different sub-array modes, allowing subsets of the telescope to be used simultaneously for various purposes like observations, calibrations, and maintenance runs. The DAQ system includes an auto-scheduler system that optimizes observation schedules based on factors like observation time, the zenith angle, and the target priority (a more detailed description of the DAQ system is in [162]). Moreover, for transient events like GRBs, the DAQ system can filter and respond to notices (alerts) received via the GCN. Upon receiving an alert during observation time, it can interrupt the current observation run and reposition the telescopes to observe the transient. This is done to minimize observation delay, allowing for the initiation of a new run as soon as the target position is reached.

3.5. H.E.S.S. data analysis

3.5.1. Data calibration

The calibration process of the data is essential for converting the recorded signal by the PMTs into a meaningful representation in terms of Cherenkov photon density. This procedure automatically follows the data observations by considering the influence of the various factors in the data-taking process from the mirror optics to the camera response. When a Cherenkov photon enters a PMT, it will create the emission of photoelectrons (p.e) via the photoelectric effect. The emitted photo electrons will generate a measurable current which is then read out as an analog-to-digital conversion (ADC) count. In the following, I give an overview of the key steps involved in the data calibration process in H.E.S.S.

The Pedestal current and night sky background

The first step of data calibration in the H.E.S.S. system involves converting electric currents from PMTs into digital counts per pixel using ADC. The converted signal contains properties of both Cherenkov and night sky background (NSB) photons. The calibration process aims at filtering out the NSB contribution and accurately determine the emitted Cherenkov radiation.
First, the pedestal (P), representing the baseline signal including electronic noise and NSB photons, is determined. The electronic noise is measured during a dedicated data acquisition run where the camera is isolated from external light sources. A number of images are taken, and the mean and width of the ADC distribution per pixel are analyzed to estimate electronic noise.
Estimating the NSB for each observation is crucial. Typically, only a fraction of PMTs in the H.E.S.S. camera are triggered from Cherenkov showers, leaving others available for NSB estimation. The PMTs with signals smaller than 6 photo-electrons (pe) and lacking neighboring pixels above 3 pe are used for NSB estimation. The NSB is usually calculated using either the pedestal width or the PMT current as shown in Figure 3.6. Although the NSB increases the pedestal distribution width, the mean pedestal remains stable.

Gain factor

The gain factor is defined as the ADC to photoelectrons conversion factor. It is determined through dedicated data collection with the camera shielded from external light and by flashing a light emitting diode (LED) with known parameters in front of a PMT. This LED flasher installed inside the camera emits pulses at 70 Hz, providing ≈ 1 photo-electron per pulse to each PMT. The resulting ADC count histogram is fitted to a model incorporating the pedestal as a

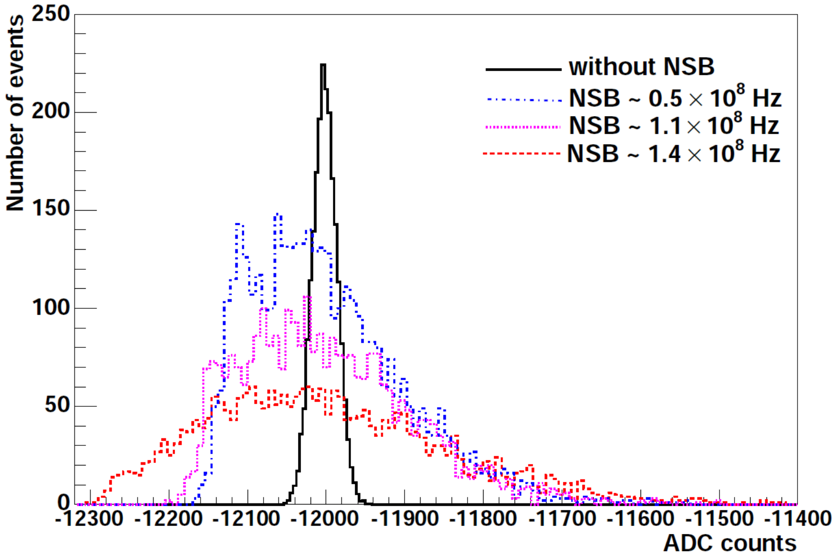

Figure 3.6.: The pedestal distributions in ADC counts show different NSB rates that contain Cherenkov light for a normal observation run from the H.E.S.S. site in different colors. In black the pedestal distribution in the dark is shown. A figure from [163]

Gaussian distribution and photo-electron distribution as Poisson distributions. In the end the two signals are convolved with a Gaussian distribution to adjusted PMT resolution [164]. Each PMT features two gain channels whenever a signal is measured in order to enhance the dynamic range of the cameras: the low-gain channel corresponding to high photon counts (above 200 p.e) and high-gain channel corresponding to low photon counts (up to 150 p.e). If a signal intensity ranges within 150 to 200 p.e, the weighted average of the high and low gain channels is used. The high gain factor (γ_e) is estimated based on the high-gain channel (HG) while the low gain (LG) is derived from the high gain value and a predetermined amplification ratio (HG/LG). Typical values of the cameras gain factor as upgraded since June 2020 recommend to use $\gamma_e =$ 60 ADC/pe and HG/LG = 14 for both dark nights and moderate moonlight nights.

Flat fielding

The flat fielding (FF) is used to address potential inhomogeneities in the PMT responses stemming from variations in the quantum efficiency (QE). The QE refers to a PMT's effectiveness in converting the incident signal into ADC and it is defined as the percentage of incident photons that are completely converted into p.e of a PMT. This calibration technique measures the relative response uniformity of individual PMTs to a consistent LED illumination. Dedicated data acquisition sessions are conducted bi-monthly, with the LED intensity adjusted to achieve ADC counts of the PMT ranging from 10 to 200 p.e for each image. Using the previously estimated gain factor and pedestal values, the flat fielding data are analyzed to derive a flat fielding factor for each pixel. This coefficient represents the ratio of the PMT signal mean to the mean of all PMTs in the camera. A typical FF coefficient distribution for a H.E.S.S. camera is shown in Figure 3.7 and shows a histogram of number of FF coefficients. The peak of the distribution is nearly at 1, indicating that most of these pixels have a FF coefficient close to the mean value, while the spread around the peak shows the variability in the pixels sensitivity. Finally, the signal amplitude of the detected Cherenkov photons representing the conversion from ADC counts to photoelectrons, represented as $A^{HG(LG)}$ in units of photoelectrons, is determined by the following expression:

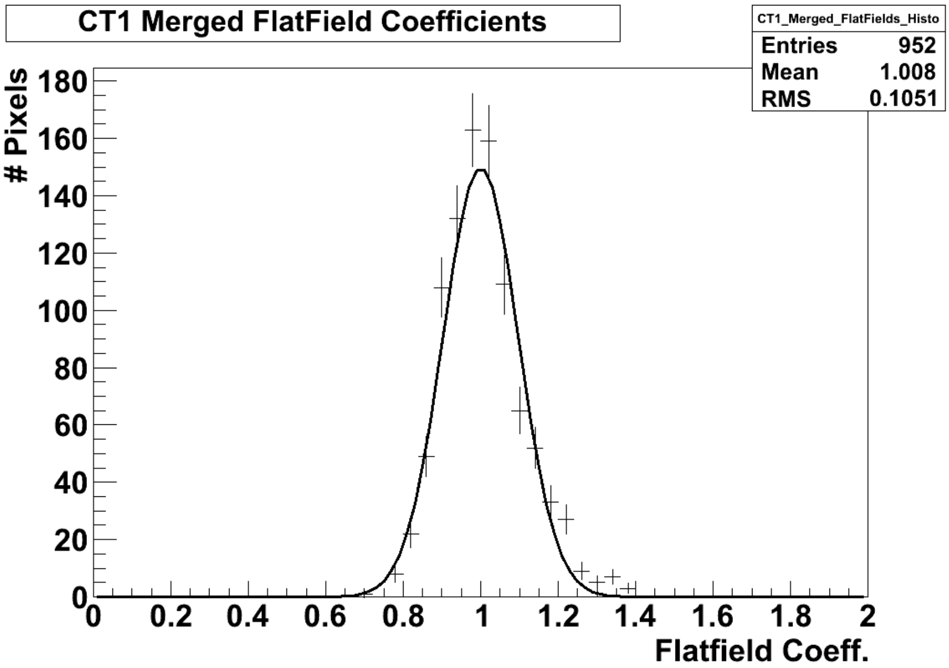

Figure 3.7.: A typical flat-field coefficient distribution of the H.E.S.S. camera. A peak around 1 indicate that most pixels have a FF value close to the mean and the spread indicate the variation in the pixels sensitivity. A figure from [163]

$$\begin{aligned} A^{HG} &= \frac{ADC^{HG} - P^{HG}}{\gamma_e} \times FF^{HG} \\ A^{LG} &= \frac{ADC^{LG} - P^{LG}}{\gamma_e} \times \frac{FF^{HG}}{LG} \times FF^{LG} \end{aligned} \tag{3.4}$$

3.5.2. Data quality check

After calibration and selection of the observation runs to be further analyzed, a data quality check is recommended. It is a very crucial step towards ensuring that high-quality data are used in the analysis. During this process, all observation runs affected by the weather and atmospheric conditions as well as the hardware/mechanical issues are filtered out. In the case of ToO observations, this process is crucial to ensure data quality as the potential signal cannot be confirmed through re-observations. By conducting data quality check thoroughly, the analysis is therefore performed once. In my analysis of GRB 221009A and other transient sources presented in this thesis, I conduct this data quality check before the high-level analysis. More details on the quality checks and selection cuts can be found in [165]. In the following, I briefly discuss different parameters that help to assess the quality of the data.

Acquisition time

The H.E.S.S. observations are conducted under a time slot of 28 min each by default and are called the observation "runs". This duration maximizes the statistics (number of photons) acquired while also minimizing variation of different parameters such as zenith angles and atmospheric conditions during the run. The data acquisition can be interrupted for various reasons including the end of dark time, hardware problems and sudden changes in weather conditions, or a ToO triggered from other instruments. The interrupted runs usually indicate faulty observation, therefore, a quality criteria only include runs with a minimum allowed duration of 10 mins in order to gather high event statistics useful for the analysis.

Pedestals and bad pixels

The pedestal refers to the baseline level of the signal in each pixel of the H.E.S.S. cameras when no Cherenkov light is present. However, some pixel are deactivated, they are not functioning correctly or are showing significant deviations in their pedestal levels. The number of bad pixels of the camera (PMTs) could be a good indication of the status of camera. If more pixels are deactivated, it is a sign that the cameras are no longer sensitive to Cherenkov light which would cause more systematic uncertainties into the analysis. Different reasons such as camera hardware problems and the camera safety system might also deactivate the camera pixels. The camera safety system usually deactivates pixels automatically to prevent serious damage that might come from bright stars in the field of view, NSB or lightning. Therefore, if the fraction of bad pixels due to hardware problems exceed 12.5% for CT1-4 and 7% for CT5, then those observation runs are excluded from the analysis. Additionally, if the fraction of deactivated pixels due to the camera safety system are above 5% for CT1-4 and 4% for CT5, then observations runs are also excluded from the analysis.

Participation fraction

The participation fraction is defined as the ratio of the number of events reported by a single telescope to the total number of triggered events in the observation run. The participation fraction criteria helps in the event reconstruction by ensuring the involvement of multiple telescopes working in stereoscopic analysis. A single event is considered to trigger multiple telescopes if their detection time difference is less than 80 ns. For a run to pass the quality criteria check, the participation fraction of each of the small telescopes (CT1-4) must be greater than 0.4 (i.e. 40%) of the total events, otherwise, their data is excluded from high level analysis [166]. In case the big camera (CT5) participates in the observation run, its minimum participation fraction is reduced to 0.04 due to its much higher trigger rate and the fact that it can be used alone to observe events.

Trigger rates

The trigger rates are defined as the number of detections of Cherenkov light from hadronic or electromagnetic showers as a function of time. The trigger rates are constantly monitored for each telescope and the number of incoming events from the same direction in clear sky conditions remains relatively constant over the course of a 28 min observation period. Under good weather conditions, the trigger rate for the small telescopes (CT1-4) is expected to be nearly 250 Hz while for the big telescope (CT5) is about 5000 Hz. However, several factors such as variation of zenith angle, and clouds or excessive NSB light affect the trigger rate. As the zenith angle increases, the telescopes tend to detect fewer events which slightly lowers the trigger rates, while a lower zenith angle results in a higher trigger rate. On the other hand, strong variations in the trigger rate could be an indication that clouds are moving in and out of the field of view, hence blocking Cherenkov light. In addition, excessive NSB light such as from moonlight might falsely trigger the PMTs resulting in elevated trigger rates. The change in trigger rates strongly affects the observed data especially the γ-ray flux energy threshold and might alter the estimated spectrum. For a good high-level analysis using quantitative data, the trigger rate fluctuation is required to be within 30% of the mean value during the observation run.

Atmospheric transparency coefficient

While trigger rate fluctuations reflect some weather effects, certain atmospheric properties are not detectable this way. For example, fires nearby the observatory can pollute the atmosphere and decrease its transparency. In addition, the distribution of aerosols affects absorption of the Cherenkov light in the atmosphere [167]. A transparency coefficient is defined to account for these atmospheric conditions that influence the detection of the Cherenkov light but are not directly observable through trigger rate fluctuations alone. This coefficient helps in correcting the data for variations in atmospheric transparency due to aerosol, pollution, to ensure that analysis is done on data with good weather conditions [168].

3.5.3. Shower reconstruction

The observed data includes different types of showers such as those initiated by γ-rays, muons, and other charged particles like electrons, protons, or heavy nuclei entering the atmosphere. However, hadronic showers are significantly more dominant by a large factor than electromagnetic showers, creating a substantial background signal that must be filtered out to detect gamma-ray photons. Electromagnetic and hadronic showers look very different on the camera which allows us to differentiate and filter out a large number of hadronic showers through shower parametrization.

Hillas reconstruction

The most standard and the oldest method for shower parametrization was proposed by Michael Hillas in 1985 [169]. In his method, Hillas suggested that an electromagnetic shower image, when captured on camera, can be represented by an elliptical shape with a two-dimensional Gaussian distribution along longitudinal and transverse axes. To describe this elliptical form of the shower image, Hillas created a set of parameters know as the Hillas parameters shown in Figure 3.8.

The Hillas parameters used to describe the elliptical shape of an electromagnetic shower image are the following:

- **Length (L):** which is measured from the longitudinal development of the shower cascade, representing the major axis of the elliptical shower image.
- **Width (W):** which is measured from the lateral development of the shower cascade, representing the minor axis of the elliptical shower image.
- **Total charge (T_q):** this is the total charge inside the ellipse, indicating the amplitude of the shower image.
- **Azimuthal Angle (ϕ):** which is the angle between the center of the camera and the ellipse's barycenter.

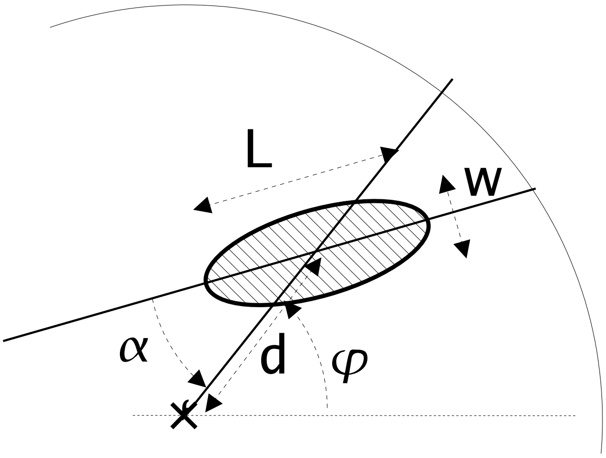

Figure 3.8.: This diagram illustrates a geometrical representation of Hillas parameters. Sourced from [170].

- **Orientation Angle (α) :** which is the angle between the major axis of the elliptical shower image and the and the axis defined by the center of the camera and the barycenter of the ellipse.
- **Nominal distance (d):** this is the distance between the camera center and the barycenter of the elliptical shower image.

The reconstruction of the initial γ-ray in H.E.S.S. can be performed using either a single telescope (CT5, i.e. in mono analysis) or through stereoscopic observations by combining data from more than one or from all the telescopes (CT1-5). For mono analysis, the direction and energy of the shower are estimated using the shape (length, nominal distance and width) and total charge of the recorded images, guided by lookup tables from Monte Carlo (MC) simulations or specific analytical functions. In stereoscopic reconstruction, the direction of the incoming photon is performed by finding where the main axes of the elliptical shower images intersect in the camera. The impact point on the ground is determined by where the telescope lines intersect (angle ϕ_i on the ground), as depicted in Figure 3.9. The photon's energy is then reconstructed using lookup tables from MC simulations.

Advanced reconstruction algorithms

Recent advancements in reconstruction techniques have introduced innovative approaches to enhance the precision and accuracy of parameter estimation in gamma-ray astronomy. Two notable methods include the Model Analysis [172] and the Image Pixel-wise Fit for Atmospheric

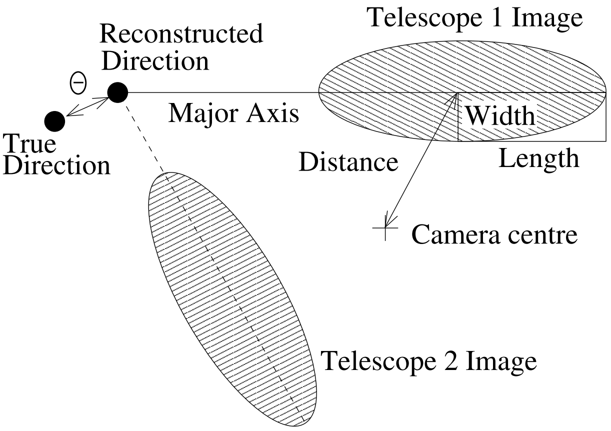

Figure 3.9.: This diagram illustrates the process of determining Hillas parameters for direction reconstruction. It shows the inferred major axes of two telescope images, which are crucial for determining the direction from which the primary particle of an air shower originated. Figure sourced from [171]

Cherenkov Telescopes (ImPACT) method [173]. The Model analysis uses a likelihood reconstruction approach by leveraging Monte Carlo template images to simultaneously reconstruct the energy and direction of the gamma-ray events using global parametrization of the shower image observed by the telescopes. The *ImPACT* method also employs Monte Carlo template images but focuses more on pixel-wise fits for atmospheric Cherenkov Telescopes. Similar to the Model analysis, the *ImPACT* analysis, uses detailed information to perform joint reconstruction of energy and direction. Through out this thesis, I perform the H.E.S.S. analysis using the *ImPACT* analysis method and a cross-check is done using the Model analysis only whenever it is possible.

The performance of the ImPACT reconstruction method has been compared to traditional techniques like the Hillas method. In Figure 3.10 a comparison that demonstrates significant improvements in angular and energy resolution across the entire energy spectrum is shown. Specifically, employing *ImPACT* results in an enhancement by a factor of 2 or more compared to traditional methods. These advancements represent significant progress in refining reconstruction capabilities, leading to more precise and reliable measurements in gamma-ray astronomy.

3.5.4. Gamma-hadron separation

The primary source and the main contributor to the background noise in ground-based γ-ray astronomy comes from the air shower initiated by CRs. Therefore, separating air showers initiated by γ-rays and those initiated by hadron CRs is very crucial for data analysis in H.E.S.S. The gamma-hadron separation can be achieved through comparison of the shower image width

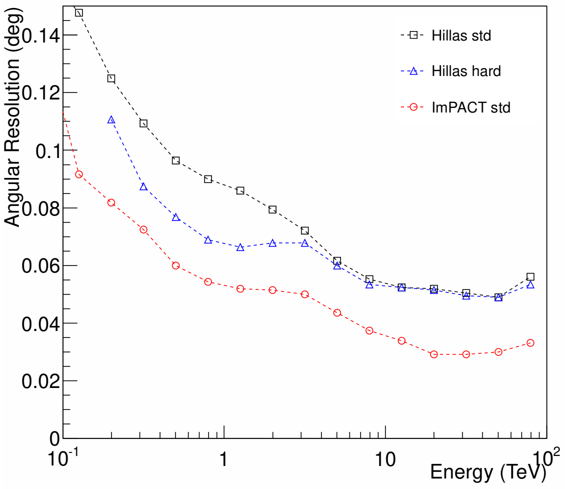

Figure 3.10.: The performance of the Hillas reconstruction method is compared to the ImPACT reconstruction method in terms of angular and energy resolution. It illustrates the angular resolution as a function of simulated energy for observations conducted at a zenith angle of 20°. This comparison provides insight into how the reconstruction methods perform across different energy levels. This figure is obtained from [173].

(W) and length (L) to their respective expected values and variances obtained from simulations as a function of image impact distance and size. Two parameters are therefore introduced for the gamma-hadron separation: the Reduced Scaled (RS) width and length and they can be defined as follows [174]:

$$\begin{aligned} RS_W &= \frac{W - \langle W \rangle}{\sigma_W} \\ RS_L &= \frac{L - \langle L \rangle}{\sigma_L}, \end{aligned} \tag{3.5}$$

where $\langle W \rangle$ and $\langle L \rangle$ are the mean width and length, and σ_W and σ_L are their standard deviations obtained from the look-up tables. γ-ray showers typically have Scaled width and length values closer to zero since their observed values match well with the expectations from electromagnetic shower from the look-up tables. If the reduced scaled parameters are closer to zero, then the image is best represented by the expected shape for the specific shower properties.

Stereoscopic observations improve the background suppression by combining the reduced scaled length and width from all telescope involved in the observations and hence the mean reduced scaled (MRS) parameters becomes:

$$\begin{aligned} W_{MRS} &= \frac{1}{N}\sum_{i=1}^{N} RS_{W,i} \\ L_{MRS} &= \frac{1}{N}\sum_{i=1}^{N} RS_{L,i}, \end{aligned} \tag{3.6}$$

where N is the number of telescopes participating in the observation of the shower image. It was demonstrated that the selection criteria are optimized and employed for various purposes including W_{MRS}, L_{MRS} and the distance θ from the constructed shower position to the source, and the image amplitude [171]. The γ-hadron separation based on the shape parameters improves the background rejection at a level of 90%.

An advanced method for gamma-hadron separation, known as multivariate analysis, uses boosted decision tree (BDT) algorithms to effectively reject background from γ-ray events [175]. A decision tree is defined and used to evaluate whether an image parameter indicates a signal or a background at each split of the BDT algorithm. A collection of these decision trees, each differing in training data and branch (split) structure, forms a forest. By averaging the results from all tress, a reliable measure of an event's likelihood of being a signal or a background ζ is determined. The ζ values distribution for an independent sample of simulated showers between 0.5 and 1 TeV with a zenith angle from 15° to 25° is displayed in Figure 3.11. For both γ-ray and CR showers the ζ values are equally distributed for this specific energy range and zenith angle.

A specific threshold in the signal-likelihood (ζ_{cut}), at each zenith angle and energy band, is set to distinguish between signal and background events. Since the distribution in Figure 3.11 varies for each zenith angle and energy band, using a single threshold for all observations would result in an inconstant signal to background ratio. This is addressed by introducing a γ-ray efficiency (ζ_γ) representing the percentage of γ-rays among the events after applying ζ_{cut}. For *ImPACT*, a γ-ray efficiency of about 83% is selected to maintain uniformity across all zenith angles and energy bands.

3.5.5. Acceptance effects and Effective area

The estimation of the instrument's ability to detect incoming γ-rays (instrument acceptance) involves complex Monte Carlo (MC) simulations and consideration of various factors. Acceptance describes the probability that an incoming particle of a given type will be detected after selection cuts. It depends on factors such as the shower's position in the field of view (FoV), the type and energy of the primary particle, the zenith angle of observation, the level of NSB,

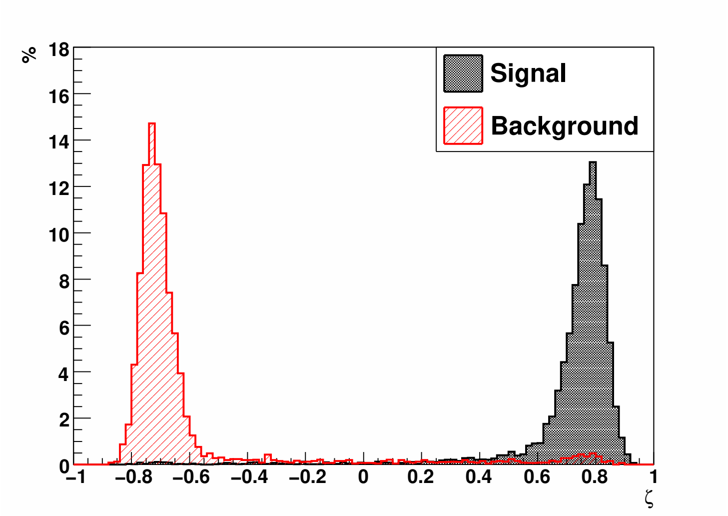

Figure 3.11.: A histogram distribution depicting the γ-ray signal to background likelihood (ζ) for an equal number of simulated γ-ray and CR showers and simulated within the energy range of 0.5 to 1 TeV with zenith angle between $15° - 25°$. This figure is obtained from [175].

and the state of the instruments. This probability of detecting an incoming particle is higher at the center of the camera's FoV and decreases towards the edges.

Conducting observations at high zenith angles ($> 50°$) means particles travel through more atmosphere than at lower zenith angle, causing more low-energy particles to be absorbed by ionizing air molecules on their way before reaching the telescope. This, therefore, results in air showers appearing very dim (small) in the camera. In addition, variations in NSB can also lead to inconsistent air shower images in the camera, which might be excluded from the analysis by the selection criteria. The state of the instruments, including any hardware updates such as mirror replacements, also affects sensitivity of the instrument. Monte Carlo simulations help to estimate acceptance for γ-ray events, but simulating background events to accurately determine the acceptance is time consuming and hence not feasible. Instead, data from regions without gamma-ray sources or using signal-free areas in the same observations can be used to determine background acceptance. This method is more accurate regarding current instrument conditions but is unreliable for sources with limited observation time.

The effective area is the area within which the telescopes are sensitive to γ-rays, extending up to hundreds of meters away from the array. It is obtained from MC simulations over a range of zenith angles, primary energies, and impact distances within an area of approximately $1\,\mathrm{km}^2$ around the array. The effective area (A_{eff}) is calculated as the ratio of detected number of events (N_{det}) to simulated number of events (N_{sim}), yielding $A_{eff} = \epsilon(E)A_{sim}$, where $\epsilon = \frac{N_{det}(E)}{N_{sim}(E)}$.

In the analysis we define the true energy (E_{true}) as the simulated primary energy and the reconstructed energy (E_{reco}) resulting directly from the analysis. In addition, we define an energy (ΔE) as the uncertainties in the energy reconstruction methods which is estimated with $\Delta E = \frac{E_{reco} - E_{true}}{E_{true}}$. A safe energy range is therefore defined as the region where $\Delta E < 10\%$, typically excluding the very-low-energy part of the spectrum and the high-energy end due to insufficient statistics [171].

3.5.6. Sky Maps

A sky map serves as a 2-dimensional histogram depicting properties of a designated celestial sky area, arranged into spatial bins. Transforming a segment of the sky onto a flat surface necessitates a projection method. Several techniques exist, each with unique traits like maintaining distances or areas, affecting their suitability for different analyses. The choice of projection method also considers the sky region's position within the selected coordinate system and its extent.

From the dataset comprising γ-ray-like events that meet the reconstruction's cut parameters, count maps can be directly generated by binning the spatial distribution of the reconstructed events. By referring to the total event number of excess counts and bin size, the bins in a sky map may contain few events, which can affect the statistical significance and clarity of the features in the sky map, making it harder to detect a γ-ray signal. To improve visualization, it's common practice to correlate the bins with Gaussian or disk kernels that roughly match the uncertainty width of air shower directional reconstruction. Since the acceptance for air showers and exposure across the field of view of an IACT varies and datasets may include multiple observation runs with different pointings, raw counts data needs adjustment for non-uniform exposure. This procedure guarantees that the bin contents across the map are comparable. Extracting the true γ-ray signal necessitates modeling such background, a topic addressed in the following section.

3.5.7. Background estimation

The counts in each bin of a sky map comprise both potential signal events and a certain number of background events. The background estimation methods consist of comparing the emission in a region where a source is expected (ON region) with that in surrounding regions where no emission is anticipated (OFF regions). In H.E.S.S., two main methods are utilized for background estimation: the *ring* background method and the *reflected-region* background method. A comprehensive overview of the various background estimation techniques is given in [176]. These two approaches involve masking and excluding nearby regions with known or expected emission, such as the Galactic plane or extended sources, from the background analysis.

- **Ring Background Method**: In this method, a ring with specified radius and thickness (OFF region) is delineated around a tested position (ON region) as illustrated in Figure 3.12. For point-like sources in extragalactic areas, the choice of radius and thickness involves a trade-off between minimizing contamination from the ON into the OFF region while ensuring a reliable estimation of camera acceptance. Adaptive sizes for the OFF region are utilized in sky regions where contamination from neighboring sources is possible. This method is commonly used in producing sky maps but has the drawback that asymmetry and non-uniformity in the telescope's acceptance must be carefully addressed.

- **Reflected Background Method**: In this method, the source position is intentionally displaced from the center of the camera, and all OFF regions are symmetrically positioned at the same angular distance. By ensuring that all regions are equidistant from the camera center, any variations in the instrument's response are minimized (refer to Figure 3.12). Consequently, this allows for the extraction of the signal without the need for extensive modeling and computation. This method is particularly advantageous when extracting data for spectral analysis.

There exist other background subtraction methods like template background method, or the FoV background method in which the background noise is estimated from the source region itself rather than from other regions in camera's FoV. These additional methods are useful for extended sources, where the integration radius of the source region is not enough to encompass all emission [176]. In all cases, regardless of the background method used, the regions in the FoV known to emit significantly VHE γ-rays should be masked when estimating the background noise.

3.5.8. Signal extraction and significance estimation

The significance of the detection of a source is determined using the Li & Ma method as described in [177]. This involves a comparison of the number of events in the ON and OFF regions on a run-by-run basis, extracted using methods outlined in Section 3.5.7, for example. A coefficient α is calculated at each position on the map and takes into account the area, acceptance, and the exposure time of the N_{ON} and N_{ON} regions. After estimating the background, the excess events N_{excess} from the source is calculated as: $N_{excess} = N_{ON} - \alpha \times N_{OFF}$, where $\alpha = \frac{\kappa_{ON} \cdot t_{ON} \cdot A_{ON}}{\kappa_{OFF} \cdot t_{OFF} \cdot A_{OFF}}$ is the relative exposure. In the later κ is the acceptance, t is the exposure time and A is the size of the ON and OFF regions respectively. Hence, the significance (S) of the excess events is

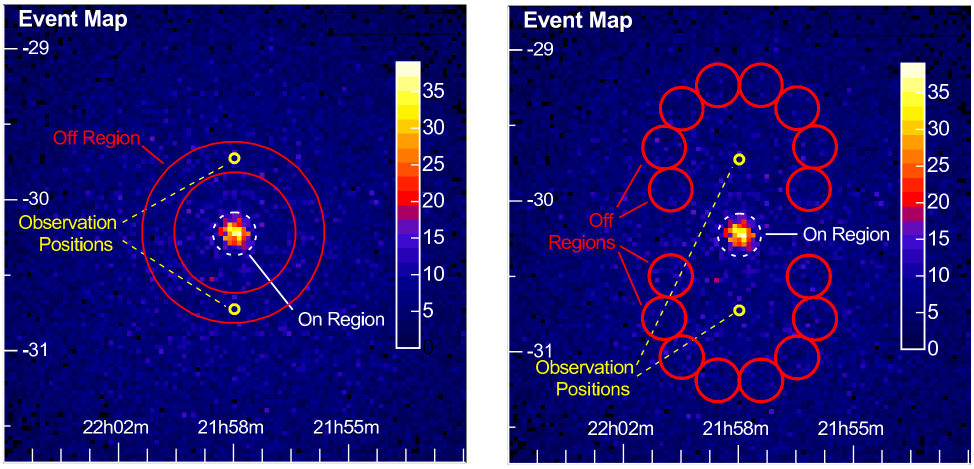

Figure 3.12.: Diagram depicting the ring background and reflected background methods, the two primary approaches for background estimation utilized in H.E.S.S.. On the left: Ring background method where the OFF region is a ring centered around the ON region. On the right: Reflected background method where the observation is conducted with an offset so that the ON region is at the same distance as the OFF regions. This figure is obtained from [176].

calculated using Eq. 17 of Li & Ma [177] as follows:

$$S = \sqrt{-2\ln(\lambda)}, \tag{3.7}$$

where λ is the likelihood ratio between the signal hypothesis and the pure background hypothesis and is calculated using the following formula:

$$\lambda = \left[\frac{\alpha}{1+\alpha}\left(\frac{N_{ON}+N_{OFF}}{N_{ON}}\right)\right]^{N_{ON}} \times \left[\frac{\alpha}{1+\alpha}\left(\frac{N_{ON}+N_{OFF}}{N_{ON}}\right)\right]^{N_{OFF}} \tag{3.8}$$

Where N_{ON} represents the count in the region of interest (ON region), N_{OFF} denotes the count in a neighboring region where no signal is anticipated. In H.E.S.S., a source is considered detected in VHE γ-ray energies if $S \geq 5\sigma$, meaning that the excess counts are significantly higher than the expected background level by more than 5 standard deviation. The number of standard deviation σ by which the observed signal differs from the background can be estimated as:

$$\sigma = \sqrt{N_{ON} + \alpha^2 N_{OFF}}$$

3.5.9. Flux and Spectral information

After rejecting the background and having applied the safe energy threshold cuts (as introduced in Sect. 3.5.5), a differential energy spectrum for a potential γ-ray source can be reconstructed. This is calculated from the number of photons detected per unit area and time, within a differential energy interval E (usually expressed in units of $1/(TeV\, cm^2\, s)$. It can be defined as:

$$F(E) = \frac{dN_\gamma}{dE} = \frac{1}{A_{eff}} \frac{dN_\gamma}{dE\, dt}, \tag{3.9}$$

where A_{eff} is the effective collection area, and is determined from the Monte-Carlo simulations. These simulations take into account the probability of detecting a γ-ray photon with a specific energy, zenith and azimuth angle, and the event offset from the observation position of the array, after gamma-hadron cuts have been applied. Typically, the effective collection area is estimated by simulating a γ-ray source with a power-law differential-energy flux assuming a photon index of -2.0 and saved through a set of lookup tables. It is crucial for a spectrum estimate, to consider that some events in the ON region may arise from the background events. Therefore, the spectrum can be estimated through the extraction of the number of events in the ON region relative to the OFF region, knowing the acceptance factor α calculated above. The differential source flux point can then be expressed as the difference between ON- and OFF-flux [166, 178] and can be estimated as follows:

$$F(\Delta E) = \frac{1}{t\Delta E} \left[\sum_{i=1}^{N_{ON}(\Delta E)} \frac{1}{A_i} - \alpha(\Delta E) \sum_{j=1}^{N_{OFF}(\Delta E)} \frac{1}{A_j} \right] \tag{3.10}$$

The derived differential spectrum can be fit in order to determine a functional representation of the γ-ray spectrum. There is however a more advanced technique for spectrum estimation known as the forward-folding method [120], in which the number of expected gamma events in the reconstructed energy depends on the probability of reconstructing an event of true energy at a reconstructed event energy. In addition, both cases of lookup tables exhibit a dependency on parameter such as zenith angle, azimuth angle, and telescope optical efficiency.

Usually, the goal of the gamma-ray astronomy is to detect γ-ray emission from potential γ-ray sources, but many of the H.E.S.S. observations result in non-detections. However, these non-detections are still valuable for understanding the acceleration and radiation mechanisms in the universe. For example, most of the observations of transients such as GRBs and the positions of different messengers such as neutrinos by H.E.S.S. turn out to be non-detections. In such case, we estimate upper limits on the flux level of the GRBs or neutrino sources, as discussed in this thesis. This approach helps exclude higher flux at a certain confidence level, thereby constraining models that predict specific flux levels [166]. For more details about the upper limit estimation the reader is referred to [166, 178].

3.5.10. Tools and analysis configuration

The H.E.S.S. event reconstruction scheme offers three main configurations for this purpose (see also [179] for details):

- The *Loose Cuts:* They are used to enhance γ-ray detection for bright sources, especially in regions with high signal-to-noise ratios, though this results in less effective background rejection. They are tailored for enhancing sensitivity to very bright γ-ray sources characterized by a steep powerlaw spectrum with an index of $\alpha > 3$. It achieves a lower energy threshold and, consequently, worsens the angular resolution compared to standard cuts.
- The *Standard Cuts:* These have stringent shower selection criteria, and are employed when the region to be studied is characterized by significant background noise, like the Galactic plane. The standard cuts are optimized for strong γ-ray sources with a powerlaw spectrum characterized by an index of $2 \leq \alpha < 3$. They are primarily employed for spectral studies, offering a balance between energy threshold and angular resolution.
- The *Hard cuts:* These are designed to prioritize faint γ-ray sources with a powerlaw spectrum characterized by an index of $2 \leq \alpha < 3$. They result in a higher energy threshold and better angular resolution compared to standard cuts, making them suitable for spectral and morphology studies.

The data analysis procedures outlined in this thesis involve several stages utilizing diverse software tools. Initial reconstruction of air showers from raw H.E.S.S. data is achieved using internal software known as *hap-18*, employing a methodology based on Hillas parameters as previously discussed. Multivariate analysis techniques, as described in [175], are then applied for gamma-hadron separation. The events reconstruction is done using a procedure from [173], which employs an image template-based maximum likelihood fit, and completed with a high-level analysis configuration known as *std_ImPACT* for the case of neutrino follow-up analysis and *loose_ImPACT* [173] for the case of GRB analysis performed in this thesis. The reconstructed air-shower properties are exported to FITS format[5] for subsequent high-level data analysis using the open-source software *Gammapy*[6] [180, 181], version 1.1. The *Gammapy* software utilizes common Python libraries such as *astropy* [182], which is specialized in general astronomical

---

[5] See https://fits.gsfc.nasa.gov/ for details.

[6] Github link: https://github.com/gammapy/gammapy

calculations involving coordinates, units, and transformations. Additionally, *Gammapy* incorporates *iminuit* [183] and *sherpa* [184] for model fitting purposes.

3.6. Conclusive remarks and outlooks

In this chapter I summarized the important concepts from observation through calibration to the data analysis principles for H.E.S.S. telescope. H.E.S.S. has been operational since 2003 and will continue to perform legacy observations until at least 2026. More than 100 VHE sources have been detected and greatly contributed to our knowledge of both Galactic and extra-galactic VHE astrophysics [185]. The H.E.S.S. array has undergone numerous upgrades that contributed more on its discoveries. For example CT5 plays a key role focusing on the 50 GeV to 10 TeV energy range. This upgrade in 2012 boosted the array's sensitivity and made it the first hybrid IACT array in the world [185, 186]. In 2016, the small telescope (CT1-4) cameras underwent significant upgrades, which increased the array's sensitivity and reduced further the readout system's dead-time and improved the trigger criteria [187, 188]. All these hardware upgrades and software improvements enabled the H.E.S.S. experiment to pursue more ambitious goals, leading to unprecedented discoveries. Recently H.E.S.S. has shifted its focus to Target of Opportunity (ToO) observations resulting in significant discoveries especially the detection of transients such as GRBs in the VHE γ-ray bands [15, 17]. In addition, H.E.S.S. started contributing to multi-messenger observations by performing follow-ups of different messengers such as neutrinos and gravitational waves [189–191]. In Chapter 4 through Chapter 6, I will present analysis and detail discussion of the selected sample of GRBs and neutrino events observed by H.E.S.S. in recent years.

4. H.E.S.S. follow-up observations of `GRB 221009A` (the Brightest of All Time, or BOAT)

Although a wide range of space- and ground-based instruments have been used to study GRBs across the electromagnetic spectrum, the detection of VHE emission from these events have been challenging. For years, GRBs were observed in γ-ray to optical bands, however VHE photons above 100 GeV remained undetected. It was only recently, thanks to advancements in the observation strategies of IACTs such as H.E.S.S., that VHE emission from GRBs was finally observed, providing new opportunities to explore the extreme physics behind powerful explosions. The detections of GeV emission from GRBs by *Fermi*-LAT show that GRBs can produce energetic emission. A notable example is GRB 130427A during which photons up to 98 GeV were detected [192], which provided additional support for the highly anticipated VHE γ-ray emission in GRBs. However, γ-rays from distant astronomical sources are significantly affected by the EBL. The EBL effect becomes more pronounced with increase of the redshift, where nearby GRBs are less attenuated and therefore require only minor corrections for EBL absorption. In Figure 4.1, the EBL absorption factor is compared for the three notable GRBs detected at VHEs. To date, there are less than 10 GRBs identified at VHE energies. Below I cite a few particularly notable ones:

- GRB 180720B: this event marked the first VHE GRB and was detected by H.E.S.S.. It was detected by numerous space telescopes, including *Swift*-BAT, *Swift*-XRT, *Fermi*-LAT, and others across various wavelengths. H.E.S.S. initiated observations nearly 10 hours after trigger as soon as the source became visible in the sky, capturing the afterglow phase at energies exceeding 150 GeV. It was situated at a relatively close distance with a redshift of z$\approx$ 0.653 (see detailed results published in [17])
- GRB 190829A: H.E.S.S. detected this GRB over three consecutive nights (4.2, 18, and 37 hours) after the trigger. For the first fours of H.E.S.S. observation, the afterglow emission was detected up to nearly 3.3 TeV. Notably, it stands as the closest GRB observed in the

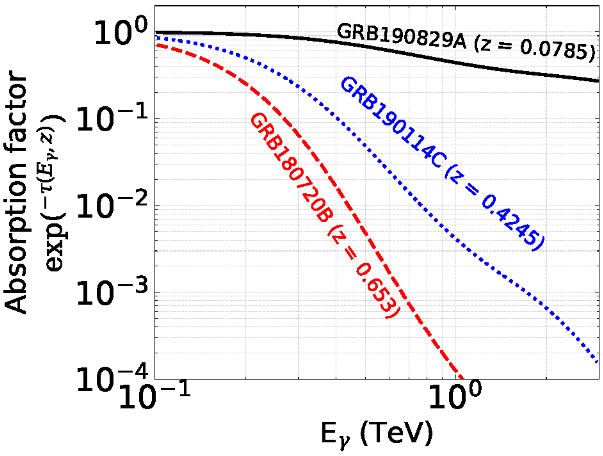

Figure 4.1.: A comparison of the EBL absorption factor for three notable GRBs detected at VHE γ-rays. The EBL absorption factor is plotted as a function of energy from 0.1 to 3 TeV, with the redshifts of each GRB indicated within the plot. The EBL model used is from [193].

VHE regime to date, boasting a redshift of $z \approx 0.0785$. Intriguingly, the analysis revealed spectral and temporal resemblances between the VHE and X-ray emissions (see details published in [15]).

- GRB 190114C: *MAGIC* telescopes detected this GRB a few minutes after the trigger at energies above 300 GeV for the first 20 minutes. This event occurred at a distance of $z = 0.425$ and detailed discussions are published in [126].

It is worth noting that all GRBs detected in the VHE range displayed notably intense X-ray afterglows (refer to Figure 4.2 for visualization).

In this chapter, I present the H.E.S.S. follow-up observations on the brightest GRB since GRB observations began (GRB 221009A). A part of this chapter was written by the H.E.S.S. collaboration as a paper for which I am the main corresponding author. It was published in the Astrophysical Journal Letters[1] [194]. Another part of the chapter was published in the ICRC2023 proceedings[2] [195] for which I am also the main corresponding author.

---

[1] The main paper is available here: `https://iopscience.iop.org/article/10.3847/2041-8213/acc405`

[2] Available here: `https://pos.sissa.it/444/705`

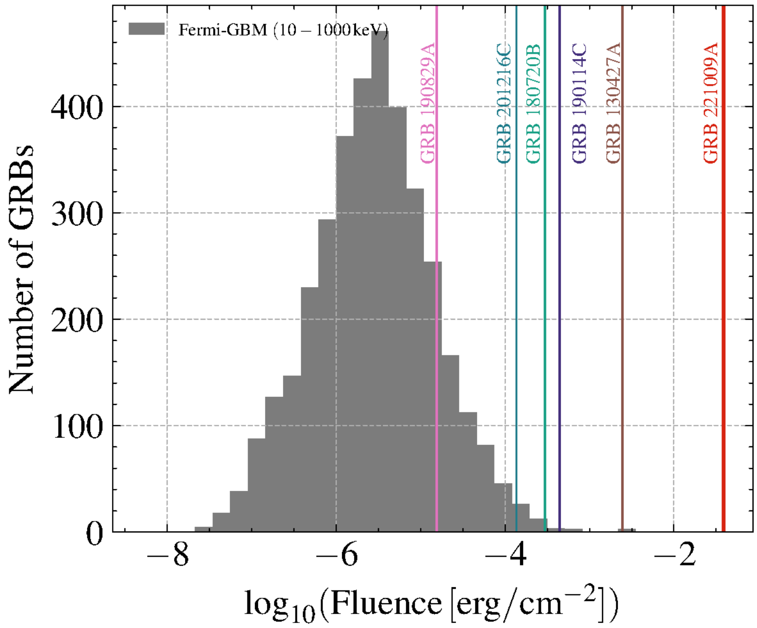

(a)

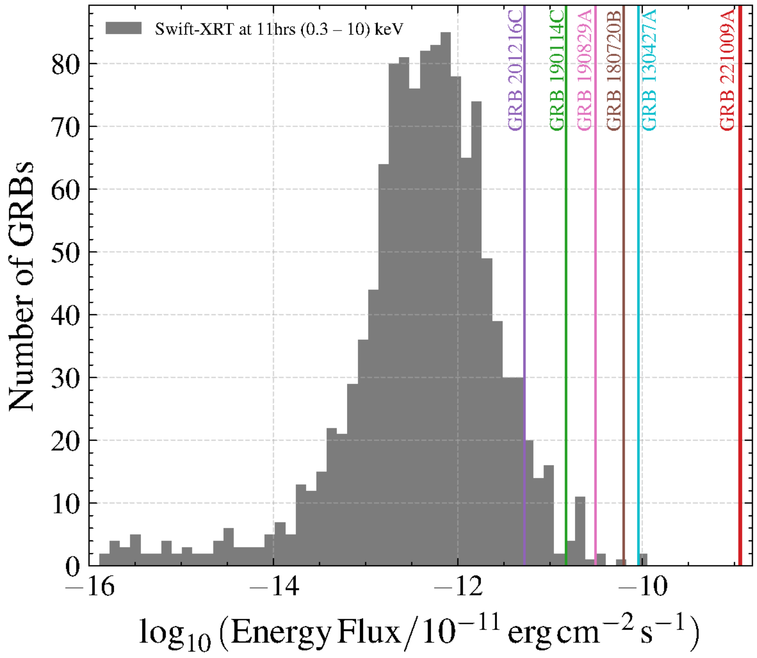

(b)

Figure 4.2.: Known VHE detected GRBs in the context of GRB observations by *Fermi*-GBM and *Swift*-XRT. The left panel shows the prompt emission fluence distribution in the energy of 10-1000 keV as measured by the *Fermi*-GBM as of 2023. Data are obtained from the fourth *Fermi*-GBM catalog [196]. The right panel shows the distribution of the afterglow energy flux at 11 hours as measured by *Swift*-XRT as of 2023. *Swift*-XRT data are obtained after [197]

4.1. GRB 221009A: Observations

4.1.1. Initial Discovery

On the 09^{th} October 2022 at 13:16:59.99 UTC, the exceptionally bright prompt emission from GRB 221009A triggered the *Fermi*-GBM [50, 198]. Although the *Fermi*-GBM notice was automatically sent out, additional information regarding classification and localization were not released due to communication problems [50]. In this chapter, I refer to the *Fermi*-GBM trigger time as T_0. At this time, the GRB was occulted by Earth for the *Swift*. When the source position then became visible, Swift was transiting the South Atlantic Anomaly (SAA) and was unable to observe the GRB [199]. One hour later, at 14:10:17 UTC, the GRB was still bright enough to trigger *Swift*-BAT, as an image trigger (in contrast to the standard rate trigger for GRBs). This caused the satellite to automatically slew to the source, allowing for follow-up observations by the *Swift*-XRT, which reported a localization of R.A. (J2000) = $19^h\ 13^m\ 03^s$, decl. (J2000)= $+19^\circ\ 48'\ 09''$ with a positional uncertainty of $5.6''$ [200]. Due to the particularly bright signal (see also Figure 4.3) and localization near the Galactic plane (with Galactic latitude of $b = 4.3$ degrees), the Swift team initially classified the event as having a Galactic origin. Several detections of the early-time emission revealed important characteristics including, to name a few:

- The first detection of TeV energy photons within a few hundred seconds after T_0 as reported by *LHAASO*, potentially up to 18 TeV [14, 201, 202].
- The redshift was estimated to be z=0.151 based on optical observations conducted with the ESO X-shooter/ Very Large Telescope (VLT) [203].
- The fluence of the GRB was measured to be approximately $0.21\,\mathrm{erg\,cm^{-2}}$ in the 20 keV–10 MeV [204] and $0.19\,\mathrm{erg\,cm^{-2}}$ in the 1–10000 keV bands, respectively [50, 205]. Typical fluence of GRBs detected by *Fermi*-GBM range around 10^{-5} to $10^{-3}\,\mathrm{erg\,cm^{-2}}$, making `GRB 221009A` one of the brightest bursts ever observed in terms of energy detected.
- A significant isotropic equivalent energy E_{iso} in the 1–10000 keV range was estimated to be nearly 1.01×10^{55} erg from the redshift and the fluence measured by *Fermi*-GBM [50]. This energy is an order of magnitude higher than the typical E_{iso} for long GRBs that ranges from 10^{52} to 10^{54} erg
- *Swift*-XRT identified rings from dust echoes [206], a phenomenon in which X-rays from a distant source scatter off interstellar dust, creating concentric ring patterns. These rings provide important information about distance and distribution of the dust along the line of sight and the X-ray source properties.

- Neutrino searches by both IceCube and KM3NeT yielded non detections [207, 208].

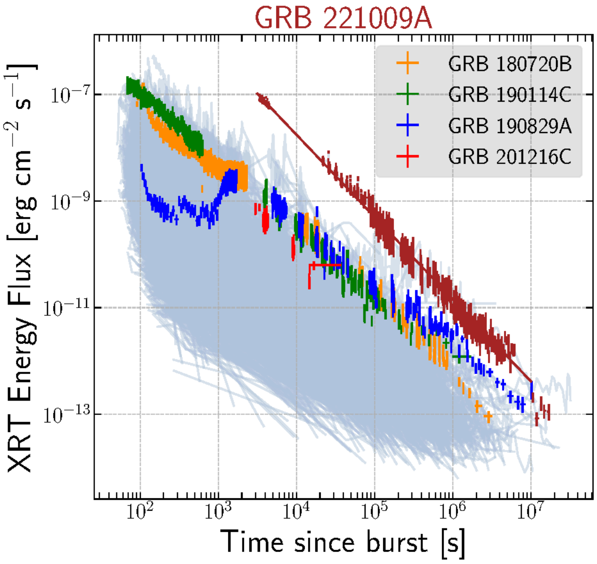

Figure 4.3.: The X-ray lightcurves for all GRBs detected by the Swift-XRT are presented, with those having associated VHE gamma-ray detections highlighted and named in color, contrasting with the rest of the GRBs depicted in gray. The data are obtained online following [197].

The X-ray and optical observations continued until the source was blocked by the Sun, revealing a characteristic decay pattern of a GRB afterglow (see Fig. 4.3 for the X-ray afterglow). Furthermore, the optical data provided indications of emission originating from an associated supernova emission which remains detectable even in the radio band up to several days after trigger [209–213].

4.1.2. H.E.S.S. Observations

The H.E.S.S. follow-up observations started on October 11, 2022 ($\simeq T_0 + 51.8\,$hours) due to the full Moon on the first and the second nights (see Fig. 4.4). H.E.S.S. started observations with all five telescopes as soon as observing conditions allowed. In the 3^{rd} night after the trigger, an extended (compared to the standard 28-minute runs) 32-minute observation run was taken in normal conditions during the dark time (when the moon was still below the horizon). A second run followed using settings optimized for observations under high levels of optical background light as is the case during times of bright moonlight [214]. H.E.S.S. observations continued until the 09^{th} night after trigger.

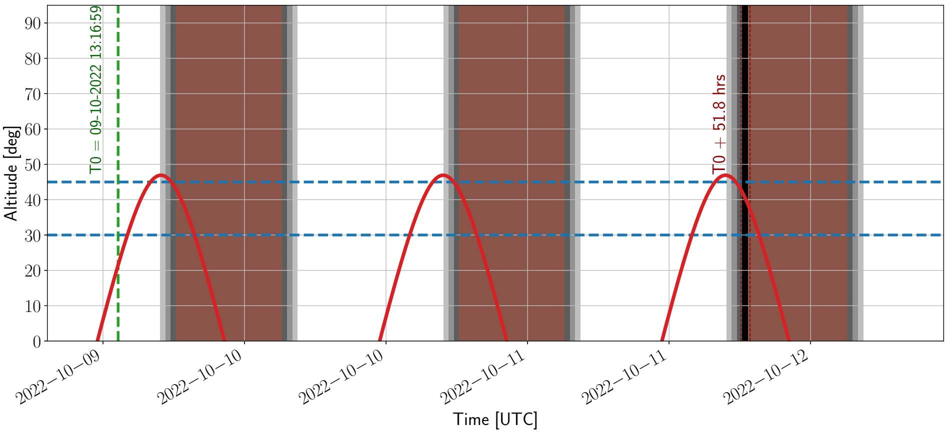

Figure 4.4.: Visibility plot of the GRB 221009A. The altitude angle evolution is shown as a function of time for GRB 221009A at the H.E.S.S. site for the night of the first observation. The trigger time (T_0) is indicated with a green dashed vertical line. The dark-red vertical dashed lines indicate the start and the end of the H.E.S.S. observations for the first night. The gray band show the twilight, the black band show the dark time, and the brown band show the bright moonlight.

The observations were conducted under very poor atmospheric conditions due to the regular biomass-burning seasons in Namibia (H.E.S.S. site) [215]. The quality of the atmospheric condition is quantified by the atmospheric transparency coefficient (ATC) [168]. A lower value of ATC indicates a lower transmission of the Cherenkov light through the atmosphere. Table 4.1 shows the corresponding ATC values for the observation run numbers (see Fig. 4.5)

The nominally accepted values of the ATC are above 0.8 and below 1.2 (see red line in Figure 4.5). During H.E.S.S. observations of GRB 221009A, the transparency coefficient were lower than the nominal value, therefore, a correction procedure has been applied (see discussions in sect. 4.2). There are additional datasets, including the ones taken on other nights, that are excluded from the analysis due to further degradation of the atmospheric conditions by the presence of the clouds. Note that CT5 data are not used for this study due to the lack of a cross-check analysis at the time of writing this thesis, hence only the data taken with CT1-4 are used. Table 4.1 summarizes the H.E.S.S. observations used in the analysis.

4.2. H.E.S.S. analysis and results

The data observed by H.E.S.S. during the follow-up campaign are analyzed using the ***ImPACT*** reconstruction procedure [173], which employs an image template-based maximum likelihood fit. To isolate the desired signals from hadronic background events, I employed a multivariate analy-

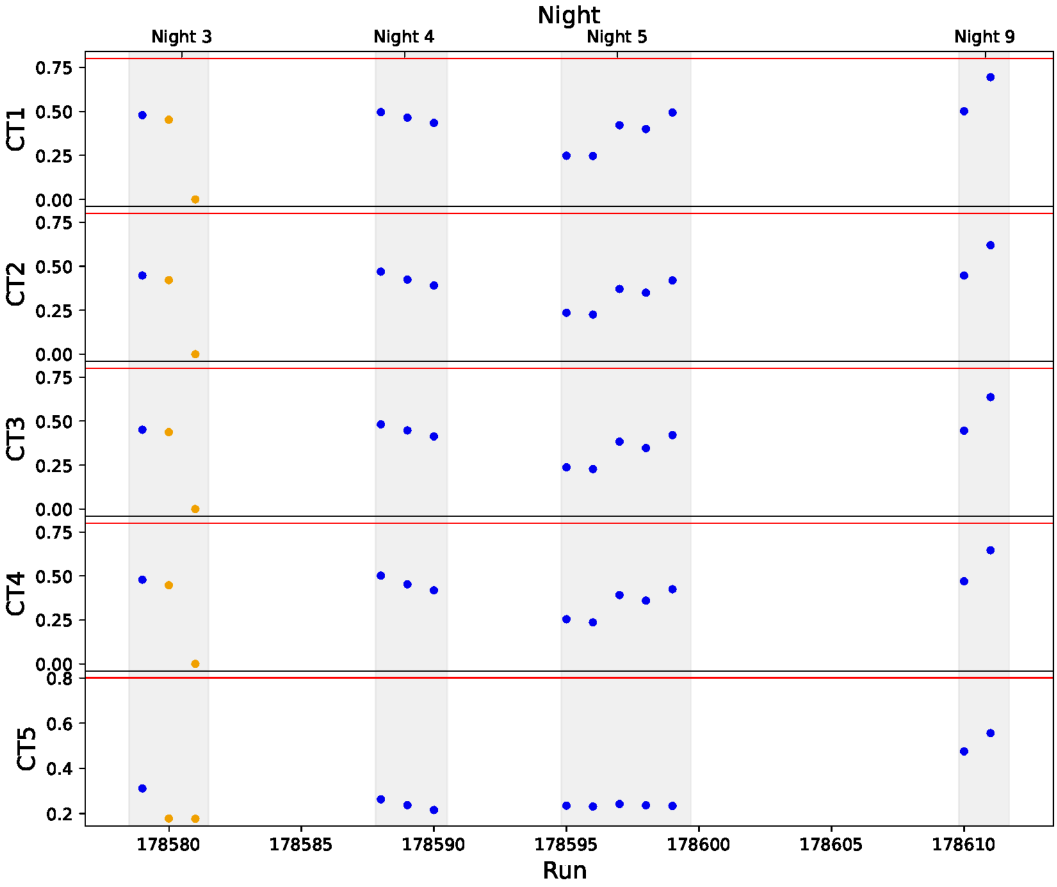

Figure 4.5.: Atmospheric transparency coefficient (ATC). A scatter plot that show the run-wise atmospheric transparency coefficient for GRB 221009A as a function of run numbers for individual H.E.S.S. telescope. The moon light observations are shown in orange while the regular observation runs are shown in blue. The horizontal red line show the minimum normal acceptable value for the ACT. The top x-axis shows the H.E.S.S. observation night since T_0. Note that night 5 was removed from the analysis due to further degradation of the atmosphere during this night.

Calendar date	Interval	$T_{\text{Start}} - T_0$ [s]	$T_{\text{End}} - T_0$ [s]	Average zenith angle [deg]	ATC
October 11 2022	Night 3	1.901×10^5	1.920×10^5	49.3	0.46
October 11 2022[a]	Night 3	1.922×10^5	1.929×10^5	52.7	0.44
October 12 2022	Night 4	2.765×10^5	2.782×10^5	49.6	0.49
October 12 2022	Night 4	2.783×10^5	2.800×10^5	52.6	0.45
October 12 2022	Night 4	2.800×10^5	2.818×10^5	57.0	0.41
October 17 2022	Night 9	7.087×10^5	7.104×10^5	51.7	0.47
October 17 2022	Night 9	7.105×10^5	7.122×10^5	56.9	0.65

Table 4.1.: H.E.S.S. observations of GRB 221009A. Column 2 denotes the number of nights after T_0. Columns 3 and 4 represent the run start and end time since T_0, in seconds, respectively. Column 5 shows the average zenith angle under which the observations were conducted and column 6 shows the Atmospheric Transparency Coefficient (ATC).

---

[a] taken under moderate moonlight

sis scheme [175] as described in section 3.5.4. The results obtained from the multivariate analysis are independently validated using a separate analysis chain based on the model analysis [216]. This involves a log-likelihood comparison between recorded shower images and templates generated semi-analytically. As mentioned in section 4.1, all observations taken during the H.E.S.S. follow-up observations on GRB 221009A suffered from atmospheric disturbance mainly caused by factors like enhanced aerosol levels. To correct for these atmospheric disturbances, I applied a correction scheme. This scheme assesses the impact of these disturbances on instrument response functions, derived from Monte-Carlo simulations. The scheme computes a correction factor for the anticipated Cherenkov light by contrasting the actual profile with the ideal profile used in the simulations. Subsequently, the correction is implemented by modifying a posteriori the instrument response functions and the reconstructed energies of events [217]. Figure 4.6 shows the excess and significance of events by comparing the corrected and uncorrected events from the atmospheric effect.

To validate these corrections I employed a dedicated analysis that uses runwise simulations taking into consideration the actual observation conditions and telescope configuration during the H.E.S.S. observation of the GRB 221009A following the methods outlined in [218]. For the γ-ray shower selection, I used loose cuts criteria known as "***loose_ImPACT***" (see details in Chapter **??**). The analysis chain consists of deriving the Hillas parameters and discards all images with Hillas amplitude lower than 40 ADC [179]. Therefore, ***loose_ImPACT*** is expected to result in lower energy thresholds, increasing the signal as well as the background counts. Subsequently, in the high-level analysis, the observed data are transformed into GADF

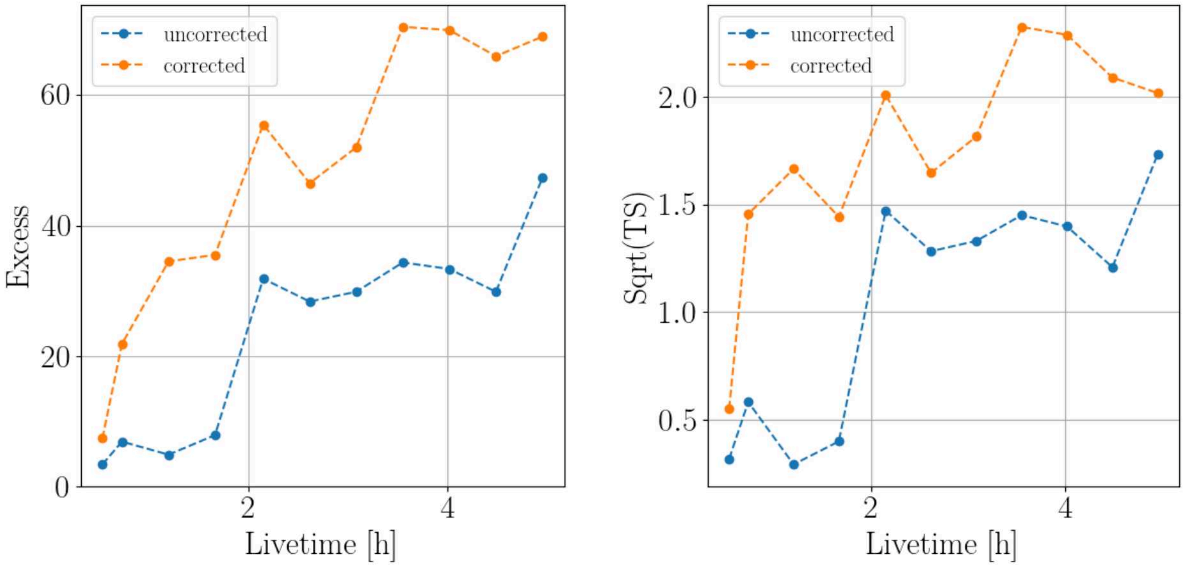

(a) Excess events as a function of livetime

(b) Significance as a function of livetime

Figure 4.6.: The Atmospheric correction scheme applied on the full datasets.

format[3] [219] and I used the open source analysis package **Gammapy (V1.0)** [180, 181]. To investigate the potential signal and reduce the risk of inadvertently incorporating emissions from unrelated sources, I created maps displaying the excess γ-ray counts and the significance. These maps cover a range of $\pm 2.0^\circ$ centered around the GRB emission position. This approach allows for a focused examination of the vicinity of the expected signal while minimizing the influence of unrelated sources, and automatically or manually removing any known bright γ-ray source.

The generation of the excess and significance maps involves the application of the ring background technique [176]. Circular ON regions, each with a radius of 0.122 degrees and centered at every point on the map, are used. The corresponding annular OFF-source regions, also centered at the same positions, have radii with inner and outer radii of 0.5 and 0.8 degrees, respectively. When computing the exposure ratio between the ON and OFF-source regions at each test position, a radially symmetric model for the background acceptance is integrated spatially over the positions within the field of view of each observation. Table 4.2 shows the results of the analysis and relevant basic statistics for the individual nights. Note that Night 5 (see Fig 4.5) has been removed from the analysis due to further degradation of the atmospheric conditions by the presence of clouds.

---

[3] `https://gamma-astro-data-formats.readthedocs.io/en/latest/index.html`

Night (s) after T_0	Livetime (h)	ON counts	OFF counts	α	Excess	Significance (σ)
Night 3	0.7305	10	144	0.0696	-0.033	-0.010
Night 4	1.4172	22	376	0.0627	-1.6	-0.324
Night 9	0.9349	7	159	0.0666	-3.6	-1.146
All	3.0827	39	686	0.0638	-4.8	-0.7

Table 4.2.: Source statistics of GRB 221009A per each night after correcting for atmospheric effects. The results are derived using ***loose_ImPACT*** analysis configuration.

When combining data from all three nights, I derived $\mathrm{N_{ON}} = 39$ event counts at the position of the source, and $\mathrm{N_{OFF}} = 686$ event counts in the off-source regions, resulting in an on-source exposure to off-source exposure ratio of $\alpha = 0.0638$. Using the statistical formulation outlined in Li & Ma [177], I calculated the excess counts to be -4.8. The $\mathrm{N_{ON}}$ events are found to be consistent with the expected background at a $-0.7\,\sigma$ level indicating no significant γ-ray excess. The excess and the significance maps derived from this analysis are illustrated in Figure 4.7.

No significant emission of VHE γ-rays was detected at the location of the GRB 221009A in either the combined datasets or in individual nightly observations. To quantify the absence of a signal, I computed upper limits. The spectral analysis is done using the reflected background method as described in [176] by using the same sizes circular ON and OFF regions as previously described. The determination of the energy threshold (E_{thr}) played a critical role in establishing the lower limit of the spectral analysis. The E_{thr} is defined as the lowest energy at which the bias between reconstructed and simulated energies is below 10%. For the combined dataset, E_{thr} was determined to be 650 GeV.

I assumed the observed spectrum to be a power law of the form:

$$\left(\frac{dN}{dE}\right)_{obs} = N_{0,obs}\left(\frac{E}{E_{0,obs}}\right)^{-\alpha_{obs}}, \tag{4.1}$$

where $N_{0,obs}$ is the flux normalisation, α_{obs} is the photon index, and $E_{0,obs}$ is the reference energy. The subscript *obs* means that parameters describe the emission observed on the Earth (observed emission). Due to EBL absorption, photons emitted at the source undergo attenuation during their journey to Earth. This phenomenon leads to the result that the observed spectrum from the source appears softer than the emitted one. To correct for this effect, the intrinsic spectrum was derived by incorporating an exponential term in the spectrum, which describes the energy-dependent EBL absorption. This correction was applied for the redshift of z=0.151. The chosen EBL model described in [193], and is defined as:

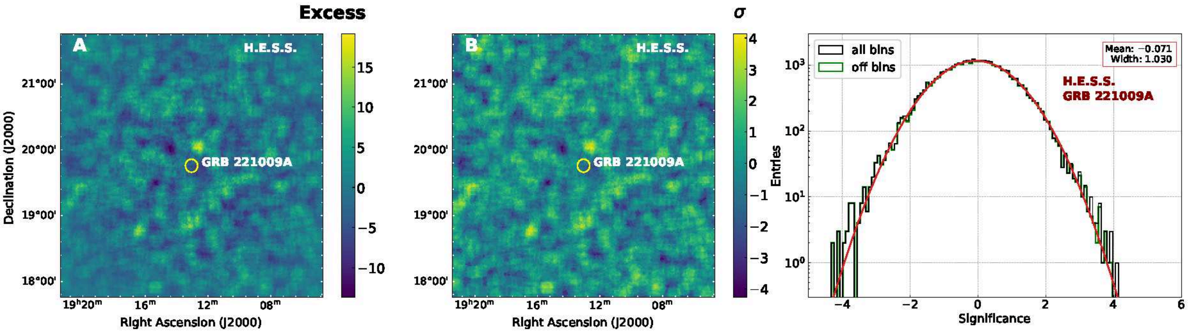

(a) Excess and significance distributions. The figure is adapted from [194]

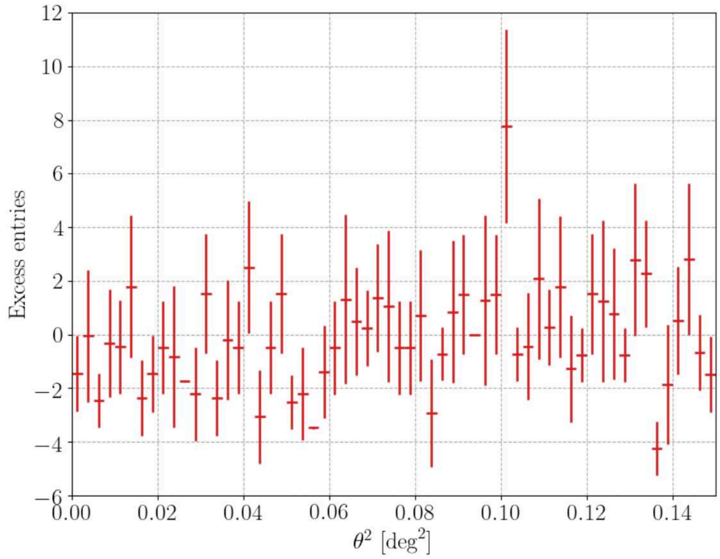

(b) θ^2 distribution in the FoV

Figure 4.7.: Top panel: Left; Excess count map computed from the H.E.S.S. observational data taken on GRB 221009A presented in Table 4.1 with a 0.1° oversampling radius (yellow circle). Middle; Significance map computed from the H.E.S.S. excess count map of GRB 221009A. Right; Significance distribution of the H.E.S.S. significance map entries in black and a Gaussian distribution fit in red. The bottom panel shows the excess of γ-like events in the skymap over the squared offset in the field of view.

$$\left(\frac{dN}{dE}\right)_{obs} = \left(\frac{dN_0}{dE}\right)_{int} e^{-\tau(E,z)}, \tag{4.2}$$

where $\tau(E, z)$ is the energy-dependent EBL absorption coefficient for a redshift z.
The intrinsic flux upper limits were obtained by fixing the photon index[4] value to -2.0, which corresponds to the mean photon index observed in GRBs detected by *Fermi*-LAT [220]. These flux upper limits are computed at 95% confidence level (C.L) using the Poisson likelihood method described in [221]. The differential flux upper limits in the form of $E^2 \frac{dN}{dE}$ are shown in Figure 4.8. Differential flux upper limits together with other basic statistics in different energy bins are shown in Table 4.3 for different observation nights. I calculated integral flux upper limits from the energy threshold (E_{thr}) to 10 TeV for each night, with the upper boundary determined as the energy above which the number of OFF events (N_{OFF}) < 10. The resulting integral energy flux upper limits are presented in Figure 4.11 and 4.12. For the combined dataset, the integral energy flux upper limit is $\Phi_{\mathrm{UL}}^{95\%} = 9.7 \times 10^{-12}$ erg cm^{-2} s^{-1}, and individual per-night integral energy flux upper limits are detailed in Table 4.5.
Systematic effects encompass uncertainties associated with atmospheric corrections, assumptions about the intrinsic energy spectrum, variations in EBL absorption models, and general uncertainties in flux and energy scale. These systematic uncertainties affect the calculated upper limits conservatively by approximately a factor of 2. There is an expected increase in the impact of systematics with energy, affecting both the differential and integral upper limits on the γ-ray flux.

4.3. Multi-wavelength context

4.3.1. *Swift*-XRT analysis

The *Swift*-XRT data were acquired using the time-sliced spectra tool[5] [197]. The time intervals were initially selected to be strictly contemporaneous with the H.E.S.S. periods. On two of the three nights however, there is no contemporaneous *Swift*-XRT data, and on the other night, there is only a single *Swift*-XRT observation. Consequently, I defined time slices in a manner that included one set of contiguous *Swift*-XRT observation immediately proceeding and following the H.E.S.S. observations. However, adhering to this rule for the third night of the H.E.S.S. observation led to an exposure time that was too low to constrain the *Swift*-XRT. To address this, I extended the time slices for this night to encompass *two* sets of contiguous *Swift*-XRT

---

[4] The fact that I am calculating differential upper limits, this choice of index does not have a very large effect on the result.

[5] `https://www.swift.ac.uk/xrt_spectra/addspec.php?targ=01126853&origin=GRB`

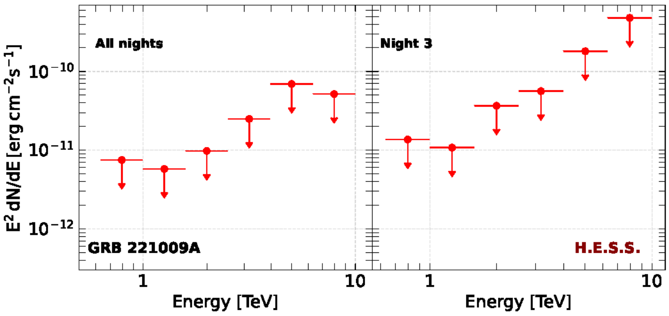

(a)

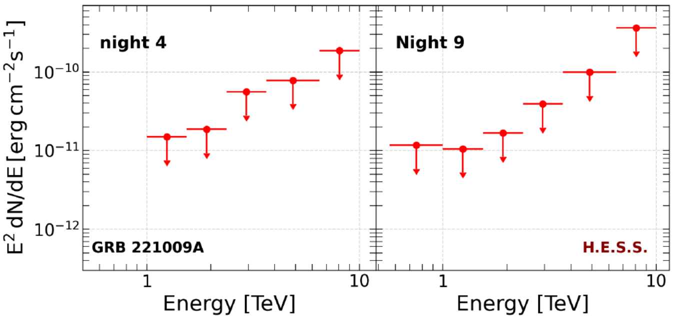

(b)

Figure 4.8.: Top panel: 95% C.L. differential flux upper limits on an intrinsic (EBL-corrected) E^{-2} GRB spectrum, derived from the H.E.S.S. observational data taken on GRB 221009A in all nights combined (left) and Night 3 only (right) [194]. Bottom Panel: same as a top panel but for night 4 (left) and night 9 (right) after the trigger.

E_{ref} [TeV]	E_{min} [TeV]	E_{max} [TeV]	dN/dE$_{UL}$[$1/(cm^2\,s\,TeV)$]	N$_{ON}$	N$_{OFF}$	α
Night 3						
0.794	0.631	1.0	1.352×10^{-11}	4	47	0.0667
1.259	1.0	1.584	4.246×10^{-12}	1	35	0.0689
1.995	1.585	2.512	5.749×10^{-12}	2	27	0.0714
3.162	2.512	3.981	3.508×10^{-12}	1	10	0.0741
5.012	3.981	6.309	4.486×10^{-12}	1	9	0.0769
7.943	6.309	9.999	4.751×10^{-12}	0	1	0.0769
Night 4						
1.241	1.0	1.540	6.081×10^{-12}	6	98	0.0625
1.911	1.540	2.371	3.180×10^{-12}	4	82	0.0625
2.943	2.371	3.652	4.030×10^{-12}	5	59	0.0625
4.870	3.652	6.494	2.058×10^{-12}	3	55	0.0634
8.058	6.494	9.999	1.792×10^{-12}	0	12	0.0612
Night 9						
0.749	0.562	1.0	1.298×10^{-12}	2	29	0.0667
1.241	1.0	1.540	4.275×10^{-12}	2	62	0.0667
1.911	1.540	2.371	2.857×10^{-12}	1	30	0.0667
2.943	2.371	3.652	2.826×10^{-12}	1	12	0.0667
4.870	3.652	6.494	2.616×10^{-12}	1	11	0.0667
8.058	6.494	9.999	3.515×10^{-12}	0	5	0.0667
All Nights						
0.794	0.631	1.0	7.420×10^{-12}	9	100	0.0714
1.259	1.0	1.585	2.273×10^{-12}	10	170	0.0741
1.995	1.585	2.512	1.531×10^{-12}	7	123	0.0741
3.1623	2.512	3.981	1.559×10^{-12}	6	71	0.0769
5.012	3.981	6.309	1.721×10^{-12}	5	51	0.0769
7.943	6.309	9.999	5.114×10^{-12}	0	13	0.0741

Table 4.3.: Results of a 1D reflected background analysis. Column 1, 2 & 3 denote the reference energy, minimum and maximum energy in different bins, respectively. Column 4, shows the 95% C.L differential flux upperlimits. The last three columns represent the ON and OFF counts in different energy bins as well as the ratio between the on-source and off-source exposure in each bin, respectively. Note that all flux upperlimits are EBL corrected.

observations on either side as shown in Figure 4.9. It is important to note that, due to the usage of the larger time bins for the *Swift*-XRT observations, the true uncertainties for strictly contemporaneous observations are expected to be underestimated. The extended *Swift*-XRT time-sliced observation windows (start and stop) are presented in Table 4.4.

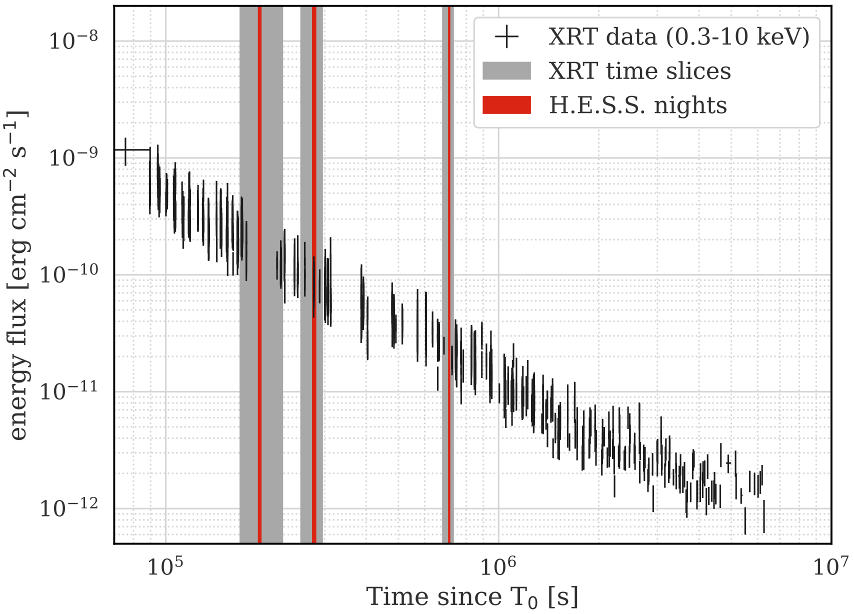

Figure 4.9.: Extended *Swift*-XRT time slices against H.E.S.S. observations window where the gray windows enclose the XRT data used in the per-night analyses.

In this analysis, I exclusively used Photon Counting (PC) data to reduce the risk of contamination from the dust rings [222, 223].

Night (s) after T_0	XRT window start	XRT window stop	exposure
Night 3	168000	223000	3 ks
Night 4	260000	291000	1.6 ks
Night 9	680000	730000	1.1 ks

Table 4.4.: Enlarged *Swift*-XRT time slices.

The *Swift*-XRT data were re-fit using ***XSPEC v12.13.0c*** with a power law of the form:

$$\frac{dN}{dE} = k\left(\frac{E}{E_0}\right)^{-\alpha}, \tag{4.3}$$

where $E_0 = 1$ keV, together with two absorption components [197]. More specifically, I used the model of the form:

`TBabs * zTBabs * powerlaw`,

where `TBabs` represents the absorption due to interstellar material in our Galaxy and `zTBabs` accounts for the absorption in the source's host Galaxy at a redshift z. The Galactic column density ($N_{\mathrm{H,gal}}$), which is a parameter that goes into `TBabs`, is set to a value of 5.38×10^{21} cm^{-2} [224].

I first performed a simultaneous fit for the three nights, where the column density at the source ($N_{\mathrm{H,int}}$) is tied across all spectra but allowed to vary, assuming that the intrinsic absorption remains constant over these timescales. For each time interval, I kept the parameters k and α free. The fitting statistic employed is the `C-statistic`[6], deemed suitable for *Swift*-XRT data. Assuming a constant $N_{\mathrm{H,int}}$, the obtained value is $N_{\mathrm{H,int}} = (1.32 \pm 0.18) \times 10^{22}$ cm^{-2}. I then refit the three time intervals separately, with $N_{\mathrm{H,int}}$ frozen to this previously determined value. The detailed results can be found in Table 4.5 and plotted in Figure 4.11. The assumption of a constant column density over these timescales, as applied in this analysis, has faced scrutiny in other GRBs, as demonstrated by the recent work such as [225] for *GRB 190114C*. In the case of GRB 221009A, there are indications of a potential higher level of absorption at earlier times, as observed in optical data [210] particularly around night 3 ($\approx$ 2 days after T_0). It is important to note that there exists a degree of degeneracy between the effects of $N_{\mathrm{H,int}}$ and α. For example, a higher $N_{\mathrm{H,int}}$ value might be partially compensated by a softer value of α, impacting the returned best-fit photon spectrum. If indeed, $N_{\mathrm{H,int}}$ is higher around night 3, then the true value of α for night 3($\approx$ 2 days after T_0) would be expected to be softer than the calculated value 1.7, possible more closely aligned with the value of 1.9 found for the other two H.E.S.S. nights (although the indices are consistent with the 2σ). The *Swift*-XRT spectra are plotted in Figure 4.10. However, a thorough investigation of this effect is beyond the scope of this study.

4.3.2. *Fermi*-LAT analysis

I conducted *Fermi*-LAT analyses to constrain the spectrum at MeV-GeV energies. The *Fermi*-LAT data analysis is performed using a likelihood comparison approach with public tools provided by *Fermi*-LAT collaboration. The *Fermi*-LAT instrument employs a similar concept as H.E.S.S., where it compares electronics read-outs with Monte-Carlo simulations and reconstructs the initial direction and energy of the parent-like γ-ray event. The resulting event list, which is publicly accessible, is then extracted for a chosen sky region and time range. These event lists are a form of 3-D maps consisting of photon counts, distributed spatially as a 2-D and

---

[6] `https://heasarc.gsfc.nasa.gov/xanadu/xspec/manual/XSappendixStatistics.html`

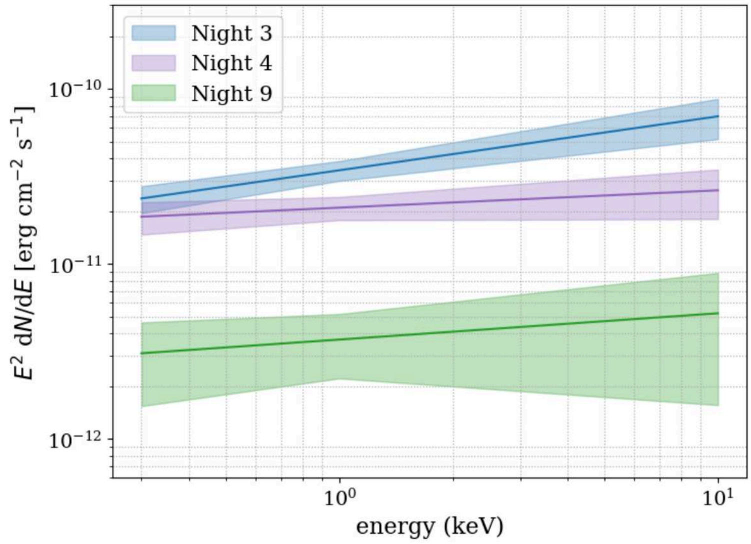

Figure 4.10.: The differential energy flux spectrum E^2 dN/dE derived from fitting the XRT data.

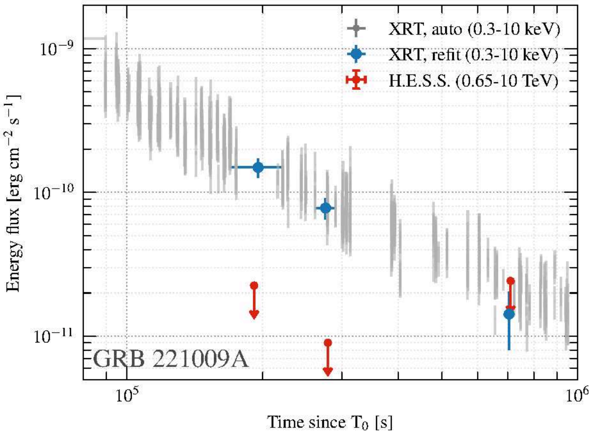

Figure 4.11.: The H.E.S.S. integral energy flux upper limits (red circles; 95% C.L.) are derived assuming an intrinsic E^{-2} spectrum. The automated XRT data (gray) are obtained from the Burst Analyser[a] [226]; multiple XRT observations around the H.E.S.S. observations are then combined and refit (blue, 1σ uncertainty). Note that the Burst Analyser assumes a larger value of intrinsic absorption than we find in our analysis and therefore returns a larger unabsorbed energy flux. The extension of the H.E.S.S. error bars in the x direction, depicting the duration of the H.E.S.S. observations, is smaller than the size of the markers.

---

[a] `https://www.swift.ac.uk/burst_analyser/01126853/`

Night	T-T$_0$ [s]	α	$k \times 10^{-2}$ [ph keV^{-1} cm^{-2} s^{-1}]	XRT en. flux [erg cm^{-2} s^{-1}]	H.E.S.S. en. flux UL [erg cm^{-2} s^{-1}]
3	$(1.68 - 2.22) \times 10^5$	1.69 ± 0.10	2.14 ± 0.30	$(14.9 \pm 2.3) \times 10^{-11}$	4.06×10^{-11}
4	$(2.61 - 2.90) \times 10^5$	1.90 ± 0.12	1.31 ± 0.20	$(7.80 \pm 1.33) \times 10^{-11}$	1.77×10^{-11}
9	$(6.85 - 7.25) \times 10^5$	1.85 ± 0.25	0.23 ± 0.09	$(1.42 \pm 0.62) \times 10^{-11}$	2.85×10^{-11}

Table 4.5.: Results of analyses of XRT and H.E.S.S. data. The entries in the first column correspond to the second column of Table 4.1. The second through fourth columns show the results of fitting XRT data in time intervals bracketing the nights during which H.E.S.S. observed the GRB, with 1σ uncertainties (statistical only). The last column lists the H.E.S.S. energy flux upper limits for the time interval defined by the third and fourth columns of Table 4.1. The XRT energy flux is calculated in the 0.3–10 keV range and the H.E.S.S. energy flux in the 0.65–10 TeV range.

a one-dimensional distribution in energy. The data are then fitted with a source model that incorporates assured positions and spectra of either a point or extended source, together with diffusion components. In this process, free parameters are adjusted to identify the nearest values that maximize the likelihood. To confirm the detection, the analysis evaluates the likelihoods of models with or without the source of interest. The model, excluding the source, serves as the null hypothesis, with its maximum likelihood noted as $L_{max,0}$. The test statistic is then calculated to compare the likelihoods as:

$$TS = -2 \ln \left(\frac{L_{max,0}}{L_{max,1}} \right), \tag{4.4}$$

where $L_{max,1}$ is the maximum likelihood model including the data (alternative model). To claim a source as a detection, a $TS \geq 25$. The *Fermi*-LAT collaboration provides model components for high-energy γ-ray sources, as well as Galactic and extragalactic diffuse emission, which can be freely accessed to build a null-hypothesis source model. If the source of interest is added to this model, the TS for the source's emission can be evaluated. I used an unbinned likelihood analysis over time intervals corresponding to each set of the H.E.S.S. observations (see Table 4.1). The analysis uses the `gtBurst` v. 03-00-00p5 tool [227]. The `P8R3_SOURCE` event class, recommended for the analysis of bright events on these timescales, along with the corresponding instrument response functions (IRF) is employed. Events in the energy range between 100 MeV and 10 GeV within a 12° radius of the burst position are selected, with applying a zenith angle cut of 100° to minimize contamination from the Earth's limb. To extract the spectrum the `PowerLaw2` model[7]

---

[7] `https://fermi.gsfc.nasa.gov/ssc/data/analysis/scitools/source_models.html`

was used and is written as:

$$\frac{dN}{dE} = N_0 \left(\frac{\alpha + 1}{E_{0,max}^{\alpha+1} - E_{0,min}^{\alpha+1}} \right) E^{\alpha}, \tag{4.5}$$

where N_0 is the normalization constant, $E_{0,max}$ and $E_{0,min}$ represent the energy range of the analysis, and α is the photon index. The background is characterized by the latest Galactic (with fixed normalization) and isotropic templates[8], while all catalog sources within 20° of the GRB position [228] are included. No significant emission from the GRB (Test Statistic < 1) is observed in the *Fermi*-LAT data during any night of the H.E.S.S. observation windows. As a result, 95% confidence level (C.L.) upper limits are computed assuming an E^{-2} spectrum. The obtained differential energy flux upper limits (spanning 100 MeV to 10 GeV) are: 7.1×10^{-10} and 2.6×10^{-10} $\mathrm{erg\,cm^{-2}\,s^{-1}}$ during Night 3 and Night 4, respectively; the upper limit for Night 3 is shown in Figure 4.13.

4.3.3. *LHAASO* results in context

To provide a more comprehensive view, I took an additional step exploring beyond what was done in the paper [194] by contextualizing the H.E.S.S. limits with the *LHAASO* detection [229] in the 0.3–5 TeV energy range (black) and in 1–5 TeV (red) (see Figure 4.12). In addition, I added the 8 hours HAWC observation [230] integrated within 1–5 TeV (darkred). This involved extrapolating both HAWC and H.E.S.S. to the model used to fit the *LHAASO* light curve, which consists of four joint power laws that describe the four-segment features in the *LHAASO* light curve: rapid rise, slow rise, slow decay, and steep decay [229] (see also Fig. 4.12). It illustrates the constraints on the *LHAASO* observations, particularly focusing on the slow decay segment (green curves) with a powerlaw index of -1.115± 0.012 [229]. Additionally, the steep decay segment (magenta) exhibits a powerlaw index of $-2.21^{+0.30}_{-0.83}$ [229]. This figure demonstrates that the upper limits from H.E.S.S. and HAWC effectively exclude the slow decay and are consistent with the steep decay observed by *LHAASO*.

4.4. Modeling the afterglow emission

4.4.1. Introduction

The code used in our afterglow modeling and the prediction of the SSC model is described and developed in [231]. This model analytically calculates the resultant photon spectra from relativistic electrons accelerated at the forward shock, where the shock evolution is described

---

[8] `https://fermi.gsfc.nasa.gov/ssc/data/access/lat/BackgroundModels.html`

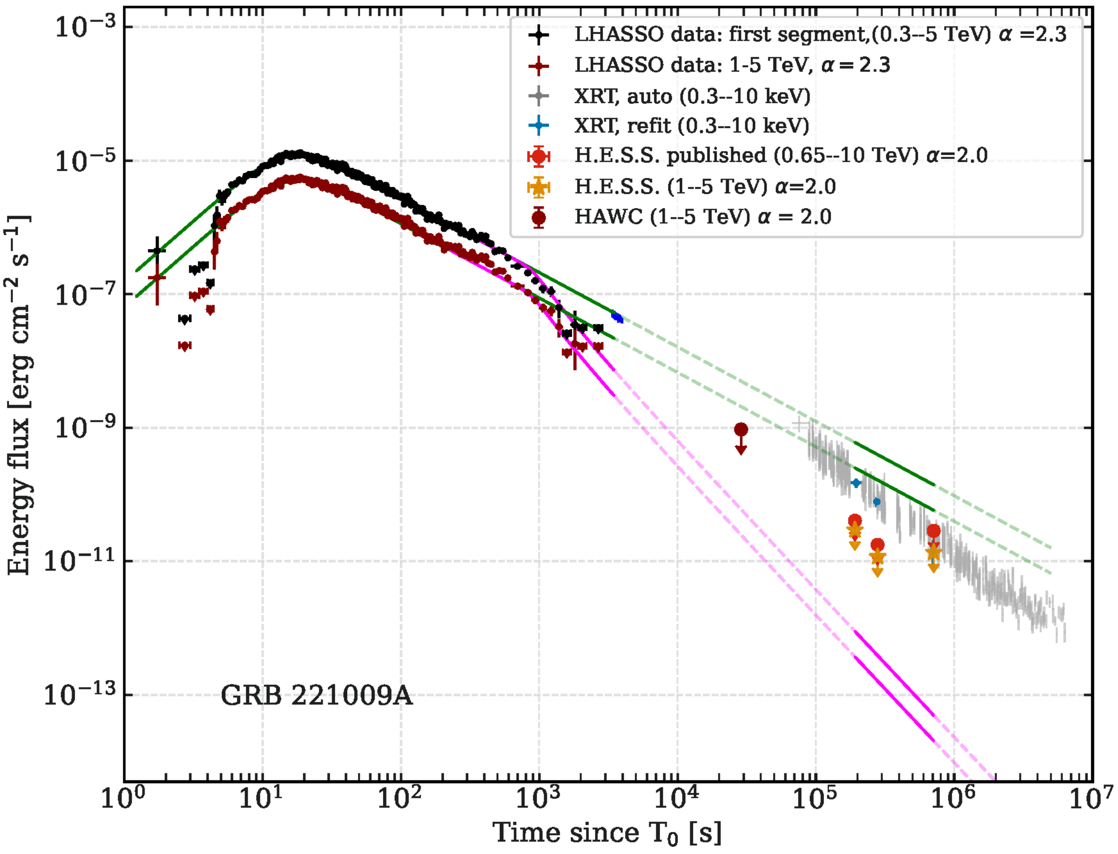

Figure 4.12.: The H.E.S.S. integral energy flux upper limits (red circles; 95% C.L.) are derived assuming an intrinsic E^{-2} spectrum. The *LHAASO* energy fluxes integrated within the [1–5] TeV energy range (red points; shared in private communication by *LHAASO* personnel) are shown for comparison to *HAWC* (darkred) and H.E.S.S. in the same energy range (in red). The black point are the *LHAASO* energy fluxes integrated over 0.3 TeV to 5 TeV. The green and magenta curves indicate the slow and steep decay segments of the broken power law model fitting the *LHAASO* data in different energy ranges, respectively.

by the Blandford-McKee solution [92]. While synchrotron emission is widely accepted as the mechanism responsible for radio, optical, and X-ray afterglows [61], as discussed in section 2.7.3, the IC up-scattering of synchrotron photons is expected to be the main mechanism for producing the VHE photons.
The parameters involved in this afterglow model include:

- $\mathrm{E_{iso}}$ (the initial isotropic energy of the fireball),
- θ_0 (the initial half-angle of the jet),
- n (the density of the homogeneous external medium),
- Γ (the Lorentz factor of the ejecta),
- p (the power-law index of the shock-accelerated electron distribution),
- ϵ_e (the fraction of the shock energy given to electrons),
- ϵ_β (the fraction of the shock energy given to the magnetic field).

In cases requiring energy injection, three additional parameters are considered such as:

- q (the index controlling the energy injection),
- $\mathrm{L_{inj}}$(the injected luminosity in the rest frame),
- and the timescale of energy injection.

The afterglow model encompasses both synchrotron emission and IC emission, making key assumptions such as:

- the homogeneity of the external medium with a constant density n or a wind profile with $\mathrm{n} \propto \mathrm{R}^{-2}$,
- the relativistic jet is uniform, meaning the energy per solid angle is independent of direction within the jet,
- the shock parameters (ϵ_e and ϵ_β), representing the fractions of shock energy given to electrons and the magnetic field, respectively) remain constant,
- the energy distribution of electrons accelerated in shocks follows a power law of the form $dN_e/dE \propto E^{-p}$,

- and the potential for achromatic flattening in the afterglow light curve due to energy injection.

Energy injection is expressed as $\mathrm{E_k} \propto \mathrm{t}^{(1-\mathrm{q})}$ [232, 233] or $\mathrm{E_k} \propto [1 + (\mathrm{t}/\mathrm{T})^2]^{(-1)}$, with T being the initial spin-down timescale [234] and q is a parameter that controls the rate at which energy is injected to the forward shock over time. Collectively, these parameters describe the physical conditions and processes contributing to the afterglow emission of GRBs. The details of the SSC numerical calculation is presented in Appendix B.1

4.4.2. A brief description of the 1-zone SSC model

In a 1-zone model, the emission is assumed to originate from a single homogeneous region, typically the forward shock region where relativistic particles (typically electrons) are accelerated as the GRB jet interacts with the surrounding medium (typically ISM, with a constant density). In this case, the afterglow spectrum often shows a synchrotron component in the lower energies and an IC component in the GeV-TeV range. Depending on the magnetic field strength, electron energy distribution and shock dynamics (like for the case of GRB 221009A) the synchrotron spectrum can peak above the energy range covered by the *Swift*-XRT, implying Klein Nishina (KN) suppression of any Inverse Compton (IC) component that peaks at higher energies. Additionally, in this model the maximum energy of accelerated electrons at the shock is characterized by the Lorentz factor of the decelerating outer shock in the self-similar model of Blandford & McKee (1976) [92] in the form of $\Gamma_{sh} \propto t^{-m/2}$. In this case, two possible scenarios involve:

- a shock propagation into a uniform medium (i.e. m= 3)
- a wind scenario (i.e. m= 1)

In the above equation, t is the time measured in the rest frame of the explosion progenitor. With the multiwavelength data, we adopted a single-zone thin shell model (see [231]), assuming self-similar expansion of a relativistic shock following an impulsive point-like explosion [92]. Within this model, we assume the radio-to-X-ray emission is produced by a single population of continuously injected electrons.

4.4.3. Model prediction and Discussion

The upper limits from H.E.S.S., when considered in conjunction with multi-wavelength observations, offer a means to constrain potential emission scenarios of GRB 221009A in the days following the prompt event. Figure 4.13 shows the spectral energy distribution (SED), incorporating the results from H.E.S.S., XRT, and LAT analyses described in previous sections.

Additionally, the optical i-band flux during the first H.E.S.S. observation period, obtained from Figure 2 of [235], and a publicly available radio observation [236] closely aligned with the first night of H.E.S.S. observations, are included in the modeling. The data are not fit by the model directly, but rather the model parameters are varied within their allowed values to find the scenarios that well explain the emission.

A synchrotron-dominated cooling model was found to better explain the observed X-ray spectrum with a photon index, $\alpha \approx 1.8$ from *Swift*-XRT (see Table 4.5), across all nights (see also [199]). This spectral behavior remained consistent above *Swift*-XRT energy range as reported by the Nuclear Spectroscopic Telescope Array (NuSTAR, 3 to 79 keV) [237]. Measurements from *Swift*-XRT analysis and NuSTAR results, suggest either an uncooled electron population or the cooled spectrum assuming a continuous injection.

As mentioned in section 4.4.2, if the emission is dominated by the IC cooling, the KN suppression could account for the hard-cooled spectrum of electrons emitting in the *Swift*-XRT range. However, reconciling this with the H.E.S.S. upper limits in the VHE range poses a challenge. Electrons that generate X-ray photons through synchrotron emission, would theoretically produce a γ-ray flux of similar or higher magnitude through IC emission. A low-density wind profile from a low-metallicity star [238], with roughly equal energy in non-thermal electrons and magnetic fields, places the synchrotron cooling breaks between radio and optical bands with $\nu_c = 3.83 \times 10^{14}$ Hz and $\nu_c = 7.34 \times 10^{18}$ Hz, for constant and wind profile, respectively. These parameters, in addition to the parameters presented in Table 4.6 are selected to maintain a slow-cooling regime, aligning well with the chosen measurement and suppress the IC flux just to reach the H.E.S.S. upper limits. For a detail discussion about the modelling, the reader is refereed to the original paper [194].

Explosion energy E	10^{54} erg
External density n_{ext}	$1.7\,\mathrm{cm}^{-3}$
Injection fraction η_{inj}	0.1%
Electron equipartition fraction ϵ_e	9×10^{-4}
Magnetic equipartition fraction ϵ_B	8×10^{-4} (0.07G)

Table 4.6.: Parameters used for single zone model fit, adopting the constant external-density solution of Bland & McKee [92].

4.5. Concluding remarks

Observation of GRB 221009A by H.E.S.S., starting 53 hours after *Fermi*-GBM detection, revealed no VHE γ-ray signal, despite its unprecedented luminosity. A 95% C.L. flux upper limit

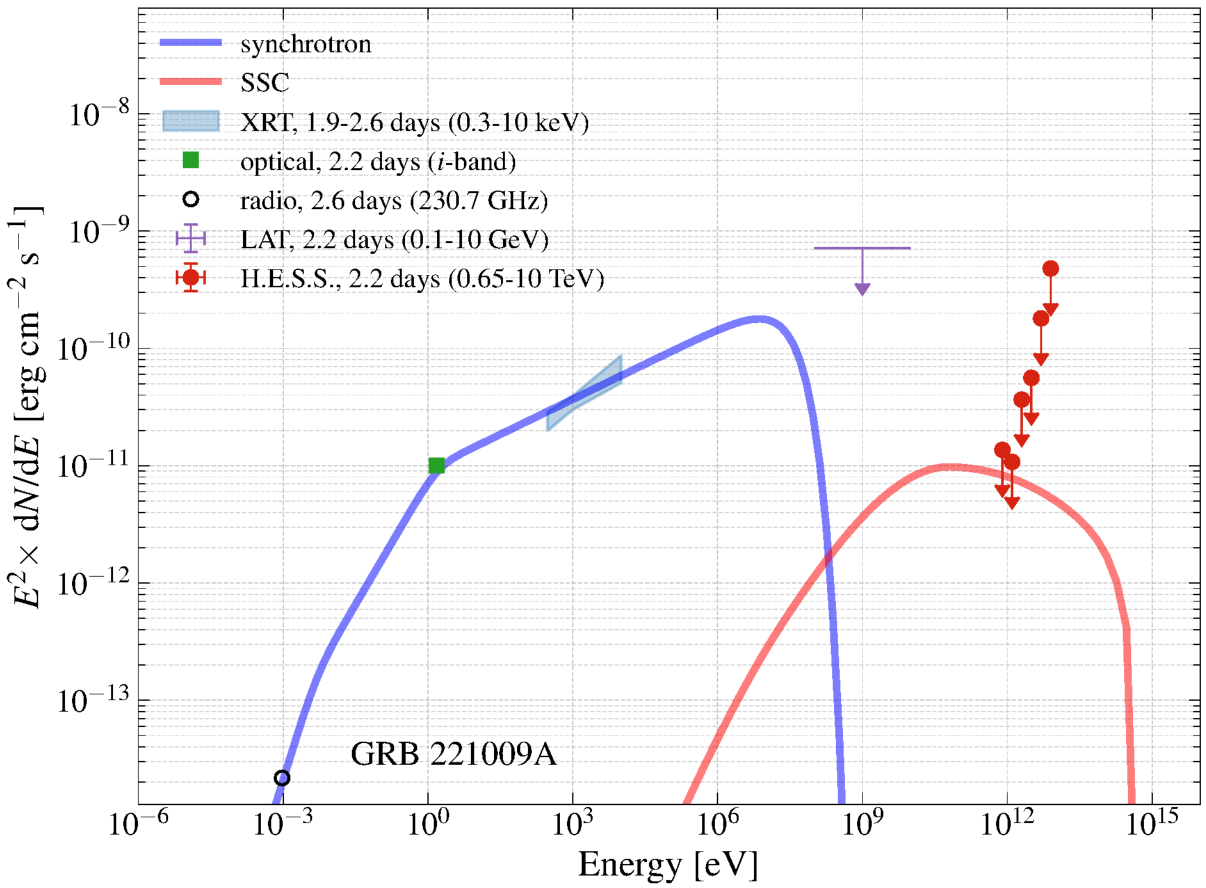

Figure 4.13.: The H.E.S.S. 95% upper limits on Night 3 (red) are plotted along with the XRT (blue, 1σ) best-fit spectrum and LAT (purple, 95% C.L.) upper limit, as well as publicly available radio data from the Submillimeter Array (black open circle; [239]) and an optical flux (green square; extracted from Figure 2 of [240]) in a multiwavelength SED. An example set of synchrotron (blue) and SSC (red) emission components — arising from a single, partially cooled electron population described in Table 4.6 — are also shown to illustrate a possible explanation of the multiwavelength observations.

of $\Phi_{\mathrm{UL}}^{95\%} = 9.7 \times 10^{-12}\,\mathrm{erg\,cm^{-2}\,s^{-1}}$ in the energy range of 0.65–10 TeV. The consistently hard X-ray spectrum across all nights with $\alpha \simeq 1.7 - 1.9$ across *Swift*-XRT and NuSTAR, alongside optical and radio data, supports synchrotron emission from a single electron population. The emission may result either from continuous injection of an uncooled spectrum or cooled hard spectrum. The photon energy spectrum is found to peak above *Swift*-XRT range, and this makes suppression of an IC emission inevitable due to KN effects, but ruling out the IC-dominated scenario per H.E.S.S. upper limits. In contrast, GRB 190829A's VHE detection and softer spectrum ($\alpha \simeq 2.0$) suggest a single component emission from X-rays to VHE γ-rays.
Observationally, these results underscore the critical role of VHE γ-ray telescopes like H.E.S.S. and *LHAASO* in constraining emission models. They highlight the need for rapid, multi-wavelength follow-up to capture diverse GRB behaviors and study non-standard particle acceleration mechanisms, while upper limits remain essential for ruling out scenarios like IC-dominated emission. An unresolved question pertains to why certain afterglows exhibit comparable X-ray and gamma-ray fluxes, as seen in GRB 190829A, while in others, like GRB 221009A, the VHE γ-ray emissions appear notably weaker. Up coming IACTs like CTA are poised to play a pivotal role in unraveling this intriguing narrative.

5. A multi-wavelength modeling of a sample of long-duration GRBs observed by HESS from 2019 to 2021

5.1. Introduction

GRB observations have remained a high priority since the start of the H.E.S.S. experiment, with the first GRB observed being *GRB 030329* back in 2003. When I joined the H.E.S.S. collaboration back in May 2020, more than 100 GRB observations had been performed with the H.E.S.S. II system [241]. To date, more than 150 GRBs have been observed. In Figure 5.1(a), a sample of all GRBs observed from 2012 to July 2023 is shown in a skymap, showing the sample with and without redshift with their respective reporting satellite and in Figure 5.1(b), all GRB observations for which CT5 took part after its upgrade are shown. There are in total more than 80 GRBs after the CT5 upgrade as of July 2023. There is an ongoing GRB catalog paper that covers all GRBs up to CT5 upgrade, and hence in this study only GRBs after the upgrade are discussed. The main objective of this study is to model the multiwavelength observations of the GRBs observed by H.E.S.S. especially focusing on those that were not studied in previous works. A requirement is that each GRB from the selected sample have a detection in at least one other waveband (generally X-rays) to put the H.E.S.S. results in context. The sample is selected based on the criteria discussed in Sect. 5.2.

5.2. Sample selection

To limit our sample, we selected GRBs that satisfy the following criteria:

- To be able to perform a point source analysis with H.E.S.S., I need to select well-localized GRBs. Therefore, I choose GRBs that were detected by *Swift*-BAT or *Fermi*-LAT since they provide localizations that are much smaller than the H.E.S.S. FoV (i.e. arcminutes

---

[1] This GRB was published in Science in 2021 [15].

[2] This GRB was published in APJL [194].

GRB Name	Satellite	Trigger (N°)	T_{90} (s)	R.A. (°)	Decl. (°)	Error (")	F (10^{-8} erg cm^{-2})	F_{low} (10^{-8} erg cm^{-2})	F_{hi} (10^{-8} erg cm^{-2})	Redshift (z)	Z (°)
190627A	Swift	911609	2.7	244.8283	-5.2898	–	11.78	9.12	14.60	1.942	44
190829A[1]	Swift	922968	56.9	44.5418	-8.9579	5.8	636.79	565.17	727.56	0.0785	23
201024A	Swift	1001514	–	125.9522	3.35444	2.7	81.13	72.86	89.88	0.999	60
210610B	Swift	1054681	69.38	243.9180	14.3977	6.7	3620.41	3567.86	3672.89	1.13	40.5
210619B	Swift	1056757	60.9	319.7161	33.8495	11.1	9490.71	9384.01	9597.51	1.937	59.8
210731A	Swift	1062336	26	300.3036	-28.059	5.8	237.05	221.57	252.57	1.2525	6
221009A[2]	Fermi	1126853	327	288.2645	19.77350	0.61	11817.66	11643.71	11991.72	0.151	52.2

Table 5.1.: Properties of the GRBs selected satisfying our selection criteria. The three first columns correspond to the name of the GRB in standard nomenclature, the name of the satellite that initially detected and reported the GRB, and trigger number for that satellite, respectively. The fourth column shows the T_{90} in seconds. The fifth through seventh column show the Right Ascension (R.A.), declination (Decl.), and the positional error in arc-seconds, reported by the detecting satellite, respectively. Reported also are the energy fluence in 15–150 keV energy range with statistical errors (90% confidence region) in the column 8 to 10, respectively [a]. The two last column shows the redshift of the source and the average zenith angle at which HESS observed the source.

---

[a] https://swift.gsfc.nasa.gov/results/batgrbcat/

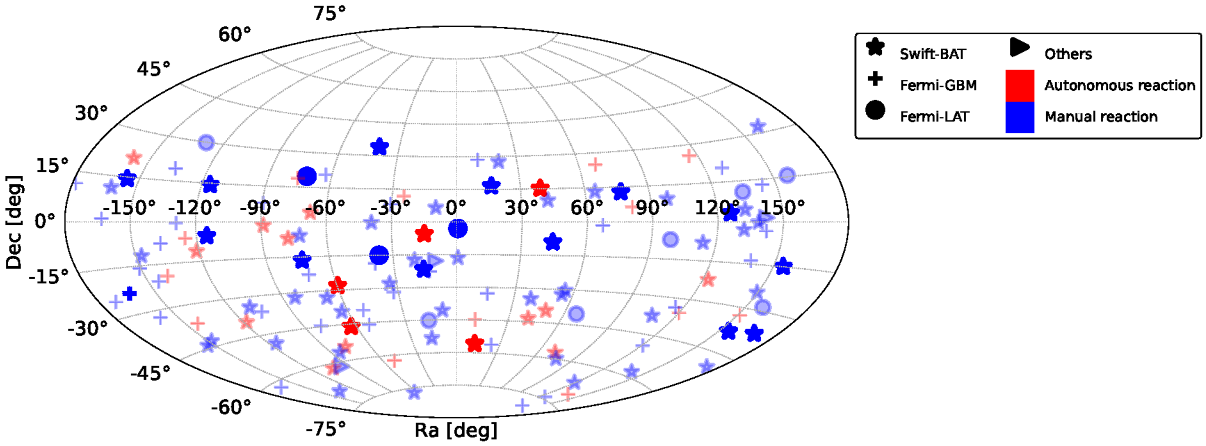

(a)

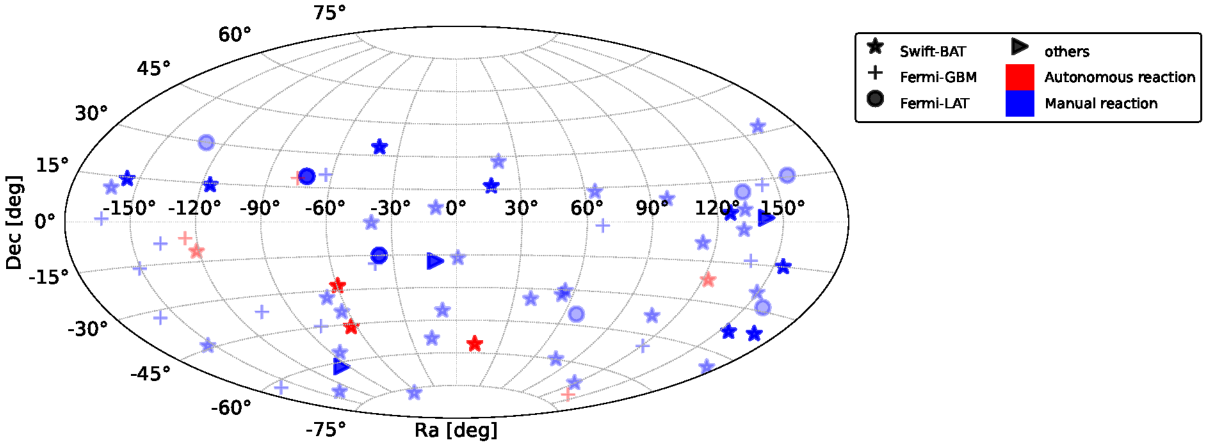

(b)

Figure 5.1.: **Top**: A sample of all GRBs observed by H.E.S.S. as of July 03, 2023. **Bottom**: A sample of all GRBs observed by H.E.S.S. as of July 03, 2023 after the CT5 camera upgrade. The autonomous reactions occur when H.E.S.S. can observe a GRB within 6 minutes of its initial detection, and manual reactions occur when the delay time for H.E.S.S. to start observations take longer. Dimmed color shows GRBs without measured redshift. In all cases, the markers show the detecting instrument whose localization is used.

and fraction of degrees, respectively) [241]. Note that the *Fermi*-LAT usually has a delay of around 1 day in reporting detections or localizations. This has an additional advantage of ensuring that, in general, *Swift*-XRT data are available, because to constrain the afterglow model adopted in this thesis, we are required to use at least two different wavebands, usually *Swift*-XRT and H.E.S.S.

- I selected GRBs observed after the CT5 camera upgrade in 2019. There is a separate ongoing study of all GRBs observed before the upgrade of the CT5 camera [242].
- VHE photons observed on the ground are subject to absorption by the EBL during their propagation through the atmosphere. For GRBs, knowing the redshift is essential for accurately correction the EBL effect, which in turn allows for the determination of the GRB's intrinsic energies (see Sect. 2.8.1 for details). As illustrated in Figure 2.13, higher redshifts result in greater absorption of GRB photons. Consequently, only GRBs with measured redshifts are selected to enable precise corrections for the EBL effect in the GRB spectra. However, redshift must be limited due to observational constraints and uncertainties in energy correction. Specifically, in the H.E.S.S. GRB observation program, GRBs with redshift $z < 2$ are prioritized over those at higher redshifts because they are less attenuated by EBL. Due to this reason, I selected GRBs with measured redshift $z < 2$.

After applying these filter on the total sample of GRBs I remain with 7 GRBs (see Table 5.1). In the analysis I removed two GRBs that were previously published (*GRB 190829A* and *GRB 221009A* [15, 194]).

5.3. Observations

In this section, I summarize the observational properties of the selected sample and the instruments that initially detected them. The GRBs in my sample are all categorized as long-GRBs, with the possible exception of *GRB 190627A*. In the early stages of the GRB afterglow modeling, particularly when there is limited information about the GRB's jet structure, the isotropic energy E_{iso} is often used. However, E_{iso} overestimates the energy if the GRB emission is collimated into a jet, which is true for GRBs. Therefore the explosive energy (E_{expl}), which represents the actual energy emitted in the direction of the jet, is used. The E_{expl} can be estimated from the E_{iso} and the jet opening angle θ_j using the relation $\mathrm{E_{expl}} \approx \mathrm{E_{iso}} \times \frac{\theta_\mathrm{j}^2}{2}$ [56, 61]. In case θ_j is unknown, E_{iso} is typically used as an upper limit of the explosion energy, or an average opening angle is assumed for beaming correction.

The *Fermi*-GBM offers a broader energy rage (10-1000 keV) compared to *Swift*-BAT (15-150 keV), hence providing a more complete measurement of the E_{iso}. However, in some cases within my sample, there is no *Fermi*-GBM detection, leaving me limited to the *Swift*-BAT's measurements, which tend to underestimate the fluence. As a results, a conversion factor is necessary. To determine this conversion factor, I compared the 10-1000 keV fluences of the *Fermi*-GBM detected GRBs, reported in the *Fermi*-GBM catalog [196], to the 15-150 keV fluences of the *Swift*-BAT detected GRBs reported in the *Swift*-BAT catalog (see Figure 5.2) [95]. I found that the average fluence reported by the *Fermi*-GBM is 6 times the average fluence reported by *Swift*-BAT. Consequently, I estimated the fluence of the GRB sample for which a *Fermi*-GBM-reported E_{iso} was unavailable, by multiplying the reported *Swift*-BAT fluence by 6. When converting from fluence to E_{iso}, I assumed a flat ΛCDM cosmology with $\mathrm{H}_0 = 68.14$ km s^{-1} Mpc^{-1} and $\Omega_\mathrm{m} = 0.318$ [243]. The estimated E_{iso} is used in the afterglow modelling to provide the E_{expl} values for the GRB sample as presented in Table 5.7.

The H.E.S.S. observation properties such as observation dates, the number of nights in which a GRB was observed, zenith angle, the number of telescopes that participated in observations and the measure of how good the atmosphere was using the atmospheric transparency coefficient (ATC) are summarized in Table 5.3.

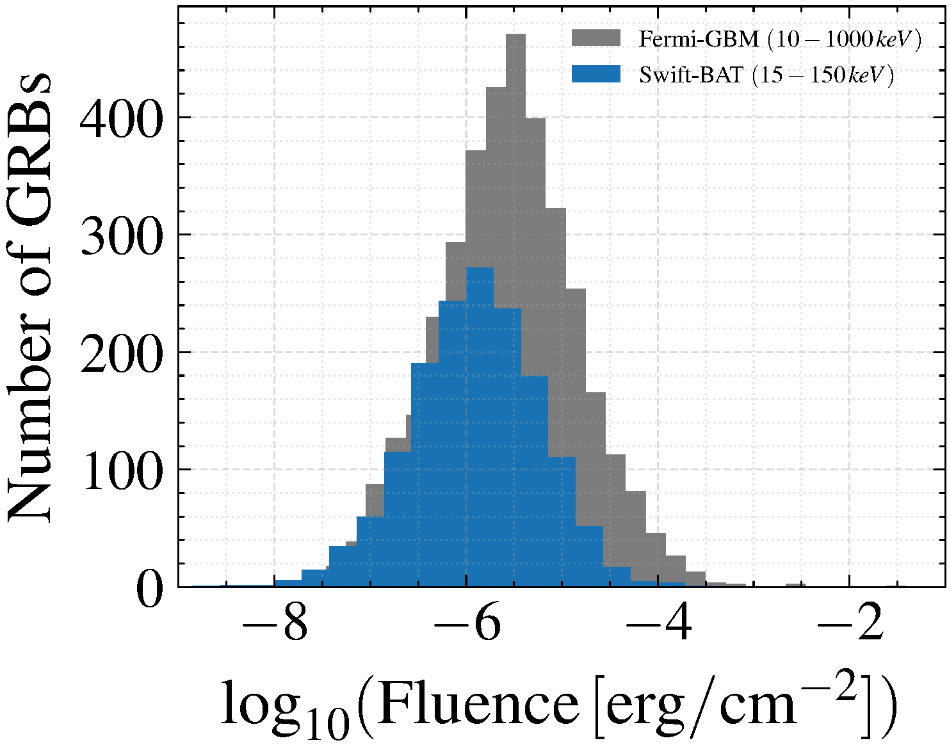

Figure 5.2.: Distribution of Fermi-GBM and Swift BAT fluences in their respective energy bands.

5.3.1. *GRB 190627A*

The *Swift*-BAT initially triggered on and localized this GRB on the 27^{th} June 2019 at 11:18:31 UTC (this time will be considered as the T_0 for this event) [244]. The early lightcurve consists of a single pulse, visible only in the softest energy channels and lasting for a few seconds [245]. The reported time integrated spectrum calculated for T_0+0.04 to T_0 + 1.78 secs is well described by a simple power law, with a photon index of 2.38 ± 0.38. The estimated energy fluence in the 15–150 keV energy band is $(9.9 \pm 2.2) \times 10^{-8}\,\mathrm{erg\,cm^{-2}}$. It was not clear whether this GRB was a short or long GRB as the duration and relative softness of the spectrum has placed it in the middle of the short and long distributions for burts detected by *Swift*-BAT. The redshift for this GRB was measured and reported from Very Large Telescope (VLT) observations and was estimated to be z = 1.942 [246].

The H.E.S.S. telescopes started observing the afterglow of this GRB ~6 hours and 21 mins after T_0. CT5 was unavailable due to technical issues and therefore only CT1-4 were available for this GRB (Table 5.3). The observations were conducted under good atmospheric conditions. However, there was only a small observation window due to the large zenith angle that also increased over time, hence H.E.S.S. took only a single extended run lasting 38 mins.

5.3.2. *GRB 201024A*

On the 24^{th} October 2020, at 02:48:59 UTC *Swift*-BAT triggered on this GRB. I will consider the *Swift*-BAT trigger time as the T_0 throughout the analysis of this GRB. The BAT lightcurve showed a one peak structure with a duration of 5 secs. The T_{90} estimated with systematic error included within (15–350 keV) is 5.00 ± 2.24 secs [247]. The redshift of $z = 0.999$ was reported for this GRB by [248]. The average time integrated spectrum of the entire burst is best fit with a simple power law model with a photon index of 2.10 ± 0.12. The fluence in the 15–150 keV energy band is $(8.1 \pm 0.9) \times 10^{-7}\,\mathrm{erg\,cm^{-2}}$ [249].

When the notification of this GRB arrived at the H.E.S.S. site in the night of 24 October 2020, it couldn't be observed due to the end of dark time, therefore the H.E.S.S. observations were conducted during the next night with a delay of nearly 22.5 hours. During this night, three observation runs were taken under good atmospheric condition.

5.3.3. *GRB 210610B*

Initially this GRB was detected by *Fermi*-GBM on 10^{th} June 2021 at 19:51:05.05 UTC [250] denoted as T_0 in this work. The GRB also triggered *Swift*-BAT 22 minutes later. This caused the satellite to automatically slew to the source, which allowed for follow-up observations by other instruments on Swift namely the *Swift*-XRT and UVOT [251]. The redshift was tentatively reported as z = 1.1345 in [252] and later confirmed by [253]. Several other satellites also were triggered by this GRB. The GBM lightcurve showed three major bright peaks with a total duration (T_{90}) of ≈55 secs in the energy range 50-300 keV. The time integrated spectrum of the first peak (T_0 +25.6 sec to T_0 +28.7 sec) is best described with a power-law function with an exponential high-energy cutoff. The model parameters such as the photon index (α) and the cutoff energy E_{peak} are equal to -0.28 ± 0.03 and 414.3 ± 11.7 keV, respectively. In this particular time range the event energy fluence in the energy band from 10–1000 keV is estimated to $(1.73 \pm 0.03) \times 10^{-5}\, erg\, cm^{-2}$.

On the 10th June 2021, H.E.S.S. started observing *GRB 210610B* from $T_0 + 36$ minutes using the *Swift*-XRT localization position. During that night, 9 observation runs were taken under good atmospheric conditions. H.E.S.S. continued observing *GRB 210610B* on the following night on June 11 taking 12 additional observation runs under good atmospheric conditions.

5.3.4. *GRB 210619B*

This event was triggered and localized by *Swift*-BAT at 23:59:25.60 UTC on 19 June 2021 (from here we call it T_0 for this GRB), and later by *Fermi*-GBM [254, 255]. *Fermi*-LAT also reported a detection, with photons up to 8.3 GeV [256] and the Konus-Wind, with photons up to ∼ 15 MeV [257]. The *Fermi*-GBM lightcurve for this burst shows a single peak followed by some extended pulses that last about 55 secs (T_{90}) within 50-300 keV. The time-integrated spectrum for the first 61.4 secs after trigger time is best described with a Band function with $E_{peak} = 210 \pm 3$ keV where the low and high energy photon index α and β are equivalent to -0.86 ± 0.01 and -1.99 ± 0.01, respectively. The measured energy fluence within this time interval is $(307.93 \pm 0.9830) \times 10^{-6}$ erg cm^{-2} within the 10–1000 keV energy range. The redshift of z = 1.937 was measured and reported by OSIRIS on the 10.4 m GTC telescope [258]. With this redshift and the resulting $E_{\gamma,\mathrm{iso}} = 4.05 \times 10^{54}$ erg, this burst falls within the 10 most luminous bursts observed by *Fermi*-GBM so far [259].

H.E.S.S. started observing this GRB at 03:05:52 on the night of 20th June 2021 nearly 3 hours after T_0. The GRB position was visible for about ∼ 2.5 hours. However, at this time the GRB was at a very low altitude and decreasing further. In addition, there was another high priority observation during this observation window, and therefore, only a single 28-minute run was taken at the end of the visibility window. This run was taken under relatively good atmospheric condition with ATC equal to 0.710.

5.3.5. *GRB 210731A*

On the 31st July 2021 at 22:21:08 UTC, the *Swift*-BAT triggered this event with the 15-350 keV lightcurve showing a single-peaked structure of the burst duration $T_{90} = 22.5 \pm 2.8$ secs [260]. One second earlier than *Swift*-BAT, this GRB triggered the *Fermi*-GBM within 10–1000 keV lightcurve showing a single peak with a duration $T_{90} = 25.9 \pm 5.3$ secs, which is in agreement with the *Swift*-BAT duration. The integrated spectra for *Fermi*-GBM was best described by a power law with an exponential cutoff whose photon indices are -0.25 ± 0.59 and -0.1 ± 0.1, and with a cutoff energy of $E_{\text{peak}} = (107 \pm 27)$ keV [260, 261]. The *Fermi*-GBM energy fluence integrated over the entire burst duration was $(3.05 \pm 0.06) \times 10^{-6}$ erg cm^{-2} within the 10–1000 keV energy range. A redshift z=1.2525 was reported using X-shooter on the Very Large Telescope [262], resulting in an isotropic equivalent energy of $E_{\gamma,\text{iso}} = (1.29 \pm 0.03) \times 10^{52}$ erg. In the analysis of this GRB and other related interpretation, we will take *Swift*-BAT trigger time as T_0 since this was considered as the T_0 when planning for the H.E.S.S. observations.

The H.E.S.S. observation of this event started immediately after the notices arrived at the H.E.S.S. site, 2 mins after T_0. The telescopes reacted automatically and 2 runs were taken, one standard run (lasting 28 minutes) and an extended run that lasted 34 minutes. The observations were conducted under normal and good atmospheric condition.

5.4. Data analysis and results

5.4.1. *Swift*-XRT analysis

The *Swift*-XRT data analysis was done using the same procedure as in the previous chapter. However, some caveats exist for individual GRBs depending on the observational properties. In general, the *Swift*-XRT data are downloaded using the time-sliced spectra tool mentioned in Chapter **??** for further re-analysis using suitable software (hereafter *XSPEC*). We are interested mostly in *Swift*-XRT data that is contemporaneous with H.E.S.S. observations. However, in most cases, there are no contemporaneous *Swift*-XRT data that are overlapping with the H.E.S.S. observation windows. If this is the case, we defined new time-slices to include more *Swift*-XRT observations on either side of the H.E.S.S. observation windows. This was the case for instance for *GRB 210610B* (both nights), for *GRB 190627A* and *GRB 201024A*. In addition, for `GRB 201024A` I extended the *Swift*-XRT window further in order for the fit to converge, resulting in utilizing all PC data from 400-50000 seconds after T_0.

Note that extending the time-slices and using larger time bins underestimates the true uncertainties for strictly simultaneous observations; this is especially visible in, for instance the second night of the `GRB 210610B` observations. The time-slices are fed into the Time-sliced Spectra

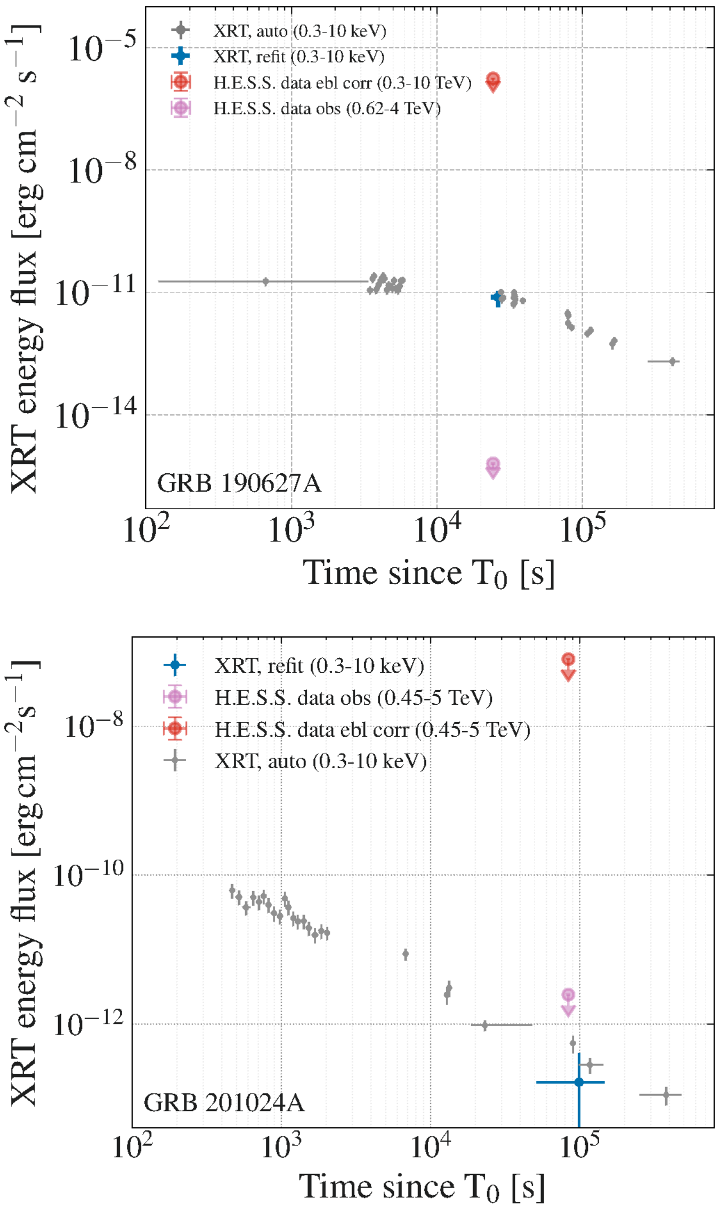

Figure 5.3.: The automated *Swift*-XRT data (gray) are obtained from the Burst Analyser. Multiple *Swift*-XRT observations around the H.E.S.S. observations window are combined and refit (blue, 1σ uncertainty). The H.E.S.S. integral energy flux upper limits (red circles for deabsorbed and purple circles for observed; 95% C.L.) are derived assuming an intrinsic power-law of the form E^{-2}. The extension of the H.E.S.S. error bars in the x direction, depicting the duration of the H.E.S.S. observations, are in some cases smaller than the size of the markers.

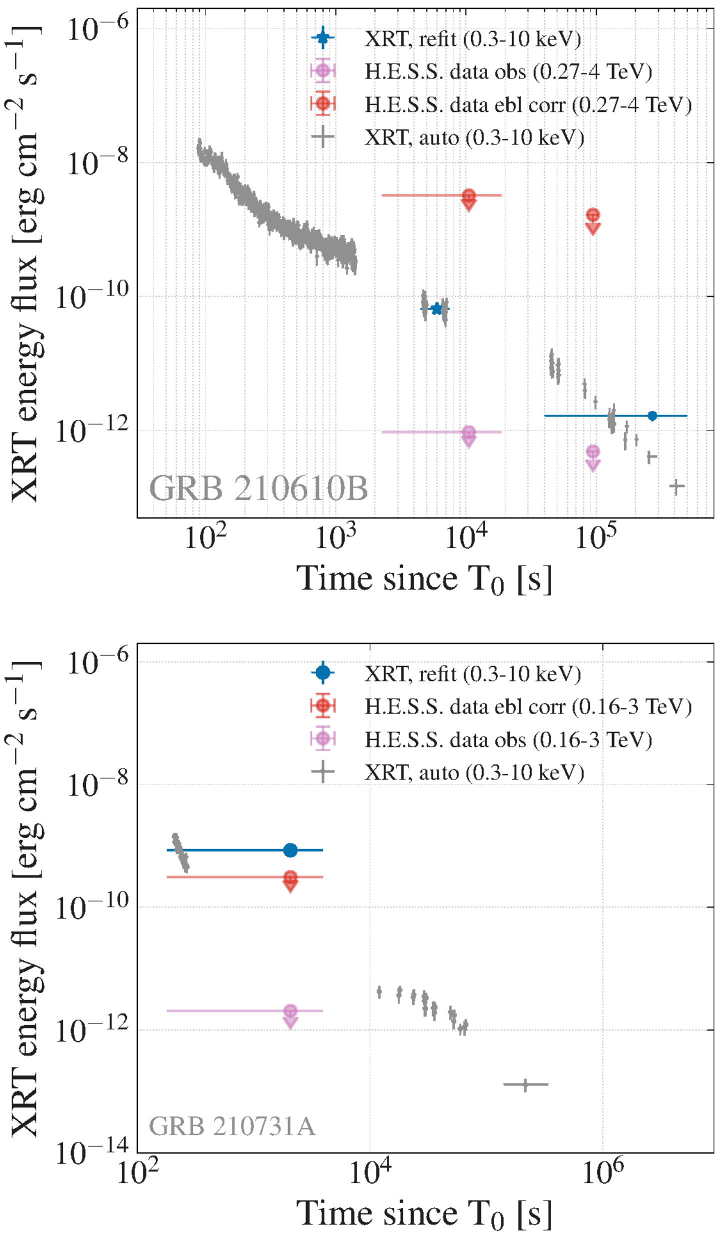

Figure 5.4.: The automated *Swift*-XRT data (gray) are obtained from the Burst Analyser. Multiple *Swift*-XRT observations around the H.E.S.S. observations window are combined and refit (blue, 1σ uncertainty). The H.E.S.S. integral energy flux upper limits (red circles for deabsorbed and purple circles for observed; 95% C.L.) are derived assuming an intrinsic power-law of the form E^{-2}. The extension of the H.E.S.S. error bars in the x direction, depicting the duration of the H.E.S.S. observations, are in some cases smaller than the size of the markers.

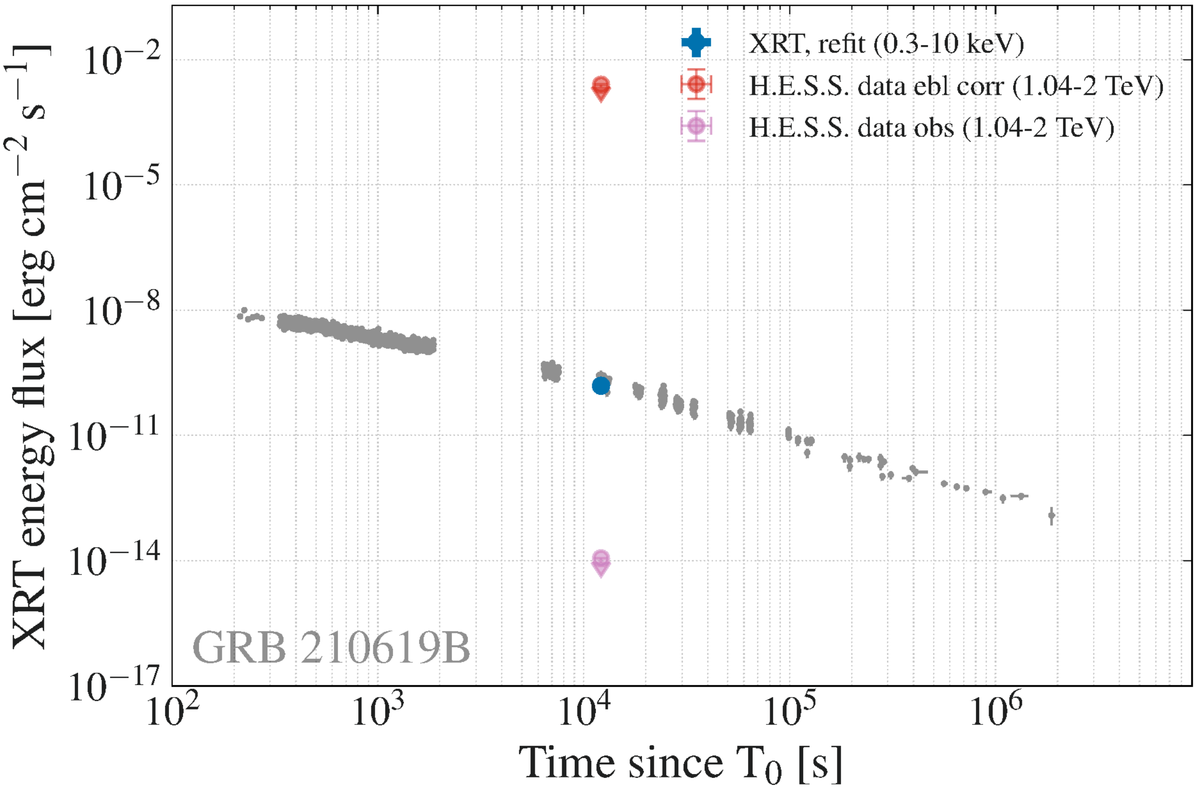

Figure 5.5.: The automated *Swift*-XRT data (gray) are obtained from the Burst Analyser. Multiple *Swift*-XRT observations around the H.E.S.S. observations window are combined and refit (blue, 1σ uncertainty). The H.E.S.S. integral energy flux upper limits (red circles for deabsorbed and purple circles for observed; 95% C.L.) are derived assuming an intrinsic power-law of the form E^{-2}. The extension of the H.E.S.S. error bars in the x direction, depicting the duration of the H.E.S.S. observations, are in some cases smaller than the size of the markers.

tool[3] and we download the resultant data products that are required for further analysis. The downloaded products include the spectra files ready for use in the *XSPEC* software, the unbinned source spectrum for the selected time interval and mode (PC or WT), the background spectrum for the selected time slice and the selected mode, both the Ancillary Response (ARF) and Response matrices (RMF) files for the selected time interval and mode, and the best-fitting model from the automatic fit in the Time-sliced Spectra tool. Note that the RMF characterizes the spectral resolution and energy distribution properties of the detector, while the ARF is a measure of the effective area of the detector as a function of energy. Both ARF and RMF files therefore ensure that the spectral analysis accurately reflects the physical properties of the source taking into consideration, the limitations and characterization of the observing instrument. For all GRBs we exclusively considered only the Photon Counting (PC) data mode (see Section 4.3.1 in previous Chapter) with the exception of *GRB 210731A* for which H.E.S.S. observed early enough that *Swift*-XRT was still observing in WT mode, therefore, WT data mode are used instead.

We refitted the *Swift*-XRT data using *XSPEC* with a power law in the form presented in Eq. 4.3. To account for the effects of absorption of photons including absorption due to interstellar material in our Galaxy, the power law is combined with two absorption components (see Eq. 4.3.1). The Galactic Hydrogen column density $\mathrm{N_{H,gal}}$ is set to a constant value obtained during the automatic analysis [197] using the Time-sliced spectra tool and are shown in Table 5.2 for each individual GRB of the sample. The automatic analysis tool obtains the $\mathrm{N_{H,gal}}$ using the method described in [263]. The spectral parameters such as the power-law normalization coefficient (k), the photon index (α), and in addition the intrinsic Hydrogen column density at the source $\mathrm{N_{H,int}}$ are kept free for each individual GRB of the sample.

I fitted the data by minimizing the C-statistic method. I present the analysis results in Table 5.2. Figure 5.6 shows an example of the resulting contours from spectral analysis of *GRB 210610B* that compares the two nights corresponding to the H.E.S.S. observation times. The multi-wavelength lightcurves showing the *Swift*-XRT and H.E.S.S. data from the sample are shown in Figure 5.3.

5.4.2. HESS analysis

The analysis procedure used for the data analysis in this Chapter is similar to the one used in Chapter 4. Unfortunately, CT5 data are not available for this study because by the time of the analysis, the cross-check analysis was not available, therefore only data taken with CT1-4 are used in this study. The entire HESS analysis is done in two steps: the low-level checks of the

---

[3] https://www.swift.ac.uk/xrt_spectra/

GRB	N (s)	$\mathbf{T}_{\text{Start}} - \text{T}_0$ **(s)**	$\mathbf{T}_{\text{End}} - \text{T}_0$ **(s)**	Exp (ks)	α	**Norm** $(10^{-4}\, ph.\, keV^{-1}\, cm^{-2}\, s^{-1})$	Int. en.flux $(10^{-12}\,\text{erg cm}^{-2}\text{ s}^{-1})$	$\text{N}_{\text{H,int}}$ $10^{22}\,\text{cm}^{-2}$	$\frac{\chi^2}{\text{dof}}$
190627A	1	20449	29000	1.43	1.91 ±0.25	(12.92 ± 5.27)	(7.65 ± 3.36)	0.22 ± 0.92	$\frac{43.20}{66}$
201024A	1	11427	476844	20.99	1.91 ± 0.64	(0.281 ± 0.392)	(0.167 ± 0.243)	2.12 ± 1.74	$\frac{5.50}{11}$
210610B	1	2272	18761	0.904	2.08 ± 0.11	(121.24 ± 9.47)	(65.40 ± 6.03)	0.25 ± 0.11	$\frac{254.8}{249}$
	2	40000	500000	21.99	1.81 ±0.09	(2.619 ± 0.418)	(1.66 ± 0.29)	0.20 ± 0.13	$\frac{19.30}{17}$
210619B	1	11285	12976	1.146	1.75 ± 0.09	(232.00 ± 20.50)	(0.016 ± 18.10)	0.05 ± 0.40	$\frac{397.70}{286}$
210731A	1	180	3959	0.06288	3.08 ± 0.11	(0.016 ± 95.80)	(0.85 ± 6.17)	0.21 ± 0.11	$\frac{371.40}{273}$

Table 5.2.: The *Swift*-XRT results of the spectral analysis for all GRBs from the sample. The first column corresponds to the GRB name in the standard nomenclature. The second column is the number of night that a GRB is observed with reference to HESS observations. The following three columns show the starting and ending time of observation after the trigger, and the exposure time in kilo-seconds. The fifth and sixth columns show the results of fitting *Swift*-XRT data in time intervals bracketing the nights during which H.E.S.S. observed the GRB, with 1σ uncertainties (statistical only) with the fitting statistics shown in the last column. The eighth column corresponds to the *Swift*-XRT integrated energy flux, calculated in the 0.3–10 keV energy range. The ninth and tenth columns show the Galactic columns density obtained with the automatic data analysis and the intrinsic column density obtained after re-fitting the data (with 1σ statistical uncertainty).

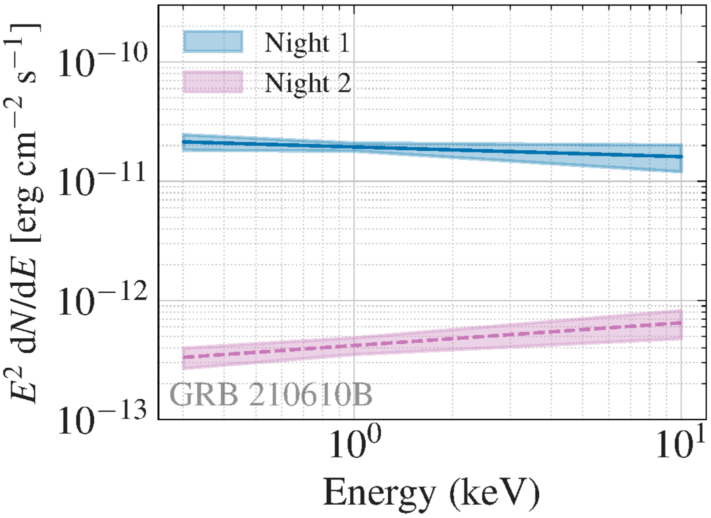

Figure 5.6.: *Swift*-XRT differential fluxes for the H.E.S.S. observations of `GRB 210610B`, assuming a spectrum in the form $dN/dE = k(E/E_0)^{-\alpha}$ with statistical uncertainties where $E_0 = 1\,keV$. The estimated uncertainties are 1σ.

data quality and the high-level data analysis. The low-level checks are employed to minimize the number of trials, (see details in Section 3.5.2). This step is done to verify that the data quality is good enough to allow us to further formulate an analysis scheme before proceeding with high-level analysis.

First, the quality of weather conditions and observational settings is assessed and considered to eliminate observations with poor data quality from the analysis. This involves identifying abrupt fluctuations in the trigger rate ($\geq 30\%$), which serve as indicators of potential issues such as passing clouds or problems in the hardware or software during data acquisition. Following this procedure, the stability of the photo-multiplier tubes (PMTs) in each telescope's Camera is monitored by examining the center of gravity, pedestal distribution, and participation fraction. The presence of a significant number of noisy or dead channels can adversely affect the reconstruction of the shower direction, introducing misleading signals into the significance maps.

In addition to these checks, night-sky background (NSB) maps for the observation runs are generated to ascertain whether bright stars were in the vicinity of the GRB position. Bright stars are identified and subsequently masked out during the high-level analysis. Following these pre-processing steps, the strategy for data analysis, including significance and spectral analysis methods, is then defined. Runs identified as problematic in the earlier stages are excluded from the analysis, and the most accurate localization of the GRB (usually the localization provided by *Swift*-XRT) is utilized.

Typically the GRB's statistics and maps from our sample are generated using the Ring Background method while the spectrum are extracted using the Reflected Background method, discussed in Chapter 4. Since all GRBs in our sample are well localized with uncertainties less than the H.E.S.S. PSF, if no detection for an individual GRB is found, the differential upper limits are derived for the GRB location, assuming a power-law spectrum with a photon index of 2.0 (this is the average photon index of GRBs observed by *Fermi*-LAT). In general, since I am deriving differential flux upper limits within, relatively small energy bins, the assumed spectral index does not have a large effect.

A detailed analysis done following the methods described in Section 4.2 shows that there is no evidence of significant excess of VHE gamma-ray events from any of the GRB positions given in Table 5.1 during the periods covered by the H.E.S.S. observations. The number of on-source ($\mathrm{N_{ON}}$) and off-source events ($\mathrm{N_{OFF}}$), the normalization factor (α), excess and statistical significance calculated using equation (17) of [177] are given for each of the 5 GRBs in Table 5.4. It is clear that the EBL strongly affected mostly the higher-redshift GRBs if we compare the observed upper limits (red) and the deabsorbed upper limits (blue) from each of the GRBs from our sample as shown in Figure 5.7.

5.4.3. *Fermi*-LAT analysis

The *Fermi*-LAT analysis for each individual GRB in the selected sample is conducted. The analyses were done using time ranges that are simultaneous with the H.E.S.S. observations. The *Fermi*-LAT data analysis was conducted using the `gtBurst` v. 03-00-00p5 [227] tool. The event class `P8R3_SOURCE`, which is the recommended event class, along with the corresponding IRFs, is used. We followed the same procedure as in Sect. 4.3.2, where only events within the 100 MeV − 10 GeV energy range and within 12° of RoI of the burst position were used. We applied a zenith angle cut of 100°. Unfortunately, none of the GRBs from our sample were detected by *Fermi*-LAT in the time range covering the H.E.S.S. observations (see Table 5.3). Therefore, using equation 4.5, we extracted the 95% C.L upper limits assuming an E^{-2} spectrum. The calculated differential energy flux upper limits from 100 MeV to 10 GeV are presented in Table 5.5.

5.4.4. Optical data

To increase the multiwavelength coverage for our sample, we searched for optical counterparts. The optical data reported in the GCNs mostly are in the form of AB magnitudes. To convert AB magnitude to flux density, we employed the following formula:

GRB name	Calendar date	Interval	$T_{Start} - T_0$ [s]	$T_{End} - T_0$ [s]	zenith [deg]	Tels	ATC
GRB 190627A							
	27th June 2019	Night 1	23449	25141	44	CT1-4	–
GRB 201024A							
	24th October 2020	Night 1	81427	83118	56.6	CT1-5	0.556
	24th October 2020	Night 1	83195	84887	49.6	CT1-5	0.660
	24th October 2020	Night 1	84972	86844	44.1	CT1-5	0.685
GRB 210610B							
	10th June 2021	Night 1	2272	3963	40.8	CT1-5	0.899
	10th June 2021	Night 1	4023	5715	39.7	CT1-5	0.900
	10th June 2021	Night 1	5771	7463	37.8	CT1-5	0.895
	10th June 2021	Night 1	8307	9999	37.8	CT1-5	0.894
	10th June 2021	Night 1	10060	11751	40.2	CT1-5	0.892
	10th June 2021	Night 1	11814	13506	44.2	CT1-5	0.894
	10th June 2021	Night 1	13569	15260	48.0	CT1-5	0.888
	10th June 2021	Night 1	15318	17010	51.7	CT1-5	0.883
	10th June 2021	Night 1	17070	18761	57.0	CT1-5	0.854
	11th June 2021	Night 2	83955	85646	52.2	CT1-5	0.901
	11th June 2021	Night 2	85710	87401	46.6	CT1-5	0.906
	11th June 2021	Night 2	87458	89148	43.6	CT1-5	0.901
	11th June 2021	Night 2	89206	90897	40.0	CT1-5	0.901
	11th June 2021	Night 2	90958	92649	39.0	CT1-5	0.898
	11th June 2021	Night 2	92709	94401	37.0	CT1-5	0.898
	11th June 2021	Night 2	94461	96152	38.3	CT1-5	0.896
	11th June 2021	Night 2	96213	97905	40.7	CT1-5	0.902
	11th June 2021	Night 2	97965	99657	44.1	CT1-5	0.905
	11th June 2021	Night 2	99719	101410	47.0	CT1-5	0.904
	11th June 2021	Night 2	101468	103160	51.7	CT1-5	0.902
	11th June 2021	Night 2	103218	104910	57.9	CT1-5	0.873
GRB 210619B							
	19th June 2021	Night 1	11285	12976	59.8	CT1-5	0.710
GRB 210731A							
	31st July 2021	Night 1	180	1871	49.3	CT1-5	–
	31st July 2021	Night 1	1928	3959	49.3	CT1-5	–

Table 5.3.: H.E.S.S. observations of the GRB sample. Column 2 denotes the number of nights after T_0. Columns 3 and 4 represent the run start and end time since T_0, in seconds, respectively. Column 5 shows the average zenith angle under which the observations were conducted. The last two columns indicate which telescopes participated in the observation and the atmospheric transparency coefficient during the observation respectively. For the runs without ATC values in the H.E.S.S. database due to technical issues, we assessed the good weather and good atmospheric condition, by looking visually whether the trigger rates are consistent with internal H.E.S.S. recommended values.

GRB	T_{start} (UTC)	N_{ON}	N_{OFF}	α	Excess	Sign.	E_{th} (TeV)	Int.en.flux (erg cm^{-2} s^{-1})
190627A	2019-06-27 17:49:20.8318	10	95	0.091	1.36	0.43	0.62	1.08×10^{-6}
201024A	2020-10-25 01:26:06.7522	34	359	0.091	1.36	0.23	0.41	4.90×10^{-8}
210610B	2021-06-10 20:28:57.2302	625	9173	0.0625	51.687	2.06	0.27	1.99×10^{-9}
210619B	2021-06-20 03:07:30.1183	8	134	0.056	0.556	0.196	1.10	0.155×10^{-3}
210731A	2021-07-31 22:24:08.0091	103	1647	0.061	3.026	0.292	0.16	1.92×10^{-10}

Table 5.4.: Results of the H.E.S.S. analysis for all GRBs from the sample. Column 1 corresponds to the name of the GRB in standard nomenclature, and the second column represents the the starting time of the HESS observation in UTC. The following columns represent the number of ON and OFF event counts, and α which the exposure ratio between the ON and OFF regions, and the excess counts and the significance. The last columns represent the energy thresholds, and the integral energy flux upper limits (EBL-corrected) above energy threshold, respectively.

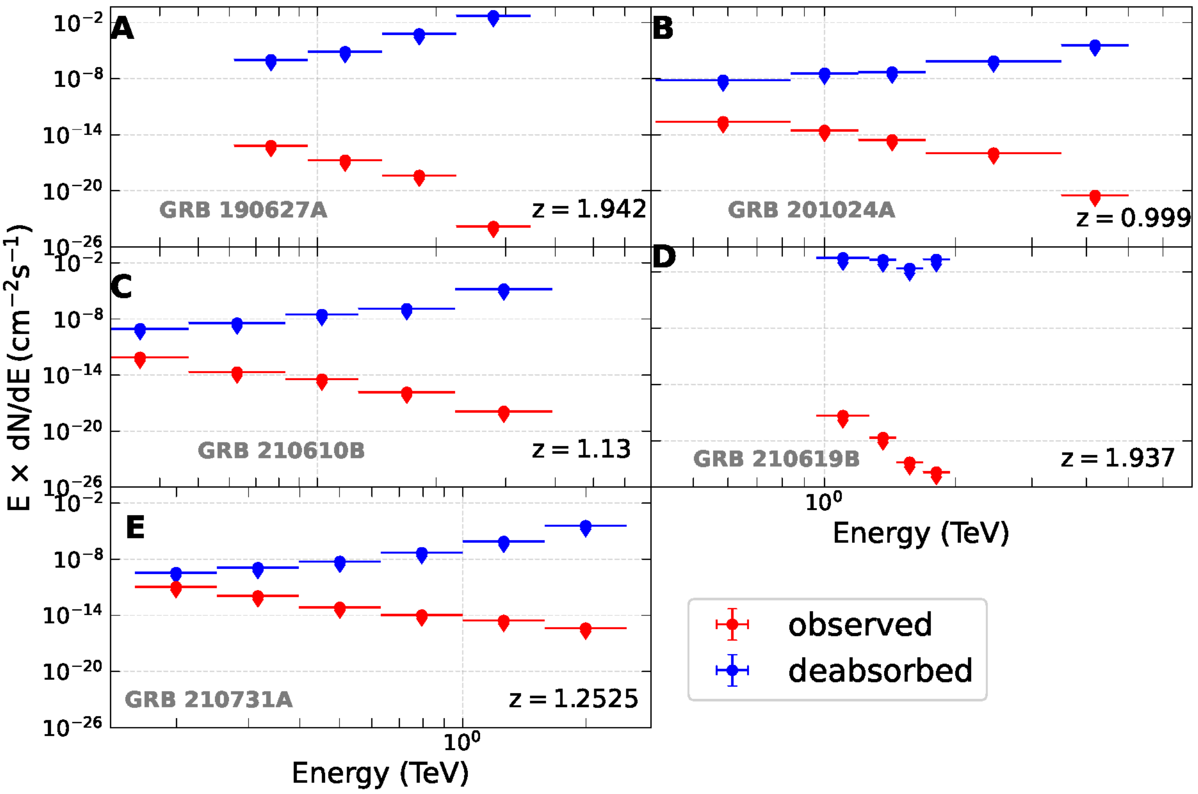

Figure 5.7.: The energy flux upper limits on an intrinsic (EBL-corrected) GRB spectrum (in blue) and observed differential energy flux upper limits (in red). The upper limits are computed at 95% C.L. derived from the H.E.S.S. observational data for all GRB sample. It can be seen that GRB with high redshift the EBL effect is large causing the deabsorbed fluxes to be many orders of magnitude higher than the observed fluxes.

GRB	Diff.en.flux ($\times\ 10^{-10}$ erg cm^{-2} s^{-1})
190627A	8.34
201024A	1.12
210610B (n_1 & n_2)	1.53 & 0.97
210619B	2.68

Table 5.5.: Results of the *Fermi*-LAT analysis for all GRBs from the sample. Column 1 represents the name of the GRB for which *Fermi*-LAT observations exists and in Column 2 we show the resulting differential energy upperlimit flux for each of the GRB from our sample.

GRB	cent. wav. (nm)	Energy (eV)	Diff.en.flux ($\times\ 10^{-12}$ erg cm^{-2} s^{-1})
190627A	623.84	1.99	(1.85±0.96)
201024A	775.11	1.60	(0.126±0.06)
210610B (n1)	623.84	1.99	(7.08±4.25)
210619B	623.84	1.99	(1.00±0.52)

Table 5.6.: Results of the optical flux calculation for all GRBs from the sample. Column 1 represents the name of the GRB for which optical observations simultaneous to H.E.S.S. observation times exist and in Column 2 we show the central wavelengths (in nanometers) for each GRB. In column 3 and 4, we present the energy (in eV) and the differential energy flux for each GRB from our sample.

$$F_\nu = 3631 \times 10^{\frac{(-m_{AB})}{2.5}}, \quad \text{where } m_{AB} \text{ is the AB magnitude.}$$

Additionally, we utilized the central frequency of the corresponding filter (e.g., r' Sloan Digital Sky Survey-SDSS filter has a central frequency $\lambda = 623.84\,nm$) to calculate differential energy fluxes through the following relation:

$$\nu F_\nu = F_\nu * c^2/\lambda.$$

Notably, the optical data sourced from the GCNs are uncorrected for effects such as the Galactic extinction. To address these we incorporated a 50% systematic uncertainty as recommended in previous works such as [264], [265] and [266]. The obtained differential energy fluxes for each individual GRB at given central wavelengths are given in Table 5.6. For the particular case of GRB 210731A, we used the optical fluxes from publications.

5.5. Afterglow Modeling

In this section, I put the HESS results into context with the multiwavelength observation by trying to find the physical interpretation. To do so, I briefly introduce the SSC model used to explain the afterglow emission from the selected sample. In this model, I require that at least the datasets from two different wavebands (e.g. X-ray from the *Swift*-XRT and VHE from the HESS) are available. The theoretical background of this model was originally published in [231] in more detail. With this model and procedure, I am not fitting anything to the data, instead I try to find a representative set of parameters that can explain the data, by systematically changing the input parameters to explore the parameter space. While this is not as rigorous an exploration as a proper fit, I am mostly interested in contextualizing the HESS results, which in many cases are generally not very constraining. An adiabatic expansion of the blast wave with a total explosion energy $\mathrm{E_{expl}} \approx \mathrm{E_{iso}} \times \theta_\mathrm{j}^2/2$ was considered. We begin by defining and computing the dynamics of the relativistic shock wave parameters that describe the physics of the shocked environment for the GRBs (see Appendix B.1). In section 4.4.1, the necessary parameters that affect strongly the model are defined. This model was applied to the recently detected H.E.S.S. GRB (GRB 190829A) (see Figure 5.8). The model is applied on the selected sample of GRBs presented in table 5.3. Representative values for individual parameters that describe the data well are shown in Table 5.7.

GRB Name	DL (10^{28} cm)	$\mathrm{E_{expl}}$ (10^{54} erg)	$\mathrm{n_1}$	η_inj	ϵ_e	ϵ_β	p
190627A	4.74	0.904	0.01	1.0	0.1	0.0061	2.1
201024A	2.09	2.8	0.01	1.0	0.01	0.001	2.09
210610B	2.43	0.26	0.01	1.0	0.06	0.013	2.2
210619B	4.72	4.05	0.2	1.0	0.0019	0.000071	1.8

Table 5.7.: Fitting parameters for all GRBs for uniform medium (constant density).

5.6. Discussions of individual GRBs

GRB 190627A: For this GRB, we compiled nearly simultaneous data from H.E.S.S., *Swift*-XRT, and optical sources. The tested model looked consistent with the observed data. Specifically, the synchrotron component clearly passes through the low-energy data points (optical and X-ray), while the IC component falls significantly below the H.E.S.S. upperlimits (ULs). A set of parameters from the constant profile that well describe the

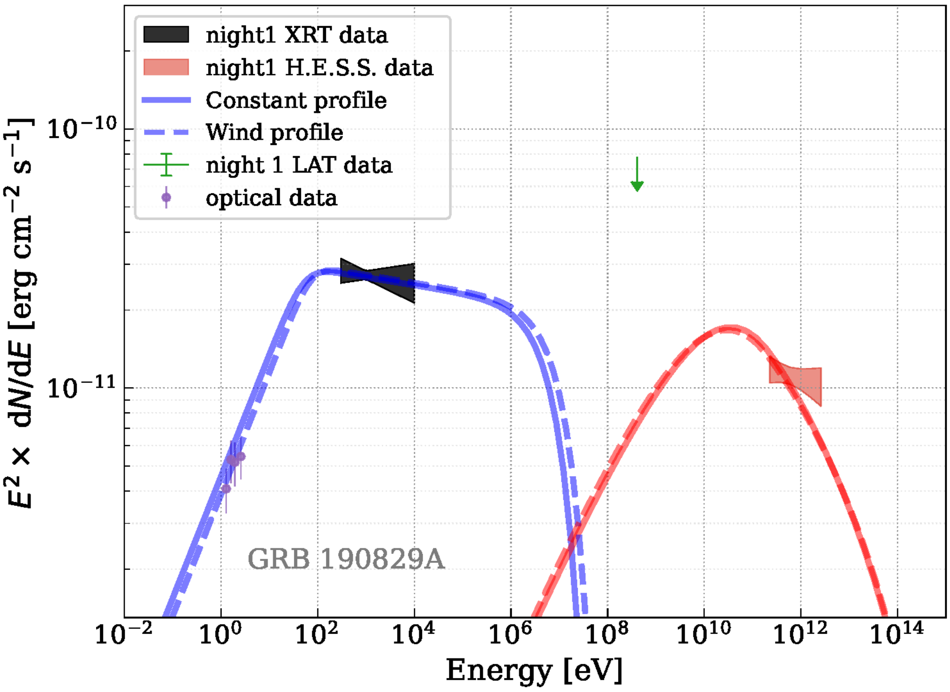

Figure 5.8.: Application of modeling on GRB 190829A using the method described above. All data are simultaneous to H.E.S.S. observation time. The dashed and solid lines represent the wind and constant density profile for both synchrotron (blue) and the IC component (red). We used the luminosity distance $DL = 0.1136 \times 10^{28}\, cm$ for for this GRB corresponding to a redshift $z = 0.0785$. In both scenario, we used $n_1 = 0.1\, cm^{-3}$, $E_{expl} = 7.5 \times 10^{52}\, erg$, electron injection index $p = 2.06$, $\sigma_u = 10^{-9}$ and $l_w = 10^4$. The parameters like (ϵ_e, ϵ_β, η_{inj}) are set to: (0.08, 0.00075, 1.0) for constant scenario and (A_{35}, ϵ_e, $\epsilon_\beta, \eta_{inj}$) are set to: (0.7,0.095,0.00082,0.8). All data are extracted from [15].

GRB Name	DL (10^{28} cm)	E_{expl} (10^{54} erg)	A_{35}	η_{inj}	ϵ_{e}	ϵ_β	p
190627A	4.74	9.04	1.7	1.0	0.08	0.00082	2.1
201024A	2.09	0.88	0.12	1.0	0.18	0.002	2.09
210610B	2.43	0.26	0.01	1.0	0.06	0.013	2.2
210619B	4.72	4.05	0.2	1.0	0.0019	0.000071	1.8

Table 5.8.: Fitting parameters for all GRBs for windy medium.

low-energy and high-energy data, are detailed in Table 5.7, and the SED fit result is visualized in Figure 5.9.

The Optical data were sourced from the GCN [267]. The optical data are generally useful in constraining the spectrum, especially when computing cooling break frequencies which would identify whether the afterglow emission is in slow or fast-cooling regimes. I computed the cooling break frequencies for both constant ($\nu_c = 1.085 \times 10^{15}\,\mathrm{Hz}$) and wind density profile($\nu_c = 5.92 \times 10^{14}\,\mathrm{Hz}$), respectively. The obtained values of the cooling break fall into the optical band suggesting that the electrons emitting optical radiation are in slow-cooling regime (electrons lose energy primary through synchrotron radiation over a longer timescale than the dynamical timescale of the blast wave) resulting in a flatter spectrum ($F_\nu \propto \nu^{-(p-1)/2}$).

The wind scenario can be well described by the parameters presented in Table 5.8. The best wind scenario requires that the explosion energy is bigger than the constant scenario with an order of magnitude implying a steeper decay afterglow or that the progenitor system is one with strong stellar winds and hence more materials are being ejected around the progenitor over time. The obtained parameter values align well with the expected values for a standard GRB model for a typical GRB [56, 268]. In both density profiles, the IC curve does not reach the H.E.S.S. upperlimits.

GRB 201024A: In addition to the X-ray and VHE data, we used preliminary optical data published in [269] which lacked Galaxy extinction correction (for this reason, a systematic 50% uncertainty was used). I modeled the afterglow emission from this GRB, and I found that the low energy emission is well consistent with the synchrotron component with both the constant and wind profiles. The γ-ray upper limits do not constrain the SSC model. With reasonable model parameters presented in Table 5.8 and Table 5.7 the wind and the constant profile IC components are not constrained by the VHE points but are consistent with the low-energy photons as presented in Figure 5.10.

Similar to the previous `GRB 190627A`, the estimated cooling frequencies for constant ($\nu_c = 2.23 \times 10^{15}\,\mathrm{Hz}$) and wind ($\nu_c = 7.51 \times 10^{16}\,\mathrm{Hz}$) density profile fall in or near the optical band, suggesting a slow-cooling regime where electrons emitting at lower frequencies cool less efficiently than those emitting at higher frequencies (e.g. X-rays). The obtained parameters are consistent with standard afterglow model parameters [56, 268].

GRB 210610B: Although this GRB was observed by H.E.S.S. during two consecutive nights, I am only discussing the afterglow emission of the first night, for which we have all the datasets (optical, X-ray, HE and VHE) also because the constraints are better on the

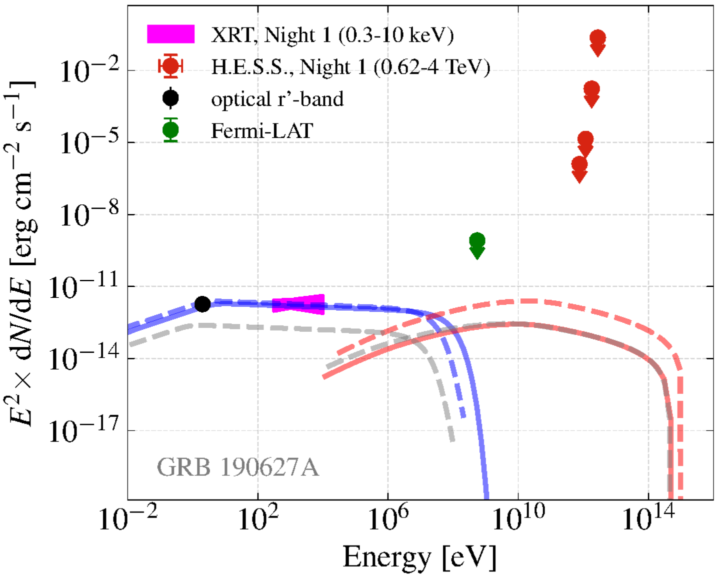

Figure 5.9.: This Figure shows synchrotron and IC curves that best describe the data. The dashed and solid lines represent the wind and constant density profiles, respectively for both synchrotron (blue) and the IC component (red). The gray curves represent the case where the wind scenario is driven by the same initial explosion energy as the constant density profile.

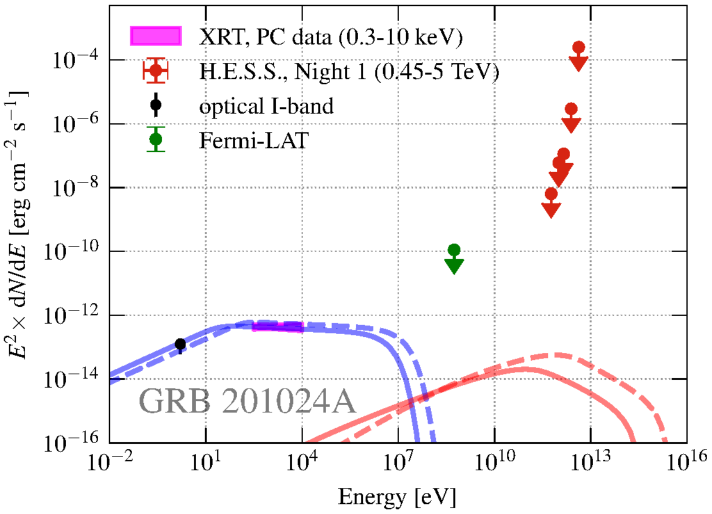

Figure 5.10.: This Figure shows the SSC model that could well explain the lower-energy (optical and X-ray) data. The dashed and solid lines represent the wind and the constant density profile, respectively for both synchrotron (blue) and the IC component (red).

first night than the second one. We acquired optical data from the GCN [270], closely aligning with the time of H.E.S.S. observations. While the constant density scenario could reproduce the low-energy emission with the synchrotron component, the wind profile model tends to under-predict the flux in the optical band. The constant and the wind profile models are both consistent with the H.E.S.S. upper limits. The reasonable model parameters that describe well the data for constant and wind scenarios are shown in Table 5.7 and 5.8, respectively, and the multiwavelength modelling of the SED is presented in Figure 5.11.

For the synchrotron component to stay within the optical data range, we require the initial explosion energy to be 2.20×10^{54} erg, which is a reasonable value for a typical GRB and also if compared to previously estimated injected isotropic energy of 2.0×10^{54} ergs [271]. The cooling break values for constant and wind density profiles are determined to be $5.097{\times}10^{15}$ Hz and $4.92{\times}10^{16}$ Hz, respectively. These values being above the optical band implies that all optical photons below or far below cooling break are emitted by slow-cooling electrons. The obtained parameters align well with the expected parameters for a standard GRB afterglow model [56, 268].

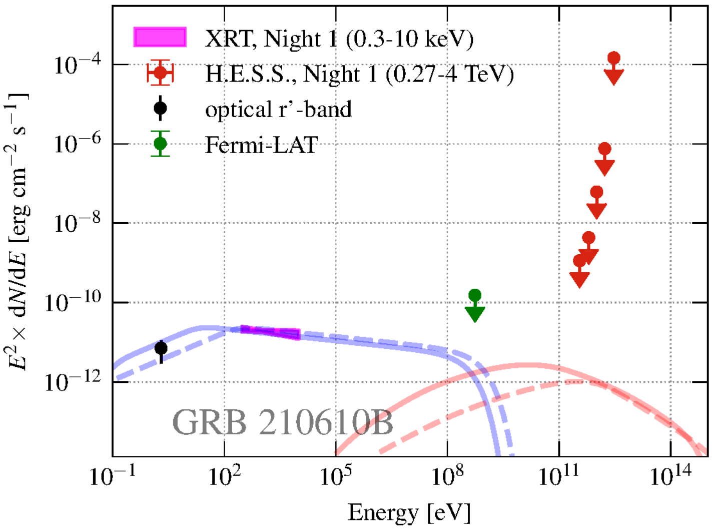

Figure 5.11.: This Figure shows the best curves scenario of the IC and synchrotron components of the SSC model for the first night of the H.E.S.S. observations. All data are simultaneous to H.E.S.S. observation time. The dashed line represent the wind profile for both synchrotron (blue) and the IC model (red).

GRB 210619B: The afterglow of this GRB was reported as being among the 10 most luminous GRBs, especially in the X-ray band (see also the representation in the Amati relation, Figure 5.13). In addition to the *Swift*-XRT and H.E.S.S. data, we estimated the differential energy flux from optical data obtained from the GCN [272]. The MWL SED, showcasing all data used for modeling, is depicted in Figure 5.12.

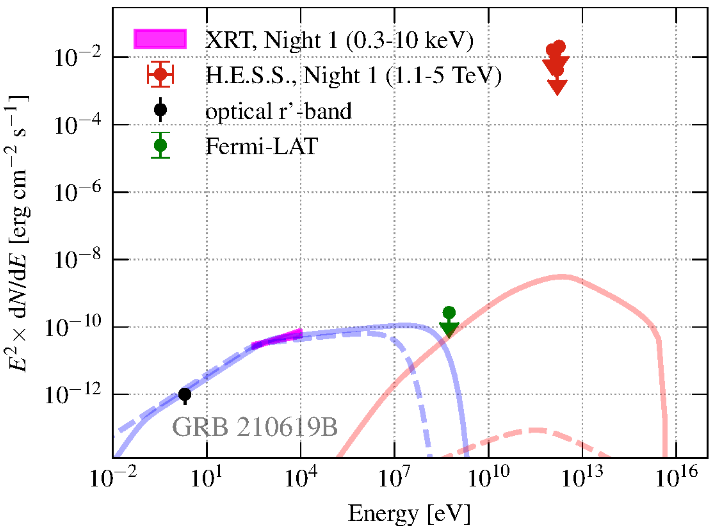

Figure 5.12.: This Figure shows the best model that define better the data with both the IC and synchrotron components. The dashed line shows the wind scenario and the solid line shows the constant density scenario. All data are simultaneous to H.E.S.S. observation time.

The parameters that describe well the emission (synchrotron and Inverse Compton) are outlined in Table 5.7 for constant density profile and in Table 5.8 for wind density profile. The figure 5.12 illustrates that the lower energy band from optical to X-ray can be effectively described by a synchrotron component for both the wind and constant medium scenarios. Additionally, the *Fermi*-LAT upper limit constrains the turnover of the synchrotron component at high energies. However, the H.E.S.S. upper limits considerably exceed the SSC curve compared to the *Fermi*-LAT data.

The obtained magnetic energy fraction is very small ($\epsilon_\beta \sim 7.1 \times 10^{-7}$, see also Table 5.7 and 5.8) compared to typical values for a GRB [268], implying a weak magnetic field in the downstream region since $B \propto \sqrt{\epsilon_\beta n}$ for a typical GRB, with n the density of the medium. With a weak magnetic field, the synchrotron emission efficiency is reduced and the afterglow emission becomes dimmer in all wave bands [273]. In this scenario, it is expected that the cooling timescale of electrons becomes longer as $t_{cool} \propto \frac{1}{B^2}$. Weak magnetic fields in GRBs could also be interpreted as the IC scattering dominating over synchrotron cooling [56]. A very small ϵ_β pushes cooling break frequencies to higher values, potentially into hard X-ray or γ-ray bands. The estimated values of the cooling breaks for both constant and wind density profiles are 2.26×10^{17} Hz and 3.91×10^{20},Hz, respectively. Although the cooling breaks fall in the high frequency range, this could still imply that the environment is composed with electrons in the slow-cooling regime for optical emission which could not affect the lower-energy spectra but become relevant for the X-ray observations.

The spectral index obtained is p = 1.8 for this GRB (see Table 5.7 and 5.8, indicating a slower decay or flatter electron distribution according to $N(\gamma_e) \propto {\gamma_e}^{-p}$, where γ_e is the electrons Lorentz factor, implying that a large proportion of high-energy electrons compared to low-energy are involved.

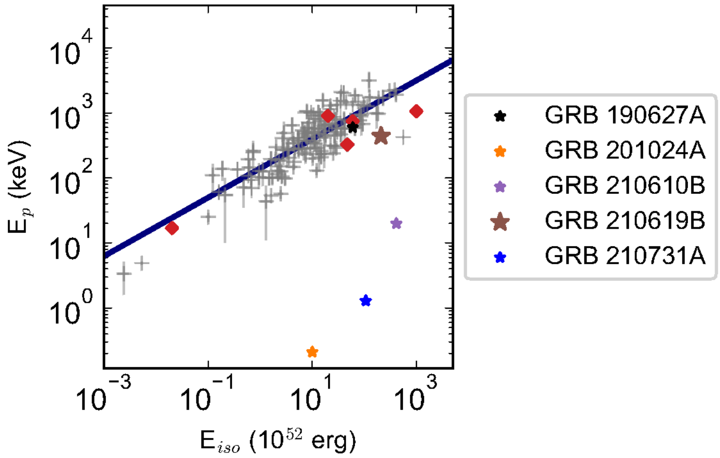

Figure 5.13.: A representation of the Amati relation that shows the known GRBs detected at VHE in red diamonds. We examine the positioning of *GRB 210619B* and other GRBs from the sample (stars) within the Amati relation. The data points in gray represent a selection of GRBs detected by *INTEGRAL*, *Konus*, *Swift*, and *Fermi*, sourced from Table 1 of [27].

GRB 210731A: The H.E.S.S. telescope commenced observations of this GRB just 2 minutes after the trigger. During this time, only the Swift-XRT WT-mode was available and through the analysis performed, I obtained the spectral index that is notably steep, with an observed value of $\alpha = 3.1$ (refer to Table 5.2) which is consistent with results from [274]. However, subsequent analysis of the late time observation (see e.g. [274]) using PC data indicates a spectral index of 1.9, implying that H.E.S.S. might have observed the GRB near the end of its prompt phase. Such spectral index ($\alpha = 1.9$) is more consistent with other measurements of the X-ray spectral index in the afterglow [197]. Alternatively, it's possible that at this time scale, the XRT was only detecting a cut-off in its WT mode data. I also attempted to fit the *Fermi*-GBM data, however, the flux in the *Fermi*-GBM was too low at this time.

The modeling of the prompt phase is beyond the scope of this thesis, so I did not explore this GRB further. We presented, however, the multiwavelength SED including *Swift*-XRT-WT differential energy fluxes, the Optical data extracted from [275] that closely aligned to the H.E.S.S. observing time frame and the H.E.S.S. upper limits in Figure 5.14.

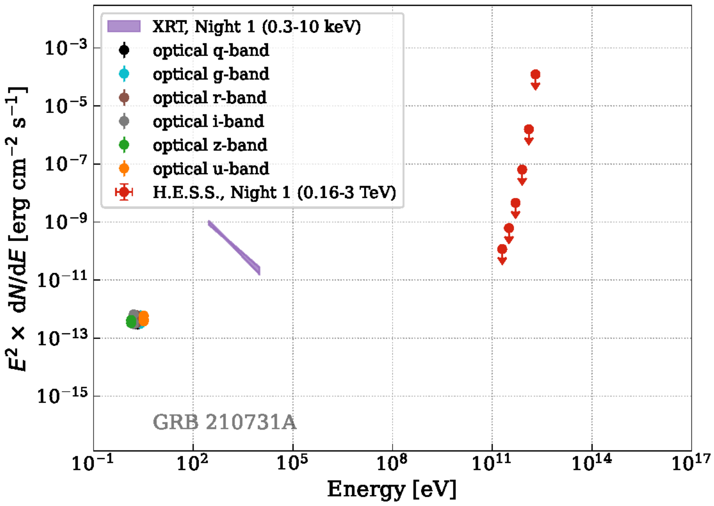

Figure 5.14.: A multiwavelength SED of GRB 210731A, showing the optical in different filters closely simultaneous to the H.E.S.S. data, the *Swift*-XRT-WT and the H.E.S.S. upper limits.

5.7. Conclusions

Since the inception of the H.E.S.S. GRB observation program, only a few GRBs have been detected in the VHE energy regime. A recent study conducted [276] aimed to elucidate why no GRB was detected before 2018 despite IACTs being operational since 2004. Intriguingly, between 2018 and 2023, five GRBs were successfully detected in the VHE regime using the existing IACTs. The study's findings suggest that loosening the observation conditions and upgrading the cameras to achieve lower energy thresholds are key factors contributing to the increased rate of VHE detection. As a result, it was concluded that with these adjustments, one GRB detection per year in the VHE regime can be expected and even more than 10 GRBs per year will be detected with the upcoming IACTs generation such as Cherenkov Telescope Array Observatory (CTAO).

The enhancement of the H.E.S.S. system through upgrades has significantly advanced the GRB observation program, enabling the follow-up of over 150 GRBs to date, as depicted in Figure 5.1. This milestone has been attained through the implementation of more flexible observation criteria, which have evolved over the years, driven by the increasing availability of multi-wavelength data and improvement of instrumentation of the H.E.S.S. telescopes thereby enhancing the likelihood of detection. In this thesis, I tested the standard synchrotron model on optical to X-ray wavelength data and compared the IC prediction with H.E.S.S. ULs to see if they would constrain the SSC model.

In this chapter, I present an analysis of a sample of GRBs observed between 2019 and 2021. My focus is on GRBs with available X-ray and optical data, supplemented by *Fermi*-LAT observations. The primary objective was to constrain the afterglow emission of these GRBs by modeling their SEDs across multiple wavelengths with the exception of *GRB 210731A* which was assumed to be a prompt emission origin due to its steep spectral X-ray index and therefore did not undergo afterglow modelling. I utilized the synchrotron and Synchrotron Self-Compton (SSC) models, applying the methodologies and numerical calculations originally developed in [231].

No evidence of VHE emission was observed from any of the individual GRB from the selected sample. We extracted the MWL lightcurves from the selected sample and no detection of VHE signal from the selected time bins was found during our analysis (see Figure 5.3). We observed strong effects due to the EBL (highest redshift is 1.942 and lowest is 0.999) as shown in Figure 5.7. The Upper limits on the VHE γ-ray flux during the observations from the selected GRB sample were derived. These 95% confidence level energy flux upperlimits corrected for EBL were not found to be at the level of the contemporary X-ray energy flux (see Figure 5.3).

The afterglow modeling, conducted for simultaneous and/or quasi-simultaneous optical, X-ray, High Energy (HE), and VHE observations, revealed several key findings. Firstly, the low-energy photons were well-described by a synchrotron model, particularly in an environment with consistent density. Furthermore, the VHE ULs did not constrain the IC component of the afterglow emission, since it did not reach the level of the VHE flux points. The main reason for this discrepancy is attributed to the consideration of higher-redshift GRB samples. Future investigations could focus on very local GRBs (with a redshift $z \leq 0.1$) observed by H.E.S.S. To provide motivation, we re-scaled the optical and *Swift*-XRT fluxes to a distance where they are at the same level as the H.E.S.S. Figure 5.15, shows the results after a consideration of different redshifts to find at which distance, one would have a nearly equal flux level in all energy bands. I found that at $z=0.5$ this particular GRB would be observed at nearly the same energy flux level (see strong color in Figure 5.15). Knowing the redshift at which the flux level across all energy band as in this case, could imply that multi-band follow-up observations can maximize the scientific return without biasing toward any single wavelength. Additionally, future works may explore low-redshift GRBs reported by *Fermi*-GBM with minimal localization uncertainties.

Such approaches could enhance our understanding of the VHE emission from GRBs and refine the applicability of the SSC model.

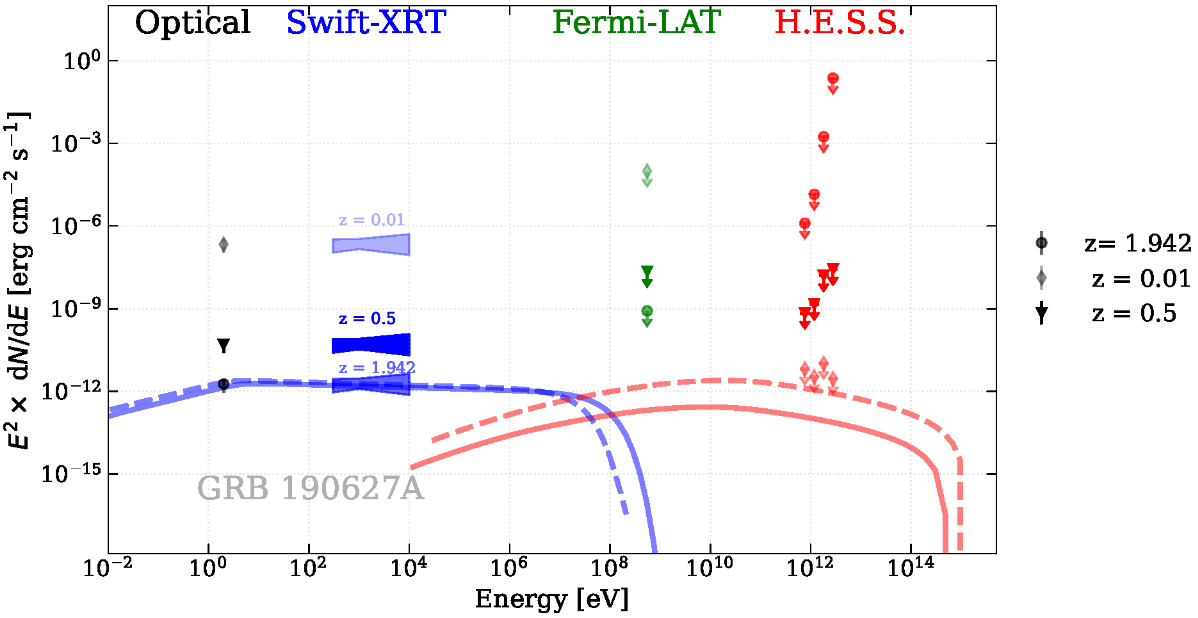

Figure 5.15.: A multiwavelength SED of GRB 190627A, showing the optical, *Swift*-XRT, *Fermi*-LAT and H.E.S.S. upperlimits. The very strong colored data (z=0.5) represent the case where the fluxes across the wave bands (optical, X-ray γ-ray are nearly at the same level).

6. H.E.S.S. real-time Follow-up observations of IceCube alerts on H.E. neutrino events between 2021 and 2022

6.1. Introduction

In the theory of beta decay, Wolfgang Pauli and Enrico Fermi postulated the existence of fundamental particles which were characterized by their neutral charge and weak interaction. This proposal, including the term "neutrino" coined by Fermi, emerged in the early to mid-20^{th} century [277, 278]. However, it wasn't until the mid-1950s that the actual discovery of neutrinos occurred. After nearly thirty years of searching, the first non-atmospheric neutrino event was finally detected during the Supernova SN 1987A explosion [325], revealing their pivotal role in the field of astronomy and astrophysics.

Neutrinos possess negligible rest masses, allowing them to travel vast distances without interaction or deflection, thanks to their weak interaction and resistance to gravity. However, their detection presents a considerable challenge. The prevailing approach for capturing astrophysical neutrinos involves observing the secondary particles generated when neutrinos interact with a medium such as ice or water, typically employing very large Cherenkov detectors. The IceCube observatory, situated at the South Pole, stands as the largest and presently most sensitive instrument for capturing high-energy astrophysical neutrinos [279]. In 2013, IceCube marked a milestone with the announcement of its first discovery of an astrophysical neutrino event [18]. Because neutrinos remain undisturbed during their propagation, potential clues to their origin may be unveiled through spatial correlations with known objects. Correlation searches between the arrival directions of high-energy astrophysical neutrinos and catalogs of high-energy photon sources, such as AGN (including blazars) [279, 280], GRBs [141, 279], clusters of galaxies, Supernovae, Tidal Disruption Events (TDEs [281]), or Starburst galaxies [282], are depicted in Figure 6.1.

The detection of an associated neutrino can provide crucial information about the processes powering these sources, such as hadronic interactions that produce neutrinos alongside CR and

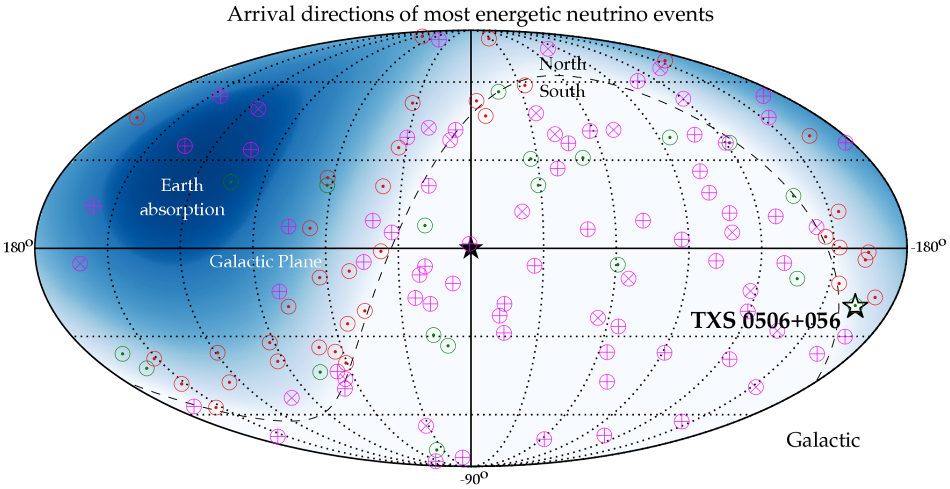

Figure 6.1.: Arrival directions of the most energetic neutrinos detected by IceCube in galactic coordinates. The star indicates the location of the blazar `TXS0506+056`. A Figure adopted from [283].

γ-rays. The main challenge lies in identifying the counterparts to these neutrino events after they are detected. After the detection of the HE neutrino, follow-up observations are conducted across multiple wavelengths from radio through γ-ray, to search for electromagnetic counterparts. However, confirming the true association of a HE neutrino event and an astrophysical source requires correlating the event's location and timing with emission from a known source or transient event. A notable example of the association of neutrino event to a known source was done back on September 09th, 2017. During this time, a HE neutrino event was detected by the IceCube and linked to a flaring blazar (`TXS 0506+056`) [284]. This marked a significant advancement for understanding particle acceleration mechanisms in these events and the role of CRs in the universe and hence the development of multi-messenger astrophysics.

The validation of multi-messenger photon and neutrino emission from this blazar revealed the necessity of real-time monitoring of neutrino events by a variety of ground- and space-based facilities. The coordination among H.E.S.S. and other experiments to align observations, facilitating quasi-simultaneous measurements of multiwavelength flux and spectrum, has been pivotal in evaluating the probability of chance correlations with the high-energy neutrino event from *IC–170922A* [284] and in refining theoretical frameworks. For nearly a decade, the H.E.S.S. transient program has been dedicated to seeking γ-ray emissions associated with high-energy neutrino alerts. This involves scanning for gamma-ray signals from established sources as well as newly identified emitters that align with the suspected origin of the neutrinos. In this chapter, we present a thorough overview of the follow-up procedures for real-time neutrino alerts conducted by H.E.S.S. during the years 2021 and 2022. Our analysis encompasses both publicly announced IceCube neutrino alerts and those shared as part of a collaborative effort between H.E.S.S. and IceCube. We place particular emphasis on intriguing correlations observed with γ-ray sources, drawing special attention to the noteworthy identification of *PKS 0625–35*, an active galactic nucleus previously identified by H.E.S.S., in association with three IceCube neutrinos. A significant fraction of this chapter was written by the H.E.S.S. collaboration as a paper for which I am a corresponding author. It was published in The Astrophysical Journal [1]. Another part of the chapter was published in the ICRC2023 proceedings[2] for which I am also one of the corresponding authors. In both studies, my tasks were to cross-check the H.E.S.S. analysis results and analyze the *Fermi*-LAT data that are counterparts of the IceCube alert events. Below I give a short introduction to the IceCube instrument and how the neutrino events propagate in the universe.

6.2. Origin and propagation processes of neutrinos

The precise origin of neutrinos is believed to be associated with astrophysical phenomena wherein particles are accelerated, subsequently decaying into neutrinos among other particles. Charged particles, γ-rays, and neutrinos are instrumental in probing point-like astrophysical sources or the interstellar medium (ISM). The propagation of these varied particle types is described in Figure 6.2. The processes involved during their propagation vary depending on the characteristics of the particles. For instance, charged particles experience deflection in the magnetic fields present within the interstellar and intergalactic medium as they journey towards Earth. As a result, they are not well-suited for accurate pointing. Another example is that photons, including X-rays and γ-rays, are neutral particles, therefore, do not experience deflection in magnetic fields, however, they can undergo partial absorption. And last but not least, neutrinos are optimal for investigating point-like sources because they remain unaffected by magnetic fields and experience minimal absorption in the interstellar medium, thanks to their small interaction cross-section.

---

[1] The paper is available here: `https://iopscience.iop.org/article/10.3847/1538-4357/ace327`

[2] Available here: `https://pos.sissa.it/444/1546`

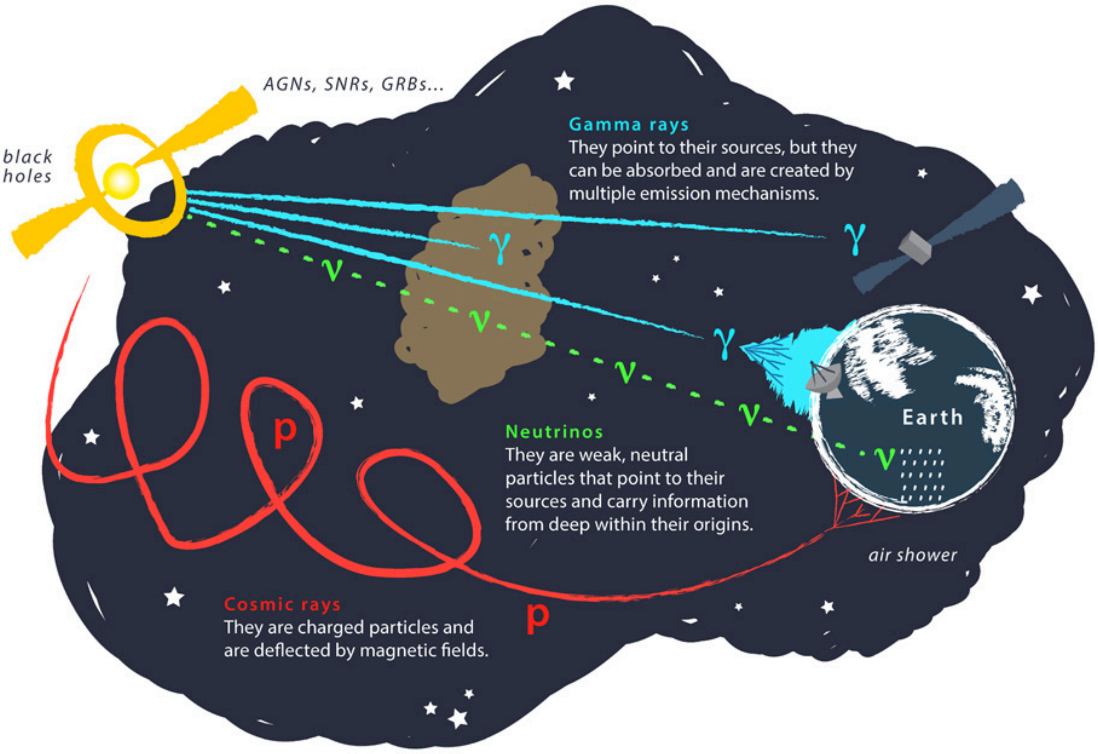

Figure 6.2.: The depiction of cosmic rays, γ-rays and neutrinos' trajectory from their origin (e.g. accreting supermassive blackholes and supernovae) to Earth. As seen in this diagram, CRs get deflected by magnetic fields, while γ-rays are absorbed by intervening materials. On the other hand, neutrinos travel almost unimpeded through Earth. A figure by Juan Antonio Aguilar and Jamie Yang from IceCube/WIPAC and from [285].

6.3. H.E.S.S. neutrino follow-up program

The current H.E.S.S. neutrino program is based on the information about the detections of neutrino candidates shared by the IceCube and ANTARES neutrino telescopes, within few seconds. The program was initiated in 2012 as a Target of Opportunity (ToO), aiming to detect VHE γ-ray counterparts to HE neutrino candidates. Following the detection of an astrophysical flux of HE neutrinos [286], and the evidence of TeV neutrino emission from AGN, *NGC 1068* [287] and flaring γ-ray blazar *TXS 0506+056* [284], it is evident that potential sources of neutrinos include AGN in their flaring state. In this study, a follow-up strategy of the H.E.S.S. telescopes to real-time neutrino alerts, along with a summary of results from November 2021 to the end of 2022 is presented. The analysis covers both public IceCube neutrino alerts and alerts exchanged as part of a joint H.E.S.S.-IceCube program. Each year, H.E.S.S. commits approximately 20 hours of observation time to conducting in-depth investigations of compelling neutrino events, with the aim of detecting VHE γ-ray emissions. Should a detection occur, then longer and more intensive follow-up observations are initiated to facilitate source characterization [288].

6.4. Sample characterization

In this section, a sample of six neutrino alerts followed-up by H.E.S.S. obtained via IceCube's singlet alert stream and the GFU program is described. Singlet alerts consist of high-energy single events likely of astrophysical origin and are further categorized into *gold* and *bronze* alerts based on their signalness probability [289]. In this context, the signalness probability represents the likelihood that a given event is of astrophysical origin compared to background events, assuming the best-fit diffuse muon neutrino astrophysical power-law flux of the form $E^{2.19}$. Events with the following characteristics are selected:

- *Gold alerts:* These are events flagged and distributed with an average signalness value above 50%.
- *Bronze alerts:* These are events characterized by an average signalness value within $30\% \geq P_{\text{astro}} \leq 50\%$.

  Note that IceCube broadcasts these alerts in real-time, typically with a latency of approximately 30 seconds, and they come with a localization uncertainty of around 1 degree, matching the typical field of view of 3.5 to 5 degrees for IACT observations.
- Additionally, GFU alerts are triggered when clusters of neutrino events around predefined sources surpass predefined significance thresholds. These alerts are accessible to H.E.S.S. through a Memorandum of Understanding (MoU), enabling fully automated follow-up

Neutrino ToO	Assoc. source	Type of alert	R.A. deg.	Decl. deg.
IC-211125A	4FGL J0258.1+2030	Bronze	45.614	19.298
IC-211208A	4FGL J0738.1 + 1742	Bronze	114.540	17.710
GFU PKS 0829+046	PKS 0829+046	GFU	127.950	4.490
GFU PKS 0625-35	PKS 0625–35	GFU	96.742	-35.497
IC-220425A	4FGL J0258.1+2030	Gold	268.374	-12.310
GFU 1ES0229+200	PKS 0625–35	GFU	38.203	20.288

Table 6.1.: A sample of six neutrino ToOs observed between 2021–2022. The first and second columns represent the name of the ToO and associated sources, respectively.

observations via a VOEvent-based alert stream. Without prior identification of promising source candidates, searches usually cover the entire region of interest defined by the uncertainty in neutrino localization.

Upon receiving an alert under favorable conditions, such as a dark night with clear weather, telescopes automatically initiate a re-pointing procedure, allowing for immediate observation of the alert. Otherwise, observations typically occur within the next few days, once suitable conditions are met. Consequently, response times vary for each alert, with the fastest recorded at less than 70 seconds.

6.5. H.E.S.S. data analysis

The main analysis pipeline for the data was the Model analysis mentioned in Chapter 4.2. I performed the cross-check analysis using the *ImPACT* reconstruction procedure, more fully described in Chapter 3.5.3 and mentioned in Chapter 4.2. For the selection of γ-ray showers, standard selection criteria are employed [179]. To seek a potential signal while preventing inadvertent inclusion of emissions from other sources, skymaps depicting excess γ-ray counts and significance within a range of +/- 2.0 degrees from the anticipated emission position, are created. For the case of events where there is no known source in the error region provided by the IceCube, upperlimits flux maps were obtained. For non-detected sources, upperlimits fluxes assuming a powerlaw spectrum with a photon index of 2.0 and using Rolke method [221] are calculated. The minimum energy threshold is determined as the energy at which the effective area reaches 10% of its maximum value, while, the maximum energy threshold is defined by the final energy bin employed in the spectrum, ensuring that the count number of background events is $N_{OFF} \geq 10$. The data analysis was conducted during the verification phase of the new CT5 camera analysis tools, thus primarily CT1-4 data are used. No significant emission is detected at the position of the neutrino events by either analysis chain. The results of the analysis are presented in Section 6.7.

6.6. Multiwavelength observations

For the subsequent observations initiated by the GFU stream or the identification of potential counterparts in a singlet alerts, we carried out multiwavelength analyses using data from the *Fermi*-LAT, the *Swift*-XRT and the Automatic Telescope for Optical Monitoring (ATOM).

6.6.1. *Fermi*-LAT analysis

A search for a possible HE γ-ray emission from neutrinos is conducted to complement the MWL data following the describtion in Chapter 4.3.2. The analysis of the *Fermi*-LAT data was performed using a binned likelihood analysis with the help of the python package *Fermipy* software (*V1.2.0*) [290], and *fermitools 2.2* [291]. The `P8R3_SOURCE` event class alongside a corresponding instrument response functions[3] is employed. The selection focused on events within the energy range of 100 MeV to 300 GeV and within a 15 degree radius of the neutrino position, with a zenith angle cut of 90 degrees applied. In addition to the `PowerLaw` model[4] employed for the γ-ray spectrum, Galactic and isotropic templates are incorporated for background[5] estimation. Moreover, all catalog sources within 25 degrees of the neutrino position [228] are included. Each analysis extended over a two-day period, spanning a day before and after the arrival time of the neutrino events. This approach aimed to enhance sensitivity to rapid and intense transients, even those lasting only a few hours. In light of the absence of any notable emission correlated with the neutrino events in the *Fermi*-LAT data during this simultaneous two-day interval with the H.E.S.S. observations, upper limits at 95% confidence level are computed. These calculations were based on the assumption of an E^{-2} spectrum for the differential energy flux between 100 MeV and 300 GeV. Resulting upper limits are shown in the SED presented in section 6.7, and plotted together with other multi-wavelength data for individual event. A particular case appeared for *IceCube-211208A* which was located 2.2 degrees away from *PKS 0735 + 178.*

An interesting case was found for the neutrino event *IC-211208A*. *Fermi*-LAT observation reveals that a Blazar *PKS 0735+178* associated with *4FGL J0738.1+1742* is located 2.2° away of the

---

[3] `https://fermi.gsfc.nasa.gov/ssc/data/analysis/documentation/Cicerone/Cicerone_LAT_IRFs/IRF_overview.html`

[4] `https://fermi.gsfc.nasa.gov/ssc/data/analysis/scitools/source_models.html`

[5] `https://fermi.gsfc.nasa.gov/ssc/data/access/lat/BackgroundModels.html`

Neutrino ToO	Source	Obs. IDS	Photon Index	Energy Flux (unabs.) $\times 10^{-12}$ erg cm^{-2} s^{-1}	Galactic Column Density $\times 10^{20}$ cm^{-2}
GFU PKS 0625-35	PKS 0625-35	00039136003-00039136004	$2.19^{0.19}_{-0.18}$	$10.7^{+1.27}_{-1.00}$	7.9
IC-211125A	4FGL J0258.1+2030	00041549003	$1.60^{0.70}_{-0.50}$	$1.80^{0.80}_{-0.50}$	24.0
GFU PKS 0829+046	PKS 0829+046	00038144014	$1.87^{0.33}_{-0.30}$	$2.30^{0.40}_{-0.30}$	2.70
GFU 1ES 0229+200	1ES 0229+200	00031249115	$1.83^{0.18}_{-0.17}$	$17.96^{0.16}_{-0.15}$	12

Table 6.2.: *Swift*-XRT data analysis parameters. The unabsorbed energy flux is obtained by integrating over the full energy range 0.3-10 keV, correcting for the Galactic column density value [292].

neutrino event, making it the best candidate of the neutrino emission. For this particular case, four weeks (2 weeks before and after the neutrino event) of data were analyzed covering the period in which the blazar was in a flaring state. The derived analysis product shows the significance of PKS 0735+178 of around 34σ located nearly at the edge of the 90% IceCube contamination of the *IC-211208A* (see Figure 6.3) and a TS of 1171.2 is derived. The Spectrum of the *PKS 0735+178* during the 4 weeks fitted by a log-parabola model is shown in Figure 6.7.

6.6.2. *Swift*-XRT analysis

The X-ray data from *Swift*-XRT [41] are analyzed using version 6.29 of the `HEASOFT` software [197], with a specific focus on data collected around the time of the neutrino ToO observations. The utilized data and the results of the analysis, integrated in the 0.3-10 keV energy range, are presented in Table 6.2. The details of the *Swift*-XRT data analysis of `IC-211208A` were published in [190], hence, not presented in Table 6.2. In addition, there is no *Swift*-XRT data obtained on `IC-220425A` event.

6.6.3. Optical data

In addition to the *Fermi*-LAT, *Swift*-XRT and H.E.S.S. data, we collected optical data in the B, V, R, and I bands (equivalent to wavelengths of 440 nm, 550 nm, 640 nm, and 790 nm, respectively) using the 75 cm ATOM telescope located at the H.E.S.S. site in Namibia [293]. The ATOM data analyzed in this study corresponds to observation times synchronized with the H.E.S.S. ToO observations. Energy fluxes for candidate sources were calculated for four neutrino follow-ups.

6.6.4. Other multiwavelength data

In addition to extracted data, we added archival and quasi-simultaneous data observed at other wavelengths where possible and presented a full spectral energy distribution. Archival data

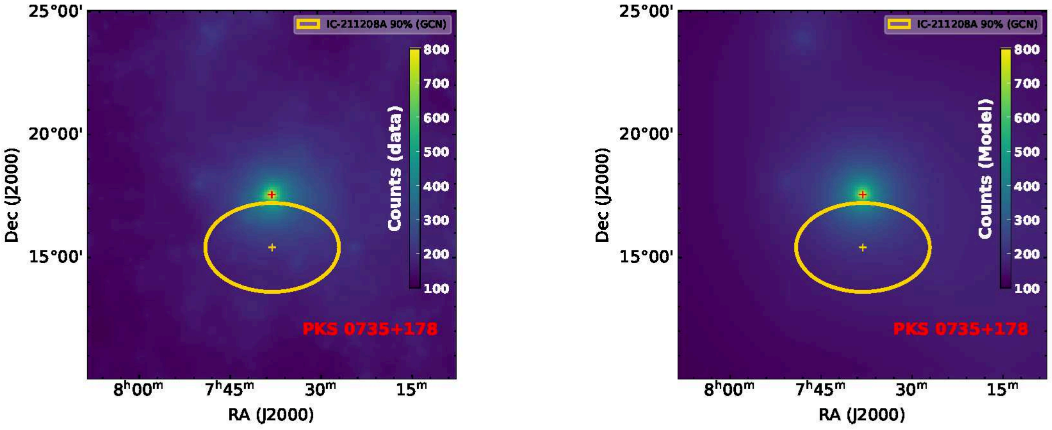

(a) Data Counts (b) Model counts

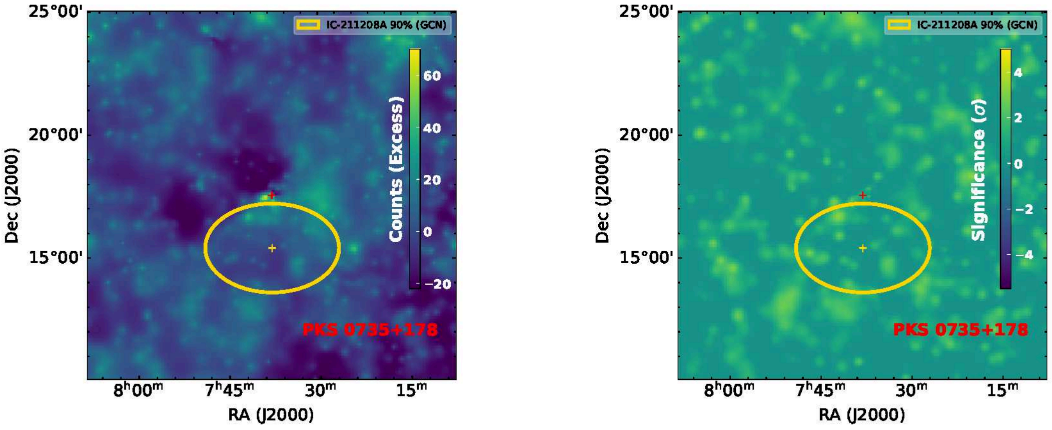

(c) Excess counts (d) Significance

Figure 6.3.: The *Fermi*-LAT analysis results for the blazar *PKS 0735+178 (4FGL J0738.1+1742)*, which coincides with a neutrino event (*IC-211208A*), are presented. Various Skymaps illustrate the IceCube 90% containment region (yellow ellipse), with the blazar's position marked in red alongside the neutrino event's reported position (yellow cross). The maps display: (a) the counts of detected γ-ray-like events, (b) the predicted γ-ray event counts from the model, (c) the excess counts calculated as the difference between observed data and the model, and (d) the statistical significance of the excess counts.

spanning the radio to gamma-ray bands were sourced from the ASDC SED Builder Tool[6] of the Italian Space Agency [294]. This comprehensive dataset incorporates information from various catalogs and databases.

6.7. Results and discussion of individual events

6.7.1. IC–211125A

A bronze neutrino track-like event *IC-211125A* was reported on November 25 2021 by IceCube, with 39% chances of being an astrophysical source (false alarm rate of 1.973/year) [295]. The neutrino event was spatially consistent with a classical Nova *AT2021afpi* [296] and the AGN `4FGL J0258.1+2030`. H.E.S.S. observed the position of the Nova a day after the IceCube detection while in the following four nights, the observation were manually carried out in a pattern defined to cover both sources. A data quality check was performed and due to bad weather conditions, which led to unstable trigger rates, only ∼5 hours of data are analyzed. No evidence of VHE emission is found, therefore, upper limits map is computed, within 0.42–100 TeV range. Figure 6.4 shows integral upper limit map centered at the position of the AGN, where the yellow circle represents the initial 90% error uncertainty on the neutrino position, and the orange circle shows more improved contours calculated using advanced offline algorithms. A multiwavelength SED which include *Fermi*-LAT and *Swift*-XRT, with H.E.S.S. upper limits derived at the position of the `4FGL J0258.1+2030` is presented in Figure 6.5.

6.7.2. IC-211208A

On December 8, 2021, another bronze neutrino flare was reported with IceCube ($P_{Astro} \approx 50.2\%$). The flare was associated with three AGNs, but only *PKS 0735+178* (z = 0.45) which located at the edge ($\sim 2^\circ$) of the 90% error region from the best fit position, was in flaring state from radio to γ-ray band. H.E.S.S. observed the blazar (*PKS 0735 +178*) for a total of 16 hours during a week, however, only ≈ 3.8 hours of data passed the data quality assessment. An analysis of H.E.S.S. data resulted in no detection in the direction of the blazar, therefore upper limits map integrated over 0.4–100 TeV are computed at 95% C.L. across the entire field of view, as shown in Figure 6.6. A multiwavelength SED is shown in Figure 6.7, including optical, X-ray as well as archival data. Both Very Energetic Radiation Imaging Telescope Array System (*VERTAS*) and H.E.S.S. detected no VHE signal and a theoretical modeling was found to be inconsistent with the data, ruling out a possibility of neutrino emission. A complete SED as

---

[6] `https://tools.ssdc.asi.it/SED/`

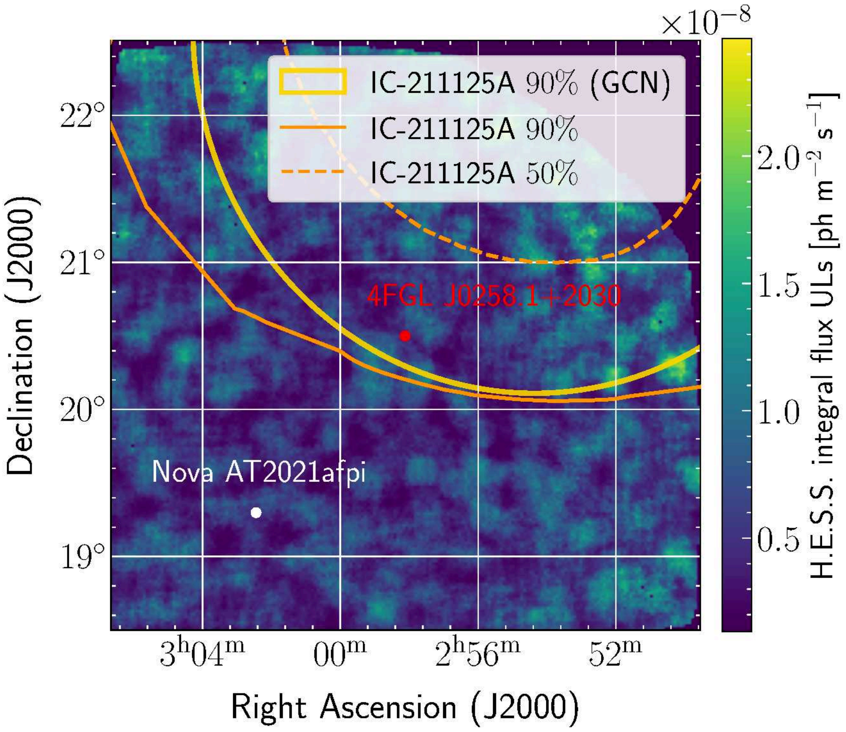

Figure 6.4.: `IC-211125A` integral upper limits map of H.E.S.S. observations at 95% C.L. The red point shows the *Fermi*-LAT position of the neutrino counterpart within the reported 90% of the positional uncertainty. In addition, the reported classical nova counterpart was found to be away of the revised and the initial 90% and 50% positional uncertainty but within the H.E.S.S. field of view.

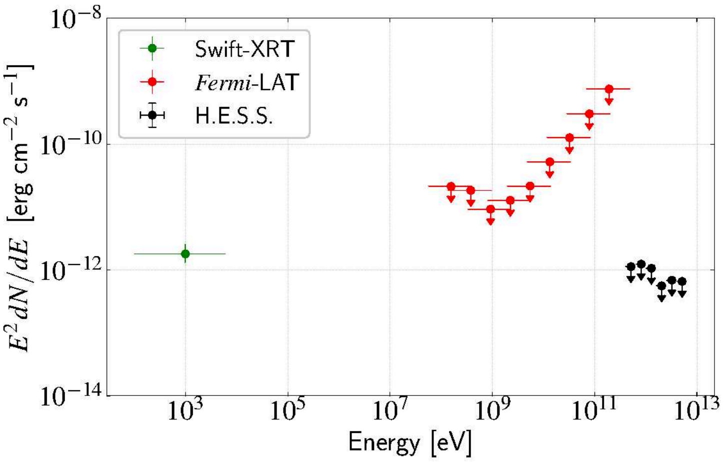

Figure 6.5.: The SED of the candidate source 4FGL J0258.1+2030 with *Fermi*-LAT upper limits (orange) and *Swift*-XRT data (red). The simultaneous H.E.S.S. follow-up of this neutrino event resulted in 95% C.L. upperlimits (magenta).

well as details on theoretical interpretation on the blazar, the reader is referred to the original paper [190]

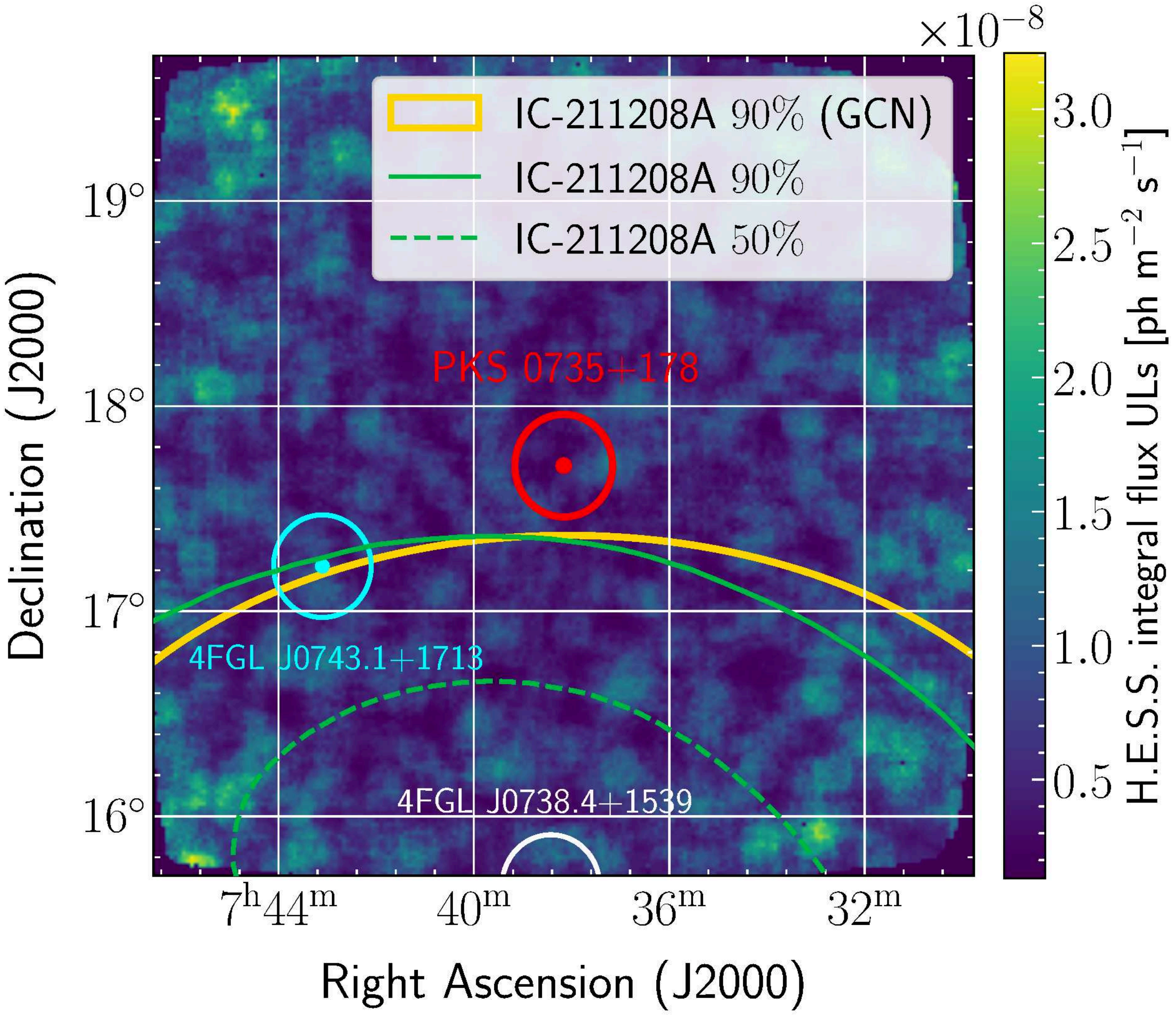

Figure 6.6.: `IC-211208A` integral upper limits map of H.E.S.S. observations at 95% C.L. estimated within [0.433 - 10] TeV energy range. The map also shows 3 possible gamma-ray counterparts of the neutrino event. Potential interest by H.E.S.S. was directed towards the flaring (in that period) blazars (red) although it was located outside the error positions of 90% reported in GNC (yellow) and two other re-estimated error radius (dotted green contour 50% and solid green contour 90%) on the neutrino position.

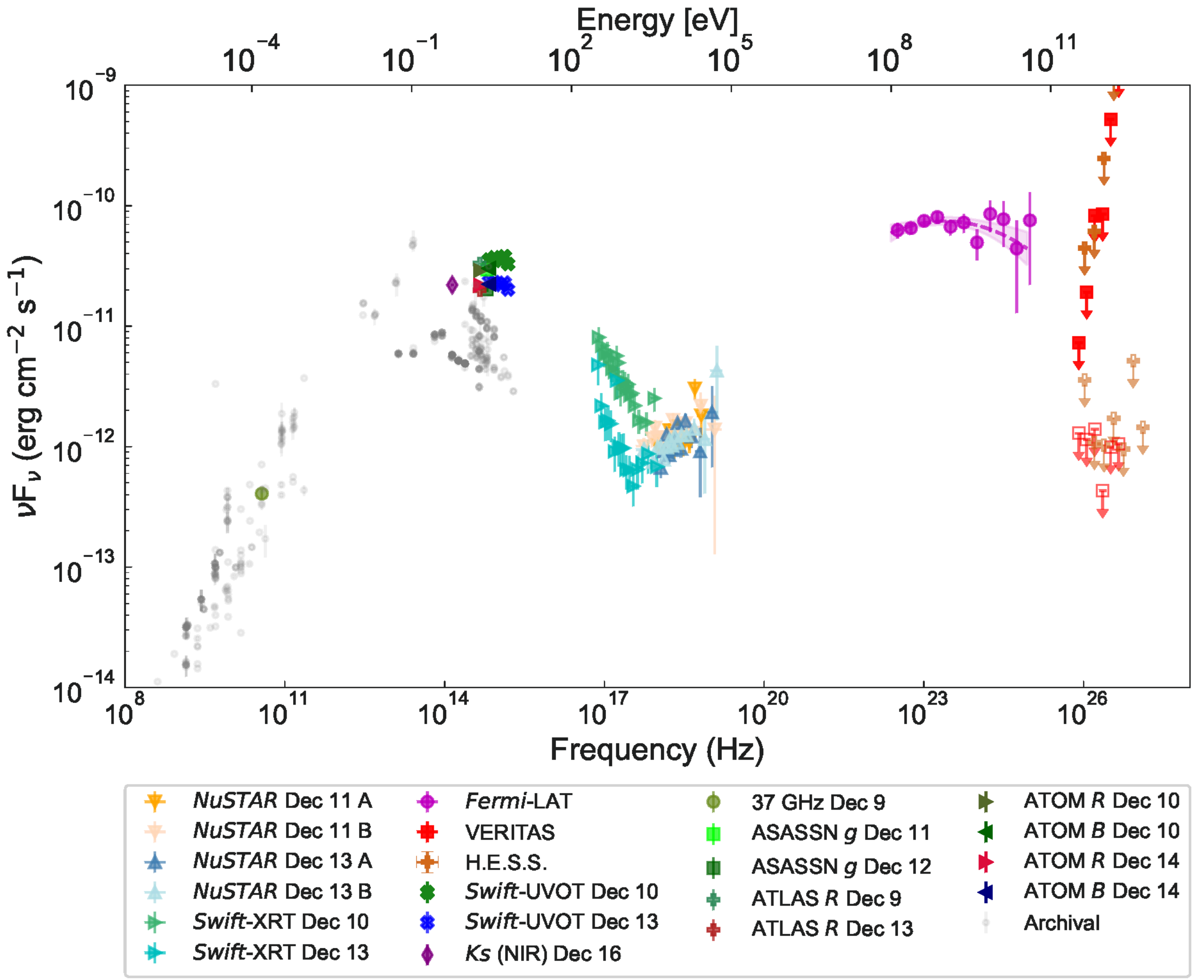

Figure 6.7.: The SED of PKS 0735+178 in December 2021 is shown with archival data spanning from radio to UV bands (gray filled circles). Spectra from *VERITAS* and H.E.S.S. were averaged over the ToO observation period. *Fermi*-LAT spectrum was averaged over four weeks. A magenta shaded region indicates the best-fit log-parabola model to the *Fermi*-LAT spectrum. Figure obtained from [190].

6.7.3. GFU PKS 0829+046

On December 22, 2021, a neutrino flare consisting of 8 events (with the most energy reaching 2 TeV), was detected by IceCube, corresponding to a significance of 3.05σ (false alarm rate of 0.055/year). The neutrino flare was spatially consistent with the blazar BL Lac *PKS 0829+046*. H.E.S.S. observed the blazar for about two days, accumulating roughly 4.7 hours of data. The analysis of H.E.S.S. data resulted in no evidence of VHE emission, and therefore, integral upper limits at 95% C.L. are computed above a threshold energy of 224 GeV. A multiwavelength SED is shown in Figure 6.8, including optical and X-ray data. No activity was spotted from blazars in the HE and VHE range, indicating that there was no correlation with the neutrino flare.

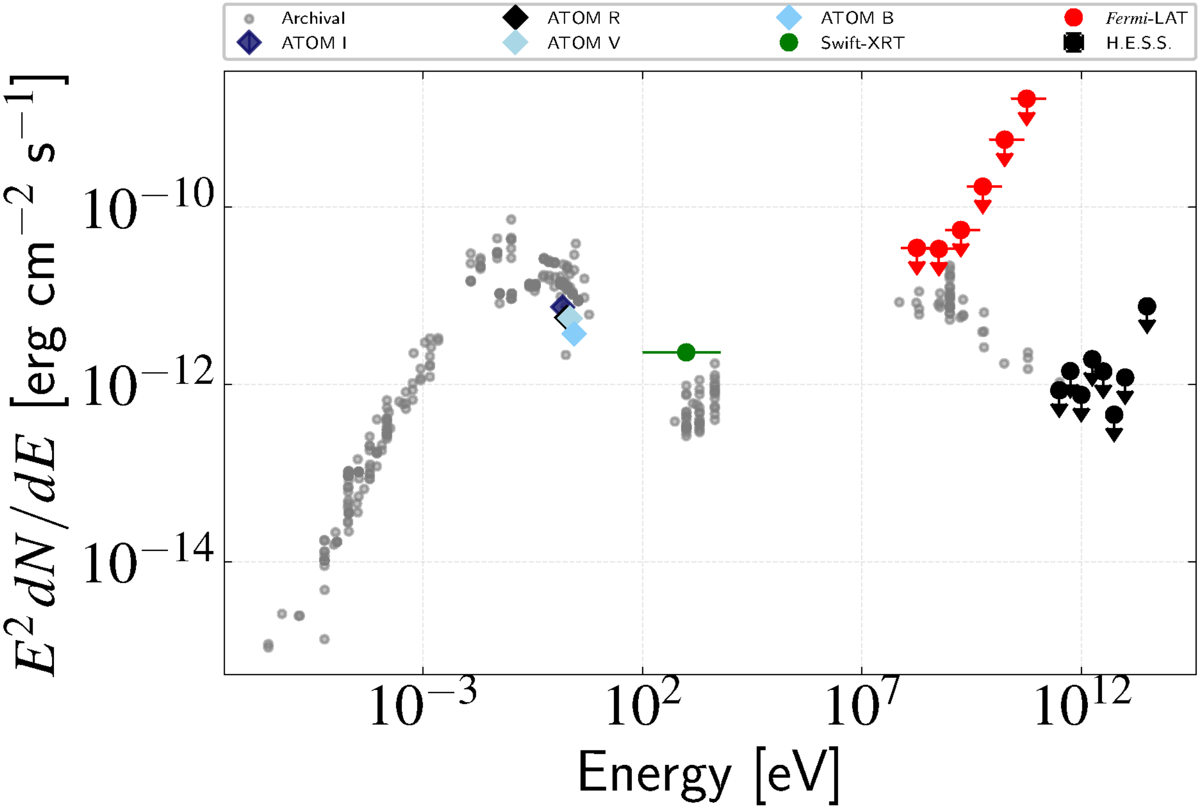

Figure 6.8.: The SED of the PKS 0829+046 (a potential counterpart of the neutrino event) using data from H.E.S.S., *Fermi*-LAT, *Swift*-XRT, and ATOM observed simultaneously. Archival data are displayed in gray. The multiwavelength observations are averaged over the two days of the H.E.S.S. ToO observation period.

6.7.4. GFU PKS 0625–35

On April 16, 2022, IceCube detected 3 neutrinos (from 63 TeV to 302 TeV) within few minutes from each other, corresponding to a significance of 3.5 σ (with false alarm rate of 0.003 per year). The neutrino flare was spatially consistent with the blazar *PKS 0625–35* which had previously detected by H.E.S.S.. In the light of this, H.E.S.S. observed the blazar over three nights after the IceCube alert, accumulating approximately three hours of data. An analysis of the H.E.S.S. data found evidence at the 3.5 σ level for VHE emission, which was modeled as a power law with a spectral index of 2.45 ± 0.42 in the 0.35 to 6.58 TeV range. A multiwavelength SED is presented in Figure 6.9, including optical and X-ray data. It can be seen that the measured fluxes in April 2022 are consistent with the archival data as well as the H.E.S.S. data from 2018 [297], indicating no new activity from the blazar and therefore no correlation with the neutrino flare.

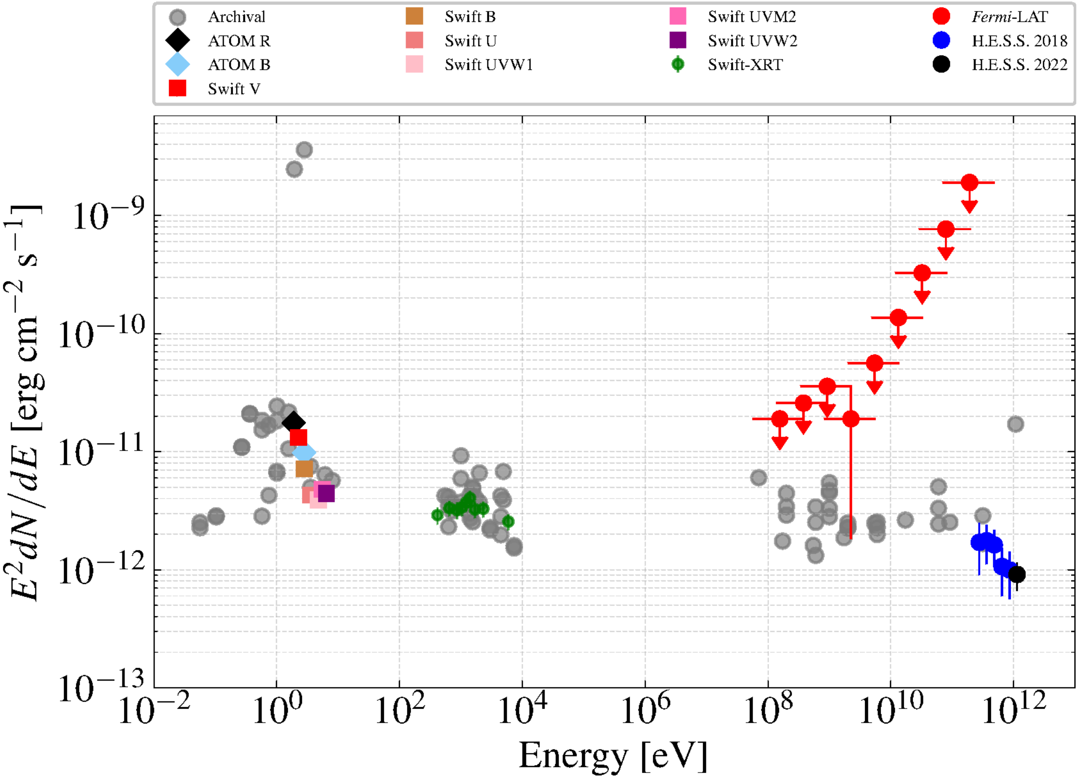

Figure 6.9.: The SED of the blazar PKS 0625−35 as observed by H.E.S.S. corrected for EBL effect (magenta) and simultaneous to *Fermi*-LAT (green), *Swift*-XRT – UVOT (in different filters), and ATOM (in different filters). Shown are also the H.E.S.S. observation of 2018 corrected for EBL (in orange) [298] and archival data (in gray).

6.7.5. IC-220425A

On April 25, 2022, IceCube detected a gold alert (with signalness probability of 17%). H.E.S.S. observations started promptly in less than 70 seconds after the neutrino detection, accumulating nearly 75 minutes of data under moonlight conditions. The analysis of H.E.S.S. data did not yield any detection, therefore, 95% C.L. integrated upper limit map between 0.35 TeV to 100 TeV, is calculated and is shown in Figure 6.10, with the updated neutrino position calculated offline. In addition, no detection was observed in optical through X-ray to γ-ray.

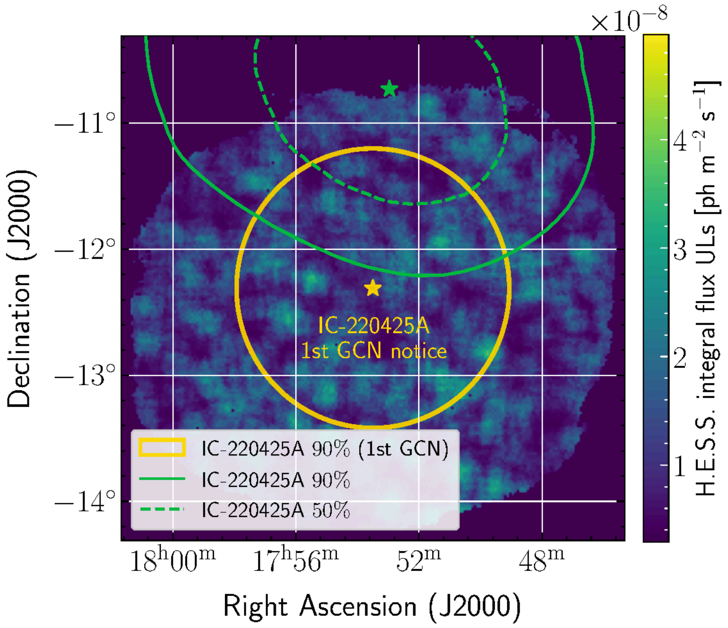

Figure 6.10.: `IC-220425A` integral upper limits map of H.E.S.S. observations at 95% C.L. The H.E.S.S. observations are performed outside the re-estimated (90% and 50%) error radius of the neutrino position. The green star shows the updated neutrino position with its statistical error positions refined offline.

6.7.6. GFU 1ES0229+200

On August 25, 2022, IceCube detected four neutrino events corresponding to a significance of 3.09σ (false alarm rate of 0.050/year) with the most energetic event reaching 1.3 TeV. The neutrino flare was spatially consistent with a high frequency peaked blazar BL Lac (*1ES0229+200*). With the flare lasting approximately 1.2 days, H.E.S.S. observed the blazar two days after the neutrino detection for 5 nights, accumulating 13.5 hours of data, but only ∼8 hours of data passed the data quality checks due to unstable weather conditions. An analysis of H.E.S.S. data did not found any evidence of VHE emission, therefore, 95% C.L. upper limits are computed.

The blazar was also detected in optical through X-ray to γ-rays wavebands. A multiwavelength SED is shown in Figure 6.11, including optical, X-ray and *Fermi*-LAT. The existing archive data are compared to new data and no evidence of a notable new activity from the blazar therefore, no correlation with neutrino flare was found.

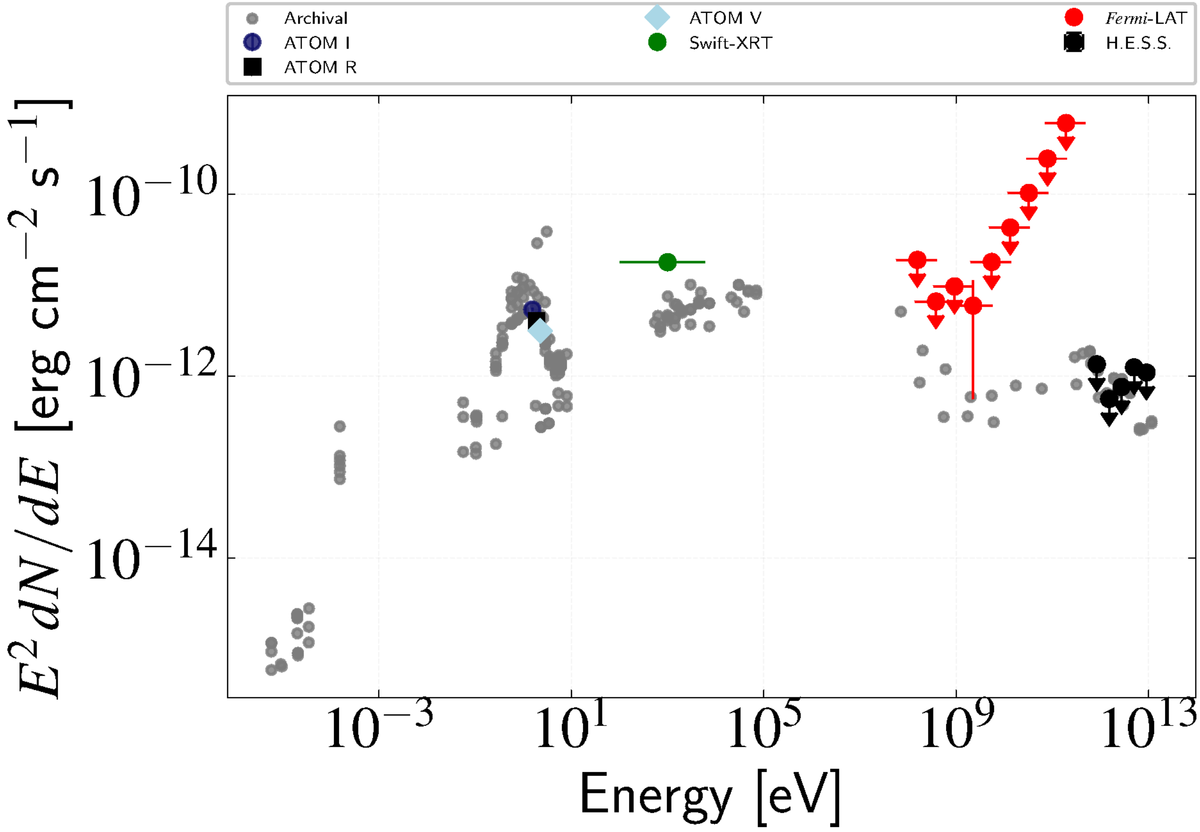

Figure 6.11.: The SED of the HBL `GFU 1ES0229+200` showing simultaneous data from H.E.S.S., *Fermi*-LAT, *Swift*-XRT, and ATOM (in its 3 filters) all of which are averaged over 5 nights spanning the ToO observation period. Archival data are displayed in gray.

6.8. Conclusions

In this chapter, we discussed and presented the analysis and follow-up strategy of the H.E.S.S. telescopes to real-time alerts from the IceCube. The search for γ-ray emissions from November 2021 to the end of 2022 neutrino events is summarized. A sample of 6 events was observed within this period based on their probability of being of astrophysical origin. Among them, two Bronze events and single Gold events are selected with 30% $\geq$ $P_{\text{astro}} \leq$ 50% and $P_{\text{astro}} \geq$ 50%, respectively, and others are γ-ray follow-up from targeted known γ-ray sources. There was no evidence of VHE emission in all events studied except for the blazar `PKS 0625-35`. However, the follow up program demonstrated the importance of multimessenger observation and could play a very important role in understanding HE astrophysical phenomena. Another notable case is for `IceCube-211208A` associated with `PKS 0735+178` which was found 2.2° away from the IceCube best-fit position immediately outside the 90% error region. For this specific event, extensive follow-up observations across the electromagnetic spectrum yielded a well-measured broadband SED of `PKS 0735+178` near the time of the IceCube event [190]. In addition, the observed SED of the blazar, showed cut-off in the TeV energies, which challenges the usual simplistic one-zone SSC model. This challenge persists unless, in an improbable scenario, the synchrotron peak extends into the far-ultraviolet band, which is not covered by the observations [190]. Addressing such challenges, among others, requires additional data and ongoing efforts to search for astrophysical neutrino emitters. This includes conducting follow-up observations of flaring blazars that coincide temporally and spatially with astrophysical neutrino events.

7. Conclusions and Outlook

In this thesis, two transient source classes are presented and discussed. The study begins with a general introduction of γ-ray astronomy and focuses on the background of GRBs. Several important radiation mechanisms responsible for generating GRBs and basic properties of prompt emission and afterglows (including synchrotron emission and SSC emission) are reviewed in Chapter 2. Additionally, a comprehensive explanation of the H.E.S.S. array focusing on its data handling and analysis methods is presented in Chapter 3.

The first source class discussed in this study are GRBs by focusing on GRB 221009A (the BOAT). Chapter 4 introduces and motivates the search for VHE γ-ray emission from GRBs by highlighting their nature, expected acceleration mechanisms and their role as the extragalactic transient objects. The follow-up observations of GRB 221009A by H.E.S.S. is described in detail, including the data analysis. I addressed the poor atmospheric challenges posed by the data by applying an advanced method for atmospheric corrections. There was no significant VHE γ-ray signal detection found in the results of either the three nights of data individually nor in the combined dataset of these three nights. A combined analysis of all nights resulted in an integral energy flux upper limit at 95% C.L. within 0.65–10 TeV of $\Phi_{\mathrm{UL}}^{95\%} = 9.7 \times 10^{-12}\ \mathrm{erg\,cm^{-2}\,s^{-1}}$. Differential energy flux upper limits are also calculated and used to construct a multiwavelength SED. With the obtained VHE upper limits, the 1-zone SSC model was explored based on an analytical model developed in [231]. We explored different possibilities in which the H.E.S.S. upper limits are nearly at the level of SSC model (i.e. upper limits constrain the model), and one possibility is presented in this thesis. Hard spectra are observed at lower energy bands indicating that most of the energetic electrons have not undergone significant cooling. Although a detail exploration of the acceleration mechanism is not carried out for the BOAT, the MWL datasets provided a valuable resource for future theoretical studies.

In Chapter 5, a search for VHE γ-ray emission from other GRBs observed by H.E.S.S. is conducted. The basic idea is to perform a search for possible VHE γ-ray emission from a sample of GRBs observed by H.E.S.S. using *Swift*-BAT or *Fermi*-LAT alerts of detected GRBs with known redshifts and available multiwavelength data. A sample of 5 GRBs are selected using suitable selection criteria, in which 4 of them were observed during the afterglow phase by H.E.S.S. and hence could be modeled using the SSC model previously described. The analysis is conducted using the standard H.E.S.S. analysis methods only using the small telescopes' (CT1-4) data since the cross-check analysis methods were not fully optimized for the big telescope (CT5) by the time of the analysis. Since no detection of VHE γ-ray emission is observed in any of GRBs, upper limits are set for the sample. In general, as expected, the higher the redshift the less constraining the upper limits. Furthermore, I found that the GRBs would need to be at a redshift of $z \approx 0.5$ for the VHE upper limit to be at the same level as the X-ray flux. I again applied the SSC model developed in [231] (see also details in B.1) to model the MWL observations. The results presented in the dedicated chapter suggest that the low-energy data (optical to X-rays) are well described by a synchrotron component for both constant density medium and wind scenarios. However, in all cases, the IC component is located far below VHE upper limits due to them being affected by the EBL effects, meaning that the VHE upper limits are not constraining the model. Recent detection of GRBs have shown that detecting VHE emission by IACTs require low redshift and bright X-ray emission. H.E.S.S. observations of GRB 221009A starting 51.8 hours post burst resulted in non detections, which could imply that γ-ray emission might not be bright enough at this time. Future works could focus on more local GRBs which are less affected by the EBL and include samples from *Fermi*-GBM that have modest localization uncertainty. It is expected that using the next-generation CTAO and loosening the observation criteria will be crucial for more VHE GRB detections and hence will allow for better studies of particle acceleration in these transients.

The second source class presented within this thesis are the neutrino events. The observation of the position of the detected neutrinos in search for γ-ray emission is conducted. The dedicated chapter outlines the neutrino events observed by H.E.S.S. from 2021 to the end of 2022. It provides a summary of the results prior to this work on a total of six events. The analysis of these 6 neutrino events using `std_ImPACT` is presented. There are no VHE γ-ray signals detected for 5 events except for one targeted observation of a blazar `PKS 0625-35`. Therefore, upper limits are computed and put into context with other MWL and archival data. A particular case of a targeted source around `PKS 0735+178` provided a well measured MWL SED. The observed SED challenged the existing one zone SSC model due to the synchrotron peak that extends far to the UV band. Detecting neutrino sources requires multi-messenger observations and MWL follow-ups in different wavebands. However, this also require well localized events. With the upgrade of the IceCube instrument and future generation of ground based telescopes, it is expected that more follow up observations and detections of neutrino events from targeted objects like blazars or GRBs will be achieved.

Bibliography

[1] Hess, Victor F., "Über Beobachtungen der durchdringenden Strahlung bei sieben Freiballonfahrten", *Phys. Z.* **1912**, *13*, 1084–1091.

[2] R. W. Klebesadel, I. B. Strong, R. A. Olson, "Observations of Gamma-Ray Bursts of Cosmic Origin", *Astrophysics Journal Letters* **1973**, *182*, L85.

[3] W. B. Atwood et al., "The Large Area Telescope on the Fermi Gamma-Ray Space Telescope Mission", *Astropysical Journal* **2009**, *697*, 1071–1102.

[4] J. Hinton, "The status of the HESS project", *New Astronomy Reviews* **2004**, *48*, 2nd VERITAS Symposium on the Astrophysics of Extragalactic Sources, 331–337.

[5] C. Bigongiari in International Europhysics Conference on High Energy Physics, HEP2005, **2005**, 20, p. 20.

[6] F. Krennrich et al., "VERITAS: the Very Energetic Radiation Imaging Telescope Array System", *New Astronomy Reviews* **2004**, *48*, 2nd VERITAS Symposium on the Astrophysics of Extragalactic Sources, 345–349.

[7] T. DeYoung, "The HAWC observatory", *Nuclear Instruments and Methods in Physics Research Section A: Accelerators Spectrometers Detectors and Associated Equipment* **2012**, *692*, 3rd Roma International Conference on Astroparticle Physics, 72–76.

[8] X. A. Huo et al. in.

[9] G. Di Sciascio, "The LHAASO experiment: From Gamma-Ray Astronomy to Cosmic Rays", *Nuclear and Particle Physics Proceedings* **2016**, *279-281*, Proceedings of the 9th Cosmic Ray International Seminar, 166–173.

[10] Z. Cao et al., "The Large High Altitude Air Shower Observatory (LHAASO) Science Book (2021 Edition)", *arXiv e-prints* **2019**, arXiv:1905.02773.

[11] A. Albert et al., "Science Case for a Wide Field-of-View Very-High-Energy Gamma-Ray Observatory in the Southern Hemisphere", *arXiv e-prints* **2019**, arXiv:1902.08429.

[12] P. Huentemeyer et al. in Bulletin of the American Astronomical Society, *Vol. 51*, **2019**, 109, p. 109.

[13] Cherenkov Telescope Array Consortium et al., *Science with the Cherenkov Telescope Array*, **2019**.

[14] LHAASO Collaboration et al., “A tera-electron volt afterglow from a narrow jet in an extremely bright gamma-ray burst.”, *Science* **2023**, *380*, 1390–1396.

[15] H. E. S. S. Collaboration et al., “Revealing x-ray and gamma ray temporal and spectral similarities in the GRB 190829A afterglow”, *Science* **2021**, *372*, 1081–1085.

[16] MAGIC Collaboration et al., “Teraelectronvolt emission from the γ-ray burst GRB 190114C”, *Nature* **2019**, *575*, 455–458.

[17] H. Abdalla et al., “A very-high-energy component deep in the γ-ray burst afterglow”, *Nature* **2019**, *575*, 464–467.

[18] M. G. Aartsen et al., “Measurement of the Atmospheric ν_e Flux in IceCube”, *Phys. Rev. Lett.* **2013**, *110*, 151105.

[19] B. P. Abbott et al., “Observation of Gravitational Waves from a Binary Black Hole Merger”, *Phys. Rev. Lett.* **2016**, *116*, 061102.

[20] W. S. Paciesas et al., “The Fourth BATSE Gamma-Ray Burst Catalog (Revised)”, *Astrophysical Journal Supplemment Series* **1999**, *122*, 465–495.

[21] N. Gehrels, P. Mészáros, “Gamma-Ray Bursts”, *Science* **2012**, *337*, 932.

[22] B. Zhang, *The Physics of Gamma-Ray Bursts*, **2018**.

[23] E. P. Mazets, S. V. Golenetskii, V. N. Il’Inskii, “Flare of cosmic gamma radiation as observed with “Cosmos-461” satellite”, *Soviet Journal of Experimental and Theoretical Physics Letters* **1974**, *19*, 77.

[24] K. Hurley et al., “Detection of a γ-ray burst of very long duration and very high energy”, *Nature* **1994**, *372*, 652–654.

[25] C. A. Meegan et al., “Spatial distribution of γ-ray bursts observed by BATSE”, *Nature* **1992**, *355*, 143–145.

[26] M. S. Briggs, THE FOURTH BATSE GAMMA-RAY BURST CATALOG (REVISED), **1999**, `https://gammaray.nsstc.nasa.gov/batse/grb/skymap/` (visited on 11/15/2023).

[27] Y.-P. Qin, Z.-F. Chen, “Statistical classification of gamma-ray bursts based on the Amati relation”, *Monthly Notices of the Royal Astronomical Society* **2013**, *430*, 163–173.

[28] D. Band et al., “BATSE Observations of Gamma-Ray Burst Spectra. I. Spectral Diversity”, *The Astrophysical Journal* **1993**, *413*, 281.

[29] Boella, G. et al., “BeppoSAX, the wide band mission for X-ray astronomy”, *Astron. Astrophys. Suppl. Ser.* **1997**, *122*, 299–307.

[30] E. Costa et al., “Discovery of an X-ray afterglow associated with the γ-ray burst of 28 February 1997”, *nature* **1997**, *387*, 783–785.

[31] L. Piro et al., “The first X-ray localization of a gamma -ray burst by BeppoSAX and its fast spectral evolution”, *Astronomy and Astrophysics* **1998**, *329*, 906–910.

[32] M. R. Metzger et al., “Spectral constraints on the redshift of the optical counterpart to the γ-ray burst of 8 May 1997”, *nature* **1997**, *387*, 878–880.

[33] S. R. Kulkarni et al., “GRB 971214”, *The Astronomer’s Telegram* **1998**, *7*, 1.

[34] A. Cucchiara et al., “A Photometric Redshift of z ~ 9.4 for GRB 090429B”, *Astrophysical Journal* **2011**, *736*, 7.

[35] F. A. Harrison et al., “Optical and Radio Observations of the Afterglow from GRB 990510: Evidence for a Jet”, *The Astrophysical Journal* **1999**, *523*, L121.

[36] E. Berger, “Short-Duration Gamma-Ray Bursts”, *Annual Review of Astronomy and Astrophysics* **2014**, *52*, 43–105.

[37] T. J. Galama et al., “On the possible association of SN 1998bw and GRB 980425”, *Astronomy and Astrophysics Supplement* **1999**, *138*, 465–466.

[38] S. R. Kulkarni et al., “The gamma-ray burst of 980425 and its association with the extraordinary radio emission from a most unusual supernova”, *arXiv e-prints* **1998**, astro–ph/9807001.

[39] C. Akerlof et al., “Prompt Optical Observations of Gamma-Ray Bursts”, *Astropysical Journal Letters* **2000**, *532*, L25–L28.

[40] S. D. Barthelmy et al., “The Burst Alert Telescope (BAT) on the SWIFT Midex Mission”, *Space Science Reviews* **2005**, *120*, 143–164.

[41] D. N. Burrows et al., “The Swift X-Ray Telescope”, *Space Science Reviews* **2005**, *120*, 165–195.

[42] P. W. A. Roming et al., “The Swift Ultra-Violet/Optical Telescope”, *Space Science Reviews* **2005**, *120*, 95–142.

[43] N. Gehrels et al., “The Swift Gamma-Ray Burst Mission”, *Astrophysical Journal* **2004**, *611*, 1005–1020.

[44] A. von Kienlin et al., “The Fourth Fermi-GBM Gamma-Ray Burst Catalog: A Decade of Data”, *Astrophysical Journal* **2020**, *893*, 46.

[45] C. Meegan et al., "The Fermi Gamma-ray Burst Monitor", *Astrophyisical Journal* **2009**, *702*, 791–804.

[46] M. Ajello et al., "A Decade of Gamma-Ray Bursts Observed by Fermi-LAT: The Second GRB Catalog", *The Astrophysical Journal* **2019**, *878*, 52.

[47] A. A. Abdo et al., "Fermi Observations of High-Energy Gamma-Ray Emission from GRB 080916C", *Science* **2009**, *323*, 1688.

[48] M. Ackermann et al., "Fermi Observations of GRB 090510: A Short-Hard Gamma-ray Burst with an Additional, Hard Power-law Component from 10 keV TO GeV Energies", *Astrophysical Journal* **2010**, *716*, 1178–1190.

[49] M. Ackermann et al., "Fermi-LAT Observations of the Gamma-Ray Burst GRB 130427A", *Science* **2014**, *343*, 42–47.

[50] S. Lesage et al., "Fermi-GBM Discovery of GRB 221009A: An Extraordinarily Bright GRB from Onset to Afterglow", *The Astrophysical Journal Letters* **2023**, *952*, L42.

[51] P. Meszaros, M. J. Rees, "Relativistic Fireballs and Their Impact on External Matter: Models for Cosmological Gamma-Ray Bursts", *The Astrophysical Jounal* **1993**, *405*, 278.

[52] T. Piran, A. Shemi, R. Narayan, "Hydrodynamics of relativistic fireballs", *Monthly Notices of the Royal Astronomical Society* **1993**, *263*, 861–867.

[53] E. Waxman, T. Piran, "Stability of Fireballs and Gamma-Ray Bursts", *Astrophysical Journal Letters* **1994**, *433*, L85.

[54] S. Kobayashi, R. Sari in Gamma-Ray Bursts: The First Three Minutes, (Eds.: J. Poutanen, R. Svensson), **1999**, p. 201.

[55] A. Gomboc, "Unveiling the secrets of gamma ray bursts", *Contemporary Physics* **2012**, *53*, 339–355.

[56] B. ZHANG, P. MÉSZÁROS, "GAMMA-RAY BURSTS: PROGRESS, PROBLEMS & PROSPECTS", *International Journal of Modern Physics A* **2004**, *19*, 2385–2472.

[57] M. J. Rees, P. Meszaros, "Unsteady Outflow Models for Cosmological Gamma-Ray Bursts", *Astrophysical Journal Letters* **1994**, *430*, L93.

[58] M. Lyutikov, R. Blandford, "Gamma Ray Bursts as Electromagnetic Outflows", *arXiv e-prints* **2003**, astro–ph/0312347.

[59] J. C. McKinney, D. A. Uzdensky, "A reconnection switch to trigger gamma-ray burst jet dissipation", *Monthly Notices of the Royal Astronomical Society* **2011**, *419*, 573–607.

[60] B.-B. Zhang et al., “A COMPREHENSIVE ANALYSIS OF FERMI GAMMA-RAY BURST DATA. I. SPECTRAL COMPONENTS AND THE POSSIBLE PHYSICAL ORIGINS OF LAT/GBM GRBs”, *The Astrophysical Journal* **2011**, *730*, 141.

[61] R. Sari, T. Piran, R. Narayan, “Spectra and Light Curves of Gamma-Ray Burst Afterglows”, *Astrophysical Journal Letters* **1998**, *497*, L17–L20.

[62] P. Kumar, “Gamma-Ray Burst Energetics”, *Astrophysical Journal Letters* **1999**, *523*, L113–L116.

[63] A. Panaitescu, M. Spada, P. Mészáros, “Power Density Spectra of Gamma-Ray Bursts in the Internal Shock Model”, *The Astrophysical Journal* **1999**, *522*, L105.

[64] L. Nava et al., “Clustering of LAT light curves: a clue to the origin of high-energy emission in gamma-ray bursts”, *Monthly Notices of the Royal Astronomical Society* **2014**, *443*, 3578–3585.

[65] W. Fong et al., “A Decade of Short-duration Gamma-Ray Burst Broadband Afterglows: Energetics, Circumburst Densities, and Jet Opening Angles”, *Astrophysical Journal* **2015**, *815*, 102.

[66] P. Beniamini et al., “Energies of GRB blast waves and prompt efficiencies as implied by modelling of X-ray and GeV afterglows”, *Monthly Notices of the Royal Astronomical Society* **2015**, *454*, 1073–1085.

[67] B. Zhang, H. Yan, “The Internal-collision-induced Magnetic Reconnection and Turbulence (ICMART) Model of Gamma-ray Bursts”, *Astrophysical Journal* **2011**, *726*, 90.

[68] B. Zhang, B. Zhang, “Gamma-Ray Burst Prompt Emission Light Curves and Power Density Spectra in the ICMART Model”, *Astrophysical Journal* **2014**, *782*, 92.

[69] K. Toma et al., “STATISTICAL PROPERTIES OF GAMMA-RAY BURST POLARIZATION”, *The Astrophysical Journal* **2009**, *698*, 1042.

[70] W. Coburn, S. E. Boggs, “Polarization of the prompt γ-ray emission from the γ-ray burst of 6 December 2002”, *Nature* **2003**, *423*, 415–417.

[71] M. Kole et al., “The POLAR gamma-ray burst polarization catalog”, *Astronomy & Astrophysics* **2020**, *644*, A124.

[72] D. R. Willis et al., “Evidence of polarisation in the prompt gamma-ray emission from GRB 930131 and GRB 960924”, *Astronomy & Astrophysics* **2005**, *439*, 245–253.

[73] D. Yonetoku et al., “Detection of Gamma-Ray Polarization in Prompt Emission of GRB 100826A”, *Astrophysical Journal Letters* **2011**, *743*, L30.

[74] H. Gao et al., “A MORPHOLOGICAL ANALYSIS OF GAMMA-RAY BURST EARLY-OPTICAL AFTERGLOWS”, *The Astrophysical Journal* **2015**, *810*, 160.

[75] A. Pe’er, “Physics of Gamma-Ray Bursts Prompt Emission”, *Advances in Astronomy* **2015**, *2015*, 907321.

[76] M. S. Briggs et al., “Observations of GRB 990123 by the Compton Gamma Ray Observatory”, *The Astrophysical Journal* **1999**, *524*, 82.

[77] R. D. Preece et al., “The BATSE Gamma-Ray Burst Spectral Catalog. I. High Time Resolution Spectroscopy of Bright Bursts Using High Energy Resolution Data”, *The Astrophysical Journal Supplement Series* **2000**, *126*, 19.

[78] L. Nava et al., “Spectral properties of 438 GRBs detected by Fermi/GBM”, *Astronomy & Astrophysics Journal* **2011**, *530*, A21.

[79] D. Gruber et al., “The Fermi GBM Gamma-Ray Burst Spectral Catalog: Four Years of Data”, *The Astrophysical Journal Supplement Series* **2014**, *211*, 12.

[80] S. Campana et al., “The association of GRB 060218 with a supernova and the evolution of the shock wave”, *Nature* **2006**, *442*, 1008–1010.

[81] M. Axelsson et al., “GRB110721A: An Extreme Peak Energy and Signatures of the Photosphere”, *Astrophysical Journal Letters* **2012**, *757*, L31.

[82] P. Mészáros, “Theories of Gamma-Ray Bursts”, *Annual Review of Astronomy and Astrophysics* **2002**, *40*, 137–169.

[83] B. Zhang, A. Pe’er, “EVIDENCE OF AN INITIALLY MAGNETICALLY DOMINATED OUTFLOW IN GRB 080916C”, *The Astrophysical Journal* **2009**, *700*, L65.

[84] J. M. Burgess et al., “TIME-RESOLVED ANALYSIS OF FERMI GAMMA-RAY BURSTS WITH FAST- AND SLOW-COOLED SYNCHROTRON PHOTON MODELS”, *The Astrophysical Journal* **2014**, *784*, 17.

[85] M. J. Rees, P. Meszaros, “Relativistic fireballs - Energy conversion and time-scales.”, *Monthly Notices of the Royal Astronomical Society* **1992**, *258*, 41.

[86] B. Paczynski, J. E. Rhoads, “Radio Transients from Gamma-Ray Bursters”, *Astrophysical Journal Letters* **1993**, *418*, L5.

[87] P. Mészáros, M. J. Rees, R. A. M. J. Wijers, “Viewing Angle and Environment Effects in Gamma-Ray Bursts: Sources of Afterglow Diversity”, *The Astrophysical Journal* **1998**, *499*, 301.

[88] R. A. Chevalier, Z.-Y. Li, “Wind Interaction Models for Gamma-Ray Burst Afterglows: The Case for Two Types of Progenitors”, *Astrophysical Journal* **2000**, *536*, 195–212.

[89] H. Gao et al., “A complete reference of the analytical synchrotron external shock models of gamma-ray bursts”, *Nucleic Acids Research* **2013**, *57*, 141–190.

[90] B. Zhang et al., “Physical Processes Shaping Gamma-Ray Burst X-Ray Afterglow Light Curves: Theoretical Implications from the Swift X-Ray Telescope Observations”, *Astrophysical Journal* **2006**, *642*, 354–370.

[91] G. Ryan et al., “Gamma-Ray Burst Afterglows in the Multimessenger Era: Numerical Models and Closure Relations”, *The Astrophysical Journal* **2020**, *896*, 166.

[92] R. D. Blandford, C. F. McKee, “Fluid dynamics of relativistic blast waves”, *Physics of Fluids* **1976**, *19*, 1130–1138.

[93] T. Piran, J. Granot in Gamma-ray Bursts in the Afterglow Era, (Eds.: E. Costa, F. Frontera, J. Hjorth), **2001**, p. 300.

[94] R. Gill, J. Granot, P. Beniamini, “GRB spectrum from gradual dissipation in a magnetized outflow”, *Monthly Notices of the Royal Astronomical Society* **2020**, *499*, 1356–1372.

[95] A. Lien et al., “The Third Swift Burst Alert Telescope Gamma-Ray Burst Catalog”, *Astrophysical Journal* **2016**, *829*, 7.

[96] E. Troja et al., “Swift Observations of GRB 070110: An Extraordinary X-Ray Afterglow Powered by the Central Engine”, *Astrophysical Journal* **2007**, *665*, 599–607.

[97] J. E. Rhoads, “The Dynamics and Light Curves of Beamed Gamma-Ray Burst Afterglows”, *The Astrophysical Journal* **1999**, *525*, 737.

[98] X.-G. Wang et al., “Gamma-Ray Burst Jet Breaks Revisited”, *The Astrophysical Journal* **2018**, *859*, 160.

[99] D. A. Frail et al., “Beaming in Gamma-Ray Bursts: Evidence for a Standard Energy Reservoir”, *Astrophysical Journal Letters* **2001**, *562*, L55–L58.

[100] A. D. Falcone et al., “The First Survey of X-Ray Flares from Gamma-Ray Bursts Observed by Swift: Spectral Properties and Energetics”, *The Astrophysical Journal* **2007**, *671*, 1921.

[101] R. Margutti, “Lag-luminosity relation in gamma-ray burst X-ray flares”, *AIP Conference Proceedings* **2010**, *1279*, 372–375.

[102] E. Kuulkers et al., “GRB 990510: On the Possibility of a Beamed X-Ray Afterglow”, *Astrophysical Journal* **2000**, *538*, 638–644.

[103] A. J. Castro-Tirado et al., “The Burst Observer and Optical Transient Exploring System (BOOTES)”, *Astronomy and Astrophysics Supplemments Serries* **1999**, *138*, 583–585.

[104] A. Panaitescu, W. T. Vestrand, “Optical afterglows of gamma-ray bursts: peaks, plateaus and possibilities”, *Monthly Notices of the Royal Astronomical Society* **2011**, *414*, 3537–3546.

[105] X.-G. Wang et al., “How Bad or Good Are the External Forward Shock Afterglow Models of Gamma-Ray Bursts?”, *Astrophysical Journal Series* **2015**, *219*, 9.

[106] J. Gorosabel, A. J. Castro-Tirado, “Archival searches for transient optical emission in the error box of the 1991 January 22 gamma-ray burst”, *Astronomy and Astrophysics* **1998**, *337*, 691–698.

[107] E. Berger et al., “The Faint Optical Afterglow and Host Galaxy of GRB 020124: Implications for the Nature of Dark Gamma-Ray Bursts”, *Astrophysical Journal* **2002**, *581*, 981–987.

[108] P. Jakobsson et al., “Swift Identification of Dark Gamma-Ray Bursts”, *Astrophysical Journal Letters* **2004**, *617*, L21–L24.

[109] A. J. van der Horst et al., “Optical Classification of Gamma-Ray Bursts in the Swift Era”, *Astrophysical Journal* **2009**, *699*, 1087–1091.

[110] G. E. Anderson et al., “Probing the bright radio flare and afterglow of GRB 130427A with the Arcminute Microkelvin Imager”, *Monthly Notices of the Royal Astronomical Society* **2014**, *440*, 2059–2065.

[111] M. Lyutikov, “Magnetic fields in GRBs”, *Advances in Space Research* **2006**, *38*, Galactic and Extragalactic Astrophysics, 1276–1280.

[112] E. S. Weibel, “Spontaneously Growing Transverse Waves in a Plasma Due to an Anisotropic Velocity Distribution”, *Phys. Rev. Lett.* **1959**, *2*, 83–84.

[113] M. V. Medvedev, A. Loeb, “Generation of magnetic fields in the relativistic shock of gamma-ray burst sources”, *Astrophysical Journal* **1999**, *526*, Cited by: 700; All Open Access, Bronze Open Access, Green Open Access, 697 – 706.

[114] Y. Lyubarsky, D. Eichler, “Are Gamma-Ray Burst Shocks Mediated by the Weibel Instability?”, *The Astrophysical Journal* **2005**, *647*, 1250 –1254.

[115] A. Bret, A. Pe’er, “On the formation and properties of fluid shocks and collisionless shock waves in astrophysical plasmas”, *Journal of Plasma Physics* **2018**, *84*, 905840311.

[116] M. S. Longair, *High Energy Astrophysics*, **2011**.

[117] G. B. Rybicki, A. P. Lightman, *Radiative Processes in Astrophysics*, **1986**.

[118] J. Hinton, W. Hofmann, “Teraelectronvolt Astronomy”, *Annual Review of Astronomy and Astrophysics* **2009**, *47*, 523–565.

[119] G. R. BLUMENTHAL, R. J. GOULD, “Bremsstrahlung, Synchrotron Radiation, and Compton Scattering of High-Energy Electrons Traversing Dilute Gases”, *Rev. Mod. Phys.* **1970**, *42*, 237–270.

[120] E. L. Ruiz Velasco, *Search and first detection of very-high-energy photons in gamma-ray bursts: an analysis with HAWC and HESS*, Heidelberg, **2021**, 1 online resource (VIII, 229 pages).

[121] H. Bradt, *Astrophysics Processes: The Physics of Astronomical Phenomena*, Cambridge University Press, **2008**.

[122] LHAASO Collaboration et al., “A tera-electron volt afterglow from a narrow jet in an extremely bright gamma-ray burst.”, *Science* **2023**, *380*, 1390–1396.

[123] C. Winkler, “The INTEGRAL mission”, *Experimental Astronomy* **1995**, *6*, 71–76.

[124] A. A. Abdo et al., “Fermi/Large Area Telescope Bright Gamma-Ray Source List”, *The Astrophysical Journal Supplement Series* **2009**, *183*, 46–66.

[125] L. Nava et al., “Constraints on the bulk Lorentz factor of gamma-ray burst jets from Fermi /LAT upper limits”, *The Monthly Notices of the Royal Astronomical Society* **2017**, *465*, 811–819.

[126] MAGIC Collaboration et al., “Teraelectronvolt emission from the γ-ray burst GRB 190114C”, *Nature* **2019**, *575*, 455–458.

[127] S. Ando, E. Nakar, R. Sari, “GeV Emission from Prompt and Afterglow Phases of Gamma-Ray Bursts”, *The Astrophysical Journal* **2008**, *689*, 1150.

[128] MAGIC Collaboration et al., “Observation of inverse Compton emission from a long γ-ray burst”, *Nature* **2019**, *575*, 459–463.

[129] S. Gagliardini et al., “On the hadronic origin of the TeV radiation from GRB 190114C”, *arXiv e-prints* **2022**, arXiv:2209.01940.

[130] B. Zhang, P. Mészáros, “Gamma-Ray Burst Afterglow with Continuous Energy Injection: Signature of a Highly Magnetized Millisecond Pulsar”, *Astrophysical Journal Letters* **2001**, *552*, L35–L38.

[131] M. G. Hauser, E. Dwek, “The Cosmic Infrared Background: Measurements and Implications”, *Annual Review of Astronomy and Astrophysics* **2001**, *39*, 249–307.

[132] A. I. Nikishov, “ABSORPTION OF HIGH ENERGY PHOTONS IN THE UNIVERSE”, *Zhur. Eksptl'. i Teoret. Fiz.* **1961**, *Vol: 41.*

[133] R. J. Gould, G. P. Schréder, “Pair Production in Photon-Photon Collisions”, *Phys. Rev.* **1967**, *155*, 1404–1407.

[134] J. V. Jelley, “High-Energy γ-Ray Absorption in Space by a 3.5°K Microwave Field”, *Phys. Rev. Lett.* **1966**, *16*, 479–481.

[135] A. Franceschini, G. Rodighiero, “The extragalactic background light revisited and the cosmic photon-photon opacity”, *aap* **2017**, *603*, A34.

[136] R. C. Gilmore et al., “Semi-analytic modelling of the extragalactic background light and consequences for extragalactic gamma-ray spectra”, *Monthly Notices of the Royal Astronomical Society* **2012**, *422*, 3189–3207.

[137] A. Domínguez et al., “Extragalactic background light inferred from AEGIS galaxy-SED-type fractions”, *Monthly Notices of the Royal Astronomical Society* **2011**, *410*, 2556–2578.

[138] J. D. Finke, S. Razzaque, C. D. Dermer, “Modeling the Extragalactic Background Light from Stars and Dust”, *Astrophysics journal* **2010**, *712*, 238–249.

[139] E. Waxman, J. Bahcall, “High Energy Neutrinos from Cosmological Gamma-Ray Burst Fireballs”, *Physical Review Letters* **1997**, *78*, 2292–2295.

[140] P. Mészáros, “Astrophysical Sources of High-Energy Neutrinos in the IceCube Era”, *Annual Review of Nuclear and Particle Science* **2017**, *67*, 45–67.

[141] M. G. Aartsen et al., “Observation and Characterization of a Cosmic Muon Neutrino Flux from the Northern Hemisphere Using Six Years of IceCube Data”, *Astroparticle Journal* **2016**, *833*, 3.

[142] B. P. Abbott et al., “GW170817: Observation of Gravitational Waves from a Binary Neutron Star Inspiral”, *Phys. Rev. Lett.* **2017**, *119*, 161101.

[143] A. Goldstein et al., “An Ordinary Short Gamma-Ray Burst with Extraordinary Implications: Fermi-GBM Detection of GRB 170817A”, *Astropysical Journal letters* **2017**, *848*, L14.

[144] M. M. Kasliwal et al., “Illuminating gravitational waves: A concordant picture of photons from a neutron star merger”, *Science* **2017**, *358*, 1559–1565.

[145] E. Troja et al., “The X-ray counterpart to the gravitational-wave event GW170817”, *nature* **2017**, *551*, 71–74.

[146] H. Abdalla et al., “TeV Gamma-Ray Observations of the Binary Neutron Star Merger GW170817 with H.E.S.S.”, *Astrophysical Journal Letters* **2017**, *850*, L22.

[147] R. Salvaterra, “High redshift Gamma-Ray Bursts”, *Journal of High Energy Astrophysics* **2015**, *7*, 35–43.

[148] V. F. Hess, “Über Beobachtungen der durchdringenden Strahlung bei sieben Freiballonfahrten”, *Phys. Z.* **1912**, *13*, 1084–1091.

[149] W. Bothe, W. Kolhörster, “Das Wesen der Höhenstrahlung”, *Zeitschrift für Physik* **1929**, *56*, 751–777.

[150] C. Evoli, The Cosmic-Ray Energy Spectrum, **2020**.

[151] A. M. Hillas, “The Origin of Ultra-High-Energy Cosmic Rays”, *Annual Review of Astronomy and Astrophysics* **1984**, *22*, 425–444.

[152] J. Matthews, “A Heitler model of extensive air showers”, *Astroparticle Physics* **2005**, *22*, 387–397.

[153] K. Kamata, J. Nishimura, “The Lateral and the Angular Structure Functions of Electron Showers”, *Progress of Theoretical Physics Supplement* **1958**, *6*, 93–155.

[154] J. Nishimura in *Kosmische Strahlung II / Cosmic Rays II*, (Ed.: K. Sitte), Springer Berlin Heidelberg, Berlin, Heidelberg, **1967**, pp. 1–114.

[155] J. K. Fabian Schmidt, CORSIKA Shower Images, **2005**, `https://www-zeuthen.desy.de/~jknapp/fs/showerimages.html` (visited on 09/11/2023).

[156] P. A. Cherenkov, “Visible Radiation Produced by Electrons Moving in a Medium with Velocities Exceeding that of Light”, *Phys. Rev.* **1937**, *52*, 378–379.

[157] A. C, Geometry of Cherenkov radiation, **2024**, `https://www.physicsforums.com/threads/geometry-of-cherenkov-radiation.1058851/`.

[158] J. D. Jackson, *Classical Electrodynamics*, Wiley, **1998**.

[159] M. de Naurois, “Blue light in the desert night”, *Nature Astronomy* **2018**, *2*, 593–593.

[160] C. Hoischen et al., “The H.E.S.S. transients follow-up system”, *Asttronomy & Astrophysics* **2022**, *666*, A119.

[161] P. Hofverberg et al. in International Cosmic Ray Conference, **2013**, p. 3092.

[162] A Balzer et al., “The H.E.S.S. data acquisition system”, *Journal of Physics: Conference Series* **2014**, *513*, 012003.

[163] R. Chalme-Calvet, M. de Naurois, J. P. Tavernet, “Muon efficiency of the H.E.S.S. telescope”, *arXiv e-prints* **2014**, arXiv:1403.4550.

[164] F. A. Aharonian, *Very high energy cosmic gamma radiation : a crucial window on the extreme Universe*, **2004**.

[165] F. Aharonian et al., “Observations of the Crab nebula with HESS”, *Astronomy & Astrophysics* **2006**, *457*, 899–915.

[166] M. Haupt, doctoralthesis, Universität Potsdam, **2020**, pp. iv, 182.

[167] M. K. Daniel, (for the CTA Consortium), "The Atmospheric Monitoring Strategy for the Cherenkov Telescope Array", *Journal of Physics: Conference Series* **2015**, *595*, 012009.

[168] J. Hahn et al., "Impact of aerosols and adverse atmospheric conditions on the data quality for spectral analysis of the H.E.S.S. telescopes", *Astroparticle Physics* **2014**, *54*, 25–32.

[169] A. M. Hillas in 19th International Cosmic Ray Conference (ICRC19), Volume 3, **1985**, p. 445.

[170] M. de Naurois in 7th Workshop on Towards a Network of Atmospheric Cherenkov Detectors 2005, **2006**, pp. 149–161.

[171] F. Aharonian et al., "Observations of the Crab nebula with HESS", *Astronomy & Astrophysics* **2006**, *457*, 899–915.

[172] M. de Naurois, Habilitation à diriger des recherches, Université Pierre et Marie Curie - Paris VI, **2012**.

[173] R. D. Parsons, J. A. Hinton, "A Monte Carlo template based analysis for air-Cherenkov arrays", *Astroparticle Physics* **2014**, *56*, 26–34.

[174] F. Aharonian et al., "Observations of the Crab nebula with HESS", *Astronomy and Astrophysics* **2006**, *457*, 899–915.

[175] S. Ohm, C. van Eldik, K. Egberts, "γ/hadron separation in very-high-energy γ-ray astronomy using a multivariate analysis method", *Astroparticle Physics* **2009**, *31*, 383–391.

[176] D. Berge, S. Funk, J. Hinton, "Background modelling in very-high-energy γ-ray astronomy", *Astronomy & Astrophysics* **2007**, *466*, 1219–1229.

[177] T.-P. Li, Y. Ma, "Analysis methods for results in gamma-ray astronomy", *Astrophysical Journal* **1983**, *272*, 317–324.

[178] S. Hoppe, PhD Thesis, Ruprecht-Karls Universität, Heidelberg, Germany, **2008**.

[179] F. Aharonian et al., "A low level of extragalactic background light as revealed by γ-rays from blazars", *nature* **2006**, *440*, 1018–1021.

[180] F. Acero et al., "Gammapy: Python toolbox for gamma-ray astronomy", **2022**, If you use this software, please cite it using the metadata from this file., DOI `10.5281/zenodo.7311399`.

[181] A. Donath et al., "Gammapy: A Python package for gamma-ray astronomy", *Astronomy & Astrophysics* **2023**, *678*, A157.

[182] Astropy Collaboration et al., “Astropy: A community Python package for astronomy”, *Astronomy & Astrophysics* **2013**, *558*, A33.

[183] H. Dembinski et al., *iminuit: Jupyter-friendly Python interface for C++ MINUIT2*, Astrophysics Source Code Library, record ascl:2108.024, **2021**.

[184] D. Burke et al., *sherpa/sherpa: Sherpa 4.16.0*, version 4.16.0, **2023**.

[185] M. De Naurois, “The H.E.S.S. experiment : current status and future prospects”, *PoS* **2020**, *ICRC2019*, 656.

[186] R. Chalmé-Calvet et al. in 34th International Cosmic Ray Conference (ICRC2015), **2015**, 842, p. 842.

[187] G. Giavitto et al., “The upgrade of the H.E.S.S. cameras”, *Nuclear Instruments and Methods in Physics Research Section A: Accelerators Spectrometers Detectors and Associated Equipment* **2017**, *876*, The 9th international workshop on Ring Imaging Cherenkov Detectors (RICH2016), 35–38.

[188] T. Ashton et al., “A NECTAr-based upgrade for the Cherenkov cameras of the H.E.S.S. 12-meter telescopes”, *Astroparticle Physics* **2020**, *118*, 102425.

[189] F. Bradascio et al., “H.E.S.S. realtime follow-ups of IceCube high-energy neutrino alerts”, *PoS* **2023**, *ICRC2023*, 1546.

[190] A. Acharyya et al., “Multiwavelength Observations of the Blazar PKS 0735+178 in Spatial and Temporal Coincidence with an Astrophysical Neutrino Candidate IceCube-211208A”, *The Astrophysical Journal* **2023**, *954*, 70.

[191] H. Ashkar et al., “The H.E.S.S. gravitational wave rapid follow-up program”, *Journal of Cosmology and Astroparticle Physics* **2021**, *2021*, 045.

[192] M. Ackermann et al., “Fermi-LAT Observations of the Gamma-Ray Burst GRB 130427A”, *Science* **2014**, *343*, 42–47.

[193] A. Domínguez et al., “Extragalactic background light inferred from AEGIS galaxy-SED-type fractions”, *Monthly Notices of the Royal Astronomical Society* **2011**, *410*, 2556–2578.

[194] F. Aharonian et al. (H.E.S.S. Collaboration), “H.E.S.S. Follow-up Observations of GRB 221009A”, *The Astrophysical Journal Letters* **2023**, *946*, L27.

[195] J. D. Mbarubucyeye et al., “H.E.S.S. follow-up observations of GRB 221009A”, *PoS* **2023**, *ICRC2023*, 705.

[196] A. von Kienlin et al., “The Fourth Fermi-GBM Gamma-Ray Burst Catalog: A Decade of Data”, *Astrophysical Journal* **2020**, *893*, 46.

[197] P. A. Evans et al., “Methods and results of an automatic analysis of a complete sample of Swift-XRT observations of GRBs”, *Monthly Notices of the Royal Astronomical Society* **2009**, *397*, 1177–1201.

[198] P. Veres et al., “GRB 221009A: Fermi GBM detection of an extraordinarily bright GRB”, *GRB Coordinates Network* **2022**, *32636*, 1.

[199] M. A. Williams et al., “GRB 221009A: Discovery of an Exceptionally Rare Nearby and Energetic Gamma-Ray Burst”, *AstroPhysical Journal Letter* **2023**, *946*, L24.

[200] S. Dichiara et al., “Swift J1913.1+1946 a new bright hard X-ray and optical transient”, *GRB Coordinates Network* **2022**, *32632*, 1.

[201] Z. Cao et al., “Very high-energy gamma-ray emission beyond 10 TeV from GRB 221009A”, *Science Advances* **2023**, *9*, eadj2778.

[202] Y. Huang et al., “LHAASO observed GRB 221009A with more than 5000 VHE photons up to around 18 TeV”, *GRB Coordinates Network* **2022**, *32677*, 1.

[203] A. de Ugarte Postigo et al., “GRB 221009A: Redshift from X-shooter/VLT”, *GRB Coordinates Network* **2022**, *32648*, 1.

[204] D. Frederiks et al., “Properties of the Extremely Energetic GRB 221009A from Konus-WIND and SRG/ART-XC Observations”, *Astrophysical Journal Letters* **2023**, *949*, L7.

[205] E. B. et. al., “GRB 221009A: The BOAT”, *The Astrophysical Journal Letters* **2023**, *946*, L31.

[206] A. Tiengo et al., “Swift/XRT discovery of multiple dust-scattering X-ray rings around GRB 221009A”, *The Astronomer’s Telegram* **2022**, *15661*, 1.

[207] KM3NeT Collaboration, “GRB 221009A: search for neutrinos with KM3NeT”, *GRB Coordinates Network* **2022**, *32741*, 1.

[208] IceCube Collaboration, “GRB 221009A: Upper limits from a neutrino search with IceCube”, *GRB Coordinates Network* **2022**, *32665*, 1.

[209] A. J. Levan et al., “The First JWST Spectrum of a GRB Afterglow: No Bright Supernova in Observations of the Brightest GRB of all Time, GRB 221009A”, *Astrophysical Journal Letters* **2023**, *946*, L28.

[210] M. D. Fulton et al., “The Optical Light Curve of GRB 221009A: The Afterglow and the Emerging Supernova”, *Astrophysical Journal Letters* **2023**, *946*, L22.

[211] A. J. Levan et al., “GRB 221009A: Hubble Space Telescope observations”, *GRB Coordinates Network* **2022**, *32921*, 1.

[212] A. J. Levan et al., “GRB 221009A: James Webb Space Telescope Observations”, *GRB Coordinates Network* **2022**, *32821*, 1.

[213] M. Williams, Swift Team, “GRB 221009A: Continued Swift Observations”, *GRB Coordinates Network* **2023**, *33305*, 1.

[214] L. Tomankova et al., “Gain settings for the upgraded H.E.S.S. CT1-4 cameras under moonlight observations”, *Zenodo* **2022**, *https://doi.org/10.5281/zenodo.7400326*, DOI `10.5281/zenodo.7400326`.

[215] P. Formenti et al., “The Aerosols, Radiation and Clouds in Southern Africa Field Campaign in Namibia: Overview, Illustrative Observations, and Way Forward”, *Bulletin of the American Meteorological Society* **2019**, *100*, 1277 –1298.

[216] M. de Naurois, L. Rolland, “A high performance likelihood reconstruction of γ-rays for imaging atmospheric Cherenkov telescopes”, *Astroparticle Physics* **2009**, *32*, 231–252.

[217] T. L. Holch et al., “Assessing aerosol induced errors in Monte Carlo based air-shower reconstruction for atmospheric Cherenkov detectors”, *Journal of Physics: Conference Series* **2022**, *2398*, 012017.

[218] M. Holler et al., “A run-wise simulation and analysis framework for Imaging Atmospheric Cherenkov Telescope arrays”, *Astroparticle Physics* **2020**, *123*, 102491.

[219] C. Deil et al., Data formats for gamma-ray astronomy - version 0.3, **2022**.

[220] M. Ajello et al., “A Decade of Gamma-Ray Bursts Observed by Fermi-LAT: The Second GRB Catalog”, *Astrophysical Journal* **2019**, *878*, 52.

[221] W. A. Rolke, A. M. López, J. Conrad, “Limits and confidence intervals in the presence of nuisance parameters”, *Nuclear Instruments and Methods in Physics Research A* **2005**, *551*, 493–503.

[222] A. Tiengo et al., “Swift/XRT discovery of multiple dust-scattering X-ray rings around GRB 221009A”, *GRB Coordinates Network* **2022**, *32680*, 1.

[223] P. A. Evans, private communication, **2022**.

[224] R. Willingale et al., “Calibration of X-ray absorption in our Galaxy”, *Monthly Notices of the Royal Astronomical Society* **2013**, *431*, 394–404.

[225] S. Campana et al., “The variable absorption in the X-ray spectrum of GRB 190114C”, *Astronomy & Astrophysics* **2021**, *649*, A135.

[226] P. A. Evans et al., “The Swift Burst Analyser. I. BAT and XRT spectral and flux evolution of gamma ray bursts”, *Astronomy & Astrophysics* **2010**, *519*, A102.

[227] G. Vianello, *gtburst: Release for Zenodo*, version 02-01-03, **2016**.

[228] S. Abdollahi et al., “Fermi Large Area Telescope Fourth Source Catalog”, *The Astrophysical Journal Supplement Series* **2020**, *247*, 33.

[229] Z. Cao et al., “A tera–electron volt afterglow from a narrow jet in an extremely bright gamma-ray burst”, *Science* **2023**, *0*, eadg9328.

[230] H. Ayala, HAWC Collaboration, “GRB 221009A: Upper limits from HAWC 8 hours after trigger”, *GRB Coordinates Network* **2022**, *32683*, 1.

[231] Z.-Q. Huang et al., “The Implications of TeV-detected GRB Afterglows for Acceleration at Relativistic Shocks”, *The Astrophysical Journal* **2022**, *925*, 182.

[232] E. Cohen, T. Piran, “Radiative Efficiencies of Continuously Powered Blast Waves”, *The Astrophysical Journal* **1999**, *518*, 346.

[233] B. Zhang, P. Mészáros, “Gamma-Ray Burst Afterglow with Continuous Energy Injection: Signature of a Highly Magnetized Millisecond Pulsar”, *The Astrophysical Journal Letters* **2001**, *552*, L35–L38.

[234] Z. G. Dai, T. Lu, “Gamma-ray burst afterglows and evolution of postburst fireballs with energy injection from strongly magnetic millisecond pulsars”, *Astronomy & Astrophysics* **1998**, *333*, L87–L90.

[235] M. D. Fulton et al., The optical light curve of GRB 221009A: the afterglow and detection of the emerging supernova SN 2022xiw, https://arxiv.org/abs/2301.11170, **2023**.

[236] L. Rhodes, K. Huang, Y. Cendes, “GRB 221009A/Swift J1913.1+1946: SMA observations”, *GRB Coordinates Network* **2022**, *32707*, 1.

[237] T. Laskar et al., “The Radio to GeV Afterglow of GRB 221009A”, *The Astrophysical Journal Letters* **2023**, *946*, L23.

[238] L. Muijres et al., “Mass-loss predictions for evolved very metal-poor massive stars”, *Astronomy & Astrophysics* **2012**, *546*, A42.

[239] L. Rhodes, K. Huang, Y. Cendes, “GRB 221009A/Swift J1913.1+1946: SMA observations”, *GRB Coordinates Network* **2022**, *32707*, 1.

[240] M. D. Fulton et al., The optical light curve of GRB 221009A: the afterglow and detection of the emerging supernova SN 2022xiw, https://arxiv.org/abs/2301.11170, **2023**.

[241] C. Hoischen et al. in 35th International Cosmic Ray Conference (ICRC2017), **2017**, 636, p. 636.

[242] F. Aharonian et al. (H.E.S.S. Collaboration, in prep), “10 years of GRB observations with the H.E.S.S. telescopes”, *Astronomy and Astrophysics* **2025**.

[243] Planck Collaboration et al., “Planck 2018 results. VI. Cosmological parameters”, *Astronomy & Astrophysics* **2020**, *641*, A6.

[244] E. Sonbas et al., “GRB 190627A: Swift detection of a burst.”, *GRB Coordinates Network* **2019**, *24888*, 1.

[245] S. D. Barthelmy et al., “GRB 190627A: Swift-BAT refined analysis (short-soft burst).”, *GRB Coordinates Network* **2019**, *24899*, 1.

[246] J. Japelj et al., “GRB 190627A: VLT/FORS2 spectroscopic redshift.”, *GRB Coordinates Network* **2019**, *24916*, 1.

[247] F. E. Marshall et al., “GRB 201024A: Swift detection of a burst with an optical afterglow”, *GRB Coordinates Network* **2020**, *28761*, 1.

[248] A. de Ugarte Postigo et al., “GRB 201024A: Redshift from GTC/OSIRIS”, *GRB Coordinates Network* **2020**, *28764*, 1.

[249] T. N. Ukwatta et al., “GRB 201024A: Swift-BAT refined analysis”, *GRB Coordinates Network* **2020**, *28778*, 1.

[250] C. Malacaria, B. Hristov, Fermi GBM Team, “GRB 210610B: Fermi GBM detection”, *GRB Coordinates Network* **2021**, *30199*, 1.

[251] K. L. Page et al., “GRB 210610B: Swift detection of a burst with bright optical afterglow”, *GRB Coordinates Network* **2021**, *30170*, 1.

[252] J. P. U. Fynbo et al., “GRB 210610B: NOT optical observations and tentative redshift”, *GRB Coordinates Network* **2021**, *30182*, 1.

[253] A. de Ugarte Postigo et al., “GRB 210610B: Redshift confirmation from GTC”, *GRB Coordinates Network* **2021**, *30194*, 1.

[254] P. D’Avanzo et al., “GRB 210619B: Swift detection of a bright burst and optical counterpart”, *GRB Coordinates Network* **2021**, *30261*, 1.

[255] S. Poolakkil, C. Meegan, Fermi GBM Team, “GRB 210619B: Fermi GBM detection”, *GRB Coordinates Network* **2021**, *30279*, 1.

[256] M. Axelsson et al., “GRB 210619B: Fermi-LAT detection”, *GRB Coordinates Network* **2021**, *30270*, 1.

[257] D. Svinkin et al., “Konus-Wind detection of GRB 210619B”, *GRB Coordinates Network* **2021**, *30276*, 1.

[258] A. de Ugarte Postigo et al., “GRB 210619B: Redshift from OSIRIS/GTC”, *GRB Coordinates Network* **2021**, *30272*, 1.

[259] M. D. Caballero-García et al., “Multiwavelength study of the luminous GRB 210619B observed with Fermi and ASIM”, *The Monthly Notices of the Royal Astronomical Society* **2023**, *519*, 3201–3226.

[260] M. Stamatikos et al., “GRB 210731A: Swift-BAT refined analysis”, *GRB Coordinates Network* **2021**, *30580*, 1.

[261] S. Lesage, C. Meegan, Fermi Gamma-ray Burst Monitor Team, “GRB 210731A: Fermi GBM Observation”, *GRB Coordinates Network* **2021**, *30573*, 1.

[262] D. A. Kann et al., “GRB 210731A: VLT/X-shooter redshift”, *GRB Coordinates Network* **2021**, *30583*, 1.

[263] R. Willingale et al., “Calibration of X-ray absorption in our Galaxy”, *onthly Notices of the Royal Astronomical Society* **2013**, *431*, 394–404.

[264] E. Derishev, T. Piran, “GRB Afterglow Parameters in the Era of TeV Observations: The Case of GRB 190114C”, *The Astrophysical Journal* **2021**, *923*, 135.

[265] Y. M. Lipkin et al., “The Detailed Optical Light Curve of GRB 030329”, *The Astrophysical Journal* **2004**, *606*, 381.

[266] F. Knust et al., “Long optical plateau in the afterglow of the short GRB 150424A with extended emission. Evidence for energy injection by a magnetar?”, *Astronomy & Astrophysics* **2017**, *607*, A84.

[267] A. Pozanenko et al., “GRB 190627A: NUTTelA-TAO optical counterpart observations.”, *GRB Coordinates Network* **2019**, *24900*, 1.

[268] R. B., private communication, **2014**.

[269] R. Gupta et al., “GRB 201024A: 1.3m DFOT optical observations”, *GRB Coordinates Network* **2020**, *28782*, 1.

[270] H. Kumar et al., “GRB 210610B: GIT optical detection”, *GRB Coordinates Network* **2021**, *30174*, 1.

[271] Y.-N. Wei et al., “GRB 210610B: The Internal and External Plateau as Evidence for the Delayed Outflow of Magnetar”, *Research in Astronomy and Astrophysics* **2024**, *24*, 075013.

[272] M. Blazek et al., “GRB 210619B: Liverpool Telescope r’-band observations”, *GRB Coordinates Network* **2021**, *30274*, 1.

[273] D. Eichler, E. Waxman, “The Efficiency of Electron Acceleration in Collisionless Shocks and Gamma-Ray Burst Energetics”, *Astrophysical Journal* **2005**, *627*, 861–867.

[274] S. de Wet et al., “The triple-peaked afterglow of GRB 210731A from X-ray to radio frequencies”, *Astronomy & Astrophysics* **2023**, *671*, A116.

[275] S. de Wet et al., “The triple-peaked afterglow of GRB 210731A from X-ray to radio frequencies”, *Astronomy & Astrophysics* **2023**, *671*, A116.

[276] H. Ashkar et al., “The Case of the Missing Very High-energy Gamma-Ray Bursts: A Retrospective Study of Swift Gamma-Ray Bursts with Imaging Atmospheric Cherenkov Telescopes”, *The Astrophysical Journal* **2024**, *964*, 57.

[277] W. Pauli, “Dear radioactive ladies and gentlemen”, *Phys. Today* **1978**, *31N9*, 27.

[278] E. Fermi, “Versuch einer Theorie der β-Strahlen. I”, *Zeitschrift fur Physik* **1934**, *88*, 161–177.

[279] M. G. Aartsen et al., “Constraints on Galactic Neutrino Emission with Seven Years of IceCube Data”, *Astrophysical Journal* **2017**, *849*, 67.

[280] D. Smith, D. Hooper, A. Vieregg, “Revisiting AGN as the source of IceCube’s diffuse neutrino flux”, *Journal of Cosmology and Astroparticle Physics* **2021**, *2021*, 031.

[281] N. Kurahashi, K. Murase, M. Santander, “High-Energy Extragalactic Neutrino Astrophysics”, *Annual Review of Nuclear and Particle Science* **2022**, *72*, 365–387.

[282] K. Bechtol et al., “Evidence against Star-forming Galaxies as the Dominant Source of Icecube Neutrinos”, *The Astrophysical Journal* **2017**, *836*, 47.

[283] A. Vieregg et al., “Astrophysics Uniquely Enabled by Observations of High-Energy Cosmic Neutrinos”, *Bulletin of the American Astronomical Society* **2019**, *51*, 185.

[284] IceCube Collaboration et al., “Neutrino emission from the direction of the blazar TXS 0506+056 prior to the IceCube-170922A alert”, *Science* **2018**, *361*, 147–151.

[285] J. G. Quiles, Investigating starburst-driven neutrino emission from galaxies in the Great Observatories All-Sky LIRG Survey, `https://astrobites.org/2024/03/02/goals-neutrinos/`, [Online; accessed 04-October-2024], **2024**.

[286] IceCube Collaboration, “Evidence for High-Energy Extraterrestrial Neutrinos at the IceCube Detector”, *Science* **2013**, *342*, 1242856.

[287] IceCube Collaboration et al., “Evidence for neutrino emission from the nearby active galaxy NGC 1068”, *Science* **2022**, *378*, 538–543.

[288] F. Schüssler, "Joint searches by FACT, H.E.S.S., MAGIC and VERITAS for VHE gamma-ray emission associated with neutrinos detected by IceCube", *PoS* **these proceedings**, *ICRC2023*, 1470.

[289] R. Abbasi et al., "IceCat-1: The IceCube Event Catalog of Alert Tracks", *The Astrophysical Journal Supplement Series* **2023**, *269*, 25.

[290] M. Wood et al., "Fermipy: An open-source Python package for analysis of Fermi-LAT Data", *PoS* **2017**, *ICRC2017*, 824.

[291] Fermi Science Support Development Team, *Fermitools: Fermi Science Tools*, Astrophysics Source Code Library, record ascl:1905.011, **2019**.

[292] R. Willingale et al., "Calibration of X-ray absorption in our Galaxy", *Monthly Notices of the Royal Astronomical Society* **2013**, *431*, 394–404.

[293] M. Hauser et al., "ATOM - an Automatic Telescope for Optical Monitoring", *Astronomische Nachrichten* **2004**, *325*, 659–659.

[294] G. Stratta et al., "The ASDC SED Builder Tool description and Tutorial", *arXiv e-prints* **2011**, arXiv:1103.0749.

[295] "IceCube-211125A: IceCube observation of a high-energy neutrino candidate track-like event", *GRB Coordinates Network* **2021**, *31126*, 1.

[296] R. Stein et al., "Classification of AT2021afpi, a possible counterpart to IC211125A, as a classical nova", *The Astronomer's Telegram* **2021**, *15069*, 1.

[297] H. Abdalla et al., "H.E.S.S. discovery of very high energy γ-ray emission from PKS 0625-354", *Monthly Notices of the Royal Astronomical Society* **2018**, *476*, 4187–4198.

[298] HESS Collaboration et al., "H.E.S.S. discovery of very high energy γ-ray emission from PKS 0625-354", *Monthly Notices of the Royal Astronomical Society* **2018**, *476*, 4187–4198.

[299] D. C. Ellison, S. P. Reynolds, "A Determination of Relativistic Shock Jump Conditions Using Monte Carlo Techniques", *Astrophysical Journal* **1991**, *378*, 214.

[300] E. L. Wright, "A Cosmology Calculator for the World Wide Web", *Publications of the Astronomical Society of the Pacific* **2006**, *118*, 1711–1715.

[301] E. L. Wright, A Cosmology Calculator for the World Wide Web, **2018**, `https://www.astro.ucla.edu/~wright/CosmoCalc.html` (visited on 07/17/2023).

Appendices

Appendix A.

Flux re-scaling with different redshift

A.1. The Inverse Square Law and re-scaling the fluxes

Essentially, I want to re-scale the flux measurements based on a change in distance, while considering how the change in distance affects the apparent flux of the object. To do this, I will need to use the inverse square law, which states that the flux decreases inversely with the square of the distance. When considering redshift (z), which accounts for the expansion of the universe, we need to take into account the change in luminosity distance D_L as well. If we denote the initial luminosity distance as D_{L1}, the initial flux as F_1, and the redshift as z, then the relationship between the initial and new flux can be expressed as:

$$F_2 = F_1 \times \left(\frac{D_{L_1}}{D_{L_2}}\right)^2 \tag{A.1}$$

In terms of redshift, we would write the following:

$$F_2 = F_1 \times \left(\frac{(1+z_2) \times \int_0^{z_2} \frac{dz}{H(z)}}{(1+z_1) \times \int_0^{z_1} \frac{dz}{H(z)}}\right)^2, \tag{A.2}$$

where $H(Z)$ is the Hubble parameter as a function of redshift. In a flat Lambda-CDM universe [243], the Hubble parameter $H(z)$ can be expressed as:

$$H(z) = H_0 \times \sqrt{\Omega_m \times (1+z)^3 + \Omega_\Lambda}, \tag{A.3}$$

where H_0 is the Hubble constant, Ω_m is the matter density parameter, and Ω_Λ is the dark energy density parameter.

Appendix B.

Numerical calculation of 1-zone SSC afterglow model

B.1. Shock parameters

After the initial burst, the explosion injects energy E_{expl} given by:

$$E_{expl} = \Gamma_{sh}^2 M c^2, \tag{B.1}$$

where M is the mass of the material swept by the shock and Γ_{sh} is the shock Lorentz factor, which determine how the shock wave decelerates after it sweeps up materials. Typically E_{expl} is on the order of $10^{51} - 10^{54}$ ergs. This explosion forms then a relativistic shock wave which moves outward at nearly the speed of light (c). There are two scenarios of the circumburst media in which the explosion may expand in: A constant density medium which is similar to the ISM and a wind-like medium in which the environment is strongly influenced by the wind of the progenitor star (e.g. like a molecular cloud). As the shock expands we can determine how far the shock has traveled from the explosion site through a relation between Γ_{sh} and the radius of the shock front from the central engine as follows:

$$R_{shock} = Const \times \frac{\Gamma_{sh}^2 c\, t_{obs}}{(1+z)}, \tag{B.2}$$

where the constant is equal to 8 for a uniform density medium and 4 for the wind medium, and comes from relativistic hydrodynamics. t_{obs} is the time since the explosion in the observer's frame and z is the redshift of the source. Therefore, from Eq. B.1, the Lorentz factor is given by:

$$\Gamma_{sh} = \sqrt{\frac{E_{expl}}{M c^2}}. \tag{B.3}$$

In the ISM scenario the density is constant, so with a volume $V = \frac{4}{3}\pi R_{sh}^3$, the swept-up mass is given by $M = n_1 m_p V$ with n_1 the number density of particles in unit of cm^{-3} and m_p the mass of proton. With these quantities, Eq. B.3 for a constant scenario becomes:

$$\Gamma_{sh} = \left[\frac{17(1+z)^3 E_{expl}}{4096\pi n_1 m_p c^5\, t_{obs}^3}\right]^{\frac{1}{8}}. \tag{B.4}$$

For a wind-like medium, we first assume that the progenitor star has a mass-loss rate $\dot{m}$ and a wind speed v_w. With these quantities, the number density $n_1(r)$ of the material at distance r, decreases as r^{-2} and is given by:

$$n_1(r) = \frac{A}{R_{sh}^2}, \quad \text{with} \quad A = \frac{\dot{m}}{4\pi v_w m_p}. \tag{B.5}$$

Here A is a constant that equals to A$_{35} \times 10^{35}\,\mathrm{cm}^{-1}$, which corresponds to a mass-loss rate of $\dot{m} = 10^{-5}\, M_\odot\, yr^{-1}$ and wind velocity $v_w = 3000\, km\, s^{-1}$ for a WR-like star. The constant A$_{35}$ ranges from 0.1 to 10 [268]. With these quantities in Eq. B.5, the Lorentz factor for wind-like medium becomes:

$$\Gamma_{sh} = \left[\frac{9(1+z)E_{expl}}{32\pi m_p c^3 A\, t_{obs}}\right]^{\frac{1}{4}}, \tag{B.6}$$

Note that the shock Lorentz factor is initially high and ranges within $\Gamma_{sh} \sim 100 - 1000$ for GRBs [22].

As the shock expands from the exploding region (upstream region) some materials are left behind (downstream or post-shock region). The material in the post-shock region also moves relativistically with a Lorentz factor Γ_2 which is slightly smaller than Γ_{sh} and is given by:

$$\Gamma_2 = \frac{\Gamma_{sh}}{\sqrt{2}},$$

which describes the bulk motion of the shocked materials. Because of the relativistic motion of the shock, there is a Doppler effect related to the post-shock region through the Doppler factor as:

$$D = 2\Gamma_2,$$

which enhances the observed radiation. This radiation is beamed into a relativistic jet toward the Earth and therefore makes the afterglow much brighter than it would be otherwise. In the post-shock region, the pressure P_2 becomes high due to the injected energy by the shock. This pressure is useful as it provides the energy that powers the afterglow emission especially through the synchrotron radiation as electrons are accelerated in the magnetic field. The post-shock pressure is related to Γ_2 through:

$$P_2 = \frac{4}{3}\Gamma_2^2 n_1 m_p c^2,$$

where n_1 is the number density of the shocked materials and is expected to range from 0.01-10 [268]. The fact that $P_2 \propto \Gamma_2$ shows that the post shock region is extremely energetic as time evolves. The number density in the post-shock region is also related to Γ_2 as:

$$n_2 = 4\pi\Gamma_2 n_1,$$

which shows the compression of surrounding region material due to the shock, and the factor $4\Gamma_2$ arises from relativistic shock jump conditions [299].

A fraction of the shock's energy goes into magnetic field, which is necessary in the acceleration of charged particles in the jet. The strength of this magnetic field is therefore given by:

$$B_2 = \left(24\pi\epsilon_\beta P_2\right)^{1/2},$$

where, ϵ_β is the fraction of the post-shock energy density that goes into magnetic field, which is a crucial parameter for synchrotron radiation which is generally expected to be dominant in GRB afterglows and ranges from 10^{-5} to 10^{-2} [268]. Using the post-shock parameters n_2 and P_2, we can calculate the oscillation plasma frequency that is caused by the charged particles, which is important to understand the dynamics of the particle acceleration. This can be obtained using:

$$\omega_p = \left(\frac{n_2 e^2 c^2}{P_2}\right)^{1/2}, \tag{B.7}$$

where e is the electric charge.

Lastly there is, an additional important shock parameter that, in the context of GRB afterglow, describes the influence of the magnetic field structures and plasma frequency in the post-shock region (downstream region) on particle acceleration and energy distribution. It is specifically a dimensionless parameter associated with the particle gyration or energy dissipation in the turbulent magnetic fields structure created behind the shock front (downstream). This parameter is defined as:

$$a = \frac{l_w\, c\, e\, B_2}{\omega_p m_e c^2}, \tag{B.8}$$

where l_w is the characteristic length scale often related to the turbulence or magnetic field structure in the shocked plasma, and m_e is the mass of electron. The values of l_w ranges from 100 to 10^4 when trying to adjust the synchrotron curve to reach the X-ray data, though this can be higher [231].

To describe the relation between the turbulence and particle acceleration (e.g. electrons) in the post-shock region, we define a new parameter called the critical length scale "a_{crit}" which determines how efficiently electrons radiate via synchrotron emission. The critical length scale is therefore defined as:

$$a_{crit} = \left(\frac{3 m_e l_w c^3}{2 e^2 \omega_p} \right)^{1/3}. \tag{B.9}$$

The magnetized maximum Lorentz factor that electrons accelerated relativistically in the post-shock region is given by:

$$\Gamma_{max,mag} = l_w \left(\frac{m_p}{m_e} \right) \epsilon_\beta \sigma_u^{-1/2}, \tag{B.10}$$

where $\sigma_u = \frac{B_2^2}{4\pi n_2 m_p c^2}$ is the external or upstream magnetization parameter. This is particularly important for modeling the synchrotron emission from GRB afterglows, as it can reveal the characteristic of the high energy tail of the spectrum. Now as the electron continuously interact with the magnetic field in the post-shock region, synchrotron radiation (photons) will be emitted whose maximum characteristic frequency radiation is given by:

$$\nu_{max}^{rad} = \frac{D\, h_1 B_2 a_{crit}^2}{2.4180 \times 10^{20} (1+z)}, \tag{B.11}$$

where $h_1 = 1.3 \times 10^6$ is a constant. The maximum synchrotron frequency is radiated by electrons in turbulent post-shock region of the relativistic shock. This is where most of energetic electrons with Γ_{max} generate highest-energy synchrotron photons. It is a crucial parameter as it helps to define the cut-off in the HE spectrum. On the other hand the minimum Lorentz factor Γ_{min} of electrons in the model is given by:

$$\Gamma_{min} = \left(\frac{p-2}{p-1} \right) \epsilon_e \left(\frac{m_p}{m_e} \right) \Gamma_2 \tag{B.12}$$

where ϵ_e is the fraction of shock energy in electrons. This parameter ranges within $10^{-3} - 0.1$ [268]. Similarly, the minimum characteristic frequency of the synchrotron radiation generated by these electrons will be:

$$\nu_{min} = D\, h_1 B_2 \Gamma_{min}^2, \tag{B.13}$$

where D is the Doppler factor. After a certain period of time, the particles (electrons) lose all their energy to radiation and hence their Lorentz factor approaches the "cooling" Lorentz factor and is given by:

$$\Gamma_c = \frac{2\Gamma_2 c}{h_0 B_2^2 R_{sh}}, \tag{B.14}$$

where $h_0 = 1.29 \times 10^{-9}\, G^{-2}\, s^{-1}$. Therefore, the synchrotron frequency becomes the cooling frequency and is defined as:

$$\nu_c = D\, h_1 B_2 \Gamma_c^2. \tag{B.15}$$

B.2. SSC spectrum parameters

For a typical GRB, the synchrotron emission occurs in the slow cooling regime when $\nu_{min} < \nu_c$. We assume that electrons are distributed in the post-shock region, within a thin homogeneous shell. The injected electrons have a broken power-law spectrum in the form of:

$$f(\nu) \propto \begin{cases} \nu^{1/3}, & \text{if } \nu < \nu_{min}. \\ \nu^{\frac{-(p-1)}{2}}, & \text{if } \nu_{min} < \nu < \nu_c \\ \nu^{-p/2} e^{-(\nu/\nu_{max})}, & \text{if } \nu > \nu_c, \end{cases} \tag{B.16}$$

where p is the spectral index of the electron energy distribution.

we calculated also the maximum Lorentz factor of the electrons in the post-shock region depending on the electron distribution whose index is p. We divided this into two cases, for the case where $p < 2$ and for the case where $p > 2$. For the first case, a new parameter η_{inj} accounts for adjusting the flux level of the model to the observed data. This parameter η_{inj} was set to 1.0 in all cases [268]. Therefore, the maximum Lorentz factor for the case $p < 2$ is given by:

$$\Gamma_{max} = \left(\frac{(2-p)}{(p-1)} \frac{m_e\, \epsilon_e}{\eta_{inj}\, m_p \Gamma_2} \right)^{\frac{1}{2-p}}. \tag{B.17}$$

And hence the maximum frequency in this case can be written as:

$$\nu_{max} = D\, h_1 B_2 \Gamma_{max}^2. \tag{B.18}$$

Now, considering an element of this homogeneous shell mentioned above, we need to compute the flux number density in that particular shell as follows:

$$\frac{dF}{dA} = m_e c^2 \|\dot{\Gamma}_{syn}\| \frac{dn}{d\Gamma_e}\frac{d\Gamma_e}{d\nu}, \tag{B.19}$$

where $\dot{\Gamma}_{syn}$ is the cooling rate due to synchrotron losses only and $\frac{dn}{d\Gamma_e}$ is the differential particle number per unit area. In this case, for a single-zone model, the maximum number flux density (i.e. the peak flux density) can be estimated to be $\left(\frac{dF}{dA}\right)_{peak}$ (i.e. at ν_{peak}). Therefore, the total differential flux density for a synchrotron emission is given by [268]:

$$f^{syn}(\nu) = f_{peak}\begin{cases}\left(\frac{\nu}{\nu_{min}}\right)^{-(p-1)/2}, & \text{for } \nu_{min} < \nu < \nu_c. \\ \left(\frac{\nu_c}{\nu_{min}}\right)^{\frac{-(p-1)}{2}}\left(\frac{\nu}{\nu_c}\right)^{-p/2}, & \text{for } \nu_c < \nu < \nu_{max} \\ 0, & \text{otherwise,}\end{cases} \tag{B.20}$$

where $f_{peak} = \frac{1}{D_L^2}\frac{h_0 m_e c^2}{3h_1} B_2 n_1 R_{sh}^3 \Gamma_2$ and with D_L the luminosity distance. For each GRB from our sample with redshift, the luminosity distance was obtained from online [300, 301] (see Table 5.7).

To compute the SSC emission one needs to first estimate the specific synchrotron radiation energy density within the source and then use it to compute the IC up-scattering of these photons by relativistic electrons. This can be done by calculating the specific radiation intensity or luminosity in the source surface at a given solid angle (i.e $I_\nu = \frac{dF}{dAd\Omega}$), by assuming that the source is homogeneous and isotropic. Adopting this model and considering the same electron distribution as the synchrotron emission (see Eq. B.19), the resulting SSC flux density, taking consideration of the full KN expression, is given by [231]:

$$F^{SSC}(\nu_{IC}) = 3\sigma_T \int_{\Gamma_{sh}}^{\Gamma_{max}} d\Gamma_e \frac{dn}{d\Gamma_e}\left(1 - \frac{h\nu_{IC}}{D\Gamma_{sh} mc^2}\right) \times \int_{\frac{1}{4\Gamma_{sh}^2}}^{1} dz g(z) F^{syn}\left(\frac{\nu_{IC}}{4\Gamma_{sh}^2} z\left(1 - \frac{h\nu_{IC}}{D\Gamma_{sh} mc^2}\right)\right), \tag{B.21}$$

where $g(z) = 1 + z + 2z\ln z - 2z^2 + \frac{1-z}{2}\left[\frac{\left(h\nu_{IC}/D\Gamma_{sh}mc^2\right)^2}{\left(1-h\nu_{IC}/D\Gamma_{sh}mc^2\right)}\right]$. Note again that Γ_e is the electron Lorentz factor in the post-shock (downstream) region. This model takes full consideration of the KN correction to accurately have a full picture at the highest photon energies.